Tests for systematic effects in supernova cosmology

Serena Nobili

Stockholm University
Department of Physics
2004

Thesis for the degree of doctor in philosophy in physics
Department of Physics
Stockholm University
Sweden

ISBN 91-7265-833-9 pp i-xii,73-74
Printed by Universitetsservice US AB, Stockholm

Abstract

Type Ia supernovae are used as standard candles to measure the energy density components of the universe. This led to the new paradigm in cosmology: only about 30% of the universe is made by ordinary pressureless matter, the rest is associated with an unknown form of energy with a negative equation of state parameter, called dark energy, able to drive the accelaration of the universe. The importance of this discovery requires to fully understand and control the possible systematic effects affecting both current and future measurements, aiming at probing the equation of state parameter, i.e. the nature of dark energy.

In this thesis, we tackle systematic effects involved in several aspects of supernova cosmology. Studies of supernova colours are used for investigating the homogeneity of the standard candle and to improve the spectral templates used for K-corrections. We have measured the intrinsic colour dispersion and assessed its correlation between different epochs of supernova evolution. We develop a technique for fitting the I-band ligthcurve and present studies of correlations of its properties with the SN luminosity. Moreover, we present a pioneer study of restframe I-band Hubble diagram extended at redshift ~ 0.5. This is found to be a valuable complementary tool for cosmological studies, and the results found are consistent with the concordance model of the universe, though the uncertainties are large. Presence of grey dust in the intergalactic medium is investigated both using the I-band Hubble diagram and supernova colour excess. Although the low statistics of the high redshift sample used do not allow to draw firm conclusions, both methods are tested and shown to be useful for probing the presence of intergalactic dust. The hypothesis of supernova population drift is tested in two different ways, both studying restframe I-band lightcurve properties and by comparing spectra of high redshift with those of nearby SNe. One distant supernova SN 2002fd (z=0.279) shows spectral similarities with 1991T/1999aa like objects. No signs of evolution in supernova properties is found in these studies, strengthening our confidence in the measured cosmological parameters.

Accompanying papers

Paper A S. Nobili, R. Amanullah, G. Garavini, A. Goobar, C. Lidman, V. Stanishev, G. Aldering, P. Astier, G. Blanc, M. S. Burns, A. Conley, S. E. Deustua, M. Doi, R. Ellis, S. Fabbro, A. S. Fruchter, G. Folatelli, S. Garmond, K. Garton, R. Gibbons, G. Goldhaber, D. E. Groom, D. Hardin, I. Hook, D. A. Howell, A. G. Kim, R. A. Knop, B. C. Lee, J. Mendez, P. E. Nugent, R. Pain, N. Panagia, C. R. Pennypacker S. Perlmutter, R. Quimby, J. Raux, N. Regnault, P. Ruiz-Lapuente, G. Sainton, B. Schaefer, K. Schahmaneche, E. Smith, A. L. Spadafora, M. Sullivan, N. A. Walton, L. Wang, W. M. Wood-Vasey, N. Yasuda
(THE SUPERNOVA COSMOLOGY PROJECT).
Restframe I-band Hubble diagram for Type Ia supernovae up to $z \sim 0.5$.
to be submitted

Paper B Nobili, S., Goobar, A., Knop, R., & Nugent, P.,
The intrinsic colour dispersion in Type Ia supernovae,
A&A, (2003), 404, 901N

Paper C G. Garavini, G. Folatelli, A. Goobar, C. Lidman, S. Nobili, G. Aldering, P. Astier, G. Blanc, M. S. Burns, A. Conley, S. E. Deustua, M. Doi, R. Ellis, S. Fabbro, A. S. Fruchter, S. Garmond, K. Garton, R. Gibbons, G. Goldhaber, D. E. Groom, D. Hardin, I. Hook, D. A. Howell, A. G. Kim, R. A. Knop, B. C. Lee, J. Mendez, P. E. Nugent, R. Pain, N. Panagia, C. R. Pennypacker S. Perlmutter, R. Quimby, J. Raux, N. Regnault, P. Ruiz-Lapuente, G. Sainton, B. Schaefer, K. Schahmaneche, E. Smith, A. L. Spadafora, V. Stanishev, M. Sullivan, N. A. Walton, L. Wang, W. M. Wood-Vasey, N. Yasuda
(THE SUPERNOVA COSMOLOGY PROJECT).
Search for spectral evolution in high-redshift Type Ia supernovae: evidence for SN 1991T/SN 1999aa-like object at z=0.279.
to be submitted

Paper D G. Folatelli, G. Garavini, S. Nobili, G. Aldering, R. Amanullah, P. Astier, C. Balland, G. Blanc, M. S. Burns, A. Conley, T. Dahlén, S. E. Deustua, R. Ellis, S. Fabbro, X. Fan, B. Frye, E. L. Gates, R. Gibbons, G. Goldhaber, B. Goldman, A. Goobar, D. E. Groom, D. Hardin, I. Hook, D. A. Howell, D. Kasen, S. Kent, A. G. Kim, R. A. Knop,

B. C. Lee, C. Lidman, J. Mendez, G. Miller, M. Moniez, M. Mouchet, A. Mourão, H. Newberg, P. E. Nugent, R. Pain, N. Panagia, O. Perdereau, S. Perlmutter, V. Prasad, R. Quimby, J. Raux, N. Regnault, J. Rich, G. T. Richards, P. Ruiz-Lapuente, G. Sainton, B. Schaefer, K. Schahmaneche, E. Smith, A. L. Spadafora, V. Stanishev, N. A. Walton, L. Wang, W. M. Wood-Vasey, N. Yasuda, T. York
(THE SUPERNOVA COSMOLOGY PROJECT).
The Nearby Supernova Cosmology Project Spectroscopic Follow-up: Uncertainty Estimation for Quantitative Studies
in prep

Publications not included in the thesis

Paper I Knop, R. A., Aldering, G., Amanullah, R., Astier, P., Blanc, G., Burns, M. S., Conley, A., Deustua, S. E., Doi, M., Ellis, R., Fabbro, S., Folatelli, G., Fruchter, A. S., Garavini, G., Garmond, S., Garton, K., Gibbons, R., Goldhaber, G., Goobar, A., Groom, D. E., Hardin, D., Hook, I., Howell, D. A., Kim, A. G., Lee, B. C., Lidman, C., Mendez, J., Nobili, S., Nugent, P. E., Pain, R., Panagia, N., Pennypacker, C. R., Perlmutter, S., Quimby, R., Raux, J., Regnault, N., Ruiz-Lapuente, P., Sainton, G., Schaefer, B., Schahmaneche, K., Smith, E., Spadafora, A. L., Stanishev, V., Sullivan, M., Walton, N. A., Wang, L., Wood-Vasey, W. M., Yasuda, N.
New Constraints on Ω_M, Ω_Λ, and w from an Independent Set of 11 High-Redshift Supernovae Observed with the Hubble Space Telescope
ApJ (2003) 598,102-132

Paper II Sullivan, M., Ellis, R. S., Aldering, G., Amanullah, R., Astier, P., Blanc, G., Burns, M. S., Conley, A., Deustua, S. E., Doi, M., Fabbro, S., Folatelli, G., Fruchter, A. S., Garavini, G., Gibbons, R., Goldhaber, G., Goobar, A., Groom, D. E., Hardin, D., Hook, I., Howell, D. A., Irwin, M., Kim, A. G., Knop, R. A., Lidman, C., McMahon, R., Mendez, J., Nobili, S., Nugent, P. E., Pain, R., Panagia, N., Pennypacker, C. R., Perlmutter, S., Quimby, R., Raux, J., Regnault, N., Ruiz-Lapuente, P., Schaefer, B., Schahmaneche, K., Spadafora, A. L., Walton, N. A., Wang, L., Wood-Vasey, W. M., Yasuda, N.
The Hubble diagram of type Ia supernovae as a function of host galaxy morphology.
MNRAS (2003) 340, 1057

Paper III G. Garavini, G. Folatelli, A. Goobar, S. Nobili, G. Aldering, A. Amadon, R. Amanullah, P. Astier, C. Balland, G. Blanc, M. S. Burns, A. Conley, T. Dahlén, S. E. Deustua, R. Ellis, S. Fabbro, X. Fan, B. Frye, E. L. Gates, R. Gibbons, G. Goldhaber, B. Goldman, D. E. Groom, J. Haissinski, D. Hardin, I. M. Hook, D. A. Howell, D. Kasen, S. Kent, A. G. Kim, R. A. Knop, B. C. Lee, C. Lidman, J. Mendez, G. J. Miller, M. Moniez, A. Mourão, H. Newberg, P. E. Nugent, R. Pain, O. Perdereau, S. Perlmutter, V. Prasad, R. Quimby, J. Raux, N. Regnault, J. Rich, G. T. Richards, P. Ruiz-Lapuente, G. Sainton, B. E. Schaefer, K. Schah-

maneche, E. Smith, A. L. Spadafora V. Stanishev, N. A. Walton, L. Wang, W. M. Wood-Vasey
(THE SUPERNOVA COSMOLOGY PROJECT).
Spectroscopic Observations and Analysis of the Peculiar SN 1999aa.
AJ submitted

Paper IV G. Garavini, G. Aldering, A. Amadon, R. Amanullah, P. Astier, C. Balland, G. Blanc, M. S. Burns, A. Conley, T. Dahlén, S. E. Deustua, R. Ellis, S. Fabbro, X. Fan, G. Folatelli, B. Frye, E. L. Gates, R. Gibbons, G. Goldhaber, B. Goldman, A. Goobar, D. E. Groom, J. Haissinski, D. Hardin, I. M. Hook, D. A. Howell, D. Kasen, S. Kent, A. G. Kim, R. A. Knop, B. C. Lee, C. Lidman, J. Mendez, G. J. Miller, M. Moniez, A. Mourão, H. Newberg, S. Nobili, P. E. Nugent, R. Pain, O. Perdereau, S. Perlmutter, V. Prasad, R. Quimby, J. Raux, N. Regnault, J. Rich, G. T. Richards, P. Ruiz-Lapuente, G. Sainton, B. E. Schaefer, K. Schahmaneche, E. Smith, A. L. Spadafora V. Stanishev, N. A. Walton, L. Wang, W. M. Wood-Vasey
(THE SUPERNOVA COSMOLOGY PROJECT).
SN 1999ac: On the presence of high velocity carbon.
to be submitted

Paper V C. Lidman, D. A. Howell, G. Folatelli, G. Garavini, S. Nobili, G. Aldering, R. Amanullah, P. Astier, C. Balland, G. Blanc, M. S. Burns, A. Conley, T. Dahlén, S. E. Deustua, R. Ellis, S. Fabbro, X. Fan, B. Frye, E. L. Gates, R. Gibbons, G. Goldhaber, B. Goldman, A. Goobar, D. E. Groom, D. Hardin, I. Hook, D. Kasen, S. Kent, A. G. Kim, R. A. Knop, B. C. Lee, J. Mendez, G. Miller, M. Moniez, M. Mouchet, A. Mourão, H. Newberg, P. E. Nugent, R. Pain, N. Panagia, O. Perdereau, S. Perlmutter, V. Prasad, R. Quimby, J. Raux, N. Regnault, J. Rich, G. T. Richards, P. Ruiz-Lapuente, G. Sainton, B. Schaefer, K. Schahmaneche, E. Smith, A. L. Spadafora, V. Stanishev, N. A. Walton, L. Wang, W. M. Wood-Vasey, N. Yasuda, T. York
(THE SUPERNOVA COSMOLOGY PROJECT).
Spectroscopic confirmation of high-redshift supernovae with ESO VLT.
in prep

Paper VI G. Folatelli, G. Garavini, A. Goobar, S. Nobili, G. Aldering, R. Amanullah, P. Astier, C. Balland, G. Blanc, M. S. Burns, A. Con-

ley, T. Dahlén, S. E. Deustua, R. Ellis, S. Fabbro, X. Fan, B. Frye, E. L. Gates, R. Gibbons, G. Goldhaber, B. Goldman, D. E. Groom, D. Hardin, I. Hook, D. A. Howell, D. Kasen, S. Kent, A. G. Kim, R. A. Knop, B. C. Lee, C. Lidman, J. Mendez, G. Miller, M. Moniez, M. Mouchet, A. Mourão, H. Newberg, P. E. Nugent, R. Pain, O. Perdereau, S. Perlmutter, V. Prasad, R. Quimby, J. Raux, N. Regnault, J. Rich, G. T. Richards, P. Ruiz-Lapuente, G. Sainton, B. Schaefer, K. Schahmaneche, E. Smith, A. L. Spadafora, V. Stanishev, N. A. Walton, L. Wang, W. M. Wood-Vasey, T. York
(THE SUPERNOVA COSMOLOGY PROJECT).
A new set of spectral quantities characterizing type Ia supernovae, and the correlations with peak luminosity.
to be submitted

Acknowledgements

I certainly take the opportunity to thank Ariel Goobar for his guidance during the past four years. He has stubbornly encouraged me to take my steps forward and grow as independent researcher, yet he was available for support any time I needed it. Working with him has been most inspiring, although it ended up by reinforcing my commitment to science.
Together with my colleagues and friends of the snova room, Rahman, Gaston and Gabriele, I have very much enjoyed spending my everyday life. But also with Martin, Edvard, Mia, Christofer, Vallery, Jakob, Pernilla and all the friends who shared with me thoughts and worries, even about physics.
To the Supernova Cosmology Project collaboration, and in particular to Chris Lidman and Rob Knop, with whom I had the opportunity to work in many occasions, I would like to express my gratitude for teaching me much about scientific research.
I am indebted to Christian Walck for all the coffee breaks we spent discussing many of my questions about statistics.
I would like to thank the people of the cake for having so enthusiastically accepted the challenge of "The cake on Friday", and made it a very special event for us all.
I am grateful to Iouri Belokopytov and Alexander Agapow, for their support with all my computer related problems. As well as to Britta Schmidt for doing her job so well, making our lives at the Physics Department a lot easier.
A very special thank goes to my family, my parents, my sister Federica and also my aunts, Miriam and Ninni, for giving me so much and always supporting me, even in my choice of living abroad. And to Gabriele, who is always by my side, making everything simpler and most enjoyable.
I dedicate this thesis to my mother, who encouraged me all along my studies, keeping saying that the sentence "I can not" does not exist.

Till sist, vill jag tacka Stockholm som har blivit min andra hemstad, där jag trivs och som jag kommer att sakna.

A mia madre

Contents

Chapter 1

Introduction

In 1998 both the Supernova Cosmology Project (SCP) and the High-Z Supernova Search Team (HZT) presented measurements of type Ia supernovae (SNe Ia), suggesting the presence of a non-zero cosmological constant, or dark energy density, causing the expansion of the universe to accelerate [40, 47]. These results, together with the assumption of a flat universe predicted by an inflationary model, would lead to a dark energy density $\Omega_\Lambda \sim 0.7$. Even without assumptions about the geometry, the supernova results alone exclude the scenario of a flat matter dominated universe at the 99 % confidence level. A few years later, measurements of the Cosmic Microwave Background Radiation (CMB) have proved the flatness of the universe (at the 2% level), first by balloon experiments, such as Boomerang and Maxima, and later on by the WMAP satellite [12, 3, 53]. The evidence for dark energy today is therefore strongly supported by cross-cutting cosmological results. The growing data sets both from the ground and space, push the measurements to the limit in which systematic uncertainties become dominant. Thus, the future of supernova cosmology is critically depending on our ability to control and correct for these uncertainties. This thesis is in the frame of the work carried on by the SCP in the last four years in this sense. It is based specifically on **Paper A** — **Paper D**, but it also involves some of the analyses described in **Paper I** —**Paper VI**, and, though these are not directly presented here, some references to them are needed to better understand the totality of this work. In general, I was involved in many aspects of the SCP project, spanning from observations at telescopes to data analysis.

In Chapter 2, I introduce cosmology and the use of supernovae as

calibrated standard candles and the low redshift Hubble diagram.

In Chapter 3, I present the results obtained using supernovae in cosmology, the accelerating universe, and the measurements of the cosmological parameters, Ω_M and Ω_Λ. This involves **Paper A**, **Paper B** and **Paper I**.

In Chapter 4, I discuss the possible systematic effects involved in supernova cosmology, e.g. extinction by dust, both in the host galaxy and in the intergalactic medium, contamination of different types of supernovae in the Hubble diagram, uncertainty in the K-corrections and the possibility of evolution of supernova properties with redshift. This involves the work in **Paper A**, **Paper B** and **Paper C**, and **Paper I**, **Paper II**.

In Chapter 5, I present the observations and reduction of the near infrared data of SN 2000fr, used in the analysis of **Paper A**, and discuss specific problems concerning astronomical observations in the NIR.

In Chapter 6, I discuss supernova properties, such as spectral homogeneity of nearby SNe, spectral comparison of low and high-z supernovae, colour properties and how this studies can be used to improve the spectral template for the K-corrections. This involves **Paper B**, **Paper C**, **Paper D** and **Paper I**, **Paper III**, **Paper IV**, **Paper V**, **Paper VI**.

Chapter 2

Type Ia Supernova Cosmology

2.1 Introduction

The goal of cosmology is the study of the history and evolution of the universe. Supernovae are excellent tools to help achieving this goal in many ways. Their use as distance indicators helps measuring not only the present value of the Hubble parameter, H_0, but allows also to follow its evolution back in time for several billion years. Because of their homogeneity and brightness, comparable to an entire galaxy under a period of a few weeks, supernovae are the most accurate known standard candles available to measure the evolution along a large part of the history of our universe. The measurement of the mass energy density as well as the vacuum density is only possible due to the homogeneity of type Ia supernova explosions. This measurements are today a reality at a level of precision which was inconceivable only a decade ago.

In this chapter we introduce some fundamental concepts to understand how supernovae can be used in cosmology.

2.2 The Standard Model

The theory of General Relativity (GR) of Einstein laid the foundations of what is today recognised as the standard model of cosmology. This is based on a "reasonable" assumption: the Universe is isotropic and homogeneous on large scales. In such a universe, the line element distance

between two objects with coordinates t, r, θ and ϕ, is expressed by the Roberson-Walker metric (RW),

$$ds^2 = -dt^2 + a(t)\left[\frac{dr^2}{1-kr^2} + r^2 d\theta^2 + r^2 \sin^2\theta d\phi^2\right] \tag{2.1}$$

where k is the curvature parameter, which assumes the value -1, 0, or 1 in a open, flat or closed universe respectively, and $a(t)$ is the scale factor. Introducing the RW metric in the field equations of General Relativity, leads to the Friedmann equation,

$$H^2(t) \equiv \left(\frac{\dot{a}(t)}{a(t)}\right)^2 = \frac{8\pi G\rho}{3} - \frac{k}{a^2} + \frac{\Lambda}{3} \tag{2.2}$$

where $H(t)$ is the Hubble parameter, whose value at present, $H_0 = H(t_0)$, is called the Hubble constant, and Λ is the cosmological constant. Eq. 2.2 describes the evolution of the universe, as far as we can observe it today. The expansion rate of the universe, $H(t)$, depends on the energy density of its components. Assuming the universe composed by different constituents, each having a fraction of density Ω_i, of the critical density,

$$\Omega_i = \frac{\rho_i}{\rho_{crit}} = \frac{\rho_i}{\frac{3H_0^2}{8\pi G}} \tag{2.3}$$

Eq. 2.2 becomes

$$H^2(z) = H_0^2\left[\Omega_M(1+z)^3 + \Omega_K(1+z)^2 + \Omega_\Lambda\right] \tag{2.4}$$

where

$$\begin{aligned} \Omega_M &= \tfrac{\rho_M}{\rho_{crit}} \\ \Omega_\Lambda &= \tfrac{\Lambda}{3H_0^2} \\ \Omega_K &= -\tfrac{k}{a^2 H_0^2} \end{aligned} \tag{2.5}$$

are the normalised dominant energy density components of the universe at the present time, each following its own equation of state $p = w\rho$. In the case of normal matter for instance $w = 0$, while $w = 1/3$ for radiation and $w = -1$ for the cosmological constant. In the case of exotic scalar fields being the source of dark energy, the value of w could even change with time, and it could in principle assume any finite value[1].

[1] In the simplest models $-1 \leq w \leq 1$, but that has been shown to be possible to circumvent.

Note that Eq. 2.4 implies $\Omega_M + \Omega_\Lambda + \Omega_K = 1$, i.e. there are only 2 independent parameters. The experimental measurements of the expanding universe and its cosmological parameters, Ω_M and Ω_Λ, is part of the aim of this work, (see **Paper I** and **Paper A**).

2.3 Redshift

A measurable effect of the cosmic expansion is the shift in wavelength that photons undergo while travelling through the universe. This makes an observer measure a longer wavelength than what was emitted, that is quantified by the *redshift* parameter, z, defined as

$$1 + z \equiv \frac{\lambda_{\rm obs}}{\lambda_{\rm emit}} \tag{2.6}$$

In the RW metric one can derive the relationship between the redshift and the scale factor,

$$1 + z \equiv \frac{a(t_{\rm obs})}{a(t_{\rm emit})} \tag{2.7}$$

As a consequence the redshift is often used in cosmology to refer to events that took place in the past when the scale of the universe was smaller.

2.4 Luminosity distance

The observed flux S from an object with intrinsic luminosity L, can be expresses as

$$S = \frac{L}{4\pi d_L^2(z)} \tag{2.8}$$

where the luminosity distance, $d_L(z)$, is a function of redshift and the cosmological parameters,

$$d_L = \frac{(1+z)c}{H_0|\Omega_k|^{1/2}} f\left(|\Omega_k|^{1/2} \int_0^z [\Omega_k(1+z')^2 + \Omega_M(1+z')^3 + \Omega_\Lambda]^{-1/2} dz'\right)$$

$$f(x) = \begin{cases} \sin(x), & k = 1, \\ x, & k = 0, \\ \sinh(x), & k = -1. \end{cases} \tag{2.9}$$

This integral can only be solved numerically. However, a Taylor expansion gives an approximation that holds in the nearby universe,

$$d_L = \frac{c}{H_0}\{z + z^2\left(\frac{1-q_o}{2}\right) + \mathcal{O}(z^3)\} \tag{2.10}$$

where the deceleration parameter, q_0, is defined as

$$q_0 = \frac{1}{2}\sum_i \Omega_i(1+3w_i) \tag{2.11}$$

Eq. 2.10 shows that in the nearby universe the luminosity distance scales linearly with the redshift, with H_0 as the constant of proportionality. At higher redshift the luminosity distance depends on the parameter q_0, or alternatively on the energy density of the universe. q_0 is called deceleration parameter for historical reasons. In an universe composed only by normal matter and cosmological constant, it will assume positive values in all the cases of energy distribution for which $\Omega_\Lambda < \Omega_M/2$, i.e. the universe decelerates, and negative values in the other cases, i.e. the universe accelerates. Thus, the luminosity distance can be used to probe cosmological parameters, given the existence of standard candles, as we will see in more details in the following sections.

2.4.1 The magnitude system

For historical reasons, it is quite common to measure luminosities of astronomical sources in logarithmic unites, called *magnitudes* or *apparent magnitudes*. These are defined as the brightness of an object through a certain filter f, as

$$m_f = -2.5\log\left(\int_0^\infty F(\nu)L(\nu)d\nu\right) + C_f \tag{2.12}$$

where $F(\nu)$ is the transmission function of the filter and C_f is a constant specific for the filter, sometimes called the filter zero point. The magnitude of an object is thus related to its luminosity distance (measured in Mpc[2]),

$$m(z) = M + 5\log d_L(z; H_0, \Omega_M, \Omega_\Lambda) + 25 \tag{2.13}$$

[2] $1Mpc = 3.26 \cdot 10^6 lightyears$, $1lightyear = 9.46 \cdot 10^{15} m$

where M is the *absolute magnitude*, which is defined as the apparent magnitude of an object if it was at the distance of 10 pc from the observer.

2.5 Type Ia Supernovae as standard candles

Supernovae are extremely bright point-like extragalactic sources. They are classified in different types, I and II, and subtypes, Ia, Ib, and Ic. Type Ia supernovae (SNe Ia) are the most luminous and homogeneous class. They are distinguished from other types thanks to a strong absorption feature due to Si II around 6150 Å, and the complete absence of hydrogen and helium lines at any time of the evolution. A typical SN Ia spectrum at the time of maximum brightness is shown in Figure 2.1, together with the Bessel standard system of photometry pass-bands [5].

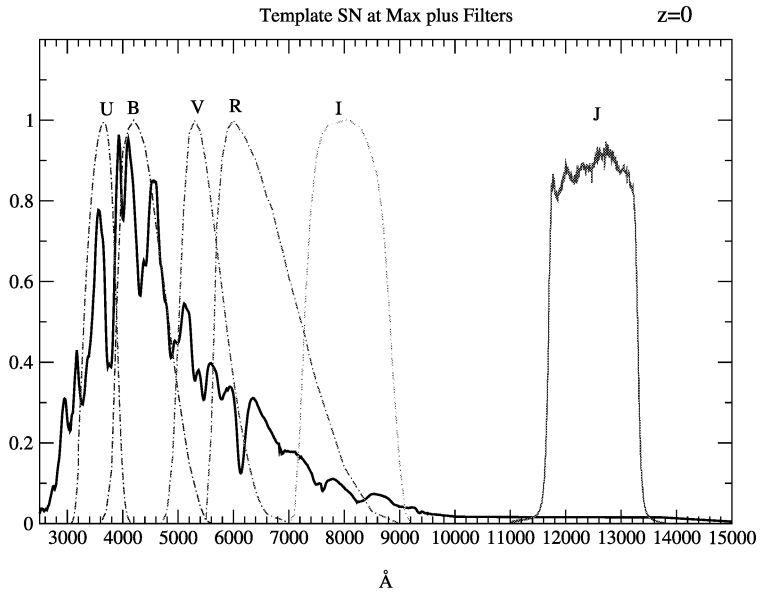

Figure 2.1: Spectral template of a typical SN Ia at the time of maximum brightness. Also plotted are the standard photometry pass-bands $UBVRIJ$ defined by Bessel [5].

There is evidence suggesting that a SN Ia is the result of a C+O white dwarf, accreting matter from a companion star until it reaches the Chandrasekhar mass[3] and thus, begin the thermonuclear explosion, [see, e.g., 8]. Even if the understanding of the physical process behind the explosion is not yet complete, this simple model helps explaining the observed homogeneity of SNe Ia. From an empirical point of view this type of supernovae show impressive similarities. The absolute magnitude measured in the B-band is $M_B \cong -19.4$ mag, depending on the value of H_0 assumed, with a dispersion of $\sim 0.3 - 0.4$ mag, [see, e.g., 7, 28]. SNe Ia show a characteristic lightcurve that peaks about 20 days after the explosion and then declines rapidly (diminishing its luminosity to about 60% in only 15 days) and fading almost completely within 1 year.

The absolute magnitude has been shown to correlate with the decline rate of the lightcurve by Phillips [44], fainter objects decline faster than brighter ones. Phillips parametrised this by computing the difference in magnitudes between the maximum of the lightcurve and 15 days after maximum, Δm_{15}. Correcting for this correlation reduces the dispersion in the absolute magnitude to $\lesssim 0.2$ mag. Since Phillips pointed out this correlation, new lightcurve parameterisations, similar to the Δm_{15}, have been introduced. The most common ones are the *multi-colour lightcurve shape method* (MLCS) [50], and the *stretch* method adopted by the SCP [41, 40]. Throughout this work we use the *stretch* method, unless otherwise specified. This is based on the observation that the entire range of SN Ia lightcurves can be obtained by simply stretching the average lightcurve along time up to 40-50 days after maximum, see Figure 2.2 [39]. This applies at least to B- and V-band. The advantage of the *stretch* method is not only in its simplicity, but also in the ability of describing the whole range of lightcurves using one parameter only, i.e. the stretch factor s. Thus, the peak magnitude can be corrected for the stretch, as $m^{\rm corr} = m + \alpha(s-1)$, in analogy to the Δm_{15} method.

SNe Ia homogeneity is also confirmed from a spectroscopic point of view. Figure 2.3 [15] shows the comparison of SNe Ia spectra at the time of maximum light. Note the Si II feature at about 6150 Å which characterise type Ia from other supernova types. The spectral homogeneity is topic of **Paper VI** and will be discussed further in Chapter 6.

[3]The Chandrasekhar mass is the limiting mass a white dwarf can reach before the gravitational force causes its collapse. Introduced by S. Chandrasekhar around 1930, corresponds to a value of about 1.4 solar masses [see 57, p. 1972].

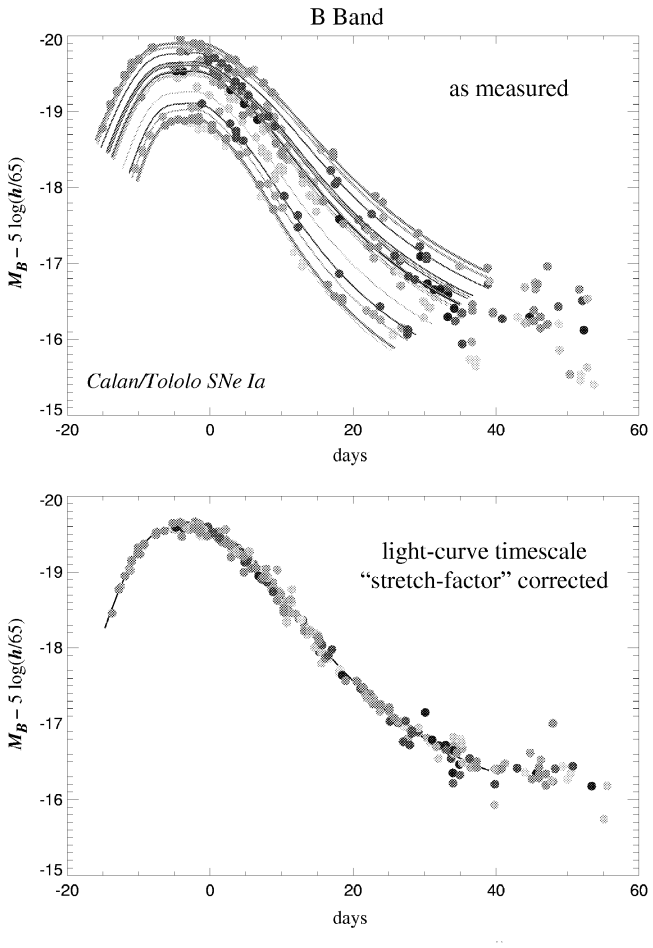

Figure 2.2: Intrinsic spread of B-band light curves of type Ia supernovae, without applying any correction (upper panel), after stretch correction. Credit [39].

With these premises, SNe Ia are the best distance indicator known to date, that can potentially be observed up z $\sim$ 2.

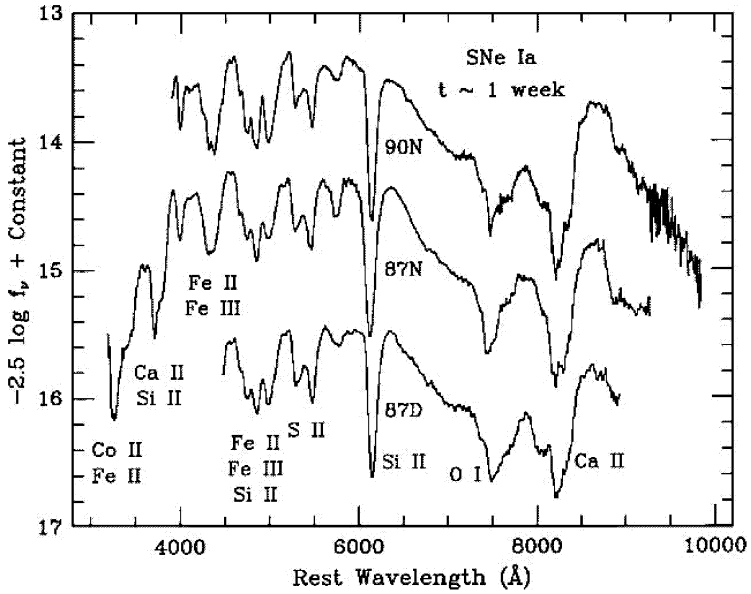

Figure 2.3: Spectral homogeneity of SNe Ia about one week past maximum brightness. Credit [15].

2.6 The expanding universe

2.6.1 A brief historical account

In order to compensate the gravitational attraction by matter, Einstein introduced the cosmological constant, Λ, in the equation of General Relativity, that, acting as a repulsive force, allowed the universe to be static, as it was believed to be at that time. However, as Friedmann pointed out, the instability of the solution of the GR equation for a homogeneous and isotropic universe was unavoidable, as any small perturbation from the assumed value, would cause the universe to start collapsing or expanding. In 1929 Edwin Hubble observed the expansion of the universe, making Einstein regret to have introduced Λ in his equations. Hubble measured recession velocities of distant galaxies and found them to be proportional to their distances, $v = H_0 \cdot d$. The proportionality constant, H_0, that we

already introduced in a previous section, was called after him and it is one of the fundamental parameters in cosmology. The Hubble diagram has been reproduced by many since, and even if the debate on the actual value of H_0 is somewhat still open, the expansion of the universe has been confirmed and it is now widely recognised.

2.6.2 Hubble diagram with type Ia supernovae

Given their nature, SNe Ia have been used as distance indicators in order to build the Hubble diagram. Figure 2.4 [42] shows the result of this exercise using 102 supernovae at redshift $0.01 < z < 0.2$. The difference between the apparent and absolute magnitude of the object, $m - M$, called *distance modulus*, is plotted against the redshift. The lower limit

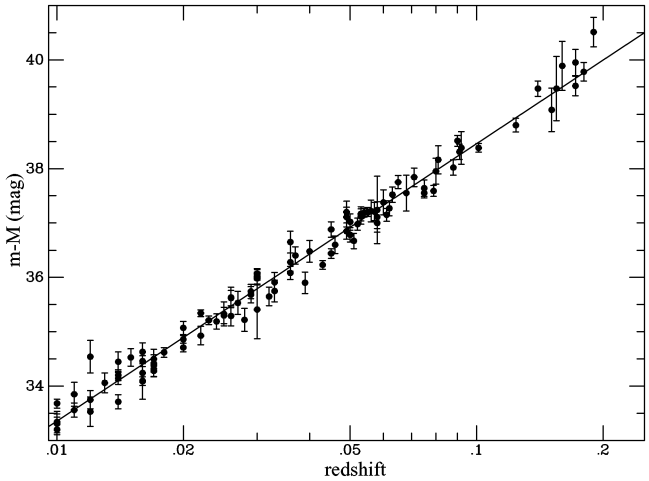

Figure 2.4: The Hubble diagram for SNIa from $0.01 < z < 0.2$. The 102 objects in this range have a residual about the inverse square line of $\sim 10\%$. Credit [42].

in redshift is set to be high enough for the determination of the distance not to be affected by peculiar velocities of the galaxy that hosts the supernova. These are typically of the order of 300 km/s. In this range of redshift the luminosity distance is nearly linear in z and the coefficient of proportionality is c/H_0, (see Eq. 2.10). The best fit to the data gives an estimate of the Hubble constant, when combined with the SNe Ia absolute magnitude.

The determination of the absolute magnitude, M, of supernovae de-

pends on the Cepheid method for calibrating the distance. Cepheids are variable stars, whose period of variation is related to their absolute brightness. The distance is then estimated measuring their apparent magnitude, and using the inverse square law. The adopted Period-Luminosity relation is the major source of systematic uncertainties involved with the method. Different teams have used Cepheids as calibrators for SNe Ia. However, their estimates of the Hubble constant agree only within the systematic uncertainty, giving and average value of $H_0 \sim 70 \pm 10 \text{km s}^{-1} \text{ Mpc}^{-1}$ [42].

The systematic uncertainties involved seems to be the major limitation in determining H_0 using SNe Ia. However, as we will see, this does not limit the use of these objects for the determination of other cosmological parameters, (see Section 3.4).

Chapter 3

The accelerating universe

3.1 Supernova search

In order to use type Ia supernovae in cosmology there is a need to discover and follow up a large number of them at a wide range of redshifts. Supernovae are in principle observable at very large distances, but the difficulties involved in their discovery at high redshift could be solved only with the introduction of wide-field CCD cameras in astronomy. A supernova explosion in a galaxy like the Milky Way is a quite rare event, happening only a few times every thousand years. However, searching in a large field of the sky, exposing in the R-band for about 10 minutes, corresponds to searching SNe in thousands of galaxies up to redshift $z \sim 0.5$. This increases significantly the probability of finding SNe Ia. For this reason, searching for nearby supernovae requires to scan larger sections of the sky than when searching for distant objects, though their brightness requires less exposure time.

In the early 90's the SCP developed a search strategy that could guarantee the discovery of a handful of supernovae for a given redshift range. This consists in observing the same field in the sky with a large field camera twice, with a time interval of about three weeks, corresponding to the rise time of the SN lightcurve. Variation of brightness of an object in the two images of the sky, could indicate the presence of an exploding supernova. Spectroscopic observations of the candidates is used to discard other variable objects, confirm the supernova type and provide an accurate measurement of the SN redshift. Multi-colour photometry observations could alternatively help to identify SNe Ia among the candidates

and constrain its redshift, though spectroscopic redshift determinations are more accurate. This strategy has also the advantage to select SNe that are on the rise or around their maximum light, a condition that is very important for fitting the SN lightcurve, and extract the peak brightness.

As more telescope time is now spent on supernova searches, the strategy has been recently improved, introducing what is called a *rolling search*. This consists in observing the same fields every 3-4 days. Since many SNe are expected to explode in the monitored region, this technique has the advantage of following the lightcurve while searching for other SNe in the same spot of the sky. This strategy has been used successfully in the most recent search campaigns by the SCP and it is fully adopted by other recently started projects, such as the the SNLS with CFHT-Megacam and ESSENCE with Mosaic Imager at CTIO 4.0m [38, 52].

Special care has to be used in searching for distant supernovae to avoid introducing systematic effects. For instance, the limiting magnitude of the search, i.e. the faintest SN magnitude detectable, can significantly affect the determination of the cosmological parameters if it was not chosen with care. This depends on the exposure time and the filter used for the observations. The choice of the filter is set according to the redshift targeted in the search. For instance, if the search is aimed to discover SNe Ia at $z \sim 0.5$, then R-band ($\lambda_{eff} \cong 0.66\mu m$) is normally preferable, that corresponds to rest-frame B-band ($\lambda_{eff} \cong 0.44\mu m$), according to Eq. 2.6. The exposure time instead is set by taking into account the efficiency of the instrument used and computing the apparent magnitude SNe Ia are expected to have at their maximum luminosity at the targeted redshift, due to the cosmology. This calculation involves performing K-corrections, described in the next section.

During the time of this thesis I was involved in several search campaigns conducted by the SCP between 2000 and 2003, using both techniques to discover SNe up to redshift $\sim$1 (see IAU circulars, 7763, 7764, 7971, 7977, 7993, 8119, 8120, 8121). I took part on the spectroscopic SN identification, involving both observations and data reduction for the determination of the SN type at the Very Large Telescope (VLT). Moreover, I was involved in observing final reference data at NOT for the supernovae discovered during the low-z spring 1999 campaign and I took part to the whole spectroscopy data set reduction, see Chapter 6. Additionally, during the spring 2000, I was involved in the search and follow

up of intermediate-z SNe of the European Supernova Consortium (ESC) campaign (IAU circular 7406).

3.2 K-corrections

Cosmological redshift induces wavelength shift toward larger values of λ. When observing a distant supernova in a certain bandpass, this correspond to a different rest-frame wavelength given by Eq. 2.6. This effect can be corrected for quite accurately, thanks to the homogeneity of the SN Ia spectra [26]. The spectrum is integrated over the rest-frame bandpass, then red-shifted and integrated over the observed bandpass. The correction, expressed in magnitudes, is called K-correction and it is given by:

$$K_{ij} = 2.5 \log \left[(1+z) \frac{\int F(\lambda) S_i(\lambda) d(\lambda)}{\int F(\lambda/(1+z)) S_j(\lambda) d(\lambda)} \frac{\int Z(\lambda) S_j(\lambda) d(\lambda)}{\int Z(\lambda) S_i(\lambda) d(\lambda)} \right] \quad (3.1)$$

where K_{ij} is the K-correction from the observed filter i to rest-frame filter j, F(λ) is the spectrum of the supernova, S(λ) is the bandpass, and Z(λ) is the spectrum corresponding to the zero magnitude of the filter, e.g. Vega spectrum. This correction is used in Eq. 2.13, as,

$$m_i(z) = M_j + 5 \log d_L(z; H_0, \Omega_M, \Omega_\Lambda) + 25 + K_{ij} \quad (3.2)$$

The main source of uncertainty is the knowledge of the supernova spectrum. Secondary sources of uncertainty are the accuracy of the filter zero magnitude and the bandpass shape, including the optics and detector.

The SN spectrum is usually not known at all epochs, since typically only few spectra are taken to allow type identification, with the exception of dedicated spectroscopic studies of SNe Ia, where the same object is observed along time to follow its spectral evolution. In order to compute the K-corrections one can either choose the spectrum of another individual SN or use spectroscopic templates, built by averaging together spectra of well observed nearby SNe Ia. In this sense, the uncertainty introduced depends on the spectroscopic diversity of SNe Ia. Thus, choosing the spectrum of a SN which is not spectroscopically identical to the one to be corrected, could affect the estimated K-correction.

However, changes in single spectral features do no significantly affect K-corrections, [36]. These are instead mainly determined by the SN colour. Therefore, the knowledge of the SN colour diminishes the uncertainty on its K-corrections. A possible exception to this is the near-infrared (NIR) region of the spectrum, where a large absorption feature, the Ca IR triplet, is observed to vary significantly among SNe Ia. Quantitative studies of this variation are missing, due to lack of a homogeneous set of spectroscopic data covering this range of wavelengths. However, due to the position of the Ca IR triplet feature in the spectrum, this affects only observations corresponding to rest-frame I-band, (see Figure 2.1).

In **Paper B** we present a thorough study of the average B, V, R, I colour as a function of time of normal SNe Ia and used the result to improve the spectral template to be used for computing the K-corrections.

3.3 Determining cosmological parameters

The use of type Ia SNe as distance indicators allow to determine cosmological parameters at a very high precision level. As we have seen in Chapter 2, nearby supernovae have been used to estimate the value of the Hubble parameter at present, H_0. However, the difficulties involved in the determination of the distance of these objects, makes this estimates not free from systematic uncertainties. Fortunately this does not affect our ability to determine the values of Ω_Λ and Ω_M, since the Hubble constant only affects the estimation of the absolute magnitude, and its contribution cancel in the equation when probing for relative distances, which is what enters in the study of the energy density components. Eq. 2.13 can be re-written as

$$m = \mathcal{M} + 5\log \mathcal{D}_\mathcal{L}(z; \Omega_m, \Omega_\Lambda) - \alpha(s-1) + K \tag{3.3}$$

where $\mathcal{M} = M - 5\log H_0 + 25$ is the Hubble-constant-free peak absolute magnitude, $\mathcal{D}_\mathcal{L} = H_0 d_L$ is the Hubble-constant-free luminosity distance, s is the stretch factor introduced in Section 2.5 and K is the K-correction. Note that $\mathcal{M}$ is one of the free parameters in the fit, together with the cosmological parameters, thus also low-z SNe are required for a robust fit of the Ω's.

The Hubble diagram is usually built in the B-band for both historical and practical reasons:

1. Supernovae are intrinsically blue, i.e. they are brighter in B- and V-band than in other bands. For example, at maximum light they are 0.5 mag brighter in B-band than in I-band.

2. Up to z∼1 the corresponding red-shifted B-band it is still in the optical region of the spectrum, in which CCD cameras have good sensitivity.

3. CCD cameras sensitivity in the B-band is usually better than in other bands, or at least at the time supernovae observations started. Recent improvement of CCD technology together with the development of infrared detectors give the possibility to extend the Hubble diagram in other bands (see **Paper A**).

4. The width-luminosity relation that standardise the supernova candle, holds in B-band.

The B-band Hubble diagram for SNe Ia up to redshift ~ 0.5 was first published in 1998 by two different teams, the Supernova Cosmology Project (SCP) and the High-Z Supernova Search Team (HZT), and allowed to determine the cosmological parameters, Ω_Λ and Ω_M, showing the acceleration of the universe.

Today, SNe Ia are still used to confirm and improve this first estimate by observing this objects at higher redshifts. **Paper I** presents space observations of 11 SNe Ia obtained at the Hubble Space Telescope (HST). This data, together with the SNe published by Perlmutter et al. [40], is used to extend the Hubble diagram to redshift ~ 1. This is shown in Figure 3.1, together with three models, obtained with different values of the cosmological parameters. The best fit assuming a flat universe is given by $\Omega_M = 0.25^{+0.07}_{-0.06} \pm 0.04$ and $\Omega_\Lambda = 0.75^{+0.06}_{-0.07} \pm 0.04$, where the uncertainties are the statistic and the systematic respectively.

3.4 The Ω_Λ – Ω_M plane

From Eq. 3.3, Goobar and Perlmutter [19] inferred an important property of the parameter space. Observations of standard candles at one given redshift z, for an assumed combination of the cosmological parameters, would be represented by a band in the Ω_Λ – Ω_M plane, where the width of the band is defined by the uncertainty on the measured apparent magnitude and the intrinsic scatter in the supernova brightness, as shown by [17]. Figure 3.2 (from [17]) shows how the allowed band changes inclination with the redshift bin observed (left panel), where an uncertainty

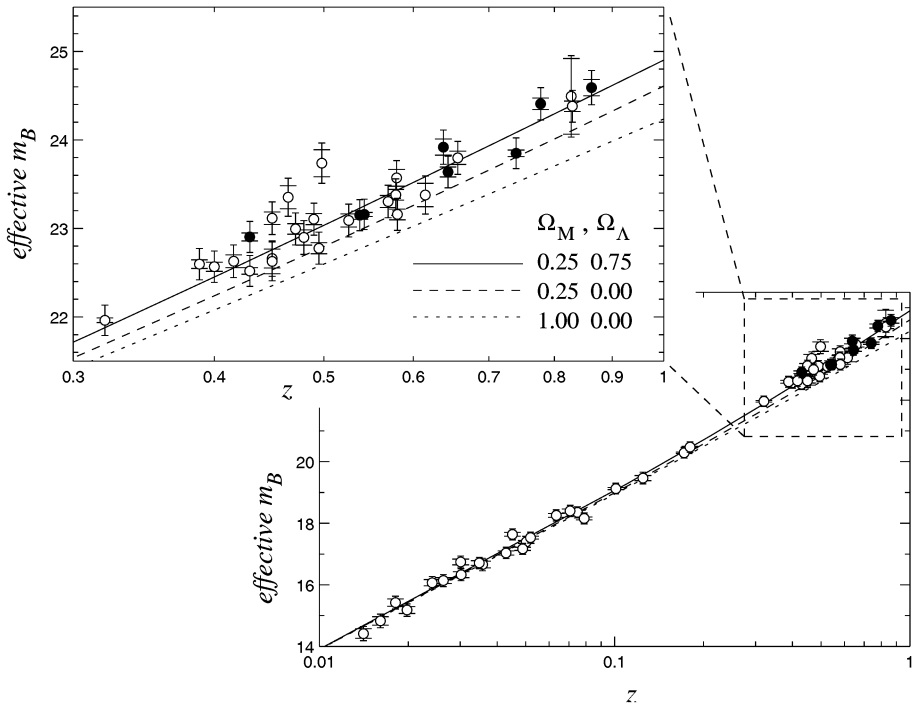

Figure 3.1: Fig. 5 from **Paper I**. Hubble diagram of effective K- and stretch corrected m_B vs. redshift for supernovae in the primary low extinction subset. Filled circles represent the HST supernovae of **Paper I**. Inner error bars show just the measurements uncertainties; outer error bars include 0.17 magnitudes of intrinsic dispersion. The solid line is the best-fit flat-universe cosmology from the low-extinction subset; the dashed lines represent the indicated cosmologies.

of 0.02 mag was assumed at all the redshift bins [1]. Since the relation between Ω_Λ and Ω_M changes with the redshift, the degeneracy is broken only if supernovae are observed all along the universe evolution at many distances (right panel). Note however, that in the hypothetical case of infinite accuracy in the magnitude measurements, two perfect standard candles at different redshifts would be enough to determine exactly the values of the cosmological parameters, assuming non-relativistic matter and a cosmological constant to be the only components of the universe.

Most data available to date spans in a redshift range up to $z \sim 1$,

[1] i.e. it was assumed that several SNe were measured for each z

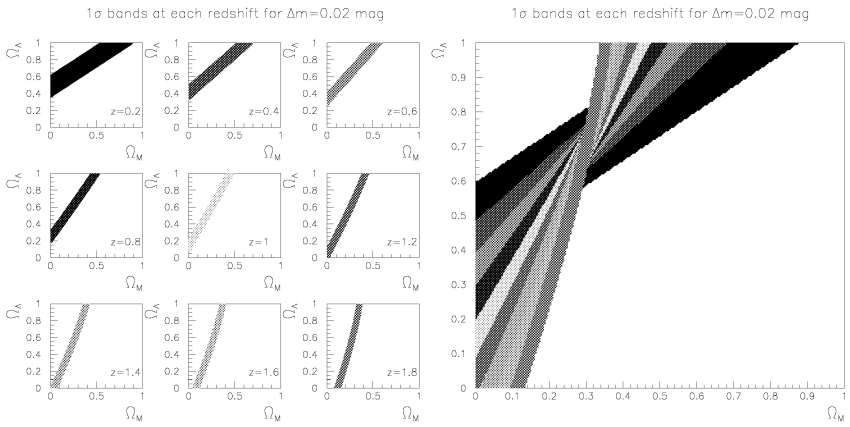

Figure 3.2: Confidence level contours obtained using supernovae of at given redshift bins, with the measurement uncertainty on the apparent magnitude assumed 0.02 mag (left panel), their combination would break the degeneracy (right panel). Credits [17].

and yet it is not sufficient to completely break the degeneracy. Figure 3.3 shows the result of the primary fit to the data presented in **Paper I** in the $\Omega_\Lambda - \Omega_M$ plane. The ellipses represent the 68%, 90% and 99% confidence level respectively. The contour plot clearly exclude a null vacuum energy density Ω_Λ=0 at the 99% C.L.

3.5 Rest-frame I-band Hubble diagram

Paper A presents the first attempt to build the I-band Hubble diagram up to redshift z $\sim$ 0.5. This work was possible thanks to recently acquired near infrared data of distant SNe Ia. The paper is based on J-band observation of three high redshift SNe, two of which, SN 1999Q and SN 1999ff [48, 54], are available in literature and one, SN 2000fr, discovered at CFHT and followed by the SCP during the spring 2000 campaign. The data and its reduction is presented in Chapter 5. The low redshift sample includes I-band data from SNe coming from three different data sets, the Calan/Tololo [21], the CfA [49] and the CfA2 [25]. A novel technique for fitting the I-band lightcurve has been developed and applied to the nearby SNe in **Paper A** (see also Section 6.6).

There are many reasons for building the Hubble diagram in the I-band. First, in order to have an (nearly) independent measurement of

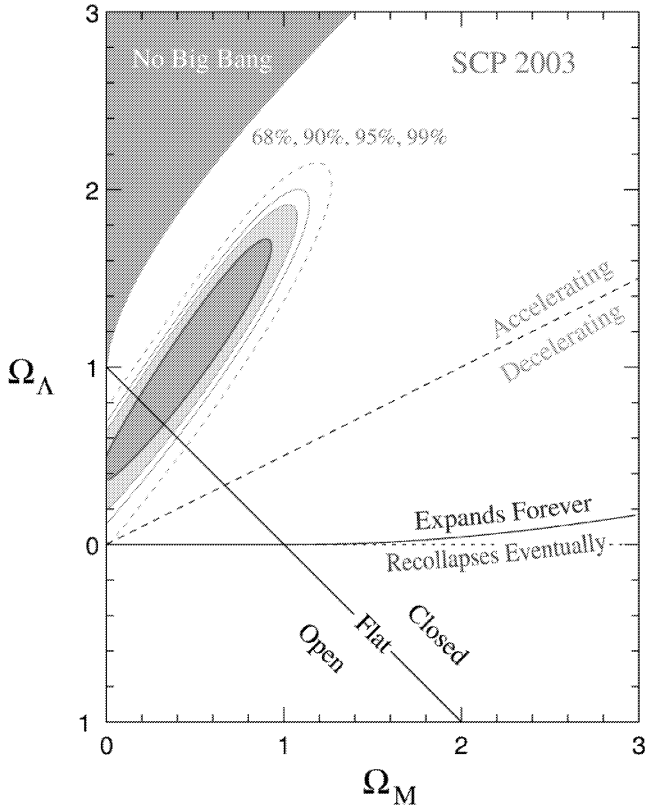

Figure 3.3: Figure 8 from **Paper I**. 68%, 90% and 99% confidence regions for Ω_Λ and Ω_M from this paper's primary analysis, the fit to the low-extinction primary subset (Fit3)

the cosmological parameters, and be able to confirm, or not, the results obtained observing SNe Ia in the B-band. Second, light at longer wavelengths is less sensitive to extinction by dust while travelling through the universe, e.g the absorption in B-band is about twice the absorption in I-band. In general, I-band measurements are affected by somewhat different systematic uncertainties than those relevant to B-band measurements. For this reason, the rest-frame I-band Hubble diagram represent an excellent complementary tool for determining cosmological parameters and controlling the possible systematic effects involved. Recently, Krisciunas et al. [27] have studied the Hubble diagram out to $z \sim 0.04$, in the infrared, corresponding to rostrum J, H and K-band. Although building

the Hubble diagram at these wavelengths is very promising for controlling systematic uncertainties in supernova cosmology, space observations will be required to be able to safely extend the analysis to high-redshift.
Figure 3.4 shows the result obtained in **Paper A** where the rest-frame I-band Hubble diagram includes 28 nearby objects, with redshift ranging between 0.01 and 0.1, and three SNe at redshift z $\sim$ 0.5. The three high-z SNe constitute a very small sample to be able to fit cosmological parameters. However, they have been compared with different models, and found that they do not contradict a flat, Λ dominated universe, $(\Omega_M, \Omega_\Lambda)$=(0.3,0.7), determined using the rest-frame B-band measurements of SNe Ia, while a flat Λ=0 universe was less favoured by the data. With this work, the feasibility of using rest-frame I-band data for cosmological reasons was established. Most importantly, possible sources of systematic uncertainties are identified and discussed (see also discussion in Section 4.7 and 6.7).

3.6 The concordance model

Other experiments, recently conducted in other fields of cosmology, have confirmed and given confidence in the results obtained using supernovae as standard candles. The most relevant was probably given by the combination of measurements of the Cosmic Microwave Background Radiation (CMBR) anisotropies, yielding $\Omega_M + \Omega_\Lambda$ together with the value of Ω_M determined by Large Scale Survey (LSS) and galaxy cluster surveys. The CMBR was formed at the time of decoupling between matter and radiation, which occurred about three hundred thousand years from the Big Bang, at a redshift $z \sim 1100$. This radiation, relic from the Big Bang, is cooling down as the universe expands, and has reached now a temperature of about 3 K, thus it is observable in the microwave region of the spectrum. This radiation has travelled through the universe quite undisturbed, conserving information on the structure of the early universe. The first measurements of the CMBR were obtained by chance by Penzias and Wilson in 1965. In 1989 the COBE satellite was launched and the temperature of the CMBR was measured at an extremely high precision. This appeared to be an excellent black body with anisotropies of the order of $\Delta T/T \sim 10^{-5}$. It is possible to show that the angular size of the first acoustic peak in the CMB anisotropies depends on the geometry of the universe, $\Omega_K = 1 - \Omega_M - \Omega_\Lambda$, and the degeneracy on Ω_M

and Ω_Λ parameters cannot be broken [13]. Measurements of the acoustic peaks in the CMBR, first by balloon experiments, BooMERANG and Maxima, [12, 3] and later by the WMAP satellite [51, 53], have proved the flatness of the universe at the percent level.

Less accurate are the results obtained by other means, measuring the mass density of the universe. The 2dF Galaxy Redshift Survey (2dFGRS) [14] indicates a matter density $\Omega_M \cong 0.3$, which together with the results of the CMBR would confirm a non-zero cosmological constant. The evolution of number density of X-ray emitting galaxy clusters [55] are also consistent with a matter density accounting for about 30% of the total energy density of the universe.

The systematic uncertainties involved in each type of experiment are of different nature, so that the cross-cutting cosmological results give a trustful scenario of the composition of the universe today. This is called the "concordance" model.

3.7 The nature of dark energy

The recent discoveries open the question of determining the nature of the dark energy, that is driving the acceleration of the universe. The presence of a cosmological constant, Λ, is not the only possible explanation for the acceleration, and, although it would seem to be the most natural one, it presents some unsolved problems. Due to its equation of state, the cosmological constant behaves as the vacuum energy of the universe. However, its measured value is 120 orders of magnitudes smaller than what would be predicted by theoretical calculations. Another source of concern is the *coincidence problem*. Since the matter density scales with the third power of the size of the universe, $\rho = \rho_0/a^3(t)$, while the vacuum energy density, ρ_Λ, is constant, it is very unlikely that we measure it at the "rare" period of its time evolution in which it has the same order of magnitude as the matter density. These problems inspired theories predicting alternative forms of energy densities able to drive the acceleration of the universe. One of the most promising ones, is a scalar field called *quintessence*, whose equation of state parameter, w_Q, varies slowly with time. The only way of understanding the nature of dark energy, and distinguish among different candidates, is to measure the equation of state parameter and, possibly, its time derivatives. Figure 3.5 (from **Paper I**) shows the most recent measurements obtained using SNe Ia. The supernova data can be com-

bined with CMB and 2dFGRS results. As the different experiments are complementary to each other, their combination allows to decrease the uncertainties on the parameters. The corresponding estimated value of the equation of state parameter is $w = -1.05^{+0.15}_{-0.20}$ (for the low-extinction subset, for details see **Paper I**), or $w = -1.02^{+0.19}_{-0.24}$ (for the full primary subset with host-galaxy extinction corrections applied). This results are compatible both with the cosmological constant, for which $w = -1$, and with a wide range of other dark energy models including quintessence. The large uncertainties involved with this analysis are manly due to the small data sample and to the small redshift range of the observations. Future experiments aiming at the discovery of large sample of SNe Ia up to z $\sim$ 2, such as the SNAP satellite, are likely to be able to solve the dark energy enigma.

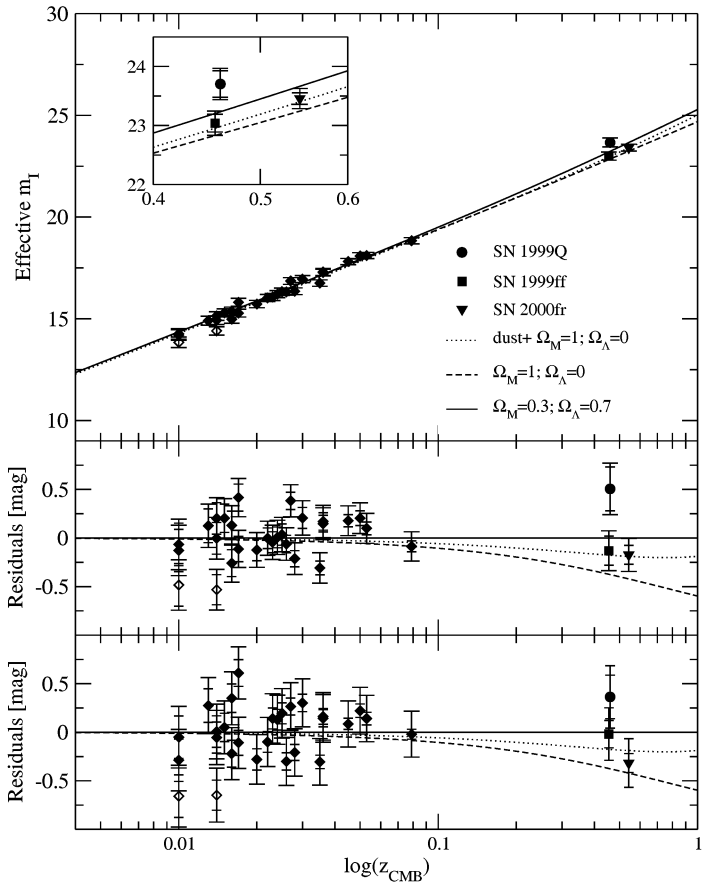

Figure 3.4: Figure 7 from **Paper A**. Effective I-band maximum vs redshift for the nearby supernovae of the Calan/Tololo, CfA and CfA2 sample, together with three supernovae at redshift ~ 0.5, corrected for the width-luminosity relation (top panel) and residuals to the $(\Omega_M, \Omega_\Lambda)$=(0.3,0.7) model (middle panel) and for the case not corrected for the width-luminosity relation (bottom panel). SN 1998es and SN 1999dq were excluded from the fit and are plotted with open symbols.

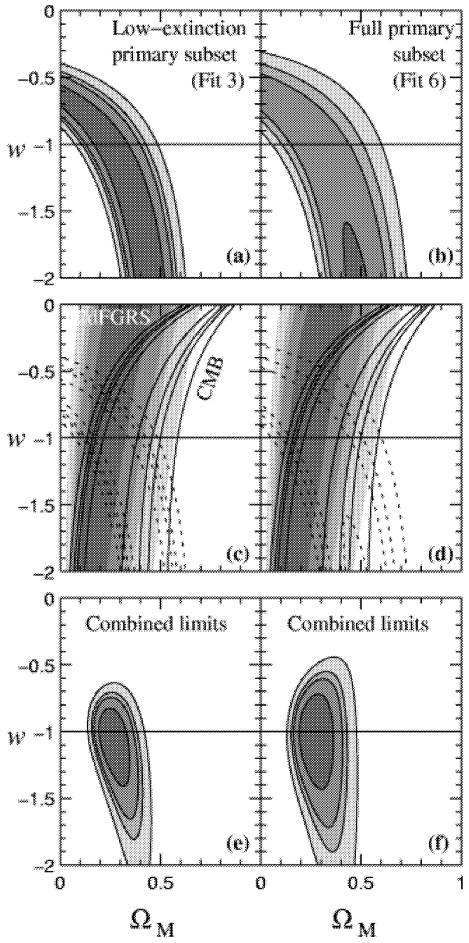

Figure 3.5: Figure 12 from **Paper I**. Joint measurements of $\Omega_{\rm M}$ and w assuming $\Omega_{\rm M}+\ \Omega_\Lambda{=}1$ and that w is not time-varying. Confidence regions plotted are 68%, 90%, 95%, and 99%. The left column (panels a, c, and e) shows fits to the low-extinction primary subset; the right column (panels b, d, and f) shows fits to the primary subset with unbiased individual host-galaxy extinction corrections applied to each supernova. The upper panels (a and b) show the confidence intervals from the SCP supernovae alone. The middle panels (c and d) overlay this (dotted lines) with measurements from 2dFGRS (filled contours) and combined CMB measurements (solid contours). The bottom panels (e and f) combine the three confidence regions to provide a combined measurement of $\Omega_{\rm M}$ and w.

Chapter 4

Systematic effects in supernova cosmology

Special care has to been taken in the control of possible systematic effects involved in the use of SNe Ia as distance estimators in cosmology. In this chapter we summarise the main known sources of uncertainties.

4.1 K-corrections

As we have seen in Chapter 3, K-corrections are necessary to convert the observed magnitudes into rest-frame bands, and depend critically on the knowledge upon supernova colours and spectral evolution. **Paper B** presents a study of mean supernova colour in B, V, R, I-band which was used to improve spectral templates of SNe Ia. At certain wavelength ranges this uncertainty becomes particularly important since our knowledge of supernova properties is more limited. In the case of **Paper I**, for instance, it was important to know the average $U - B$ colour since some of the observations correspond mainly to rest-frame U-band, or their K-corrections partially extend to this region of the spectrum. This is illustrated in Figure 4.1 where the red-shifted (z=0.6) spectral template of SN Ia at maximum is plotted together with the red-shifted UBV pass-bands and rest-frame RIJ. R-band, used for the observations along with I-band, corresponds roughly to B-band, extending in part to the U. Though the amount of the effect is different for different redshifts, the problem generally involves supernovae at redshift z > 0.5. SN Ia properties in the U-band are not well established yet due to lack of data.

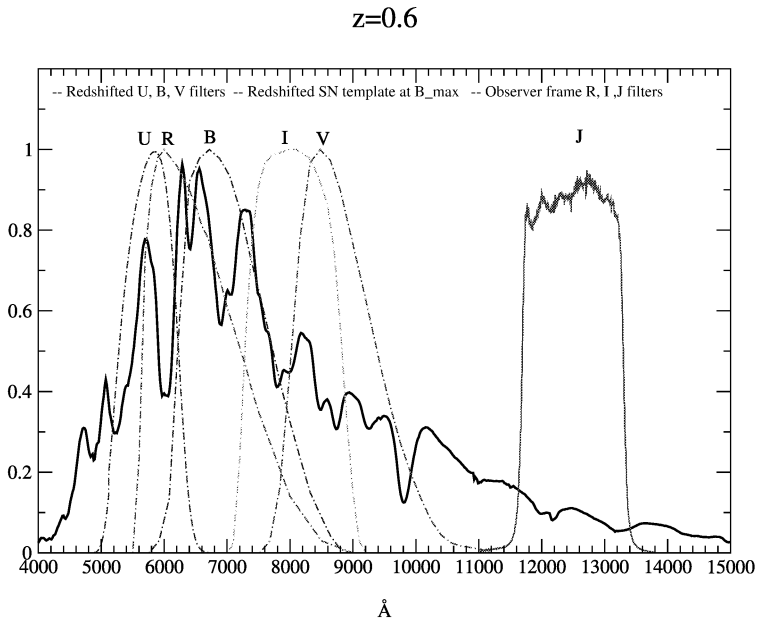

Figure 4.1: Spectral template at maximum red-shifted at z=0.6. Also plotted are the red-shifted UBV pass-bands and rest-frame RIJ.

To solve this problem, literature values of $U - B$ at the time of B-band maximum from 5 nearby SNe were used, resulting in an estimate of -0.4 mag, approximately 0.2 mag bluer than the one used in Perlmutter et al. [40] and possibly in Riess et al. [47]. It should be noted here, that a bluer average colour of high-z SNe compared to nearby ones was observed in the HZT data [28]. However, this effect was not observed in our data sample, as shown in Figure 4.2, possibly due to a better understanding of the blue part of the spectra, and therefore a better estimate of the K-corrections needed to compute the rest-frame $B - V$ colour from the measured $R - I$ (or similar bands).

4.2 Host galaxy extinction

Dust in the host galaxy could obscure the supernova and make it look fainter. This effect can be controlled by looking at multi-colour mea-

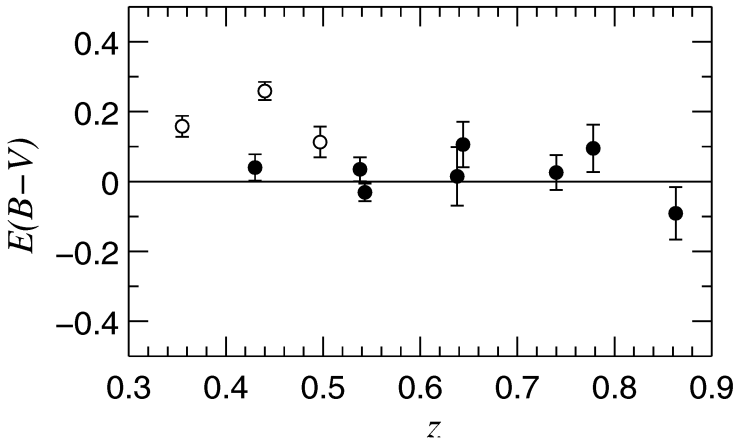

Figure 4.2: Figure 4 from **Paper I**. A plot of $E(B-V)$ as a function of redshift for the 11 HST-observed supernovae presented in the paper. Error bars include only measurement errors. Filled circles are those supernovae in the low-extinction subset (Subset 2 in **Paper I**).

surements, and with some assumptions on dust properties. The method usually adopted for determining the amount of extinction in the host galaxy, is comparing the measured $B-V$ colours, both at maximum and at late time, with the expected colours for un-reddened supernovae [46]. Figure 4.3 (from [46]) shows $B-V$ colour evolution for six supernovae, whose behaviour is extremely similar at late time, even for SNe dramatically differing from the average in their earlier evolution. The measured colour excess, $E(B-V)$, is then used to compute the extinction in the observed band, assuming the extinction law derived by Cardelli et al. [9], which is parametrised using R_V ($\equiv A(V)/E(B-V)$). The value of R_V depends essentially on the size of the grains composing the dust and its density. For the Milky Way dust, the average value is estimated to be $R_V = 3.1$, though this is found to be larger in high density regions. The average value is usually assumed to be the same in all galaxies. This is generally a good approximation, certainly holding for low-extincted objects, for which an error in the estimate of R_V would only contribute marginally in the corrections. However, when computed for highly extincted supernovae, the correction results are generally overestimated [46], probably indicating a different value of R_V. Thus, highly reddened objects are often discarded from the sample. This was the case

for an handful of objects in **Paper A**, **Paper B** and **Paper I**. For example, in Figure 4.2, the highly extincted supernovae, plotted with open symbols, were excluded from the subset used for the cosmology fit.

Another limitation in our ability of determining the host galaxy extinction, is given by colour intrinsic dispersion. Studies on SNe Ia colours carried in **Paper B**, have been used to determine this limits,

$$\begin{aligned} \sigma_{A_V}^{\mathrm{B-V}} &= 3.1 \cdot \Delta_{\mathrm{BV}}^{\mathrm{corr}} \\ \sigma_{A_V}^{\mathrm{V-R}} &= 6.2 \cdot \Delta_{\mathrm{VR}}^{\mathrm{corr}} \\ \sigma_{A_V}^{\mathrm{R-I}} &= 4.1 \cdot \Delta_{\mathrm{RI}}^{\mathrm{corr}} \\ \sigma_{A_V}^{\mathrm{B-I}} &= 1.4 \cdot \Delta_{\mathrm{BI}}^{\mathrm{corr}} \\ \sigma_{A_V}^{\mathrm{V-I}} &= 2.5 \cdot \Delta_{\mathrm{VI}}^{\mathrm{corr}} \end{aligned} \tag{4.1}$$

where R_V was assumed equal to 3.1, and the dependence on supernova phase was neglected. The conclusion reached by this analysis is that the

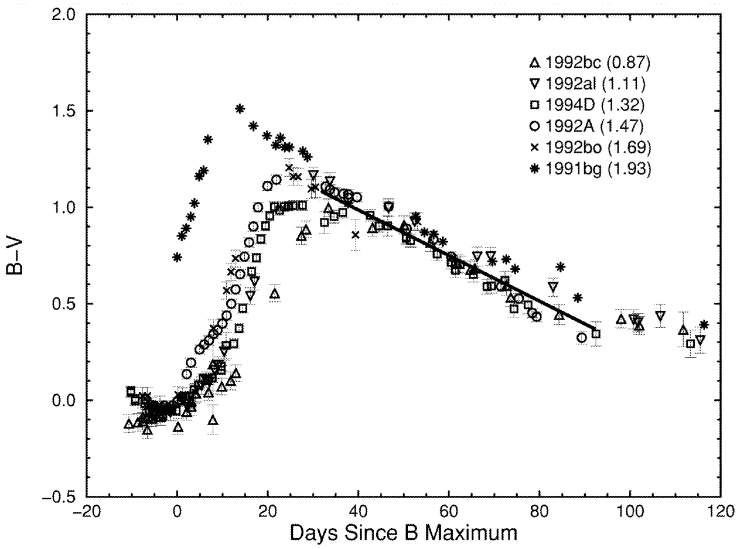

Figure 4.3: $B - V$ colour evolution for six SNe Ia that likely suffered little or no reddening from dust in their host galaxies. These six events, whose $\Delta m_{15}(B)$ parameters are indicated in parentheses, cover a wide range of initial decline rates and peak luminosities. The solid line corresponds to the Lira (1995) fit to the colour evolution during the phase interval $30 \leq t_V \leq 90$. The epoch of B_{max} is assumed to occur 2 days before the epoch of V_{max} (Leibundgut 1988). (Credit [46])

extinction correction cannot be safely determined better than at 0.1 mag level, when using colours in which there is intrinsic dispersion. However, the dispersion measured in $V - R$ in **Paper B** is compatible with no intrinsic dispersion, indicating measurement of this colour to be the best choice for determining host galaxy extinction corrections.

4.3 Non-Ia contamination

The inclusion of other types of SNe in the Hubble diagram could affect the determination of cosmological parameters, e.g. one of the first seven SNe published by the SCP [41] is now believed to be a core-collapse supernova [36]. Spectroscopic data are aimed to avoid this source of confusion.[1] However, the low signal-to-noise for high-z supernova spectra can sometimes make the type identification uncertain. At high redshift, the Si II λ6150 Å feature, characterising type Ia SNe, is cut out of the range in optical spectra. Thus, type Ic:s look very similar to the type Ia spectra, making the identification more uncertain. In cases of good signal-to-noise spectra, however, the identification is possible thanks to shallower features, namely the S II W, in the region 5000-5500 Å, and the Si II in the region 3900-4100 Å. **Paper C** presents 15 spectra of 13 high-z SNe Ia, and addresses the problems connected with their type identification. For example, Figure 4.4 shows the spectrum of SN 2000fr, (z=0.543), compared to spectra of different supernova types, highlighted are the features that allow its identification as a type Ia. It has been shown, that multi-colour information can be used to reduce contamination by other supernova types at high redshift [11]. With an ideal data set, including both multi-colour photometry and spectroscopy, we would be able to assure negligible contamination by other supernova types in the Hubble diagram.

4.4 Supernova Population drift

It has been suggested that distant supernovae could be intrinsically fainter than the local ones, due to a drift in the properties of the environment in which supernova explosions occur. Though there are no evidence supporting this hypothesis, this is still a viable possibility that cannot be

[1] No spectra were available for that SN, colour information and redshift from the host galaxy were used for the classification.

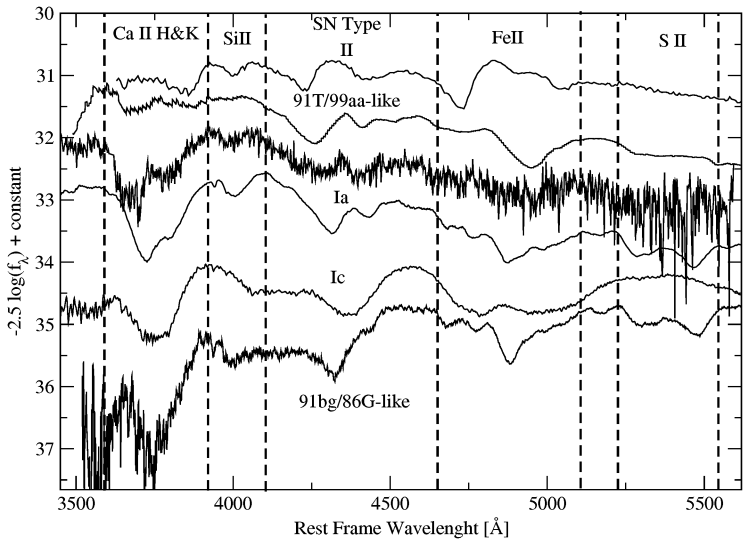

Figure 4.4: Figure 2 from **Paper C**. The spectrum of SN 2000fr, z=0.543, compared to spectra of different types of nearby supernovae. Highlighted are the features that allow its identification as a type Ia.

excluded yet. In order to test for supernova evolution, we compare observed properties of nearby SNe with distant ones.

In **Paper C**, we analyse spectra of 13 distant supernovae and compare them both qualitatively and quantitatively to spectra of nearby SNe and find no indication for evolution. The quantitative comparison is done using spectral indicators, such as velocities of supernova features and Equivalent Widths (EW), the latter introduced in **Paper VI** to study properties of nearby SNe (see Chapter 6). A general worry is the complete absence of very faint (fast declining lightcurve) and very bright (slow declining lightcurve) objects discovered at high redshift. While the absence of underluminous objects is expected due to selection effects (see Section 4.7), the lack of bright objects is surprising, and could be indicative of evolution in supernova properties with redshift. Among the sample presented in **Paper C**, one supernova, SN 2002fd (z=0.279), shows similarities with spectra of slow-decliner supernovae and we classified it as 1991T/1999aa-like. Though lightcurve data of this supernova is missing, and we could not confirm it to be actually overluminous, SN 2002fd represent the only reported case of a possible peculiar supernova observed at high-z up to date.

Rest-frame I-band lightcurves can be also used to test for supernova evolution. In nearby SNe, the secondary peak appears about 20 days from the first maximum, and it is more prominent in normal and overluminous SNe Ia and completely absent in underluminous ones. This relation can be used as an indication against supernova evolution when seen in the lightcurve of distant objects, e.g. a supernova showing the second peak is not intrinsically underluminous. This argument is used in **Paper A**, where three high-z SNe rest-frame I-band lightcurves are fitted by templates showing this characteristic. Moreover among them, SN 2000fr shows evidences for the second peak, even without a fit to the nearby lightcurve templates.

Another worry is in the possible dependence of supernova properties with host galaxy type, as this could in principle affect the cosmological results. **Paper II** builds the rest-frame B-band Hubble diagram for groups of SNe hosted in given galaxy types. The sample used is composed by the 42 high-z SNe Ia from the [40], plus 18 SNe of the Calan/Tololo sample and 12 SNe of the CfA sample. The scatter observed in the Hubble diagrams correlates with host galaxy morphology, being smaller for SNe Ia in early type hosts than in late type hosts. In all cases the acceleration of the universe is confirmed.

4.5 Grey dust

Presence of dust in the intergalactic medium (IGM) was proposed for the first time in 1999 as an alternative explanation for the observed dimming of SNe Ia [1, 2], and the issue was addressed both by the SCP and the HZT [40, 47]. An homogeneous distribution of dust with small reddening, "grey" dust, would have the same effect on the Hubble diagram of distant supernovae as the cosmological constant and would not be discovered by tests on colours, such as those generally performed on $E(B-V)$ distribution.

Aguirre [1] argued that mechanisms able to expel only large dust grains into the IGM were possible. The minimum size of the grains, escaping the galaxies, would determine the optical properties of the dust, e.g the value of R_V in the parametrisation by Cardelli et al. [9]. The minimum grain size, $a_{\min}$, is set by studying ejection mechanisms, but also, experimentally, by the measured emission from the microwave background radiation. The optical properties of such a dust would have a very

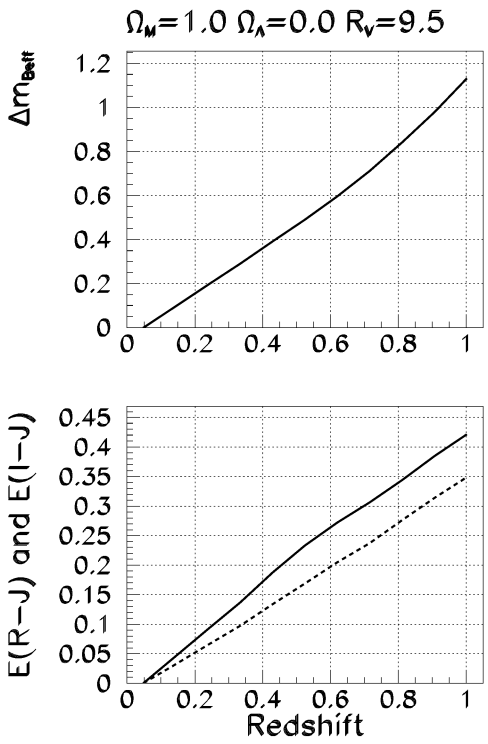

Figure 4.5: Figure from [35]. Dimming of SNe Ia effective magnitude vs. redshift in a flat $\Lambda = 0$ universe with a homogeneous distribution of grey dust in the IGM (top panel); expected colour excess in the observed magnitude vs. redshift (bottom panel).

weak wavelength dependence, therefore called "grey" dust. Assuming a value of $a_{\min}$ between 0.08 and $0.12\mu m$, which correspond to R_V between 4.5 and 9.5, Goobar et al. [18] computes the redding expected for a homogeneous distribution of large grain dust in the IGM, whose density is such to explain the measured dimming of type Ia supernovae at redshift $z \sim 0.5$.

Figure 4.5 shows the dimming of SNe Ia effective magnitude vs. redshift in a flat universe with $\Omega_\Lambda = 0$ and a homogeneous distribution of grey dust with a R_V=9.5 (top panel) and the expected colour excess in the observed magnitude, $E(R-J)$ and $E(I-J)$, vs. redshift (bottom panel). At redshift $\sim$0.5, the effect of grey dust, in such a universe, is about $\sim$

0.2 mag. Accurate multi-colour measurements of SNe Ia should be able to distinguish the effect of grey dust from the cosmological constant.

Paper A uses the measured magnitude in the rest-frame I-band Hubble diagram for three SNe Ia at redshift $z \sim 0.5$, to test the dust model as compared to the cosmological models. Although the dust model is not favoured by a simple χ^2 test, there is a need to increase the sample of rest-frame I-band data at high-z in order to make the test more robust. In the same work, a method for testing the presence of grey dust using multi-colour measurements was developed. The preliminary sample of three high-z SNe Ia was used to test the method, and investigate the systematic effects involved.

Note that colour measurements of quasars have been used to constrain intergalactic dust and its effects on high-z sources [31]. These results rule out the possibility for IG dust to be the only cause of the observed dimming of SNe Ia.

4.6 Gravitational lensing

Although this effect is not directly investigated in this thesis, gravitational lensing is an important source of systematic uncertainty for very distant supernovae. Massive objects interposed in the space between the source and the Earth, can act as lenses and artificially augment (or diminish) the object brightness. An example of lensed supernova is the case of SN 1997ff at redshift ~ 1.7, [4, 32].

Gravitational lensing depends upon the distribution of matter in dark matter halos. While extreme cases in which all matter is clumped in very massive objects would cause significant dimming of supernovae already at redshift as low as ~ 0.5, more realistic assumptions of matter distribution, would make this effect important only beyond redshift ~ 1. Gravitational lensing would increase the dispersion in the Hubble diagram and therefore the uncertainties on the estimate of cosmological parameters. For a complete review of gravitational lensing in astronomy see e.g. [56], while for the effect of lensing on supernova cosmology see discussions in e.g. [40, 28, 42]. This effect could severely limit our ability to using luminosity distance indicators at very high redshifts, however, observing a large sample of SNe could allow to average out this effect.

4.7 Other effects

4.7.1 Colour corrections

Colour corrections are necessary to combine or compare data from different telescopes. This correction takes care of differences between the responses of each instrument filter and the standard system used as reference. Systematic uncertainties in the colour corrections can depend upon how well the filter band-pass, the optics and the CCD transmission of the instrument used for the observations is known, and on the definition of the system used as reference, e.g. the Bessel system [5]. Both in **Paper A** and **Paper B**, we have found potential systematic differences between SN data from different samples which probably depend on the transformation between the system used[2]. Figure 4.6 shows the low-z Hubble diagram from **Paper A**, where SNe from different data set are plotted with different symbols. Table 4.1 lists for each data sample the average redshift, the number of SNe, the weighted mean and standard deviation of the residuals in the Hubble diagram and the average uncertainty. The latter is dominated by the uncertainty in the redshift due to peculiar velocities in the host galaxies, assumed 300 km/s. The Calan/Tololo sample shows a small offset to the best fit model, which is, however, compatible with statistical fluctuations. Note that, this is the set including SNe at higher redshift, which are therefore less affected by peculiar velocities. The r.m.s. of the CfA sample is the largest, however, we note that only 6 SNe are in this sample, making the statistical significance more uncertain.

For the near infrared observations, where the reference system is not as well determined as in the optical, the problem could be more severe. In particular there is an offset between the IR (Persson) and Optical (Johnson) systems that we estimated to be 0.036 ± 0.012 mag. This was done both by comparing colours of A0 stars from the Hipparcos catalogue with the 2MASS catalogue, and by using the transformations given by the 2MASS experiment between the J_{LCO} (Persson) to the J_{BB} (Bessel & Brett) for a A0 star, following Carpenter [10]. Differences between the two methods, of the order of 0.02 mag, are compatibile with statistical fluctuations.

[2]Note that two of the samples used in **Paper A**, the Calan/Tololo and CfA sample, were used in the analysis of **Paper B**.

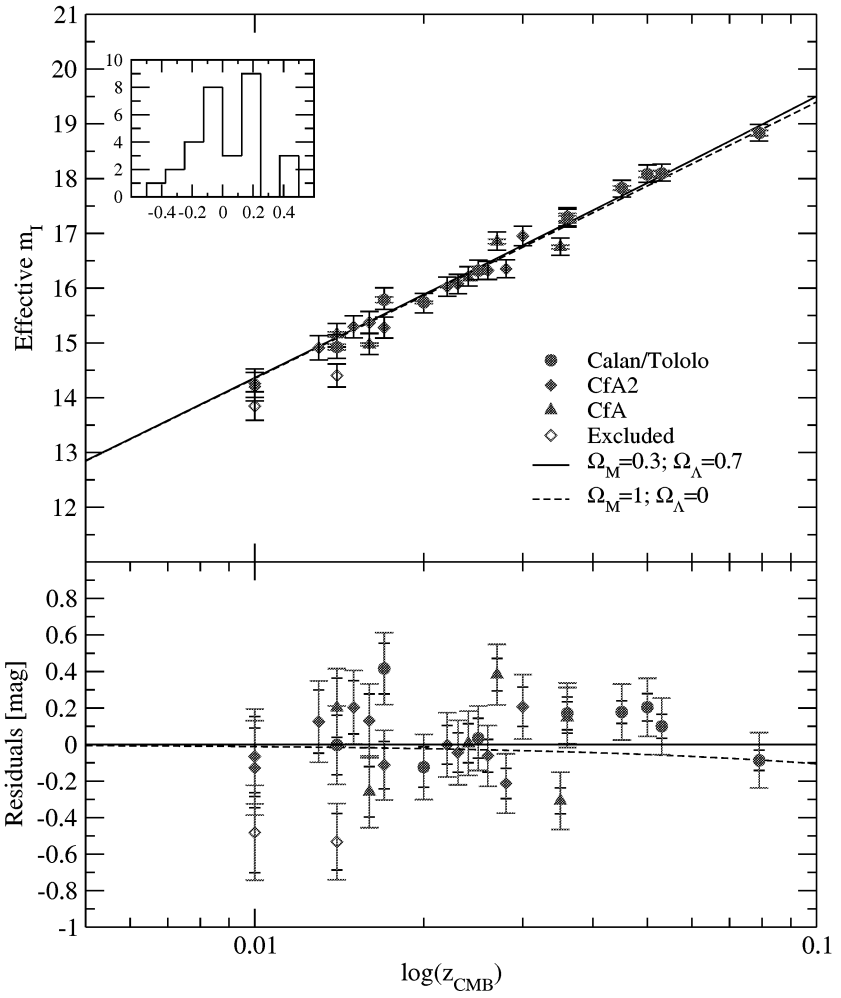

Figure 4.6: Figure 7 from **Paper A**. Effective I-band maximum vs redshift for the nearby supernovae of the Calan/Tololo, CfA and CfA2 sample. The data have been corrected for the stretch-luminosity relation and for Milky Way and host galaxy extinction. The r.m.s. along the concordance model line is $\sigma = 0.19 \pm 0.02$ mag. Subracting the contribution of the average uncertainty, results in 0.14 mag estimated intrinsic dispersion. SN 1998es and SN 1999dq were excluded from the fit and are plotted with open symbols.

	$\langle z \rangle$	n	$\overline{x}_w$ [a]	σ_w [b]	σ_z^{300}
C/T	0.037 (0.021)	9	0.08 ± 0.06	0.16 ± 0.06	0.10 ± 0.04
CfA	0.025 (0.009)	6	0.003 ± 0.12	0.27 ± 0.06	0.11 ± 0.03
CfA2	0.018 (0.007)	11	-0.02 ± 0.05	0.14 ± 0.04	0.14 ± 0.05

Table 4.1: Dispersion measured in the Hubble diagram for each of the sample, corrected for the width-luminosity relation; $\langle z \rangle$ is the average redshift of the sample, and its standard deviation given between brackets; n is the number of data points; $\overline{x}_w$ and σ_w are weighted mean and standard deviation of residuals in the Hubble diagram about the best fit model to the whole data sample, and σ_z^{300} is the average uncertainty and r.m.s. around that value. C/T stands for Calan/Tololo.

[a] If R_i are residuals in the Hubble diagram and w_i are the weights, then
$\overline{x}_w = \sum w_i R_i / \sum w_i \pm m_{w2}/\sqrt{n_{eff}}$
$m_{w2} = \sum w_i R_i^2 / \sum w_i$
$n_{eff} = \sum {w_i}^2 / \sum w_i^2$
[b] $\sigma_w = m_{w2} \pm \sqrt{(m_{w4} - m_{w2}^2)/(4 n_{eff} m_{w2})}$

4.7.2 Selection effects

Supernovae found near the limiting magnitude of the search can bias the results obtained using these objects as distance indicators, i.e the Malmquist bias [33, 34]. Due to the narrow distribution of intrinsic brightnes, this effect is quite small for SNe Ia, up ~ 0.04 mag [42], and can affect both nearby and distant supernovae. What is relevant to the determination of the cosmological parameters, however, is only the difference between the low and the high redshift samples biases. For the case of **Paper I**, nine of the eleven high-z supernovae were discovered at maximum light. The reason for this selection was in the fact that only spectroscopically confirmed supernovae were chosen for the follow-up and, among these, only the more distant objects were observed with the HST. The Malmquist bias was estimated for both nearby and distant sample used in the analysis of **Paper I**, and was found comparable. Note that these selection criteria are likely to take place every time the use of the observing facilities is time limited or strongly depending weather conditions. Dedicated experiments such as the SN factory, the SNLS or in the future the SNAP satellite, will be able to reduce the effect of the Malmquist bias.

Chapter 5

Near-Infrared Data

In this chapter we describe general problems concerning the reduction of near-infrared (NIR) data and we discuss the method followed for the data reduction of SN 2000fr. The optical data of this supernova was used in **Paper I**, its spectrum is discussed in **Paper C**, and its near infrared data was used in **Paper A**.

5.1 Observing in the NIR

The main limitation for observing in the NIR is the high sky emission, which is particularly strong at these wavelength range, typically 16 $mag/arcsec^2$, and the atmospheric absorption, defining only a few wavelength ranges at which ground based observations are feasible. Figure 5.1 shows the atmospheric transmission in the NIR wavelengths region compared to the JHK band-passes of some of the filters available at ISAAC VLT. Observations usually consist of multiple images of the target to be combined following a specific reduction technique. Moreover, since the sky brightness vary significantly with time, this must be monitored quite often during the observations and in the vicinity of the target. The time spent to monitor the sky is usually comparable to the time spent integrating on the source. One can distinguish between different techniques, namely *nodding*, *dithering* and *mosaicing*, chosen mainly depending on the brightness of the target, its extension and the population of the field, but also on the telescope used for the observations.

Nodding refers to the technique in which the telescope is pointed *on* and *off* the source, so to have a sky frame for each sky image. In case

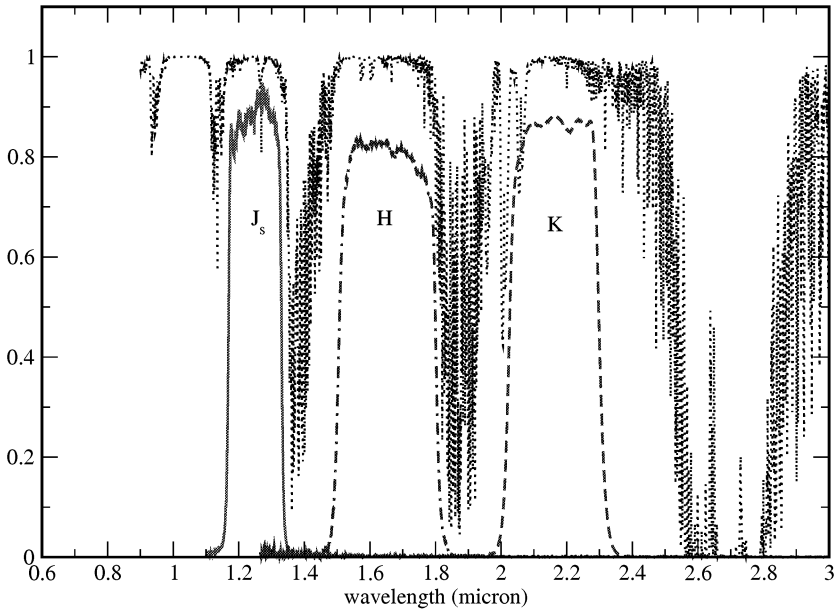

Figure 5.1: Atmospheric transmission in the NIR wavelength region, compared to the J_sHK filters available at ISAAC VLT.

of a very dense field and/or an extended source, the size of the nodding required can be quite large. This technique was more common for single element detectors and is gradually disappearing with the introduction of array detectors and the use of large telescopes for which quick oscillations are not easily achieved.

In the *dithering* technique, the telescope is shifted, usually by a small offset, according to a pattern, see Figure 5.2. Thus, the target will always be centred in a different point of the image for each one of the exposures. In this case, images taken immediately before and after the frame are combined together in a sky frame to be subtracted from the image. *Dithering* was used during the observations of SN 2000fr.

Mosaicing is a dithering with larger offsets between the different exposures. This allows to cover a larger region of the sky, however, it requires that at least some parts of each frame overlaps to enable the image alignment during the data reduction process.

NIR observations are typically made without a shutter, and many detectors do not even have one. As infrared arrays saturate very quickly,

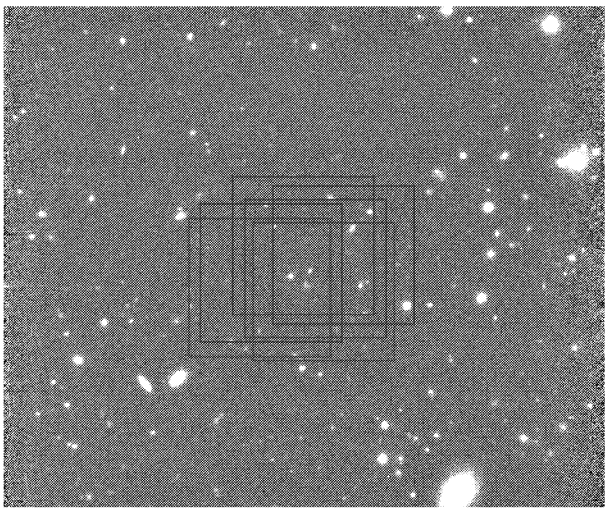

Figure 5.2: Example of Dithering technique. The telescope is pointed at different position in the sky, and images are acquired for each of the positions.

they need to be read-out often. The integration time between read-outs varies between a fraction of a second up to 20-30 seconds, depending on the wavelength range and the brightness of the target. Thus, several frames are co-added to produce one image. This is usually automatically done at the telescope, and the individual frames might not be available.

Dark current and read-noise are more important than for CCDs, thus requiring many dark frames to be taken frequently during the observations. Typically the dark current is about 1 e^{-1}/s or less, the read-noise for the ISAAC VLT Hawaii detector is 11 e^{-1}. The exposure time is chosen to be comparable to what is spent on the object and on the calibration stars.

Flat field frames are usually taken at twilight or during the night since the sky is so bright at IR wavelengths, faint stars are usually not visible in the raw images. Dome flats are not recommended, because of the uneven thermal emission from the dome itself that could affect the images. The flat field is the combination of different frames dithered between exposures.

5.2 The data set

SN 2000fr (z=0.543) was discovered by the Supernova Cosmology Project (SCP) during a search run in spring 2000 (see IAU Circular No. 7763). The search, aimed at the discovery of z $\sim$ 1 supernovae, was conducted in I-band with the CFH-12k camera on the Canada-France-Hawaii Telescope (CFHT). Due to the depth of the search, SN 2000fr was found about 11 rest-frame days before maximum. It was followed photometrically in both optical and near infrared, and two spectra were taken at different epochs. The spectra confirmed that it was a type Ia at z=0.543. NIR observation were performed with ISAAC at the Very Large Telescope (VLT) at three epochs and again about one year later to acquire reference images of the host galaxy, see Table 5.1.

Date (MJD)	Epoch (days)	Exposure time (s)
51685.06	0.41	4500
51709.02	15.94	3600
51731.96	30.80	3600
52096.00	266.69	7080

Table 5.1: Summary of data taken for SN 2000fr in J_s-band at VLT with ISAAC. The epoch after B-band maximum light is quoted in the rest frame. The time of maximum, determined from the optical lightcurve fit to the HST data, is 51684.5 ±0.2 days (**Paper I**).

Each observation consists of a series of 20 to 60 images with random offsets between them. The observations were done with the ISAAC J_s filter, which is narrower than most J-band filters. Figure 5.3 shows a comparison between J_s and J Persson filters, together with the atmospheric transmission. The main advantage in using the J_s filter is that it cuts off the regions of atmospheric fluctuations between 13500 and 15000 Å. This makes the zero point generally very stable.

5.3 Data Reduction

The NIR data reduction depends on the technique used for the observations, although one can define a guideline which is common in all cases. Here we briefly summarise the reduction used for SN 2000fr.

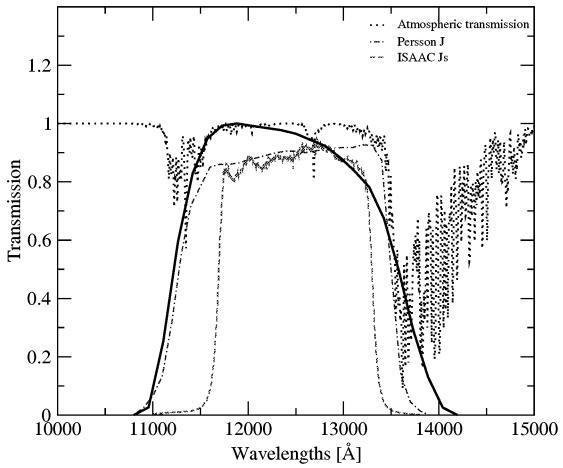

Figure 5.3: Comparison between the standard J Persson filter, the J_s filter at ISAAC used for the observations of SN 2000fr and the I-band red-shifted at z=0.543. The atmospheric transmission is also plotted.

1. Dark subtraction. Dark frames with exposure time similar to the exposure time of the object images, are selected and combined. The combined dark frame is then subtracted to all the frames (both flat fields and target objects).

2. Flat fields. All the flat field frames are combined in a normalised flat, to be used to divide all the frames.

3. Sky subtraction. Building up and subtracting the sky is the most critical step of IR data reduction. We use 10 frames to build the sky for each frame. The five frames taken immediately before and five taken immediately after, are averaged together and a *min-max* rejection is performed on a pixel by pixel basis to exclude the two highest and lowest values. The average frame is the sky frame to be subtracted to the image. This process is repeated for each of the images. As the same frames are used repetitively to compute the sky frame for different images, this process automatically introduces correlation between the frames, which is difficult to quantify. The sky noise expected after sky subtraction is:

$$\sigma_{\mathrm{SKY}} = \sqrt{\frac{\bar{S}}{\mathrm{NDIT} * \mathrm{NEXP} * \mathrm{G}} \left(1 + \frac{1}{N}\right)} \qquad (5.1)$$

where $\bar{S}$ is the mean value of the sky in ADU before subtraction, NDIT is the number of read-out averaged together to produce one frame, NEXP is the number of exposures, G is the instrument gain, i.e. 4.5 electrons/ADU for ISAAC in the SW imaging mode, and N is the number of independent frames used to build the sky frame, i.e. 6 in our case, since 4 have been excluded by the *min-max* rejection. Figure 5.4 shows an example of one frame of the data of SN 2000fr, before and after sky subtraction.

4. Image registration, re-sampling and combination. After sky subtractions, objects are eventually visible in the frames. The stars can be used to determine the shift to be applied for aligning all the images, if this information is not already available in the image headers. Both integer pixel (`IP`) or a sub-integer pixel (`SP`) shift can be chosen in this step, however, `SP` shift would introduce a farther correlation between neighbourhood pixels, that should be accounted for in the determination of the measurement uncertainty. Finally the images are re-sampled to the same grid and averaged.

Cosmic rays and bad pixels can be identified during the process and are masked out in the final combination.
To reduced the data we used an external package XDIMSUM in IRAF[1]. The main feature of this package is in the possibility to optimise the sky subtraction. This is done in two steps. First, the sky is computed statistically for each pixel, and the exclusion of the two highest values guarantee the exclusion of sources from the calculation of the sky. The combined sky-subtracted image is thus used to build a mask of objects. This allows in the second step to exclude the objects from the average while re-computing the sky to be subtracted. To check the results of XDIMSUM, we alternatively applied standard IRAF tasks together with some specific routines written by Chris Lidman[2], to produce all the steps from 1 to 4 above. In what follows we indicate the results obtained in this way as `CL` and with `XD` the results obtained using XDIMSUM.

Standard stars were observed with the same technique used for the science target, to allow flux calibration. This data could be reduced in

[1]IRAF is distributed by the National Optical Astronomy Observatories, which are operated by the Association of Universities for Research in Astronomy, Inc., under cooperative agreement with the National Science Foundation.

[2]Chris Lidman is part of the SCP collaboration and former P.I. of the instrument ISAAC at ESO.

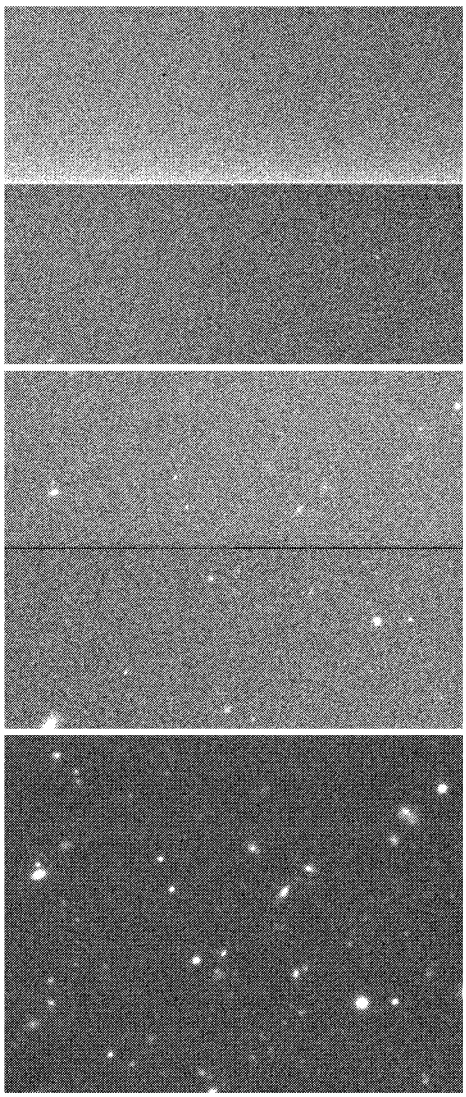

Figure 5.4: One frame of the IR data of SN 2000fr before (top panel) and after sky subtraction (middle panel). The horizontal bright line visible on the top panel, is the division in four parts of the detectors (the vertical line is hardly visible here). After registration, all the frames are averaged together (bottom panel).

jd	$\frac{t-tmax}{1+z}$	flux	J_s(mag)
51685.059	0.41	713.83 ± 58.28	22.50 ± 0.09
51709.020	15.94	264.56 ± 54.24	23.58 ± 0.22
51731.961	30.80	396.29 ± 54.65	23.14 ± 0.15
51685.059	0.41	746.48 ± 50.70	22.45 ± 0.08
51709.020	15.94	232.93 ± 43.53	23.72 ± 0.20
51731.961	30.80	349.51 ± 44.83	23.28 ± 0.14

Table 5.2: Photometry on the `CL` reduced images (top) and `XD` reduced images (bottom).

the same way as the object images, however, due to a higher signal-to-noise ratio, standard stars are typically about 10-12 mag, we followed a slightly simpler procedure. In fact, after applying dark and flat frames to the images, a simple subtraction between them is enough to make appear the standard star from the sky background. The photometry obtained in all the frames are then averaged to compute the zero point (ZP) of the night.

5.4 Photometry

The combined supernova images for each night were aligned with the reference images. Field stars were used to scale the images to the one with best seeing. The second epoch was chosen as photometric reference. Thus, point spread function (psf) photometry was performed on the supernova, were the psf was defined by the field stars. Photometry was performed in both `XD` and `CL` reduced data, and the results are given in Table 5.2.

The ZP of the second epoch has been computed using the photometry of the standard stars during that night. Since the standard stars were observed in the ISAAC J_s filter, we computed the correction from the J magnitude system, defined by Persson [43], to J_s and found -0.012 mag. As the standard stars used were G dwarfs, spectra of an A0V and G0V stars were used for this purpose. The zero point for the second epoch was found to be $ZP = 24.819 \pm 0.014$, and the object magnitude is computed as:

$$J_s = ZP - A_{J_s} \cdot X - 2.5 \log \frac{flux}{G * exptime} \tag{5.2}$$

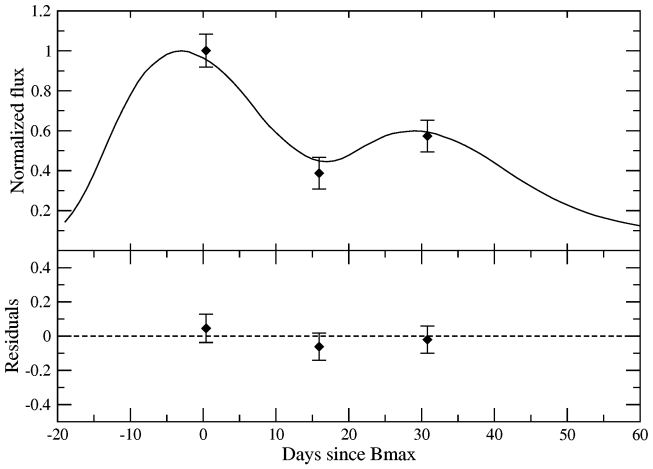

Figure 5.5: Figure 9 from **Paper A**. Rest-frame I-band lightcurve of SN 2000fr in normalised flux. Time axis in days since B maximum. The template fitting the data is the nearby SN 1992bc.

where A_{J_s} is the atmospheric correction for VLT, 0.06 at Paranal, X is the airmass during the observations, equal to 1.177 for the second epoch, and *exptime* is the exposure time, 20 sec. The J_s magnitude is then K-corrected to rest-frame I-band.

An alternative way, is to transform the J_s measurement of the supernova into the J system and then K-correct from J to rest-frame I-band. This, however, leads to the same result as in the method described above. Figure 5.5 shows the rest-frame I-band lightcurve in units of flux normalised to the peak value. The template fitting the data is the nearby SN 1992bc.

A general source of uncertainty is given by the definition of the J standard system. Comparing the two system, one defined by Persson et al.[43], usually used to calibrate IR data, and one by Bessel and Brett [6]. Following Carpenter [10], the transformation between the two systems in J-band is: J_{BB}=J_{LCO}+0.036 ($\pm$0.012).

5.5 Comparison of the two reduction methods

Table 5.2 shows the results obtained with the two different reduction methods. Differences in the photometry are of the order of 5-14%, depending on the epoch. The two methods differ essentially for the double iteration applied by XDIMSUM to the data to improve the sky frame once a map of objects has been built.

As both `XD` and `CL` reduced images show a residual background left in the final results, we subtracted it out before repeating the photometry measurements, to see whether this was relevant. As expected, the background did not affect the psf photometry, and the measurement in the background subtracted images, for both `XD` and `CL` reduced images, was consisted with the photometry in the non-subtracted images.

Thus, we compared the results from the two reductions, looking for differences that could affect the measured photometry. The signal-to-noise ratio of the bright stars in the field for each of the epochs was in agreement between the two reductions. The statistical distribution of sky values in the whole image was also used to compare the two methods, and it is shown in Figure 5.6. We found no significant differences between them at any epochs.

The photometry of the bright stars in the field was also used for the comparison. Figure 5.7 shows the difference in magnitude measured in the two reductions plotted versus the measurements in the `CL` images. As expected, the difference increases for fainter objects, and the dispersion at magnitudes ~ 23, that is about the magnitudes of our SN, the difference is quite large. The standard deviation of the plots showed in Fig. 5.7 for magnitudes fainter than 21 is 0.07 for the first epoch, 0.12 for the second epoch and 0.13 for the third epoch. The results of the two reductions agree within this dispersion. From this analysis we conclude that the difference in the reduction, in particular the way the sky is computed and subtracted, becomes important only for objects fainter than 22 - 23 mag, reached in an exposure time of about 3500 - 4500 s.

As the goal of supernova cosmology is to measure even more distant supernovae, NIR observations become increasingly important, and as such space based observations will be crucial to overcome this kind of problems.

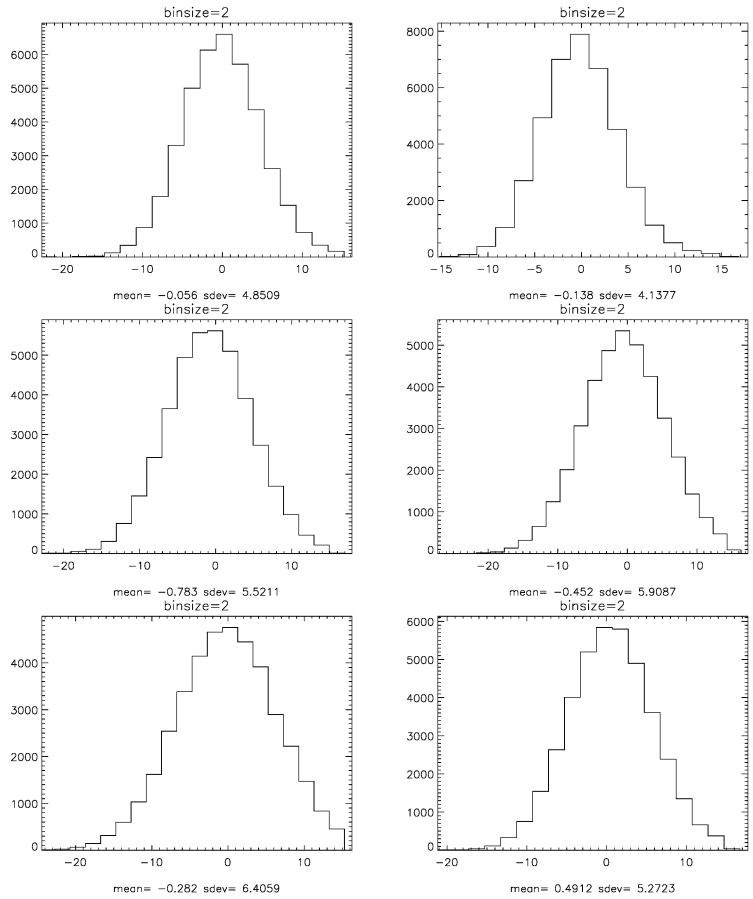

Figure 5.6: Comparison between the sky statistic in the two reduction methods `XD` (left panels) and `CL` (right panels); from top to bottom: 1st, 2nd and 3rd epochs.

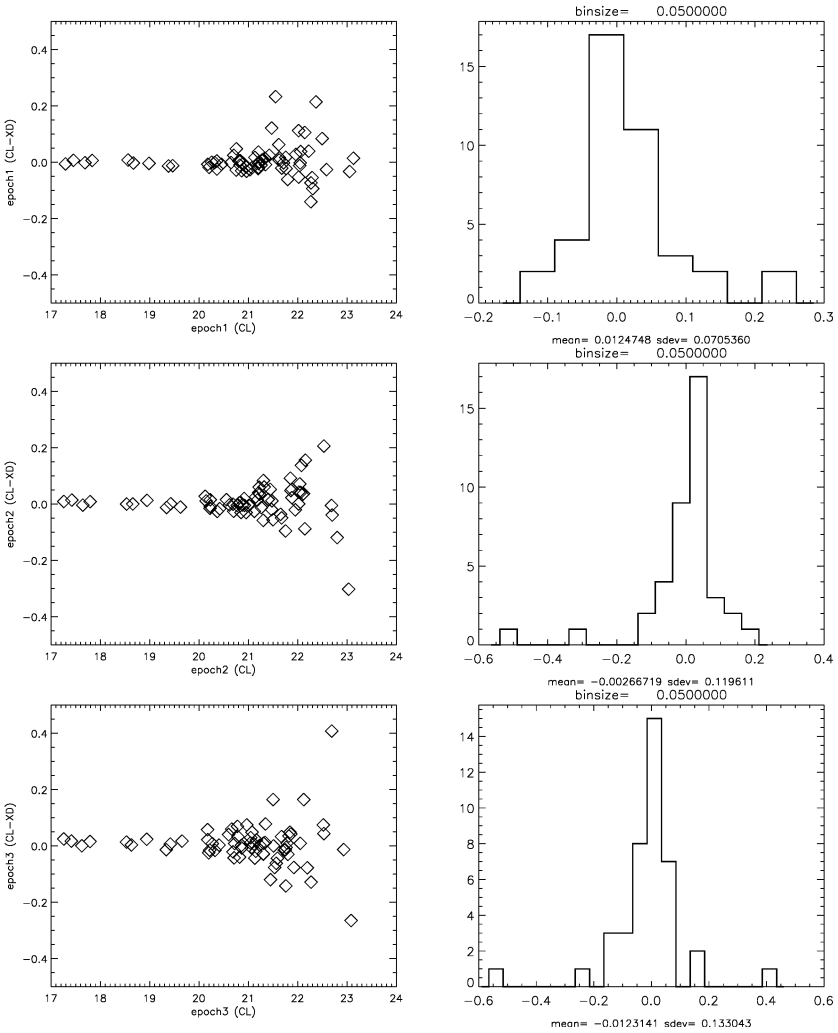

Figure 5.7: Difference of magnitude measured in the `XD` and `CL` images versus the measurements in the `CL` images. The histograms on the right refer to stars fainter than 21 mag only.

Chapter 6

Studies of supernova properties

Given the use of SNe Ia in cosmology, the study of their properties become of fundamental importance to better define the standard candle and to be able to keep systematic uncertainties under control. In this section I describe the work we have done to study properties of both nearby and distant supernovae.

6.1 The low-z 1999 campaign

During the spring of 1999 the Supernova Cosmology Project (SCP) coordinated an intensive campaign in order to discover and follow up a large number of nearby supernovae. The campaign involved many different telescopes all over the world and the data set collected is the successful result of a broad collaboration. A total of 37 SNe were discovered up to redshift $z \sim 0.24$, of which 19 were of the type Ia. Figure 6.1 shows the redshift distribution of the type Ia SNe of this sample. The data consists of both photometry and spectroscopy. This work, however, focus on the spectroscopy data only. During more than 30 nights of observations at 8 different telescopes (APO 3.5m, CTIO 4m, ESO 3.6m, INT, KPNO 4m, Lick 3m, MDM 2.4m, NOT) a total of about 100 spectra were collected. Spectra and images of the host galaxy were observed about one year later. During the time of this thesis, I have been involved in the observations of the host galaxy images at the Nordic Optical Telescope (NOT), and in the data reduction and analysis of the spectroscopy data of the SNe Ia in

this sample. Table 6.1 collects informations for each of the 19 SNe, such as Milky Way reddening, date of B-band maximum, host galaxy name and type, and epochs at which the supernova was observed. The epoch was obtained by preliminary lightcurve fits for most SNe. No dating is known for three SNe, SN 1999at, SN 1999bf and SN 1999bh, for which only late time photometry follow-up is available. Figure 6.2 shows the distribution of epochs at which the spectra were observed, that extends from 15 days before B-band maximum (for SN 1999ac) up to 58 days after B-band maximum (for SN 1999aa).

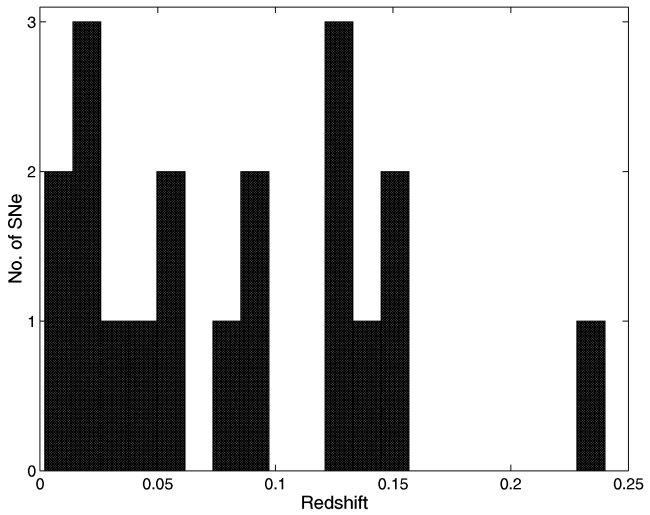

Figure 6.1: Redshift distribution of the SNe of the spring 99 sample.

The data were reduced using IRAF routines. Each frame was bias subtracted and divided by a normalised flat field. The sky background was fitted all along the image, and subtracted to the frame before performing the spectra extraction. This was done using a variance weighted aperture extraction, or optimal extraction, [23]. The one dimensional spectra were calibrated in wavelengths using comparison arc lamp spectra. Extraction of sky spectra on the same image were used to cross check the accuracy of the calibration. Finally, spectrophotometric standard stars were used to flux calibrate the supernova spectra. The reduction scheme adopted for this data set are described in **Paper D**, together with the estimate of statistical uncertainties and studies on systematic uncertainties. These

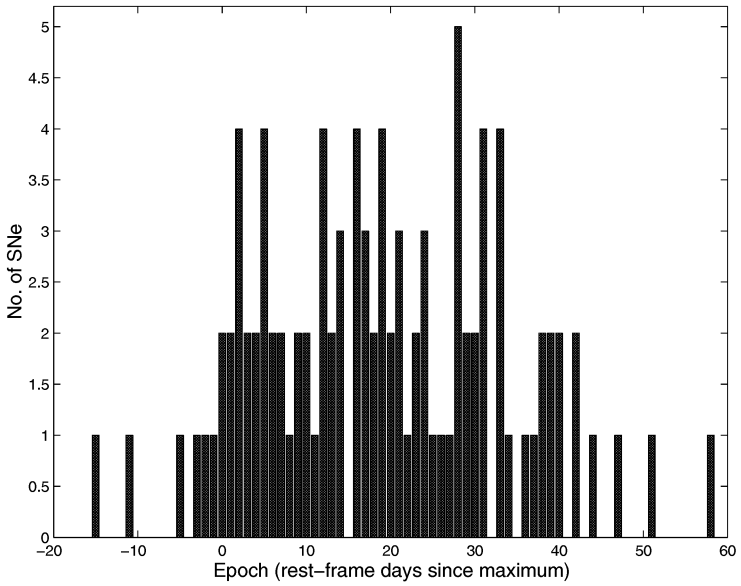

Figure 6.2: Epoch distribution of the spectra collected for the spring 1999 SNe, given in the rest-frame days since B-band maximum.

were estimated when possible using different methods:

- In all the cases for which more than one standard star was observed during the night, these were used to estimate the systematic uncertainty. The set of stars for each night were calibrated using the sensitivity function, and their spectra compared to the corresponding tabulated spectra. The one star deviating most was then excluded from the sample and the sensitivity function was calculated again on the new sample, and used to calibrate the excluded star. Its deviation from the tabulated spectrum was taken as an estimate of an overall systematic uncertainty of the night. The result of this estimate for each night is reported in **Paper D**.

- Whenever the same object was observed in two different instrument settings, we have compared the outcoming spectra in the overlapping wavelength region. This was possible for a number of spectra. The result found is comparable with the estimates obtained using the standard stars. In a few cases the same object was observed at

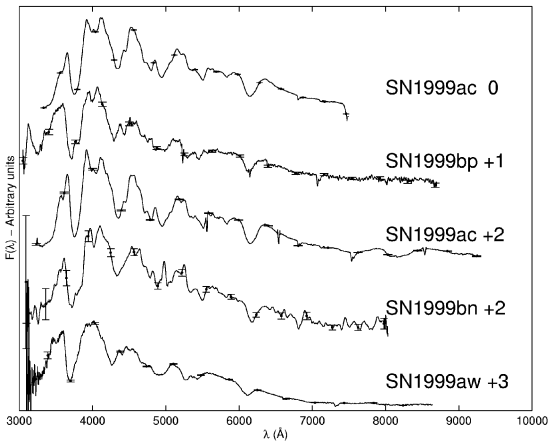

Figure 6.3: Spectra around maximum of the spring 99 sample.

different telescopes during the same night. The comparison between their spectra gave an independent check for systematic effects.

Figure 6.3 shows spectra obtained during the 1999 campaign for several SNe around the time of B-band maximum.

Two supernovae in the sample were especially well followed, with 15 spectra from -11 days to +58 days for SN 1999aa, and 13 spectra from -15 days to 42 days for SN 1999ac. These are peculiar supernovae, and a detailed study of their spectra have been carried and are reported in **Paper III** and **Paper IV** respectively. Figure 6.4 shows the time series for SN 1999aa (from **Paper III**), which is an interesting SN as it shows spectral characteristics in between a normal type Ia and a SN 1991T-like, possibly suggesting that these two SNe are the result of the same kind of progenitor system.

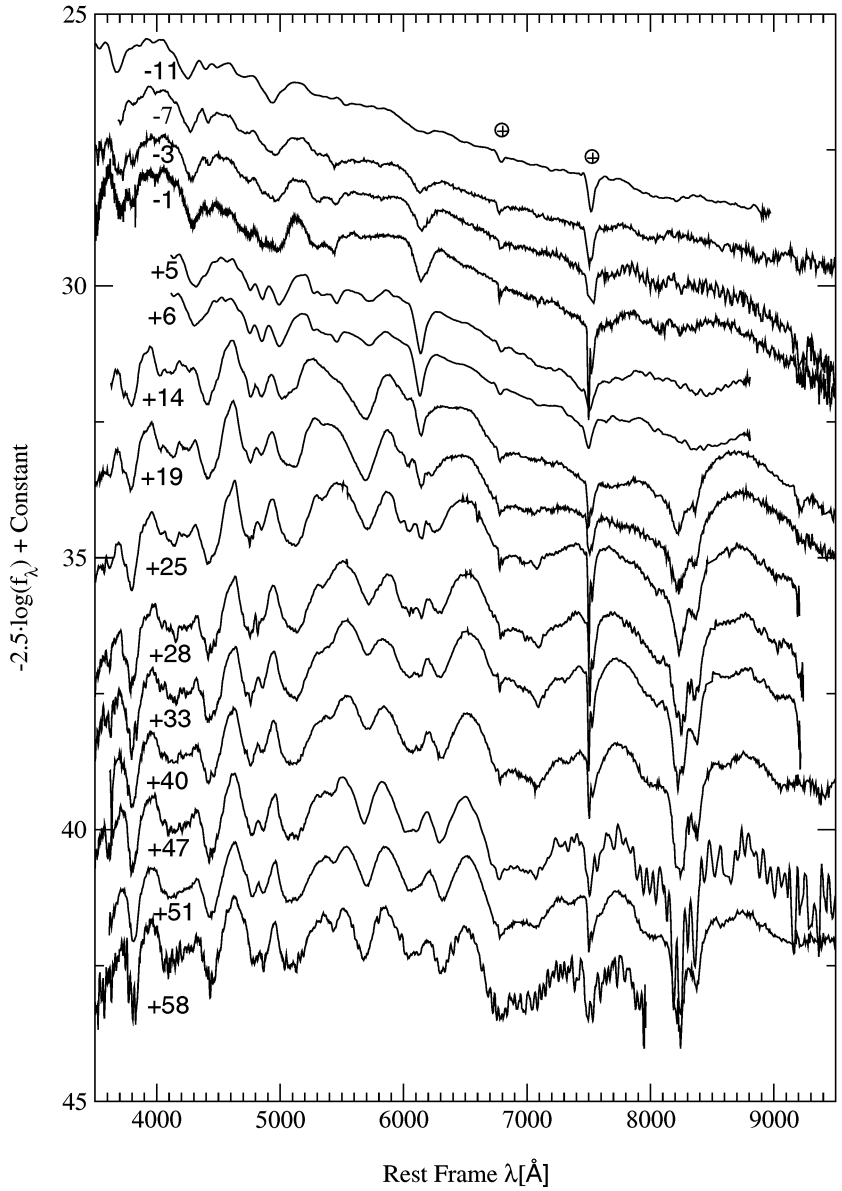

Figure 6.4: Figure 2 from **Paper III**. Time series of SN 1999aa

Table 6.1: Information on the Spring 1999 type Ia SNe.

SN Name	z	E($B-V$) (MW)	Date of max.[a]	Host Galaxy	Host Type[b]	Epochs[c]
1999aa	0.0144	0.040	24-02-99	NGC 2595	SAB(rs)c	−11,−7,−3,−1,5,6,14,19,25, 28,33,40,47,51,58
1999ac	0.0095	0.046	13-03-99	NGC 6063	Scd	−15,−9,0,2,8,11,16,24, 28,31,33,39,42
1999af	0.097	0.029	22-02-99	Anon.	Sa/I0pec:	−5,1,17,19,27
1999ao	0.054	0.065	10-03-99:	Anon.	Sa:	5,7,10,13,18,29,34,40
1999ar	0.15	0.031	08-03-99	Anon.	Sab:	6
1999at	0.027	0.029	(?)	Anon.	E/S0	1 spectrum
1999au	0.124	0.032	02-03-99	Anon.	Sb:	12,17,20,24,31
1999av	0.05	0.031	08-03-99	Anon.	E/S0	2,5,9,12,15,31,42
1999aw	0.04	0.032	12-03-99	Anon.	unknown	3,5,9,12,16,24,31,38
1999be	0.019	0.047	10-03-99:	Anon.	unknown	14,19,26,33,37,44
1999bf	0.24(?)	0.022	(?)	Anon.	unknown	1 spectrum
1999bh	0.0172	0.015	(?)	NGC 3435	Sb	3 spectra
1999bi	0.123	0.027	08-03-99	Anon.	Sb:	6,12,13,29,36
1999bk	0.096	0.027	13-03-99	Anon.	E/S0	4,7,9,10,22,30
1999bm	0.143	0.024	18-03-99:	Anon.	Sb:	3,6,21,28
1999bn	0.129	0.059	21-03-99	Anon.	Sb:	2,14,22,27
1999bp	0.077	0.034	23-03-99	Anon.	Sb:	−2,0,1,6,13,17,23,30
1999bq	0.149	0.043	20-03-99:	Anon.	E/S0	3,18,23,28
1999by	0.0021	0.016	09-05-99	NGC 2841	SA(r)b	1,6,16,27,34

[a] Dates followed by a colon are determined by spectral dating.

[b] Types followed by a colon are taken from spectral classification.

[c] In rest-frame days since B-band maximum light.

6.2 A new set of spectral indicators

Spectral indicators allow quantitative characterisation of spectra and consent to find correlation with lightcurve properties. For instance, properties of two spectral features, the silicon ratio [$\mathcal{R}$(Si II)] and calcium ratio [$\mathcal{R}$(Ca II)] were found to correlate with the luminosity [37].

The low-z 99 sample, together with eight SNe Ia, whose spectra are available from literature, was used to further explore the possibility of characterising supernovae using spectral indicators. **Paper VI** introduces measurements similar to equivalent widths (EW), with the exception to refer to a pseudo-continuum since the continuum of supernova spectra is not well defined. The pseudo-continuum is defined as a straight line fit between two local maxima. The mathematical definition of EW measurement is:

$$\text{EW} = \sum_{i=1}^{N} \left(1 - \frac{f_\lambda(\lambda_i)}{f_c(\lambda_i)}\right) \Delta\lambda_i, \tag{6.1}$$

where λ_i ($i = 1, \ldots, N$) are the central wavelength values of bins of size $\Delta\lambda_i$ over the span of the feature; $f_\lambda(\lambda_i)$ and $f_c(\lambda_i)$ are the measured flux and the fitted continuum flux in each bin i respectively. Eight spectral features were identified on spectra around maximum and chosen to describe supernova spectra. These are listed in Table 6.2, where the wavelength ranges limiting the features are also given. Figure 6.5 shows these features on spectra at maximum and a later epochs. Note that some of them blend with others at some epochs which changes between supernovae.

Feature ID	Mnemonic Label	Blue-ward limit range (Å)	Red-ward limit range (Å)
1	"Ca II H&K"	3500 – 3800	3900 – 4100
2	"Si II 4000"	3900 – 4000	4000 – 4150
3	"Mg II 4300"	3900 – 4150	4450 – 4700
4	"Fe II 4800"	4500 – 4700	5050 – 5550
5	"S II W"	5150 – 5300	5500 – 5700
6	"Si II 5800"	5550 – 5700	5800 – 6000
7	"Si II 6150"	5800 – 6000	6200 – 6600
8	"Ca II IR"	7500 – 8000	8200 – 8900

Table 6.2: Table 3 from **Paper VI**. Features definition and wavelength limits.

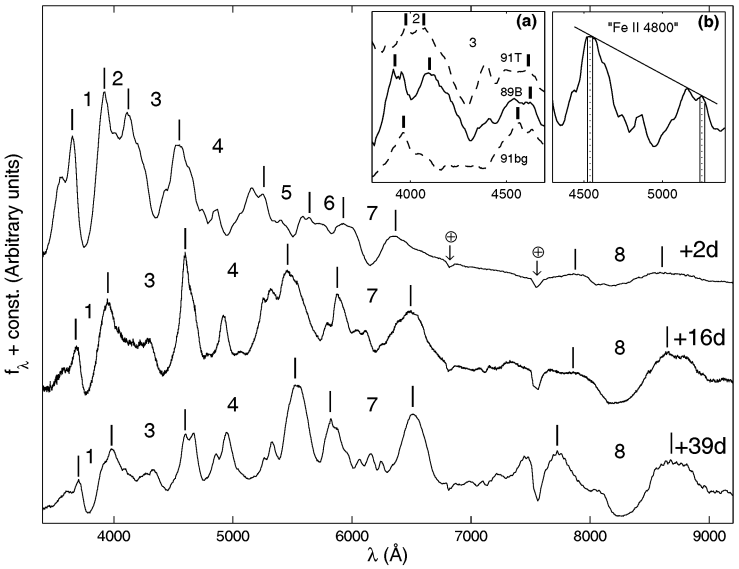

Figure 6.5: Figure 1 from **Paper VI**. SNe Ia spectral evolution and feature definitions for three epochs: 2, 16 and 39 days after maximum light. Numerical labels correspond to the following adopted feature names: **1**- "Ca II H&K"; **2**- "Si II 4000"; **3**- "Mg II 4300"; **4**- "Fe II 4800"; **5**- "S II W"; **6**- "Si II 5800"; **7**- "Si II 6150"; and **8**- "Ca II IR". Short vertical lines show the approximate positions where the pseudo-continuum is taken in each case. Feature ranges change with time and, due to blending, some weaker features are not considered at later epochs. Note that, as the SNe leave the photospheric phase, pseudo-continuum points correspond to emission peaks. *Panel* (**a**): the region of features #2 and #3 for near-maximum spectra of SN 1991T (top), SN 1989B (middle), and SN 1991bg (bottom). Feature #2 is not defined in the case of 1991bg-like SNe. Adopted feature limits are marked with vertical lines. *Panel* (**b**): an example of the pseudo-continuum trace for "Fe II 4800" on a normal SN Ia near the time of maximum light. Here, solid vertical lines show the regions where the pseudo-continuum is fitted. Dotted lines mark the measurement limits.

However empirical, this definition allows to study spectral evolution, as it is fully exploited in the paper, and defines different behaviour for slow decliner supernovae, compared to normal SNe Ia and fast decliner supernovae. Moreover, EW measurements have been used to define parameters that were found to correlate with absolute magnitude.

6.3 Comparing low and high-z SN spectra

We have used EWs, introduced in **Paper VI**, and expansion velocity measurements, to make quantitative comparison between nearby and distant SN spectra. **Paper C** analyses in details spectra of 11 high-z SNe Ia with $0.279 < z < 0.912$, and reports the results of this comparison. The main information on the data set are collected in Table 6.3, such as IAU name for each object, redshift, date of the observation, epoch since B-band maximum, instrument used for the observation, instrumental setting, telescope, exposure time, the signal-to-noise ratio for pixel, percentage of host galaxy light on the total observed flux and type identification.

Possible systematic effects due to reddening or poor resolution can affect the EW measurements, however, the main potential source of uncertainty is host galaxy contamination. In the observed spectrum, the host galaxy light is mixed with the SN flux, and therefore will affect the determination of the pseudo continuum of the spectrum. A statistical comparison of supernova templates and host galaxy spectra was used to determine the fraction of contamination and subtract the host galaxy from the spectrum, with an uncertainty estimated to be about 10 % level of the total flux. In order to determine the uncertainty on the EW measurements due to incomplete host galaxy subtraction, we have artificially added a well defined host galaxy contamination to non contaminated supernovae, and measured the effect on the EW. The results are added in quadrature to the statistical uncertainty.

The clear distinction of the behaviour of EW evolution between normal type Ia supernovae and peculiar ones, both 1991bg-like and 1991T-like, is visible in many features. However, due to the lower signal-to-noise ratio of the distant supernovae we only used the evolution of the deeper features, "Mg II 4300", "Fe II 4800" and "Ca II H&K", shown in Figure 6.6, where the normal SNe (also called Branch-normals) are plotted with closed circles, and the peculiar SNe are plotted with open symbols.

The lines are the average evolution of the normal SNe only. In general, the high redshift SNe have been found to have the same behaviour as the local sample in this first study. In particular this comparison confirms quantitatively the identification of one of the supernovae, SN 2002fd, as 1991T/1999aa-like (see discussion in Section 4.4).

Measurements of expansion velocities of the supernova ejecta is also a mean for distinguishing under-luminous, fast decliner supernovae. At high redshift, the only spectral feature resolved for carrying this study is the Ca II H&K. Figure 6.7 shows the time evolution of the expansion velocity, measured from the Doppler shift of the minimum of this feature, for both nearby and high redshift SNe. The under-luminous supernovae are characterised by lower velocities than normal ones, as shown by SN 1991bg and SN 1999by in the figure. All the high-z SNe in the sample are found consistent with the behaviour of normal luminosity SNe.

6.4 Colour studies

The study of colour evolution and intrinsic colour dispersion can be important in many ways. We have already pointed out their importance for the K-corrections, but also for the determination of the supernova extinction. This include both extinction by dust in the host galaxy or large grain dust in the intergalactic medium.

Paper B presents a study of supernova colours applied to SNe Ia from Calan/Tololo and CfA surveys. The average evolution, the intrinsic dispersion and the correlation of colours at different epochs is studied for $B-V$, $V-R$, $R-I$, $B-I$ and $V-I$. Figure 6.8 (Figure 3 from **Paper B**) shows as an example the $B-V$ evolution for the Calan/Tololo and the CfA data sets separately. The time axis is in rest-frame days since the time of B-band maximum, and the B-band stretch factor is divided out, so that $t' = t/s_B(1+z)$. Estimates of host galaxy extinction, computed by Phillips et al. [46], were used to correct the observed magnitudes. The average evolution for each data set is described by the solid line determined as a spline interpolation of the weighted average computed in four day wide bins. The dashed line represents the evolution found for the same colour of the other data set. Interestingly, the colours were found to correlate with the B-band stretch factor, even for R and I colours, for which this correlation was not assessed yet. A later study, presented in **Paper A**, has shown that this also holds for the I-band peak magnitude.

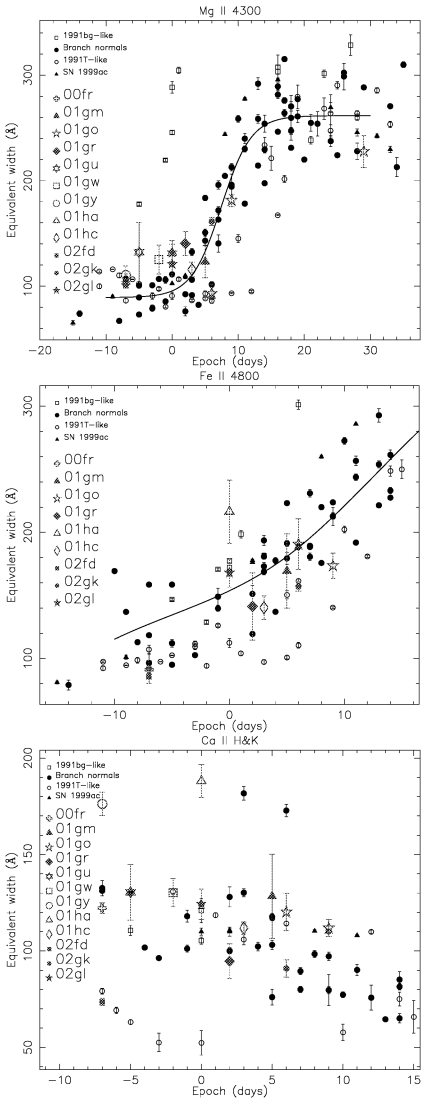

Figure 6.6: Figure 5, 6 and 7 from **Paper C**. EW measurements of the high redshift supernovae compared with local SNe. The solid line indicate the empirical model for normal supernovae as described in **Paper VI**, for "Mg II 4300" (top panel), "Fe II 4800"(middle panel) and "Ca II H&K" (bottom panel). No models are plotted for the latest.

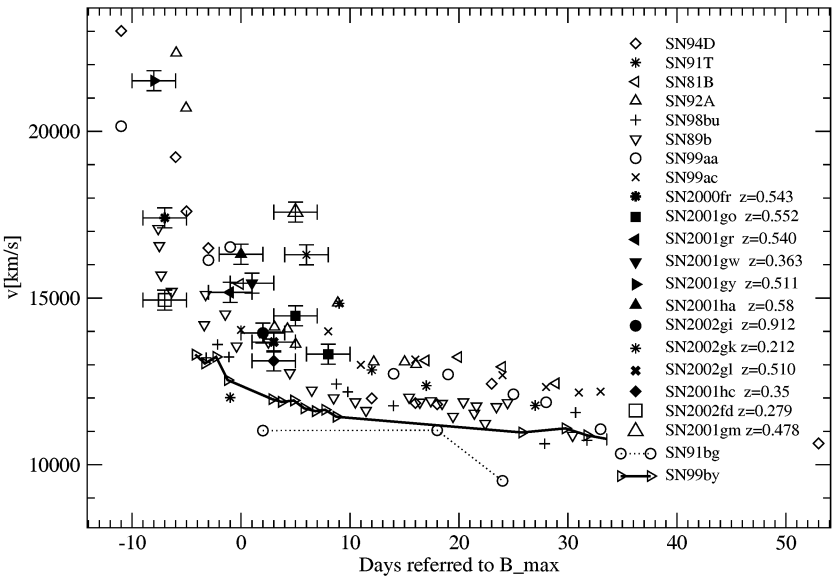

Figure 6.7: Figure 6 from **Paper C**. Ca H&K expansion velocities of high-redshift supernovae presented in **Paper C** compared with local SNe. The solid and dotted lines indicate the values of extreme under-luminous SNe SN 1999by [16] and SN 1991bg [29] respectively.

As the B-band stretch is divided out from the time axis, the curves fitted to the data, correspond to $s_B = 1$ supernovae.

Taking into account the measurement uncertainty, the intrinsic dispersion around the curves was computed for each of the colours at different epoch bins. The case of $V - R$ at epochs later than 25 days after B-band maximum was found compatible with null intrinsic dispersion. In general, the presence of an intrinsic dispersion is a limitation in the possibility of determining the amount of extinction the supernova underwent, since one cannot measure it better than the intrinsic dispersion. In **Paper B** we compute the limits to which the extinction can be determined in each band.

Another important aspect of this work was to determine the correlation between colours at different epochs, e.g. the possibility for a supernova that is bluer than average at a given time, to be still bluer at later time. The results of **Paper B**, the colour evolution curves, the intrinsic dispersion and the correlation of colours at different epochs, were all used

to study colours of high-z SNe in the analysis presented in **Paper A**.

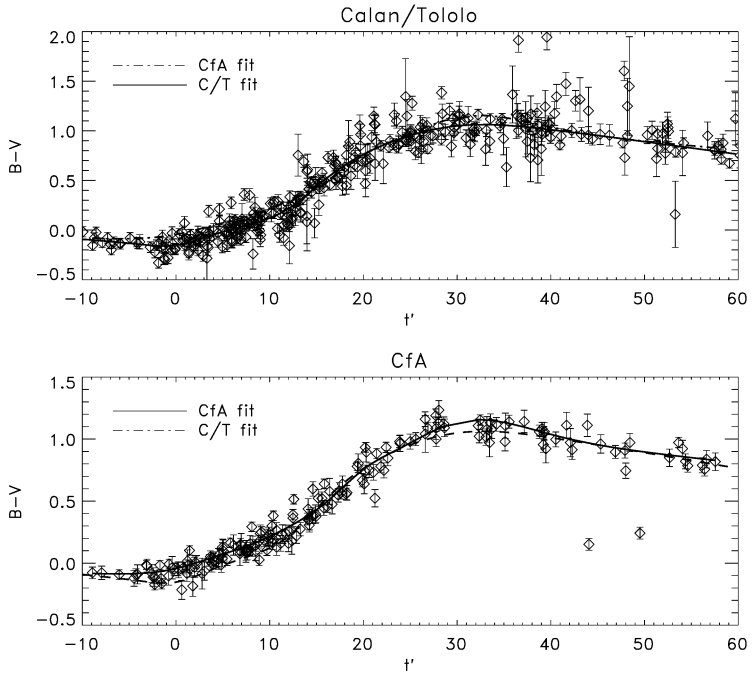

Figure 6.8: Figure 3 from **Paper B**. $B-V$ evolution for the two data sets. The solid line represents always the curve found for the current set, while the dashed line is the curve found for the same colour of the other set. The time axis is in days since B-maximum, divided by the stretch factor, s_B.

6.5 Spectral templates

Our knowledge of supernova colours can be used to improve the spectral templates developed by Nugent et al. [36]. In the work described in this thesis, there are two different approaches, the one adopted in **Paper B** and the one developed by Robert Knop[1] and adopted in **Paper I**. In the first, colours of a nearby sample of SNe Ia were corrected for extinction by dust in the host galaxy, before determining the average colour evolution, as described in the previous section. Instead, in **Paper I** the supernovae

[1]Robert Knop is part of the SCP collaboration and lead author of **Paper I**.

were not corrected for extinction, and a blue-side ridge-line fit was performed to the supernova colour curves. The most reddened supernovae were excluded before performing the fit, and an asymmetric uncertainty was assumed for each of the data points more than 1σ to the red side of the fitted model, such to allow this points to contribute to the χ^2 only as if they were 1σ away. The main difference in the second approach is that it does not rely on the estimate of host galaxy extinction. Figure 6.9 shows the $B-V$ and $R-I$ evolution for all the SNe in the sample. The data are corrected for host galaxy extinction, and the solid line is the curve describing the evolution, according to **Paper B**. For comparison, the curve found by R. Knop is plotted as dashed line, note however, that this is not fitted to the data plotted but to the un-corrected data.

Differences in the estimated colours, affect our precision in the K-corrections. We have build two spectral templates, one for each of the methods described. Figure 6.10 shows the difference between K-corrections found using the two spectral templates in different cases. At redshift 0.4, 0.5 and 0.6 from observed R to rest-frame B-band (left panel) and at z=0.543 from J_s at ISAAC VLT to rest-frame I (right panel). The first case is relevant for **Paper I**, while $z = 0.543$, as well as the J_s at ISAAC VLT, are chosen as example, since it was relevant for the analysis of SN 2000fr presented in **Paper A**.

The difference found in the K-corrections calculated using the two spectral templates are to be taken as systematic uncertainty in the analysis, unless one of the two methods is proved to be more robust than the other. For instance, the case at $z = 0.6$ in Figure 6.10 shows larger differences between the two calculations. This is explained by the fact that the observed R-band at this redshift extends partially to U-band when put to rest-frame. As the templates of **Paper B** where not corrected for the colours in U-band the discrepancy is quite large, and the templates of **Paper I** should be used.

6.6 The I-band lightcurve

The I-band lightcurve has a very characteristic shape. In normal type Ia SNe a second peak appears between 20 and 40 days after the time of B-band maximum. We have developed a fitting technique applied to 42 nearby SNe, which is described in **Paper A**. Figure 6.11 illustrates the method, consisting in two B-band templates fitting the two lightcurve

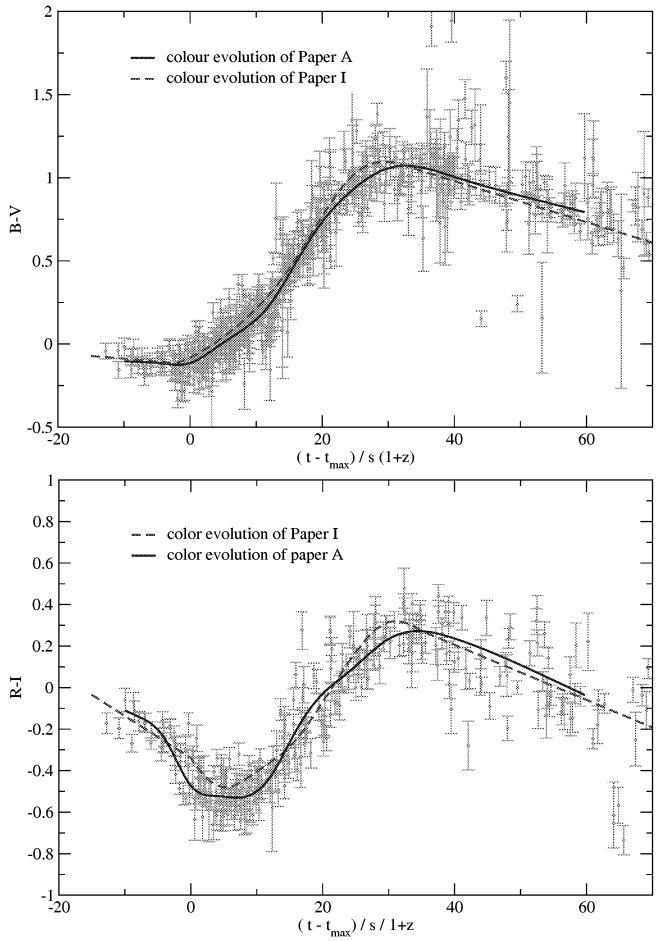

Figure 6.9: $B-V$ and $R-I$ evolution for the two data sets combined. The data have been corrected for host galaxy extinction. The solid line represents the curve found in **Paper B**, the dashed line is the result of the analysis made by R. Knop for **Paper I**, found without correcting the data for the host galaxy extinction.

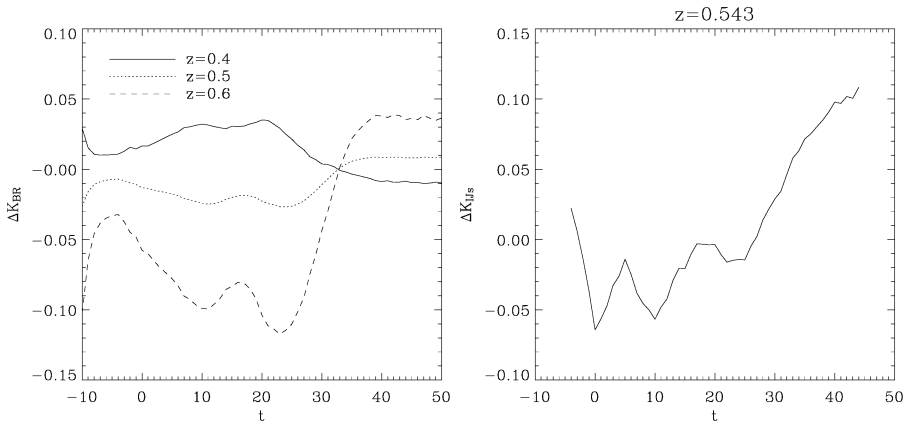

Figure 6.10: Difference between the K-correction estimated using the spectral templates of **Paper B** and of **Paper I**, from R to B at z=0.4, 0.5, 0.6 (left panel) and from J_s of ISAAC and I for z=0.543 (right panel). The larger difference found at z=0.6 (left panel) is mainly due to the contribution of the U-band colour in the K-corrections, since the spectral template in **Paper B** were not corrected in this band.

peaks respectively. Five parameters are used for the fit: the time and amplitude of the first peak, the time and amplitude of the second peak, and a stretch factor for the time axis. The choice of the template used for the fit is probably not unique, and could be improved. For instance, we noticed a trend in the residuals of the fit in the rise part of the lightcurve. A possible solution in this sense, could be to use two different templates, for the first and second peak respectively.

It has been noted that the secondary peak appears earlier and it is lower in fainter objects, and later and more prominent in bright ones, and it is completely absent for subluminous supernovae, [22]. We have proved this qualitative statement by measuring the correlation on the data. The study presented in **Paper A** showed that both first and second peak magnitudes correlate with the B-band stretch factor (see Figure 6.12), confirming the findings in **Paper B**, also discussed in Section 6.4 of this thesis. The error bars in Figure 6.12 include the contribution of peculiar velocities of the host galaxies, which we assumed to be 300 km/s. The dispersion measured as r.m.s. about the line fitted on the data, is 0.19 $\pm$ 0.02 mag. However, this should be taken as upper limit of the disper-

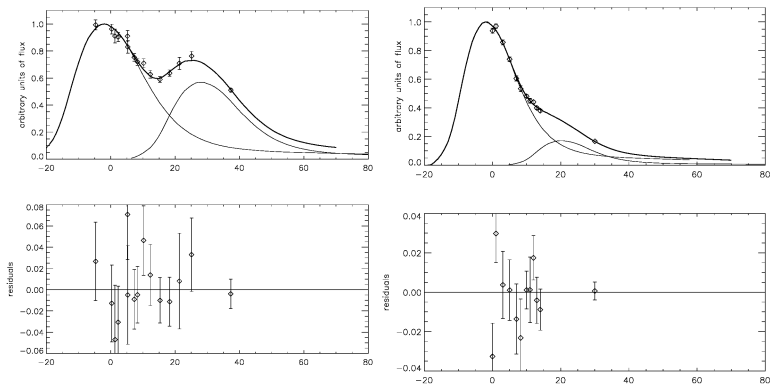

Figure 6.11: The I-band lightcurve of the nearby supernova SN 1995al in arbitrary units of flux, fitted using the method developed in **Paper A**. Two B-band templates are used to fit the first and second peak respectively, for a total of 5 parameters. The time axis is in days since B-band maximum.

sion. In order to disentangle the intrinsic dispersion from the scatter due to peculiar motions and measurement errors, we subtracted the average uncertainty geometrically to the r.m.s. resulting in $\sigma = 0.14$ mag.

Another interesting correlation found in **Paper A**, is the one between the time of the second peak and the B-band stretch factor, shown in Figure 6.13, confirming the expected correlation.

Figure 6.14 shows the difference between the two peaks, $I_{max} - I_{sec}$, versus the B-band stretch factor, s_B (top panel) and versus the I-band stretch factor, s_I (middle panel), and s_B versus s_I (bottom panel). Some of the supernovae are labelled since they show a behaviour somewhat deviant. These three panels together show that the correlation between the stretch factor in B and I-band is probably not linear. In particular, we note that the difference of the two peaks increases with the stretch, for $s_B < 0.9$, and decreases for larger s_B. The dependence on s_I of the same difference is not as clear. If SN 1997br and SN 1998ab are excluded, the data show a linear trend.

6.7 The supernova properties in I-band.

The study presented in **Paper A** using I-band data of nearby SNe Ia, allows to compare properties of supernovae in different bands, e.g. to check whether supernovae that behave in a different way than normal

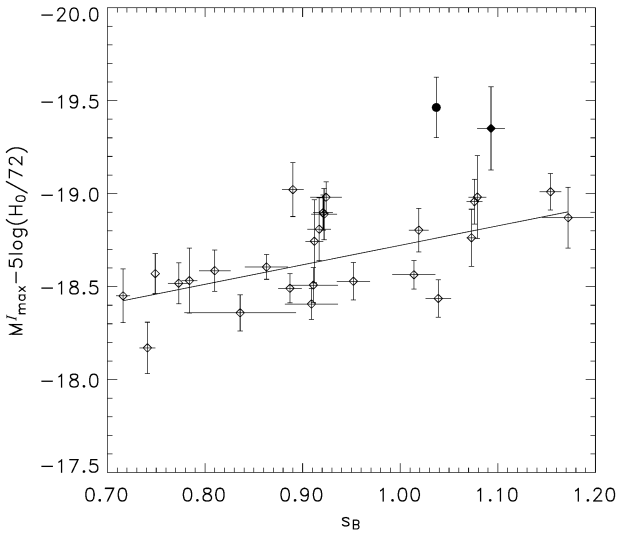

Figure 6.12: Figure 3 from **Paper A**. I-band peak absolute magnitude versus stretch in B-band. Two peculiar supernovae, SN 1998es (filled diamond) and SN 1999dq (filled circle), were excluded from the fit.

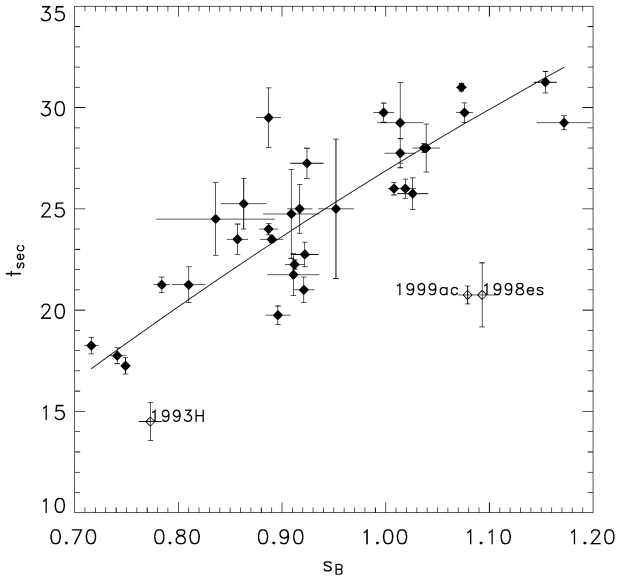

Figure 6.13: Figure 4 from **Paper A**. The time of the second peak in days since B-band maximum versus the B-band stretch factor.

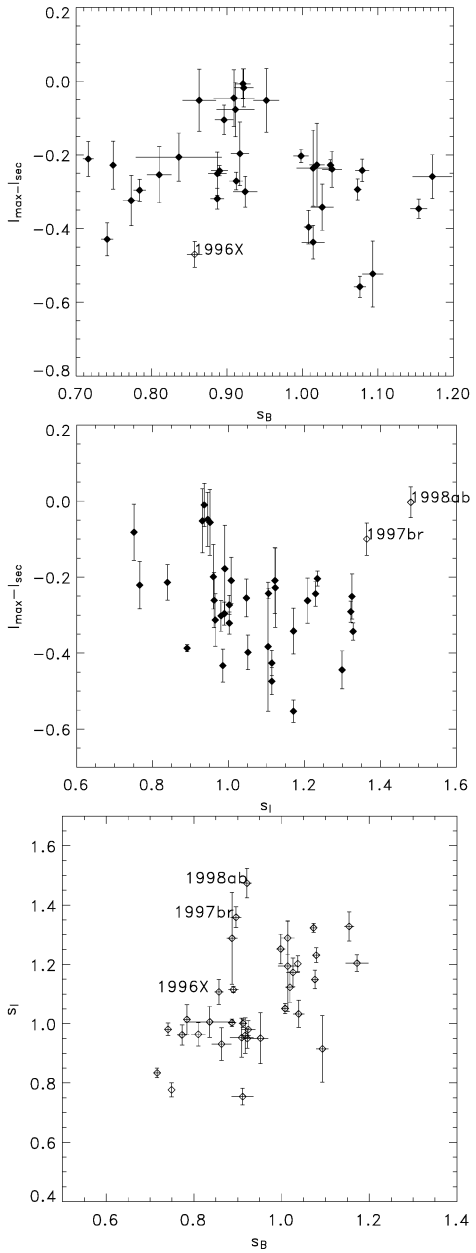

Figure 6.14: Difference between the two peaks, $I_{max} - I_{sec}$, versus the B-band stretch factor, s_B (top panel) and versus the I-band stretch factor, s_I (middle panel), and s_B versus s_I (bottom panel). The labelled supernovae are somewhat deviant from the correlation shown by the ensemble.

SNe at shorter wavelengths, show the same behaviour in the I-band. In particular, we note that a sub-sample of SNe included in the analysis are classified as spectroscopic peculiar. These are SN 1995bd, SN 1997br, SN 1998ab, SN 1998es, SN 1999aa, SN 1999ac, SN 1999dq and SN 1999gp, classified as over-luminous 1991T/1999aa-like [24, 30], and SN 1993H which is reported to have spectroscopic similarities between SN 1992A and the under-luminous SN 1986G [20]. Some of these SNe show also peculiar behaviour in optical bands, such as SN 1999ac, whose lightcurve rises slowly as a over-luminous and declines as a normal SN [45].

The behaviour in I-band of most of these "peculiar" SNe is found consistent with that of normal SNe Ia, with a few exceptions. In the width luminosity relation, shown in Figure 6.12, two supernovae, SN 1998es and SN 1999dq, that are already brighter than average, became even brighter when corrected for host galaxy extinction. Their deviation, which is about 2 - 3σ from the fitted line, could indicate that they are intrinsically redder rather than reddened. One of these SNe, SN 1998es, is also deviant from the average behaviour shown in Figure 6.13, together with SN 1999ac and SN 1993H. Note that the uncertainty on the fitted B-band stretch for SN 1999ac, due to the asymmetry of the lightcurve, can only partially account for its deviation in the figure. In the relations showed in Figure 6.14, other two peculiar SNe are identified as possible outliers. These are SN 1997br and SN 1998ab. Interestingly, only SN 1998es and SN 1999dq are somewhat deviant in the Hubble diagram, as shown in Figure 6.15, where the peculiar SNe are highlighted by grey boxes. Note that, SN 1993H (solid box), is not deviant in the Hubble diagram.

In their recent work, Krisciunas et al. [27] built the Hubble diagram in the near-IR for J,H and K-band. They report the peak magnitude of the peculiar SNe, SN 1999aa, SN 1999ac and SN 1999aw, to be within the dispersion of the normal SNe Ia.

The results of this work suggest that supernovae that deviates from the average standard candle properties in optical band, might have more homogeneous I-band and NIR-band luminosity. Thus, building the Hubble diagram at longer wavelengths might be less affected by systematic effects due to intrinsic scatter.

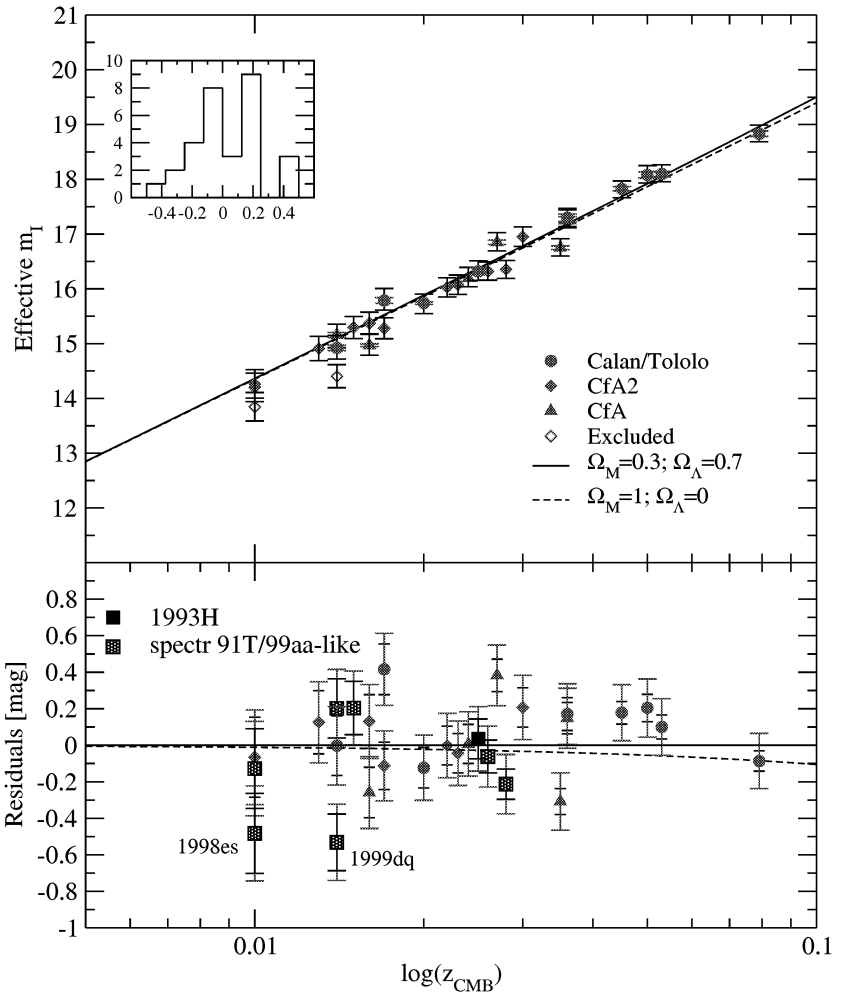

Figure 6.15: Low-z Hubble diagram from **Paper A**, where the peculiar SNe have been plotted with different symbols.

Table 6.3: Summary of high-z spectroscopy data set from **Paper C**.

SN	z[a]	Date (MJD)	Epoch[b]	Instrument	setup	telescope	Exposure time (s)	S/N	Galaxy[c] %	ID
2000fr	0.543	51676.2	-5.5(2)	FORS1	300V grism + GG435	VLT-UT1	7200	10	16	Ia
2001go	0.552	52021.3	5.6(1)	FORS1	300V grism + GG435	VLT-UT1	200	6	19	Ia
2001go	0.552	52058.1	29.5(1)	FORS1	300V grism + GG435	VLT-UT1	9000	2	53	Ia
2001gr	0.540	52021.0	2(2)	FORS1	300V grism + GG435	VLT-UT1	3600	3	57	Ia
2001gw	0.363	52021.4	-1(2)	FORS1	300V grism + GG435	VLT-UT1	1200	3	19	Ia
2001gy	0.511	52021.3	-7,5(1)	FORS1	300V grism + GG435	VLT-UT1	2400	4	20	Ia
2001ha	0.58	52022.0	0(2)	FORS1	300V grism + GG435	VLT-UT1	3600	3	6	Ia
2001hc	0.35	52022.1	0(2)	FORS1	300V grism + GG435	VLT-UT1	1800	7	14	Ia
2001gm	0.478	52021.3	5(2)	FORS1	300V grism + GG435	VLT-UT1	2400	2	?	Ia
2002gi	0.912	52407.2	2(2)	FORS2	300I grism + GG435	VLT-UT4	7200	2	?	Ia
2002gl	0.510	52413.1	-5(2)	FORS2	300V grism + GG435	VLT-UT4	3000	5	23	Ia
2002fd	0.279	52376.1	-7(2)	FORS2	300V grism + GG435	VLT-UT4	600	29	28	**Iapec**

[a] From host galaxy if 3-digits

[b] Uncertainties quoted in parenthesis

[c] Estimated in percentage on the total observed flux by statistical methods.

Chapter 7

Summary and outlook

The main goal of this thesis was to study systematic effects involved with the use of type Ia supernovae as distance indicators, such as extinction by dust in the host galaxy or in the intergalactic medium, contamination of other supernova types in the Hubble diagram, estimates of the K-corrections, and possible drift in supernova population.

Studies of properties of nearby supernovae were used to improve our knowledge of the standard candle. The average $B-V$, $V-R$, $R-I$, $V-I$ and $B-I$ colour evolution of SNe Ia was applied to improve existing spectral templates, used for computing K-corrections. Moreover, intrinsic colour dispersion as well as correlation of this dispersion at different epochs was studied and presented in **Paper B**. The intrinsic colour dispersion limits our ability to determine the amount of extinction due to dust in the host galaxy or in the intergalactic medium, as investigated in **Paper B** and discussed in Section 4.2 and 6.4.

Spectral properties of high redshift supernovae were compared to those of nearby objects, using spectral indicators such as EW and expansion velocities, and found in agreement, pointing out no spectral evolution and therefore confirming the reliability of SNe Ia as distance indicators. Moreover, the discovery of the first supernova, SN 2002fd, with spectral properties resembling those of slow-decliner 1991T/1999aa-like supernovae, gives additional support against the hypothesis of evolution with redshift as an alternative to dark energy (**Paper C**). The presence of a second peak in the I-band lightcurve of high redshift SNe was also used for testing the evolution hypothesis (**Paper A**), which was not supported by the results.

Problems connected with type identification of high redshift supernovae, important to avoid contamination by other supernova types in the Hubble diagram, were also addressed in **Paper C**.

A novel technique for fitting I-band lightcurve was developed and applied to 42 nearby SNe. A width-luminosity relation was found between both I-band first peak and the second peak magnitude, with the B-band stretch factor. Other correlations between properties of the I-band lightcurve and the SN luminosity were also identified, such as between the time of the second peak and the stretch factor.

The SNe in this sample with redshift $z > 0.01$ were used to build the Hubble diagram, which was also extended up to $z \sim 0.5$ adding three high-z SNe (**Paper A**). This was found to be in agreement with the concordance model of the universe, although more high quality, well sampled lightcurve data is needed to be able to use this as a complementary tool in experimental cosmology.

Finally, a large data sample including about 100 spectra of SNe Ia was collected during the low-z 1999 campaign. The reduction of this data sample allowed to develop methods for estimating possible systematic uncertainties in the SN spectra. These are presented in **Paper D** and discussed in Section 6.1. This data set was used to study SN properties in **Paper III**, **Paper IV** and **Paper VI**.

None of the results presented in this work, are challenging the current scenario of the universe. On the contrary, some confirm the present results and increase our confidence in the use of supernovae as distance indicators. Due to the flow of data collected by large experiments and the data expected to be collected in the near future, the main limitation will certainly be due to our control upon the systematic effects involved. This is both affecting the determination of the cosmological parameters at very high precision, and the measurements of the equation of state parameter to determine the nature of dark energy. In this sense the studies and the techniques developed and presented in this work will become increasingly important as new data is analysed.

Bibliography

[1] Aguirre, A. N., 1999, ApJ, 512, L19

[2] Aguirre, A. N., 1999, ApJ, 525, 583

[3] Balbi, A., P. Ade, J. Bock, et al., 2000, ApJ, 545, L1

[4] Benítez, N., A. Riess, P. Nugent, et al., 2002, ApJ, 577, L1

[5] Bessell, M. S., 1990, PASP, 102, 1181

[6] Bessell, M. S. and J. M. Brett, 1988, PASP, 100, 1134

[7] Branch, D. and D. L. Miller, 1993, ApJ, 405, L5

[8] Branch, D. and G. A. Tammann, 1992, ARA&A, 30, 359

[9] Cardelli, J. A., G. C. Clayton, and J. S. Mathis, 1989, ApJ, 345, 245

[10] Carpenter, J. M., 2001, AJ, 121, 2851

[11] Dahlén, T. and A. Goobar, 2002, PASP, 114, 284

[12] de Bernardis, P., P. A. R. Ade, J. J. Bock, et al., 2000, Nature, 404, 955

[13] Efstathiou, G. and J. R. Bond, 1999, MNRAS, 304, 75

[14] Efstathiou, G., S. Moody, J. A. Peacock, et al., 2002, MNRAS, 330, L29

[15] Filippenko, A. V., 1997, ARA&A, 35, 309

[16] Garnavich, P. M. et al., 2001, astro-ph/0105490

[17] Goobar, A., 2001, Nuclear Physics B Proceedings Supplements, 95, 8

[18] Goobar, A., L. Bergström, and E. Mörtsell, 2002, A&A, 384, 1

[19] Goobar, A. and S. Perlmutter, 1995, ApJ, 450, 14

[20] Hamuy, M., J. Maza, M. Wischnjewsky, et al., in International Astronomical Union Circular (1993)

[21] Hamuy, M., M. M. Phillips, N. B. Suntzeff, et al., 1996, AJ, 112, 2391

[22] Hamuy, M., M. M. Phillips, N. B. Suntzeff, et al., 1996, AJ, 112, 2438

[23] Horne, K., 1986, PASP, 98, 609

[24] Howell, D. A., 2001, ApJ, 554, L193

[25] Jha, S., PhD Thesis (Harvard University, 2002, 2002)

[26] Kim, A., A. Goobar, and S. Perlmutter, 1996, PASP, 108, 190

[27] Krisciunas, K., M. M. Phillips, and N. B. Suntzeff, 2003, ArXiv Astrophysics e-prints

[28] Leibundgut, B., 2001, ARA&A, 39, 67

[29] Leibundgut, B., R. P. Kirshner, M. M. Phillips, et al., 1993, AJ, 105, 301

[30] Li, W., A. V. Filippenko, R. R. Treffers, et al., 2001, ApJ, 546, 734

[31] Mörtsell, E. and A. Goobar, 2003, Journal of Cosmology and Astro-Particle Physics, 9, 9

[32] Mörtsell, E., C. Gunnarsson, and A. Goobar, 2001, ApJ, 561, 106

[33] Malmquist, K., 1924, Medd. Lund Astron. Obs. Ser. II, 32, 64

[34] Malmquist, K., 1936, Stockholm Observatory Medd., 26

[35] Nobili, S., C. Lidman, G. Aldering, et al., 2001, Bulletin of the American Astronomical Society, 33, 1333

[36] Nugent, P., A. Kim, and S. Perlmutter, 2002, PASP, 114, 803

[37] Nugent, P., M. Phillips, E. Baron, D. Branch, and P. Hauschildt, 1995, ApJ, 455, L147+

[38] Pain, R. and SNLS Collaboration, 2002, Bulletin of the American Astronomical Society, 34, 1169

[39] Perlmutter, S., G. Aldering, S. Deustua, et al., 1997, Bulletin of the American Astronomical Society, 29, 1351

[40] Perlmutter, S., G. Aldering, G. Goldhaber, et al., 1999, ApJ, 517, 565

[41] Perlmutter, S., S. Gabi, G. Goldhaber, et al., 1997, ApJ, 483, 565

[42] Perlmutter, S. and B. P. Schmidt, 2003, astro-ph/0303428

[43] Persson, S. E., D. C. Murphy, W. Krzeminski, M. Roth, and M. J. Rieke, 1998, AJ, 116, 2475

[44] Phillips, M. M., 1993, ApJ, 413, L105

[45] Phillips, M. M., K. Krisciunas, N. B. Suntzeff, et al., in From Twilight to Highlight: The Physics of Supernovae (2003)

[46] Phillips, M. M., P. Lira, N. B. Suntzeff, et al., 1999, AJ, 118, 1766

[47] Riess, A. G., A. V. Filippenko, P. Challis, et al., 1998, AJ, 116, 1009

[48] Riess, A. G., A. V. Filippenko, M. C. Liu, et al., 2000, ApJ, 536, 62

[49] Riess, A. G., R. P. Kirshner, B. P. Schmidt, et al., 1999, AJ, 117, 707

[50] Riess, A. G., W. H. Press, and R. P. Kirshner, 1996, ApJ, 473, 88

[51] Sievers, J. L., J. R. Bond, J. K. Cartwright, et al., 2003, ApJ, 591, 599

[52] Smith, R. C., C. Aguilera, K. Krisciunas, et al., 2002, Bulletin of the American Astronomical Society, 34, 1232

[53] Spergel, D. N., L. Verde, H. V. Peiris, et al., 2003, ApJS, 148, 175

[54] Tonry, J. L., B. P. Schmidt, B. Barris, et al., 2003, ApJ, 594, 1

[55] Tozzi, P., P. Rosati, M. Nonino, et al., 2001, ApJ, 562, 42

[56] Wambsganss, J., 1998, Living Reviews in Relativity, 1, 12

[57] Weinberg, S., Gravitation and cosmology: Principles and applications of the general theory of relativity (New York: Wiley, —c1972, 1972)

Paper A

Astronomy & Astrophysics manuscript no. March 3, 2004
(DOI: will be inserted by hand later)

Restframe *I*-band Hubble diagram for type Ia supernovae up to $z \sim 0.5$

S. Nobili[1], R. Amanullah[1], G. Garavini[1], A. Goobar[1], C. Lidman[17], V. Stanishev[1], G. Aldering[5,4], P. Astier[7], G. Blanc[5,7], M. S. Burns[8], A. Conley[5,9], S. E. Deustua[5,10], M. Doi[11], R. Ellis[12], S. Fabbro[13,4], A. S. Fruchter[14], G. Folatelli[1], R. Gibbons[5], G. Goldhaber[5,9], D. E. Groom[5,4], D. Hardin[7], I. Hook[15], D. A. Howell[5], A. G. Kim[5,4], R. A. Knop[2,3,4], B. C. Lee[5], J. Mendez[18,19], P. E. Nugent[5,4], R. Pain[7], N. Panagia[14], C. R. Pennypacker[5], S. Perlmutter[5], R. Quimby[5], J. Raux[7], N. Regnault[5,23], P. Ruiz-Lapuente[19], G. Sainton[7], B. Schaefer[20], K. Schahmaneche[7], E. Smith[2], A. L. Spadafora[5], M. Sullivan[21,12], N. A. Walton[16], L. Wang[5], W. M. Wood-Vasey[5,9], and N. Yasuda[22]
(THE SUPERNOVA COSMOLOGY PROJECT)

[1] Department of Physics, Stockholm University,AlbaNova University Center, S–106 91 Stockholm, Sweden
[2] Department of Physics and Astronomy, Vanderbilt University, Nashville, TN 37240, USA
[3] Visiting Astronomer, Kitt Peak National Observatory, National Optical Astronomy Observatory, which is operated by the Association of Universities for Research in Astronomy, Inc. (AURA) under cooperative agreement with the National Science Foundation.
[4] Visiting Astronomer, Cerro Tololo Interamerican Observatory, National Optical Astronomy Observatory, which is operated by the Association of Universities for Research in Astronomy, Inc. (AURA) under cooperative agreement with the National Science Foundation.
[5] E. O. Lawrence Berkeley National Laboratory, 1 Cyclotron Rd., Berkeley, CA 94720, USA
[6] Department of Physics, Stockholm University, SCFAB, S-106 91 Stockholm, Sweden
[7] LPNHE, CNRS-IN2P3, University of Paris VI & VII, Paris, France
[8] Colorado College 14 East Cache La Poudre St., Colorado Springs, CO 80903
[9] Department of Physics, University of California Berkeley, Berkeley, 94720-7300 CA, USA
[10] American Astronomical Society, 2000 Florida Ave, NW, Suite 400, Washington, DC, 20009 USA.
[11] Department of Astronomy and Research Center for the Early Universe, School of Science, University of Tokyo, Tokyo 113-0033, Japan
[12] California Institute of Technology, E. California Blvd, Pasadena, CA 91125, USA
[13] Centro, Multidisiplinar de Astrofísica, Instituo, Superior Técnico, Lisbo
[14] Space Telescope Science Institute, 3700 San Martin Drive, Baltimore, MD 21218, USA
[15] Department of Physics, University of Oxford, Nuclear & Astrophysics Laboratory Keble Road, Oxford, OX1 3RH, UK
[16] Institute of Astronomy, Madingley Road, Cambridge CB3 0HA, UK
[17] European Southern Observatory, Alonso de C ordova 3107, Vitacura, Casilla 19001, Santiago 19, Chile
[18] Isaac Newton Group, Apartado de Correos 321, 38780 Santa Cruz de La Palma, Islas Canarias, Spain
[19] Department of Astronomy, University of Barcelona, Barcelona, Spain
[20] University of Texas, Department of Astronomy, C-1400, Austin, TX,78712, U.S.A.
[21] Department of Physics, University of Durham, South Road, Durham, DH1 3LE, UK
[22] National Astronomical Observatory, Mitaka, Tokyo 181-8588, Japan
[23] Now at LLR, CNRS-IN2P3, Ecole Polytechnique, Palaiseau, France

Received ...; accepted ...

Abstract. Using a novel technique for fitting restframe *I*-band lightcurves of type Ia supernovae, a Hubble diagram including 26 SNe with $0.01 < z < 0.1$ was constructed. Adding three SNe at $z \sim 0.5$ yields results that support the expectations for a flat Λ-dominated "concordance universe" $(\Omega_M, \Omega_\Lambda)$=(0.3,0.7). The high redshift supernova NIR data was also used to test for systematic effects in the use of SNIa as distance estimators. A flat, $\Lambda = 0$, universe where the faintness of supernovae at $z \sim 0.5$ is due to gray dust homogeneously distributed in the intergalactic medium is disfavored based on the high-z Hubble diagram using this preliminary data-set. However, the uncertainties are large and no firm conclusion may be drawn. We also show that more supernovae are necessary to set limits on intergalactic dust based on $B - I$ and $B - V$ color measurements. The high redshift restframe *I*-band lightcurves are better fit by templates that show a second peak than by templates without a second peak, suggesting that they are not intrinsically subluminous.

Key words. cosmology:observations, supernovae: general

1. Introduction

Observations of type Ia supernovae (SNe) in restframe B-band up to $z \sim 1$ and above have shown that they are significantly dimmer than expected in a universe without a cosmological constant or some other form of dark energy (Garnavich et al., 1998; Riess et al., 1998; Perlmutter et al., 1999; Tonry et al., 2003; Knop et al., 2003). The evidence for dark energy is supported by cross-cutting cosmological results, such as the measurement of the cosmic microwave background anisotropy, which indicates a flat universe (De Bernardis et al., 2000; Jaffe et al., 2001; Sievers et al., 2003; Spergel et al., 2003); the evolution in the number density of X-ray emitting galaxy clusters (Borgani et al., 2001; Henry , 2001) and galaxy redshift surveys (Efstathiou et al., 2002), the two latter indicate that $\Omega_{\rm M} \approx 0.3$. Taken together, these independent measurements suggest a concordance universe ($\Omega_{\rm M}$,Ω_Λ)=(0.3,0.7). However, the SN Hubble diagram remains the most direct approach currently in use for studying cosmic acceleration and, thus, systematic effects affecting the observed brightness, of type Ia supernovae should be carefully considered. These include: uncorrected host galaxy extinction (see e.g. Rowan-Robinson (2002)), dimming by photon-axion mixing over cosmological distances (Csaki et al., 2001; Deffayet et al., 2001; Mörtsell et al., 2002), dimming by intergalactic gray dust (Aguirre, 1999a,b; Mörtsell & Goobar, 2003) and intrinsic luminosity evolution (Drell et al., 2000).

Determining cosmological distances through type Ia supernovae fluxes at longer restframe wavelengths offers potential advantages, e.g. less sensitivity to dust along the line of sight, either in the host galaxy or in the intergalactic medium. On the other hand, the "standard candle" properties at these wavelengths and the possibility of additional systematic effects need to be investigated.

Using restframe I-band, the uncertainty due to extinction by dust is greatly reduced as compared with restframe B-band measurements. For example for Milky-Way type dust ($R_V = 3.1$) the ratio of extinction for the two bands is sizable, $A_B/A_I \sim 2-3$. In general, the extinction corrections become less sensitive to our knowledge of the intrinsic supernova colors and dust properties.

I-band lightcurves typically show a second peak 15-30 days after the first maximum. It has been suggested that the intensity and time-difference between the first and second I-band peak are related to the intrinsic luminosity of the type Ia SNe, appearing later and more evident for normal type Ia and earlier and fainter for subluminous ones (Hamuy et al., 1996a; Wang, 2003). Thus, building I-band lightcurves for type Ia supernovae offers the possibility of finding means for probing brightness evolution.

The scope of this work is to test the feasibility of using restframe I-band for cosmological distance measurements, using data available to date, and assess the importance of observing in this wavelength range for the future samples of SNe. For that purpose, we develop a template fitting technique to estimate the first ($I_{\rm max}$) and second ($I_{\rm sec}$) I-lightcurve peaks, which we apply to 42 nearby SNe Ia. $I_{\rm max}$ is used to build a SN Ia Hubble diagram reaching out to $z \sim 0.5$. Infrared data of a supernova at redshift $z = 0.543$, SN 2000fr, is presented and used in the Hubble diagram, together with other two SNe in the same reshift range, available in literature, SN 1999Q (Riess et al., 2000) and SN 1999ff (Tonry et al., 2003). The properties of the second peak in the restframe I-band lightcurves are investigated. Furthermore, additional color information is used to test for extinction by non-conventional dust for three $z \sim 0.5$ supernovae.

2. I-band lightcurve fit

The second lightcurve peak seen in nearby type Ia SNe, varies in strength and position with respect to the primary maximum, and complicates the use of a single parametrized template for lightcurve fitting, which is currently often applied for B and V-band, (see e.g. Perlmutter et al. (1997); Goldhaber et al. (2001) for example of the timescale stretch factor approach).

We have developed a method for fitting I-band lightcurves using five free parameters. The underlying function is a combination of two standard B-band templates of type Ia supernovae[1]. Our fitting procedure can be summarized as follows: one B-band template is used to fit the time (t_1) and the first peak magnitude (I_1), together with a stretch factor (s_I), which is also applied to the second B-band template shifted in time to fit the time (t_2) and magnitude of the second peak (I_2). In general, $I = I_1\mathcal{B}(s_I(t-t_1)) + I_2\mathcal{B}(s_I(t-t_2))$, where $\mathcal{B}$ is the B-band lightcurve template. The five parameters fitted are thus: $\{t_1, t_2, I_1, I_2, s_I\}$, (see Table 1). A similar approach has also been proposed by Wang (2003) who calls it "super-stretch" to emphasize its extension of the stretch approach.

Contardo et al. (2000) proposed a model composed of as many as 4 functions for a total of 10 parameters in order to fit all $UBVRI$-bands. Their method used two Gaussian functions to fit the two peaks together with a straight line to fit the late time decline and an exponential factor for the pre-max rising part of the lightcurve. This method describes type Ia SNe lightcurve in all optical bands, though, as the authors recognize, does not represent accurately the second peak in the I-band due to the influence of the linear decline. However, the main disadvantage of their method is the large number of free parameters, thus the need for the object to be extremely well sampled.

The use of the standard B-band template of type Ia supernovae reduces the number of free parameters by a factor of two. Moreover, with this choice, no additional functions are needed to fit the pre-max rising part of the lightcurve nor the late time decline. Implicitly, we have thus assumed that the rising part of the lightcurve in I-band is the same as in B-band. As our goal is only to measure the position and amplitude of the first two peaks, we limit the fit to 40 days after maximum, neglecting the late time decline. Note that, unless otherwise specified, the supernova phase always refers to the time relative to restframe B-band lightcurve maximum.

Send offprint requests to: S. Nobili , serena@physto.se

[1] The B-band template in Nugent et al. (2003) has been used.

t_1	time of the peak of the first $\mathcal{B}$ template
I_1	peak magnitude of the first $\mathcal{B}$ template
t_2	time of the peak of the second $\mathcal{B}$ template
I_2	peak magnitude of the second $\mathcal{B}$ template
s_I	stretch factor of the time axis
$t_{\max}$	time of the first I-lightcurve peak
$I_{\max}$	first I-lightcurve peak magnitude
$t_{\sec}$	time of the second I-lightcurve peak
$I_{\sec}$	second I-lightcurve peak magnitude

Table 1 Summary of the parameters used in this work to describe the I-band lightcurve. The first five parameters are determined by fitting the data (see text for details). The next four parameters are the actual time and peak values of the lightcurve. Note that $I_1 = I_{\max}$ by construction.

2.1. The data set

We applied this method to fit a sample of local SNe for which both B and I-band data are available in the litterature from the Calan/Tololo (Hamuy et al., 1996a), CfA (Riess et al., 1999) and CfA2 (Jha , 2002) data sets. Data from three other well studied individual supernovae were also included: SN 1989B (Wells et al., 1994), SN 1994D (Richmond et al., 1995) and one subluminous supernova: SN 1991bg. There are at least two available data sets in restframe I-band for SN 1991bg, one published by Filippenko et al. (1992) with quite good coverage from about 3 days after B-band maximum light to +60 days, another one published by Leibundgut et al. (1993) with four data points, the first of which is at the time of B-band maximum. The agreement between the two data sets was assessed by comparing the measurements taken at the same date, i.e. JD=2448607, where we found a difference of 0.06 mag. This was considered to be the uncertainty for the four data points from Leibundgut et al. (1993) since they scatter more and no error-bars were reported in the original paper.

2.2. Fitting method and results

Only supernovae with at least 6 data points and a coverage in time constraining both peaks, were selected for lightcurve fitting. This resulted in a total of 42 SNe. Table 2 lists the parameters resulting from the fitting procedure. Note that the fit was performed in units of flux, while the parameters given in the table are transformed to magnitudes. Prior to fitting, all data points were K-corrected to restframe I-band as in (Kim et al., 1996; Nugent et al., 2003), assuming standard Bessel I-band, using the spectral template in (Nobili et al., 2003) and time information from the available B-band data. Note that the values of I2 reported in Table 2 are not the actual magnitudes of the secondary peak , $I_{\sec}$, but a parameter indicating the size of the contribution of the secondary B-band template to the overall I-band template.

A potential source of systematic uncertainties is in the K-corrections due to the wide Ca IR triplet absorption feature, found to vary considerably among Type Ia supernovae (Nugent et al., 2003). However, up to $z \sim 0.1$ the contribution of this feature is in general not critical to the precision of the K-corrections. For more distant SNe this could be a source of systematic uncertainty that has to be taken into account.

In Figure 1 all the fitted lightcurves are shown. They are sorted in chronological order, except for the two very subluminous supernovae: SN 1991bg and one of the supernovae in the CfA2 data-set, SN 1997cn, displayed at the bottom of the figure. As no date of B-band maximum light is known from the literature for SN 1997cn, the origin of the time axis was put to the epoch ($JD = 2450597.75$) when this supernova was first observed. Note that the second peak for the sub-luminous supernovae is almost completely absent, resulting in a value of $I_2 \sim 2.5$ to 3 magnitudes fainter than I_1.

Our sample also includes SNe that are classified as spectroscopic peculiar, showing similarities with the over-luminous SN 1991T (Li et al., 2001; Howell , 2001). These are SN 1995bd, SN 1997br, SN 1998ab, SN 1998es, SN 1999aa, SN 1999ac, SN 1999dq and SN 1999gp. One supernova, SN 1993H, was reported to show similarities with the spectrum of the peculiar under-luminous 1986G (Hamuy et al., 1993). However, not all of these show peculiarities in their I-band lightcurve shape when compared to spectroscopic normal SNe Ia. Recently, Krisciunas et al (2003), built the Hubble diagram for SNe Ia in infrared J, H and K-bands out to $z = 0.04$, and reported that three spectroscopic peculiar SNe, SN 1999aa, SN 1999ac and SN 1999aw, do not show a behavior different than that of normal SNe. In the attempt to assess the homogeneity of SNe as standard candles in the I-band, we choose not to exclude the peculiar SNe from our sample, and monitor possible deviant behavior of these objects.

Analyzing the results of our fits, we found that type Ia SNe show a variety of properties for the I-band lightcurve shape. In particular we noticed that the lightcurve could peak between -3 days and +4 days w.r.t. $B_{\max}$, as shown in Figure 2 (left panel). The time of the second peak, $t_{\sec}$ (relative to $B_{\max}$), is shown in the right panel. The distribution of $t_{\max}$ is centered at day -1.3 and has a dispersion of $\sigma = 1.6$ days. $t_{\sec}$ is centered at 23.6 with a dispersion of $\sigma = 4.1$ days.

The reduced χ^2 for the fits given in Table 2 are generally around unity, except for a few cases. In particular we note that SN 1994D has a $\chi^2/dof \sim 26$. The uncertainties for this supernova may be underestimated. But, even assuming them to be of the order of a few percent (see Knop et al. (2003)), the reduced χ^2 remained large, possibly indicating the limitations of the fitting template. As in other cases we find a systematic trend in the residuals, especially in the rising part of the lightcurves, that suggest this fitting model could be improved. It should be noted however, that this is not affecting the results reported in this work, as only a handful of SNe in our sample have data on the lightcurve rise.

While the χ^2 gives a measurement of the goodness of the fit, in the next section we test the robustness and accuracy of the parameter estimation in our fitting method, reported in Table 2.

2.3. Monte-Carlo tests of the fitting method

Given the heterogeneous origin of the data sample, the quality and the sampling of the individual SN lightcurves vary consid-

SN	z	s_I	t_1	I_1	t_2	I_2	χ^2/dof
1989B[1]	0.002	1.099 ± 0.125	-0.581 ± 1.540	11.760 ± 0.059	23.129 ± 2.068	12.505 ± 0.174	0.52
1991bg[4]	0.005	1.107 ± 0.033	3.398 ± 0.358	13.539 ± 0.006	28.766 ± 1.075	16.494 ± 0.113	1.43
1992al[4]	0.015	0.960 ± 0.060	1.354 ± 1.143	15.101 ± 0.046	27.688 ± 1.206	15.512 ± 0.073	0.18
1992bc[4]	0.020	1.149 ± 0.031	-1.850 ± 0.154	15.687 ± 0.014	27.360 ± 0.479	16.486 ± 0.025	1.80
1992bg[4]	0.035	0.951 ± 0.086	1.448 ± 1.983	17.707 ± 0.063	27.479 ± 3.438	17.949 ± 0.059	1.38
1992bh[4]	0.045	1.194 ± 0.153	0.041 ± 1.030	18.060 ± 0.032	25.580 ± 1.991	18.539 ± 0.098	0.80
1992bo[4]	0.019	0.981 ± 0.021	-0.862 ± 0.191	16.130 ± 0.016	22.932 ± 0.392	16.956 ± 0.042	3.75
1992bp[4]	0.079	0.931 ± 0.055	-0.805 ± 0.829	19.107 ± 0.034	27.101 ± 1.246	19.318 ± 0.077	0.90
1993ag[4]	0.049	0.953 ± 0.066	0.965 ± 1.307	18.519 ± 0.051	26.721 ± 2.193	18.759 ± 0.058	0.32
1993H[4]	0.024	0.962 ± 0.034	-1.796 ± 1.080	16.771 ± 0.046	20.622 ± 0.943	17.523 ± 0.050	3.57
1993O[4]	0.051	1.288 ± 0.155	-1.293 ± 1.592	18.326 ± 0.045	23.809 ± 1.470	18.836 ± 0.038	1.86
1994ae[3]	0.004	1.051 ± 0.017	-1.104 ± 0.144	13.397 ± 0.018	26.626 ± 0.314	14.026 ± 0.042	1.74
1994D[2]	0.002	0.892 ± 0.004	-1.024 ± 0.044	12.183 ± 0.004	25.190 ± 0.090	12.835 ± 0.008	26.47
1994M[3]	0.023	0.964 ± 0.039	0.155 ± 1.009	16.604 ± 0.041	24.557 ± 0.884	17.140 ± 0.064	3.20
1994T[3]	0.035	0.754 ± 0.028	2.663 ± 1.497	17.589 ± 0.052	29.927 ± 1.038	17.839 ± 0.052	3.55
1995al[3]	0.005	1.173 ± 0.049	-1.130 ± 0.518	13.540 ± 0.024	24.432 ± 0.785	14.155 ± 0.058	0.83
1995bd[3]	0.016	1.204 ± 0.028	-0.291 ± 0.122	16.137 ± 0.012	25.913 ± 0.345	16.629 ± 0.058	2.94
1995D[3]	0.007	1.289 ± 0.055	-1.596 ± 0.673	13.727 ± 0.027	24.433 ± 0.719	14.453 ± 0.037	0.52
1995E[3]	0.012	1.040 ± 0.036	-0.012 ± 0.608	15.432 ± 0.027	26.035 ± 0.781	16.087 ± 0.050	0.86
1996ai[3]	0.003	1.118 ± 0.024	-2.066 ± 0.497	13.997 ± 0.022	24.894 ± 0.504	14.673 ± 0.022	9.86
1996bl[3]	0.036	0.980 ± 0.030	1.557 ± 0.445	17.176 ± 0.025	28.794 ± 0.745	17.695 ± 0.033	3.02
1996bo[3]	0.017	1.115 ± 0.010	-0.968 ± 0.125	15.751 ± 0.005	23.727 ± 0.176	16.261 ± 0.013	15.12
1996C[3]	0.030	1.033 ± 0.046	2.349 ± 1.102	17.009 ± 0.035	28.416 ± 1.187	17.478 ± 0.034	3.85
1996X[3]	0.007	1.107 ± 0.042	-2.286 ± 0.354	13.414 ± 0.013	23.998 ± 0.748	14.178 ± 0.033	1.03
1997bp[5]	0.008	1.252 ± 0.050	0.897 ± 0.263	14.166 ± 0.006	25.583 ± 0.473	14.626 ± 0.017	1.19
1997bq[5]	0.009	1.001 ± 0.014	0.372 ± 0.104	14.591 ± 0.017	25.108 ± 0.229	15.138 ± 0.017	2.91
1997br[5]	0.007	1.359 ± 0.035	0.655 ± 0.119	13.706 ± 0.021	20.491 ± 0.454	14.285 ± 0.034	3.03
1997cn[5]	0.017	0.840 ± 0.055	-1.370 ± 0.899	16.512 ± 0.030	24.189 ± 1.207	18.204 ± 0.162	1.37
1997dg[5]	0.031	1.006 ± 0.052	-1.660 ± 1.070	17.341 ± 0.042	25.647 ± 1.797	17.743 ± 0.050	4.21
1997e[5]	0.013	1.014 ± 0.050	-2.542 ± 0.394	15.500 ± 0.011	22.809 ± 0.387	16.061 ± 0.028	4.43
1998ab[5]	0.027	1.474 ± 0.050	-0.432 ± 0.328	16.573 ± 0.022	18.892 ± 0.631	17.011 ± 0.034	3.64
1998dh[5]	0.009	1.003 ± 0.012	-0.381 ± 0.171	14.116 ± 0.015	25.896 ± 0.277	14.680 ± 0.024	0.76
1998es[5]	0.011	0.915 ± 0.112	-2.957 ± 0.419	14.104 ± 0.016	24.503 ± 1.588	14.901 ± 0.088	0.88
1998v[5]	0.018	0.950 ± 0.033	0.808 ± 0.500	15.871 ± 0.013	25.598 ± 0.612	16.095 ± 0.050	5.84
1999aa[5]	0.014	1.323 ± 0.015	0.273 ± 0.074	15.289 ± 0.007	25.183 ± 0.186	15.860 ± 0.028	10.57
1999ac[5]	0.009	1.231 ± 0.025	1.175 ± 0.268	14.357 ± 0.006	22.628 ± 0.445	15.048 ± 0.030	1.48
1999cl[5]	0.008	0.982 ± 0.121	-0.292 ± 0.538	13.166 ± 0.022	21.870 ± 1.267	13.690 ± 0.097	0.30
1999dq[5]	0.014	1.202 ± 0.027	-0.538 ± 0.136	14.834 ± 0.007	25.074 ± 0.214	15.302 ± 0.013	2.83
1999gp[5]	0.027	1.328 ± 0.049	-2.626 ± 0.284	16.449 ± 0.010	25.037 ± 0.535	17.016 ± 0.024	2.87
2000cn[5]	0.023	0.777 ± 0.024	-0.806 ± 0.199	16.730 ± 0.016	23.857 ± 0.406	17.222 ± 0.063	2.78
2000dk[5]	0.017	0.834 ± 0.016	-1.877 ± 0.201	15.812 ± 0.007	23.669 ± 0.413	16.260 ± 0.047	7.22
2000fa[5]	0.021	1.123 ± 0.051	-0.233 ± 0.279	16.357 ± 0.038	24.733 ± 0.475	16.840 ± 0.106	0.09

Table 2 Results of the *I*-band lightcurve fit of 42 nearby supernovae: t_1 and I_1 are the parameters for the time and amplitude fitted on the first *B*-band template, t_2 and I_2 are the parameters for the time and amplitude fitted on the second *B*-band template, and s_I is the stretch factor. The data were taken from: [1] Wells et al. (1994); [2] Richmond et al. (1995); [3] Riess et al. (1999); [4] Hamuy et al. (1996a); [5] Jha (2002); [6] Filippenko et al. (1992); Leibundgut et al. (1993).

erably. Only a few supernovae have excellent time coverage in the *I*-band, resulting in a wide range of accuracy in the fitted parameters. The robustness of the fitting procedure was tested for all circumstances of data quality and time sampling in our sample by means of Monte Carlo simulations. We generated 1000 sets of simulated lightcurves for each supernova. The synthetic data points had the same time sampling as the real lightcurves and with deviations from the best fit template by randomization according to the measurement errors (assumed Gaussian). The simulated lightcurves were fitted using the same method as for the experimental data sets. The distribution of the fitted parameters on the simulated data was used to compare with the input data from the fits of the experimental data. The mean value in the distribution of each parameter coincide generally with those expected within one standard deviation, not giving evidence for biases. This lends confidence that the fitting procedure is robust, and given the model of the lightcurve template will not yield biased estimations of the parameters. However, of 42 supernovae, 2 cases showed significant deviations, both identified as spectroscopic peculiar SNe,

- SN 1997br: in about 3% of the cases we found $\chi^2/dof \geq 7$. These cause the distributions to have different standard de-

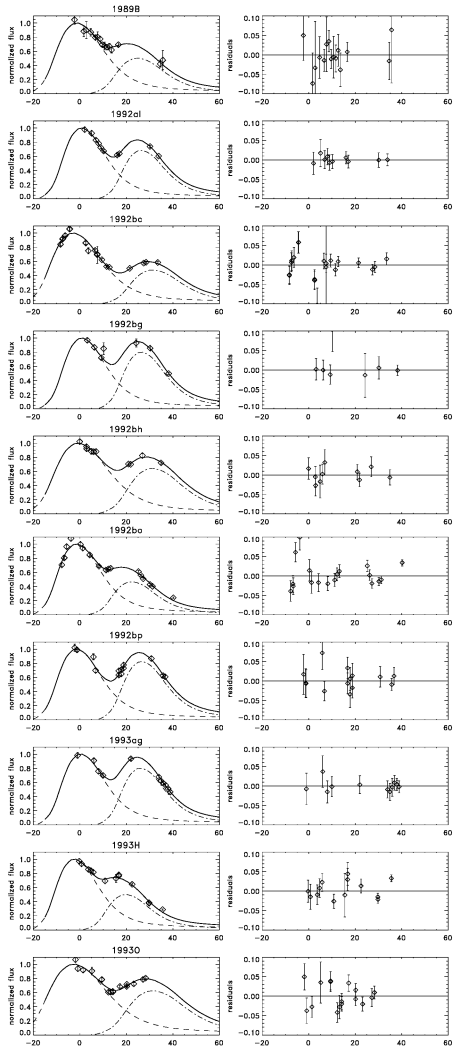

Fig. 1 I-band lightcurve fits. On the ordinate is the flux normalized to the first peak, on the abscissa the restframe time since B-band maximum. The dashed line and the dash-dotted line represent the two B-band templates used to fit the first and second peak respectively.

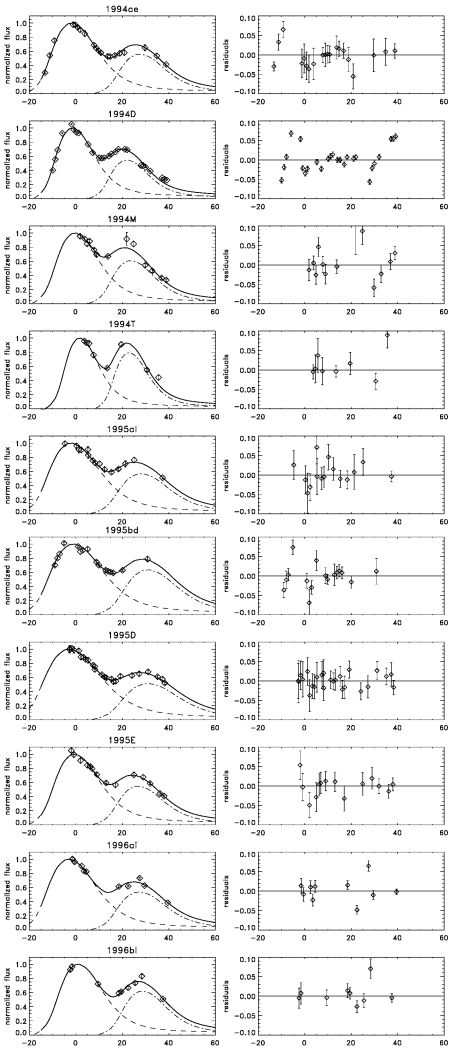

Fig. 1 continued. I-band lightcurve fits. On the ordinate is the the flux normalized to the first peak, on the abscissa the restframe time since B-band maximum. The dashed line and the dash-dotted line represent the two B-band templates used to fit the first and second peak respectively.

viation than what is computed as uncertainty by the fitting procedure. Excluding them results in the expected distributions.

– SN 1998ab: the simulated data sets result in two populations of parameters, which reduces to one when imposing a cut on $\chi^2/dof \leq 6$. Note that about 78% of the simulations satisfy this condition.

In both cases a cut of the tail of the χ^2 distribution was enough to discriminate between the results, thus these supernovae were kept in the remaining analysis since the χ^2/dof of the fits to the real data fulfilled these criteria.

For the rest of the supernovae, the simulations confirmed the expected parameters, giving general confidence in the ro-

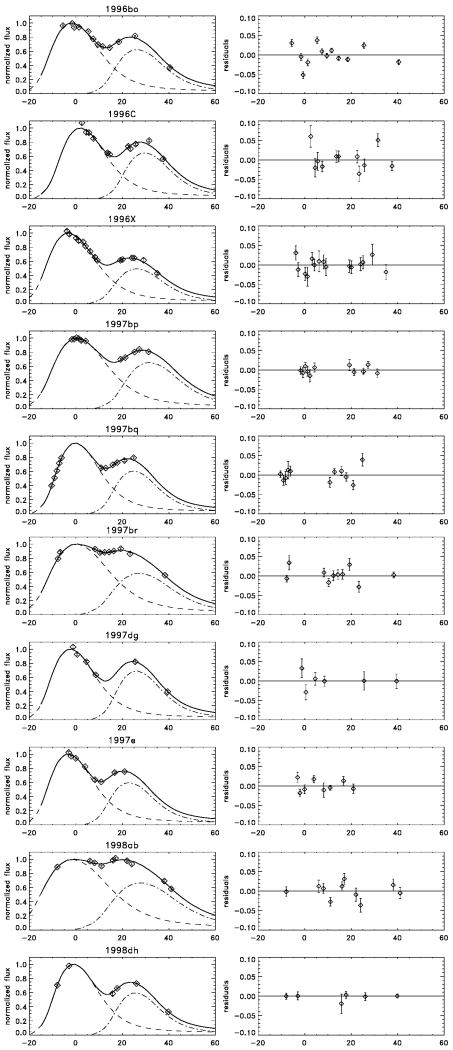

Fig. 1 continued. *I*-band lightcurve fits. On the ordinate is the flux normalized to the first peak, on the abscissa the restframe time since *B*-band maximum. The dashed line and the dash-dotted line represent the two *B*-band templates used to fit the first and second peak respectively.

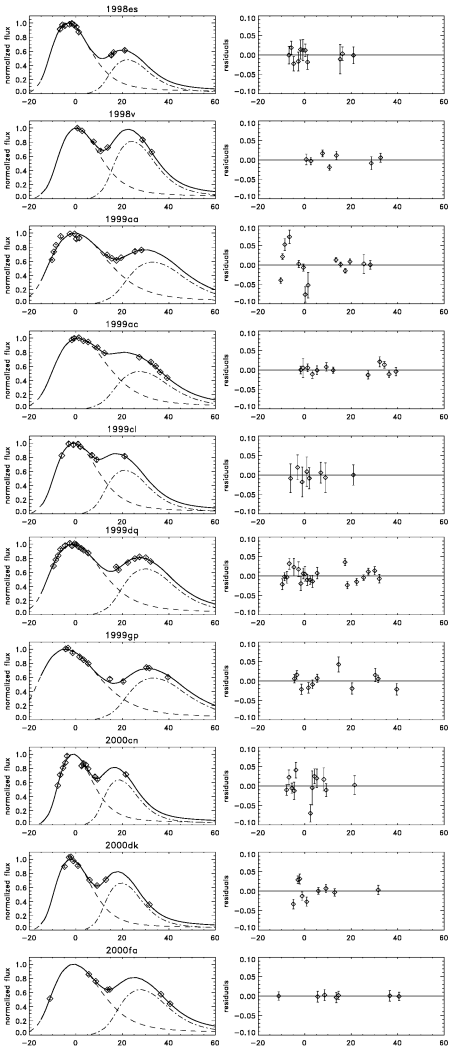

Fig. 1 continued. *I*-band lightcurve fits. On the ordinate is the flux normalized to the first peak, on the abscissa the restframe time since *B*-band maximum. The dashed line and the dash-dotted line represent the two *B*-band templates used to fit the first and second peak respectively.

bustness of the procedure and the accuracy of the uncertainties on the parameters given in Table 2.

2.4. Intrinsic variations

We investigated possible relations between *I*-band and *B*-band parameters. Published *B*-band data, when avalaible, was fitted using a template in order to determine the time of maximum luminosity, the stretch factor, s_B, and the amplitude of maximum, m_B, following Goldhaber et al. (2001). A width-luminosity relation was found for the first *I*-band lightcurve peak. Figure 3 shows the *I*-band absolute magnitude versus the stretch factor in *B*-band for SNe with $z_{CMB} \geq 0.01$, where the distance (in Mpc) to each SN was calculated from its redshift, assuming a

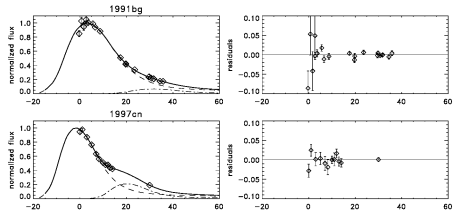

Fig. 1 continued. I-band lightcurve fits of the under-luminous supernovae SN 1991bg and SN 1997cn. The dashed line and the dash-dotted line represent the two B-band templates used to fit the first and second peak respectively. Note that the second peak is fitted as ~ 3 mag fainter than the first peak.

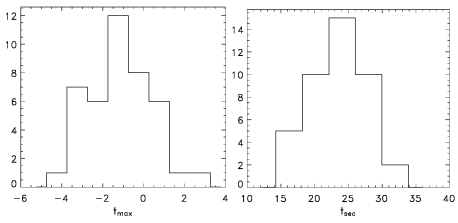

Fig. 2 Distribution of the time of I-band maximum referred to the time of B-band maximum (left panel) and the distribution of the time of second maximum referred to the time of B-band maximum (right panel).

value for the Hubble constant, $H_0 = 72$ km s^{-1} Mpc^{-1}. The error bars in Figure 3 include an uncertainty of 300 km/s on the redshifts from the possible peculiar velocities of the host galaxies. Corrections for Milky Way and host galaxy extinction were also applied, i.e.

$$M^I_{\rm max} - 5\log(H_0/72) = I_{\rm max} - A_I^{MW} - A_I^{host} - 25 - 5\log(d_L)$$

The host galaxy extinction corrections applied to most of the supernovae are those estimated by Phillips et al. (1999). The extinction for the supernovae in the CfA2 data set was calculated following the same procedure, using their B and V-band photometry. SN 1995E has been excluded from the sample as it is highly extincted (see also discussion in Nobili et al. (2003)). Two supernovae in the sample, the spectroscopic peculiar SN 1998es and SN 1999dq, plotted with filled symbols in Figure 3, appear intrinsically redder than average, and become $\sim 2-3\sigma$ deviant from average after correction for host galaxy extinction. Before introducing lightcurve shape corrections, the spread measured in the $M^I_{\rm max}$ excluding these two SNe, is about 0.23 mag (0.29 mag if they are included). The solid line shows the best fit to the data, obtained for a slope $\alpha_I = 1.05 \pm 0.20$ and an absolute magnitude for a stretch $s_B = 1$ supernova equal to $M^I_{\rm max}(s_B = 1) = -18.72 \pm 0.03$ mag [2]. The dispersion measured as r.m.s. on the data along the fitted line is 0.19 ± 0.02 mag. In order to disentangle the intrinsic dispersion from the statistical scatter due to the measurement uncertainties, the average of the latter is subtracted (geometrically), resulting in $\sigma = 0.14$ mag. We consider this an estimate of the intrinsic dispersion of the stretch corrected I-band lightcurve maximum. A somewhat weaker correlation was found between the peak magnitude and the stretch in I-band, s_I, with an r.m.s. of ~ 0.21 mag, about the best fit line.

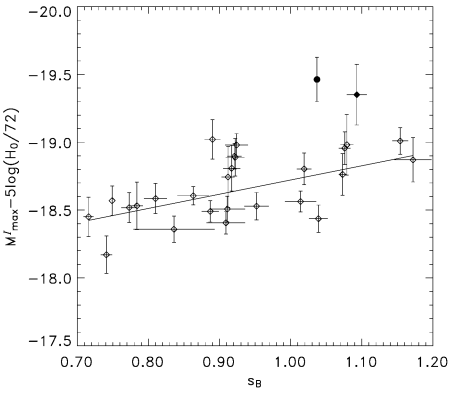

Fig. 3 I-band absolute magnitude versus stretch in B-band. The best fit gives $\alpha_I = 1.05 \pm 0.20$ and $M^I_{\rm max}(s_B = 1) = -18.72 \pm 0.03$ mag. The two deviating supernovae, SN 1998es (filled diamond) and SN 1999dq (filled circle), were excluded from the fit.

A correlation was found between $t_{\rm sec}$ and the stretch factor in B-band, as shown in Figure 4. There are three outliers labeled in the figure, SN 1993H , SN 1998es and SN 1999ac, which are identified as spectroscopically peculiar supernovae. However, other supernovae in our sample also classified as spectroscopically peculiar, behave as "normal" type Ia SNe. A linear fit to the data was done, excluding the outlier SNe.

Figure 5 shows a possible correlation found between $I_{\rm sec}$, corrected for the luminosity distance and both Galaxy and host galaxy extinction, and the stretch s_B, at least for $s_B < 0.9$. All of these correlations, shown in Figure 3 - 5, were expected since it has been suggested that the location and the intensity of the secondary peak depends on the B-band intrinsic luminosity of the supernova (Hamuy et al., 1996a).

Figure 6 shows the I-band stretch, s_I, plotted versus B-band stretch, s_B, where some of the supernovae, three of which peculiars, are labeled. A correlation between this two parameters is found.

We have investigated the possible existence of further relations between the fitted parameters, but found no statistically significant correlations.

3. The I-band Hubble Diagram

The fitted values of $I_{\rm max}$ were used to build a Hubble diagram in I-band. A total of 28 supernovae of the sample considered

[2] The value fitted for $M^I_{\rm max}$ depends on the value assumed for the Hubble parameter, $H_0 = 72$ km s^{-1} Mpc^{-1}. However, its value is not used in any of the further analysis presented in this paper.

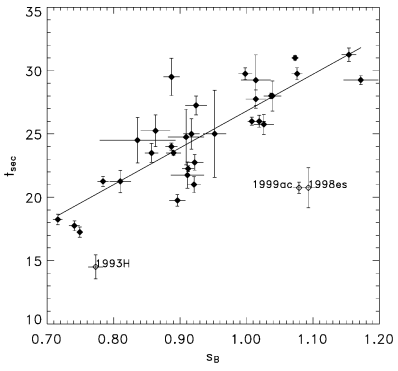

Fig. 4 Time of the second peak since B_{max} vs the stretch in B-band. The supernovae labelled are all classified as spectroscopically peculiar.

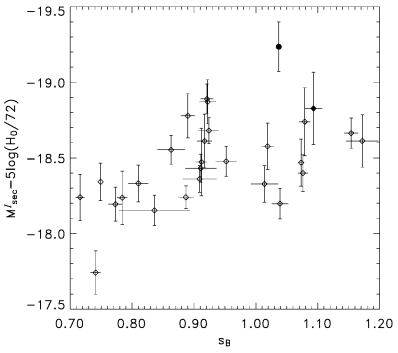

Fig. 5 Absolute magnitude of the secondary peak versus the stretch in B-band. The two deviating supernovae in Figure 3 are SN 1998es (filled diamond) and SN 1999dq (filled circle).

here are in the Hubble flow having a redshift $z_{CMB} \geq 0.01$[3]. The maximum redshift in this sample is 0.1.

The width-luminosity relation found between the fitted absolute I-band magnitude and the B-band stretch factor was used to correct the peak magnitude, with a $\alpha_I = 1.05 \pm 0.20$ as measured in the previous section, similarly to what is usually done in B-band (Perlmutter et al., 1999). The peak magnitude was also corrected for Milky Way and for host galaxy extinction:

$$m_I^{\rm eff} = m_I + \alpha_I(s_B - 1) - A_I^{host} - A_I^{MW} \quad (1)$$

The effective magnitude, $m_I^{\rm eff}$ for the nearby supernovae, listed in Table 3, have been used for building the Hubble diagram in I-band, shown in Figure 7. The estimated intrinsic uncertainty

[3] The lower limit chosen in previous works by the SCP is slightly higher. However, we include these lower redshift SNe in the sample in order to increase the statistical significance. Cutting the Hubble diagram above $z = 0.015$ would in fact, decrease the sample by about a 30 %. Note however, that this choice does not affect significantly any of the results.

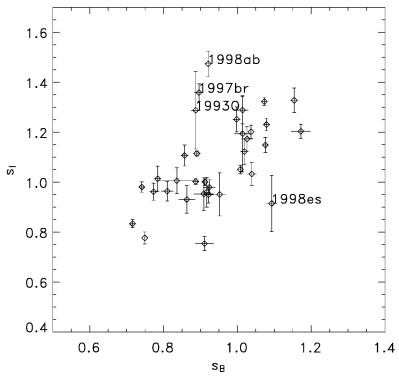

Fig. 6 I-band lightcurve stretch, s_I, versus B-band stretch, s_B. The labeled supernovae are somewhat deviant from the correlation shown by the ensamble. SN 1998ab, SN 1997br and SN 1998es are classified as peculiar.

of 0.14 mag has been added in quadrature to the outer error bars of the plotted data, while the inner error bars include an uncertainty on the redshifts due to peculiar velocities in the host galaxies. The solid line represents the best fit to the data for the concordance model $\Omega_M = 0.3$ and $\Omega_\Lambda = 0.7$. The fitted parameter, $\mathcal{M}_I$, is defined (as in Perlmutter et al. (1997)) to be

$$\mathcal{M}_I \equiv M_I - 5\log H_0 + 25 \quad (2)$$

where M_I is the I-band absolute magnitude for a B-band stretch $s_B = 1$ supernova. The two redder supernovae, SN 1998es and SN 1999dq, were excluded from the fit, and are plotted with different symbols in Figure 7. The value fitted is $\mathcal{M}_I = -3.07 \pm 0.04$, with $\chi^2 = 26.89$ for 25 degrees of freedom. Note that if no correction $\alpha_I(s_B - 1)$ is applied the dispersion in the Hubble diagram becomes 0.23 ± 0.03 mag, somewhat smaller than the corresponding dispersion measured in the "uncorrected" B-band Hubble diagram. The stretch-corrected I-band dispersion measured (0.14 mag) agrees with the estimate given by Hamuy et al. (1996b) ($\sim$ 0.13 mag) using 26 SNe of the Calan/Tololo sample. Moreover, we computed the dispersion in the Hubble diagram for the three data sets separately. Table 4 lists for each sample, the average redshift, the number of SNe, the weighted mean and standard deviation of the residuals in the Hubble diagram and the average uncertainty. The latter is dominated by the uncertainty on the redshift, σ_z^{300}, which depends on the assumed peculiar velocity of the host galaxy. The relative contribution of this uncertainty decreses with redshift. The same weighted standard deviation was measured in the Calan/Tololo and CfA2 sample, while a larger value was found in the the CfA sample, though it is consistent within the uncertainties with the values for the other two samples (see Table 4). Note that, the average uncertainty, σ_z^{300}, for the CfA2 sample is larger than for the other samples, and it is comparable to the dispersion. This is due to the lower redshift distribution of the CfA2 sample. A small offset, 0.08 ± 0.06

	$\langle z \rangle$	n	$\overline{x}_w$ [a]	σ_w [b]	σ_z^{300}
Calan/Tololo	0.037 (0.021)	9	0.08 ± 0.06	0.16 ± 0.06	0.10 ± 0.04
CfA	0.025 (0.009)	6	0.003 ± 0.12	0.27 ± 0.06	0.11 ± 0.03
CfA2	0.018 (0.007)	11	-0.02 ± 0.05	0.14 ± 0.04	0.14 ± 0.05

Table 4 Dispersion measured in the Hubble diagram for each of the sample, corrected for the width-luminosity relation; $\langle z \rangle$ is the average redshift of the sample, and its standard deviation given between brackets; n is the number of data points; $\overline{x}_w$ and σ_w are weighted mean and standard deviation of residuals in the Hubble diagram about the best fit model to the whole data sample, and σ_z^{300} is the average uncertainty and r.m.s. around that value.

[a] If R_i are residuals in the Hubble diagram and w_i are the weights, then
$\overline{x}_w = \sum w_i R_i / \sum w_i \pm m_{w2} / \sqrt{n_{eff}}$
$m_{w2} = \sum w_i R_i^2 / \sum w_i$
$n_{eff} = \sum w_i^2 / \sum w_i^2$

[b] $\sigma_w = m_{w2} \pm \sqrt{(m_{w4} - m_{w2}^2)/4 n_{eff} m_{w2}}$

SN	s_B	z_{CMB}	$m_I^{\rm eff}$
1992al	0.917 ± 0.012	0.014	14.934 ± 0.050
1992bc	1.076 ± 0.008	0.020	15.727 ± 0.022
1992bg	0.952 ± 0.017	0.036	17.301 ± 0.066
1992bh	1.014 ± 0.022	0.045	17.816 ± 0.040
1992bo	0.741 ± 0.008	0.017	15.809 ± 0.054
1992bp	0.863 ± 0.022	0.079	18.838 ± 0.049
1993H	0.773 ± 0.011	0.025	16.333 ± 0.065
1993O	0.887 ± 0.012	0.053	18.111 ± 0.052
1993ag	0.909 ± 0.027	0.050	18.092 ± 0.061
1994M	0.810 ± 0.016	0.024	16.215 ± 0.058
1994T	0.911 ± 0.025	0.036	17.279 ± 0.061
1995bd	1.172 ± 0.026	0.014	15.139 ± 0.045
1996C	1.039 ± 0.013	0.027	16.861 ± 0.038
1996bl	0.924 ± 0.016	0.035	16.759 ± 0.034
1996bo	0.890 ± 0.011	0.016	14.983 ± 0.025
1997bq	0.912 ± 0.009	0.010	14.263 ± 0.026
1997dg	0.836 ± 0.057	0.030	16.954 ± 0.080
1997E	0.784 ± 0.008	0.013	14.910 ± 0.045
1998ab	0.921 ± 0.010	0.028	16.354 ± 0.029
1998es	1.093 ± 0.014	0.010	13.846 ± 0.028
1998V	0.922 ± 0.013	0.017	15.280 ± 0.024
1999aa	1.073 ± 0.005	0.015	15.293 ± 0.017
1999ac	1.079 ± 0.009	0.010	14.200 ± 0.019
1999dq	1.037 ± 0.000	0.014	14.405 ± 0.010
1999gp	1.154 ± 0.011	0.026	16.325 ± 0.034
2000cn	0.749 ± 0.000	0.023	16.075 ± 0.052
2000dk	0.716 ± 0.007	0.016	15.372 ± 0.057
2000fa	1.019 ± 0.010	0.022	16.027 ± 0.040

Table 3 List of SNe used in the Hubble diagram. $m_I^{\rm eff}$ is the peak magnitude corrected for the dust extinction and for the width-luminosity relation, following Eq. 1. The quoted uncertainties do not include the redshift contribution due to peculiar velocities in the host galaxies, assumed equal to 300 km/s.

mag, was measured in the Calan/Tololo sample to the best fit model, however, this is compatible with statistical fluctuations.

4. High redshift supernovae

Next, we explore the possibility of extending the Hubble diagram to higher redshifts, where the effects of the energy density components are, in principle, measurable. The restframe *I*-band data available to date for this purpose is unfortunately very limited. It consists of only three supernovae at redshift $z \sim 0.5$ observed in the near infrared (NIR) J-band collected during three different campaigns conducted using different facilities and by two different teams. Keeping all of these sources of systematic errors in mind, we include the three supernovae in the Hubble diagram to show its potential and complementary with respect to the standard *B*-band Hubble diagram.

The following sections describe the three high redshift supernovae, SN 2000fr, SN 1999ff and SN 1999Q, and the lightcurve fitting procedure used.

4.1. SN 2000fr

SN 2000fr was discovered by the Supernova Cosmology Project (SCP) during a search for type Ia supernovae at redshift $z \sim 1$ conducted in *I*-band with the CFH-12k camera on the Canada-France-Hawaii Telescope (CFHT). The depth of the search allowed us to discover this supernova during its rise time about 11 rest-frame days before maximum B-band light.

The supernova type was confirmed with two spectra taken at the Keck II telescope and VLT, showing that it was a normal type Ia at $z = 0.543$, see Lidman et al. (2004); Garavini et al. (2004) for an extensive analysis of the spectrum. This supernova was followed-up in restframe *B*, *V* and *I* filters involving both ground and space based facilities. Approximately one year later, when SN 2000fr had faded sufficiently, infrared and optical images of the host galaxy without SN were obtained. The optical lightcurve has been fitted yielding a stretch parameter $s_B = 1.064 \pm 0.011$, (Knop et al., 2003). Using restframe $B - V$ measurements at the time of $B_{\rm max}$ Knop et al. (2003) concluded that the possible reddening of SN 2000fr due to dust in the host galaxy was negligible, (see also Section 6 for a more extensive discussion). The Milky Way reddening is $E(B - V) = 0.030$ mag (Schlegel et al., 1998).

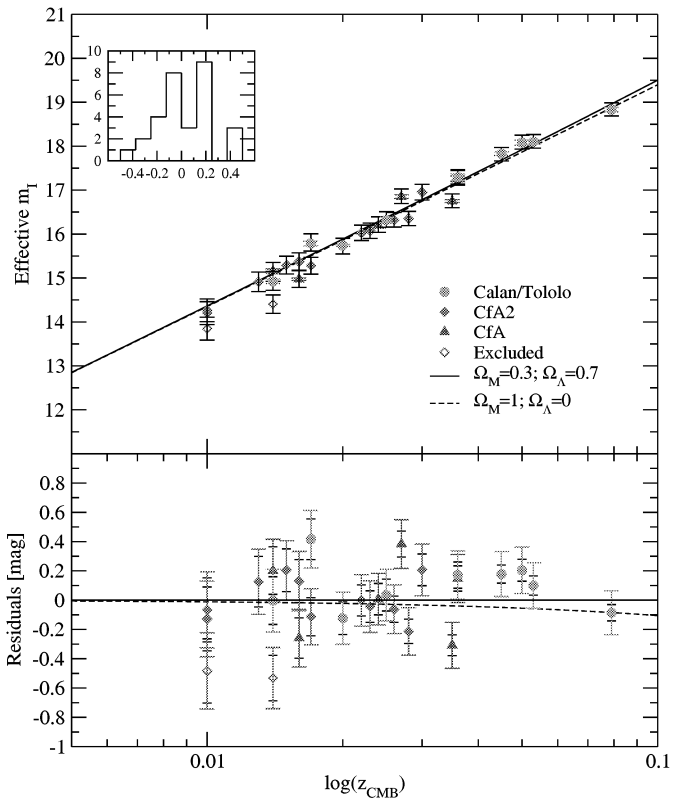

Fig. 7 Effective *I*-band maximum vs redshift for the nearby supernovae of the Calan/Tololo, CfA and CfA2 sample. The data have been corrected for the stretch-luminosity relation and for Milky Way and host galaxy extinction. The r.m.s. along the concordance model line is $\sigma = 0.19 \pm 0.02$ mag. Subracting the contribution of the average uncertainty, results in 0.14 mag estimated intrinsic dispersion. SN 1998es and SN 1999dq were excluded from the fit (see text) and are plotted with open symbols.

The near-infrared data was collected with ISAAC at the VLT telescope. It consists of J_s-band observations during three epochs and a final image of the host galaxy without the SN (see Table 5). Each data point is made of a series of 20 to 60 images with random offsets between exposures. The observations were done in the J_s filter, which is narrower than other *J*-band filters. Figure 8 shows a comparison between J_s and *J* Persson filters, together with the atmospheric transmission, and the spectral template at maximum.

The advantage in using a narrow *J* filter is that its transmission function cuts off entirely the region of strong atmospheric absorption between 13500 and 15000 Å. Consequently, the zero-point is significantly more stable than the one of standard *J*. This was very useful, because all of the ISAAC data was taken in queue mode, where typically only one or two standard stars are observed during a night, chosen from the list of Persson et al. (1998). All data, except the reference images, were taken during photometric nights and the difference in the zero-points from one night to the next were less than 0.01 magnitudes.

MJD	Epoch	J_s(mag)	*I*(mag)
51685.06	0.41	22.50 ± 0.09	23.42 ± 0.10
51709.02	15.94	23.57 ± 0.22	24.45 ± 0.23
51731.96	30.80	23.14 ± 0.15	24.02 ± 0.16

Table 5 Summary of J_s data for SN 2000fr. The quoted errors are due to statistical Poisson noise and the uncertainty on the ZP (contributing for 0.01 mag). Epochs are in restframe relative to *B*-band maximum. Restframe *I*-band is obtained through cross-filter *K*-correction from the observed J_s-band to Bessel *I*-band, and adding the offset found between optical and IR systems. The uncertainties also include the contribution from *K*-corrections, estimated to be 0.05 mag at all epochs considered.

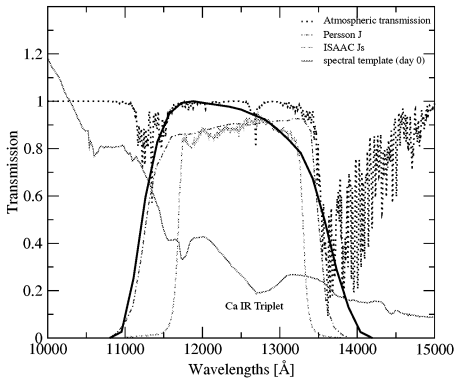

Fig. 8 Comparison between the standard J Persson filter, the J_s filter at ISAAC used for the observations of SN 2000fr and the I-band redshifted to z=0.543. The atmospheric transmission is also plotted. The spectral template at day 0 is on an arbitrary flux scale for readibility purpose.

The data was reduced using both internally developed routines and the XDIMSUM package in IRAF[4]. The results were found in agreement within the quoted uncertainties. The supernova images where aligned with the host galaxy images and flux scaled to the one with best seeing, using the field stars before performing PSF photometry. The results are given in Table 5. The stated uncertainties include the statistical Poisson noise and the uncertainty on the estimate of the zero point, added in quadrature.

The J_s-band magnitude takes into account a color term which arises from the difference between the J filter of the standard star system and the J_s filter used in ISAAC. This correction was small ~ 0.012 mag.

The cross-filter K-correction, K_{IJ_s}, to convert from J_s-band to rest-frame I-band, has been calculated following Kim et al. (1996) using the spectral templates given in Nobili et al. (2003). This was cross-checked using the spectral templates developed in Knop et al. (2003). The difference found, has been treated as the uncertainty in the K-corrections, $\sigma_K = 0.05$ mag.

Another source of uncertainty is found in relating IR and optical photometric systems. We estimated a difference of about 0.05 mag between the LCO system, to which the IR photometry of the high-redshift SNe is tied, and the Bessel & Brett system used for optical photometry. Comparing A0V stars from the Hipparcos Input Catalogue and the 2MASS catalogue, we found the transformation between the two standard systems. This was confirmed using the relations in Carpenter (2001), from which one can derive $J_{BB} = J_{LCO} + 0.036(\pm 0.012)$. This correction was applied when trasforming from the observed IR band to restframe I-band.

[4] IRAF is distributed by the National Optical Astronomy Observatories, which are operated by the Association of Universities for Research in Astronomy, Inc., under cooperative agreement with the National Science Foundation.

4.2. SN 1999ff

SN 1999ff was discovered by the High-Z Supernova Search Team (HZT) during a search conducted at CFHT using the CFH-12k camera in I-band (Tonry et al., 2003).[5] The supernova was confirmed spectroscopically as a type Ia at redshift $z = 0.455$. The Milky Way reddening is $E(B-V) = 0.025$ mag (Schlegel et al., 1998).

J-band observations, corresponding to restframe I-band, reported in the paper, were taken at Keck using NIRC in two epochs only. The J-band filter available at Keck is very similar to the ISAAC-J_s, shown in Figure 8. For consistency with the treatment of both the low redshift supernovae and SN 2000fr we computed the K-corrections using the templates in Nobili et al. (2003). We found differences with the results published in Tonry et al. (2003), due to the use of an incorrect filter in those calculations (Brian Schmidt, private communication). The I-band magnitudes were also corrected for the offset found between the optical and IR systems, as explained in the previous section. The restframe I-band magnitudes obtained this way are reported in Table 6. The published optical R-band data were used to fit restframe B-band lightcurve using the stretch method. The time of maximum was confirmed within 1 day with a best fit for the stretch $s_B = 0.82 \pm 0.05$.

MJD	Epoch	I(mag)
51501.29	5.01	23.47 ± 0.11
51526.31	22.21	24.06 ± 0.24

Table 6 Summary of IR data of SN 1999ff. Epochs are in restframe relative to B-band maximum ($MJD_{\max} = 51494$); restframe I-band magnitudes are computed applying K-corrections to the observed J-band data published in Tonry et al. (2003), and adding the offset found between optical and IR systems. The uncertainties also include the contribution from K-corrections, estimated to be 0.05 mag at all epochs considered.

4.3. SN 1999Q

SN 1999Q was discovered by the HZT using the CTIO 4 m Blanco Telescope, (Riess et al., 2000). It was spectroscopically confirmed to be a type Ia at redshift $z = 0.46$. The Milky Way reddening is $E(B-V) = 0.021$ mag (Schlegel et al., 1998).

J-band observations were done at 5 different epochs, the first was observed at NTT SOFI and the following epochs at Keck NIRC. Our K-corrections to the data disagree with the value applied to all epochs in Riess et al. (2000), with differences up to ~ 0.1 mag at late time. The restframe I-band computed are given in Table 7.

Restframe B-band lightcurve was not reported in the original paper. However, publicly available data at HST were used to estimate the B-band stretch factor. This was obtained by fixing

[5] Another supernova, SN 1999fn, was followed in J-band by the HZT during the same search. However since it was found in a highly extincted Galactic field, E(B-V)=0.32 mag, and since it was strongly contaminated by the host galaxy, we did not include it in our analysis.

the time of maximum to $MJD_{\max} = 51194.65$ (Tonry, private communication). The value fitted is $s_B = 1.061 \pm 0.025$.

MJD	Epoch	I(mag)
51204.2	6.9	23.84 ± 0.15
51216.4	15.18	24.12 ± 0.18
51239.3	30.9	24.48 ± 0.15
51243.3	33.88	24.31 ± 0.15
51261.3	45.98	24.70 ± 0.20

Table 7 Summary of IR data of SN 1999Q. Epochs are in restframe relative to *B*-band maximum; restframe *I*-band magnitudes are computed applying *K*-corrections using the spectral template in (Nobili et al., 2003) to the observed *J*-band data published in Riess et al. (2000), and adding the offset found between optical and IR systems. The uncertainties also include the contribution from *K*-corrections, estimated to be 0.05 mag at all epochs considered.

4.4. Lightcurve fit of the high redshift supernovae.

The *I*-band lightcurves of the high redshift supernovae are not well sampled in time as the low redshift sample analyzed in this work. There are only few data points for each SN, making it impossible to perform the 5 parameter fit. Thus, we used the results of the fit of the local sample of supernovae to build a set of *I*-band templates, which in turn have been used to fit the high redshift SN lightcurves.

The best fit lightcurve for each of the 42 supernovae in our low-redshift sample can be viewed as defining an *I*-band template. The high-redshift supernovae are fit to each template with a single free parameter, $I_{\max}$, the absolute normalization of the template. In all the cases we assumed the time of $B_{\max}$ to be known from the sources for the published data, and our *B*-band lightcurve fit for SN 2000fr given in Knop et al. (2003). A χ^2 comparison was used to choose the best low redshift template. In the case of SN 1999Q, the data point at day +45 was excluded from the fit for consistency, since only data up to day +40 were used to fit the low redshift lightcurves.

Figs. 9-11 show the comparison of the data with the best fit template for each of the supernovae. Table 8 gives the results of the fit together with redshift, the number of data points, the template giving the best fit and the χ^2. As there are few data points for each SN, the χ^2 parameter has little significance for estimating the goodness of the fits. Thus, to estimate the possible systematic error in the measured peak magnitude from the selection of lightcurve template, we computed the r.m.s. of the fitted I_{max} of all the lightcurve templates giving a $\chi^2 \leq \chi^2_{min} + 3$. This systematic uncertainty is reported also in Table 8. In the cases of SN 1999ff and SN 2000fr this is quite small, and compatible with the scatter due to the statistical uncertainties, thus, it is a conservative estimate. For SN 1999Q the systematic uncertainty is larger than what would be justified statistically. Moreover, this SN is well fitted by the template of SN 1999ac, giving a similar χ^2 than the best fit one, but a fitted I_{max} about 0.2 mag brighter.

We note that SN 1999ff is fitted by the template of a nearby SN with a very different s_B. Trying to impose the template to have a similar *B*-band stretch as the SN, has given a fitted value of I_{max} in agreement with the one reported in Table 8, within the quoted statistical uncertainty.

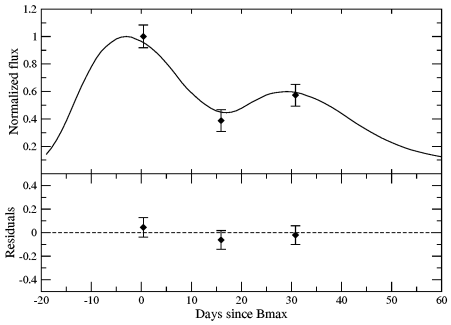

Fig. 9 *I*-band fit for SN 2000fr. Best fit was obtained with the template of the nearby SN 1992bc, out of 42 templates. The fit was performed with only one free parameter, the peak magnitude, $I_{\max} = 23.42 \pm 0.08$ mag. Supplemental data from the *B*-band (not shown) is used to fix the date of maximum.

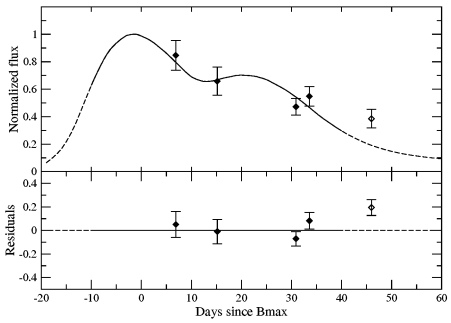

Fig. 10 *I*-band fit for SN 1999Q. Best fit was obtained with the template of SN 1989B, out of 42 templates. The fit was performed with only one free parameter, the peak magnitude, $I_{\max} = 23.66 \pm 0.08$ mag. *B*-band date of maximum fixed to $MJD_{\max} = 51194.65$ (Tonry, private communication). The dashed line is beyond the templates definition. Thus, only data in the range of definition, plotted with closed symbols, are considered for the fit.

4.5. Monte-Carlo test of the fitting method

A Monte-Carlo simulation was run in order to test the fitting method applied to the high redshift SNe. The uncertainties on the data were used to generate a set of 1000 SNe, randomly distributed around the data points, at the same epochs of the data. All the simulated data sets were in turn fitted with the 42

SN	z	s_B	n	$I_{\max}$	template	χ^2	A_J^{MW}
SN 2000fr	0.543	1.064 ± 0.011	3	23.42 ± 0.08 ± 0.05	SN 1992bc	0.79	0.027
SN 1999ff	0.455	0.82 ± 0.05	2	23.25 ± 0.10 ± 0.09	SN 1992bc	0.26	0.022
SN 1999Q	0.460	1.061 ± 0.025	4	23.66 ± 0.08 ± 0.21	SN 1989B	2.54	0.019

Table 8 List of the high redshift type Ia SNe used in this work. Columns are: redshift, number of data points used in the fit, magnitude of the peak resulted from the fit (both statistical and systematic uncertainties are given), best fit template, χ^2 of the fit, Milky Way extinction in the J-band.

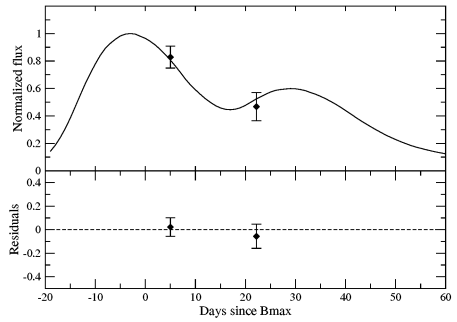

Fig. 11 I-band fit for SN 1999ff. Best fit was obtained with the template of SN 1992bc, out of 42 templates. The fit was performed with only one free parameter, the peak magnitude, $I_{\max} = 23.25 \pm 0.10$ mag. Supplemental data from the B-band (not shown) is used to fix the date of maximum.

templates and the one giving the minimum χ^2 was selected for each simulation. The distribution of the maximum peak fitted in each of the simulated data sets around the value fitted on the experimental data was studied to check for systematic uncertainty in the fitting procedure. This was found to be robust, always selecting the same template as the one giving the best fit for all the three SNe. No bias was found, therefore confirming the peak magnitude fitted with this method. The uncertainty on $I_{\max}$ reported in Table 8 was consistent with the dispersion in the distribution measured on the simulations.

5. The *I*-band Hubble diagram up to $z \sim 0.5$

The goal of this work is to add the three high redshift SNe in the Hubble diagram. The I-band peak magnitudes of the high redshift supernovae, reported in Table 8, were thus corrected for Milky Way extinction. Note that all the SNe have been reported not to suffer from extinction in the host galaxy.

The Hubble diagram has been built both without and with width-luminosity correction (case a and case c respectively), were the systematic uncertainties on the peak magnitudes of the distant supernovae, listed in Table 8, are added in quadrature to the statistical uncertainties. Cases b and d are like a and c but neglecting the systematic uncertainties in Table 8. Figure 12 shows the extended Hubble diagram (case c), where an intrinsic uncertainty of 0.14 mag has been added in quadrature to the measurement errors of the plotted data. The solid line represent the best fit to the nearby data for the concordance model $\Omega_M = 0.3$ and $\Omega_\Lambda = 0.7$. Also plotted is the model for $\Omega_M = 1$ and $\Omega_\Lambda = 0$ (dashed line). The bottom panel shows the residuals obtained for case a. Table 9 lists the χ^2 values for the high redshift SNe to each of the model. The concordance model results are consistent with the data. The low statistics of the high redshift sample is insufficient to draw strong conclusions on cosmological parameters.

$(\Omega_M, \Omega_\Lambda)$	χ^2_a	χ^2_b	χ^2_c	χ^2_d	dof
(0.3,0.7)	2.91	3.93	5.05	11.24	3
(1,0)	7.21	11.39	14.53	33.32	3
$(1,0)_{dust}$	3.43	5.60	6.64	17.57	3

Table 9 χ^2 of the high redshift data to each model, without stretch correction and with systematic uncertainties added in quadrature (χ^2_a), neglecting the systematic uncertainties (χ^2_b), with stretch correction and adding the systematic uncertainties in quadrature (χ^2_c) or neglecting them (χ^2_d).

The scatter between the z∼0.5 points is 0.38 ± 0.08 mag, i.e. slightly too large to be consistent with the quoted measurement errors. In this sense, and also given the very limited statistics available, additional unidentified systematic uncertainties on the distant SNe cannot be excluded.

A general problem concerns J-band observations, that correspond to the restframe I-band at the redshift considered. Infrared data reduction and calibration, involving conditions rapidly evolving with time, remain more problematic to what is the case at optical wavelengths. Moreover, the standard star systems used are somewhat less well established.

Some uncertainties are specific to the sample considered here. The different fitting methods applied to the restframe I-band lightcurve for the low and high redshift samples can be easily overcome if distant supernovae are followed at NIR wavelengths with better time coverage. Both the low and high redshift samples used in this analysis are rather heterogeneous, as they were collected from different data sets. Future data sets collected with a single instrument would naturally solve this problem.

6. SN colors and study of gray dust

Multi-color photometry allows for extinction tests for non-standard dust with only weak wavelength dependence, such as the reddening by a homogeneous population of large grain dust, as proposed by Aguirre (1999a,b). Assuming a density of gray dust in the intergalactic (IG) medium to explain the observed

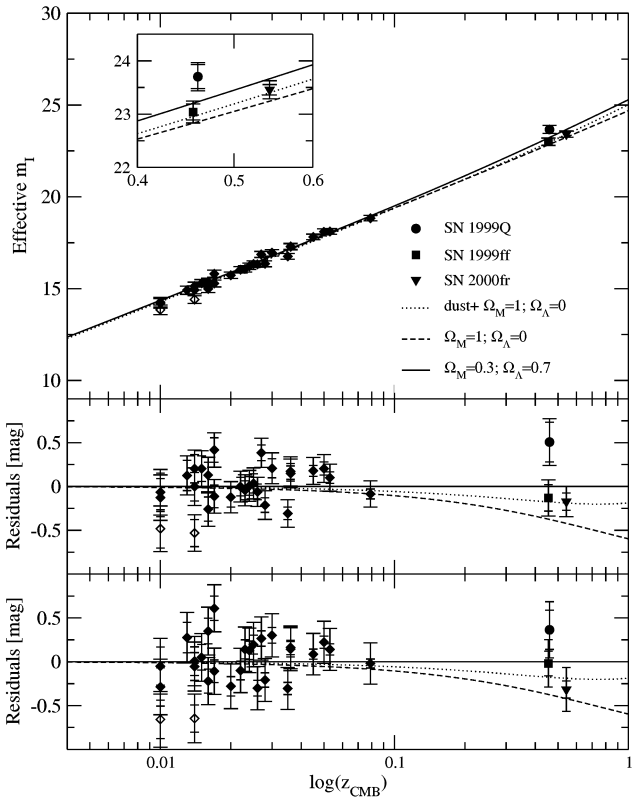

Fig. 12 Effective *I*-band maximum vs redshift for the nearby supernovae of the Calan/Tololo, CfA and CfA2 sample, together with three supernovae at redshift $\sim$ 0.5 for case *c* (top panel), residuals to the $(\Omega_M, \Omega_\Lambda)$=(0.3,0.7) model for case *c* (middle panel) and case *a* (bottom panel). SN 1998es and SN 1999dq were excluded from the fit (see text) and are plotted with open symbols.

dimming of supernovae at redshift $z = 0.5$ with $\Omega_M = 1$ and $\Omega_\Lambda = 0$, we calculated the expected color extinction following Goobar et al. (2002a) using the SNOC Monte-Carlo package (Goobar et al., 2002b), for two cases of $R_V = 4.5$ and $R_V = 9.5$ and a comoving dust density between z=0 and the SN redshifts.

For two of the three SNe considered in this work we computed rest frame $B - V$ and $B - I$. For the third supernova, SN 1999Q, only $B - I$ is available. Table 10 and 11 lists the colors for all the SNe, corrected for Milky Way extinction. The color evolution has been compared to models for a Λ dominated universe and a $\Omega_M = 1$, $\Omega_\Lambda = 0$ universe with presence of gray dust (R_V=4.5 and R_V=9.5) accounting for the faintness of type Ia supernovae at $z \simeq 0.5$, and it is shown in Figure 13. The error bars include also the intrinsic color dispersion contribution.

The χ^2 has been computed for both $B - V$ and $B - I$ evolution for each supernova and for all the supernovae together (see Table 12). The correlations between SN colors at different epochs found in (Nobili et al., 2003) were taken into account. However, we note that, although this correlation should be taken into account in the calculations, neglecting it would not change significantly the conclusions of the analysis. Although individual supernovae give χ^2 values that would seem to distinguish between the models being compared, the combination of the three SNe disfavour such conclusions. For instance, Riess et al. (2000) used the $B - I$ color of SN 1999Q to rule out the gray dust hypothesis. However, when combined with the other two supernovae in this analysis, SN 1999ff in particular, for which we also have used $B - V$ color, no such conclusion may be drawn.

To make our test for gray dust more robust a different approach was followed. The method of least squares has been used to combine color measurements along time for each supernova (see Cowan, 1998, p.106 for details) for details. The residuals of each supernova colors to the expected model, plotted in Figure 13, are weighted averaged together, and the covariance matrix is used as weight in the calculation. In the following, we refer to $E(X - Y)$, to describe the color excess of

day	$B-I$
SN 2000fr	
0.38	-0.36 ± 0.11
14.98	-0.33 ± 0.23
28.95	1.47 ± 0.16
SN 1999ff	
6.10	0.00 ± 0.12
27.05	1.44 ± 0.24
SN 1999Q	
5.84	-0.46 ± 0.16
13.67	-0.07 ± 0.19
28.46	1.16 ± 0.16
31.01	1.49 ± 0.16

Table 10 Restframe $B-I$ colors in magnitudes for the three high redshift SNe. Time is divided by the B-band stretch.

day	$B-V$
SN 2000fr	
-7.35	-0.16 ± 0.05[a]
-2.98	-0.14 ± 0.05[a]
4.99	-0.08 ± 0.05
13.16	0.27 ± 0.08
20.42	0.64 ± 0.07
30.15	1.03 ± 0.09
SN 1999ff	
-7.99	0.01 ± 0.08[a]
1.91	-0.04 ± 0.09
1.98	0.09 ± 0.12
2.91	0.21 ± 0.12
19.55	0.70 ± 0.09
28.75	1.20 ± 0.20

Table 11 Restframe $B-V$ colors in magnitudes for the two of the high redshift SNe. Time is divided by the B-band stretch.

[a]data not included in the analysis because out of the range in which Nobili et al. (2003) studies color correlations.

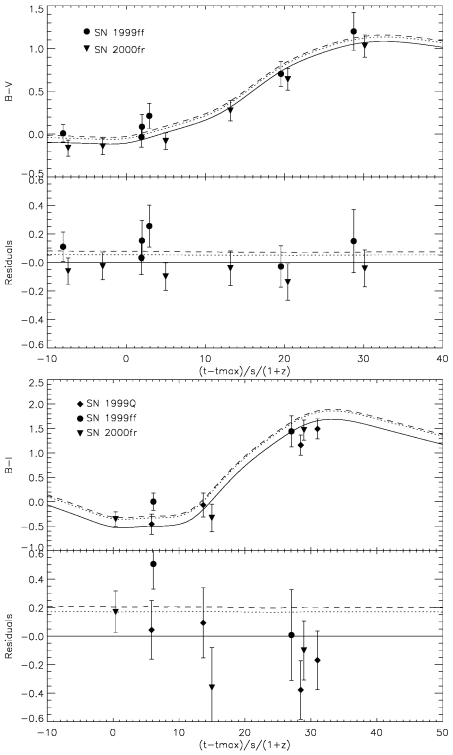

Fig. 13 High redshift SNe color evolution, $B-V$ (top panel) and $B-I$ (bottom panel), compared to a Λ dominated universe (solid line) and to an $\Omega_M = 1$, $\Omega_\Lambda = 0$ universe with presence of gray dust with R_V=4.5 (dashed line) and R_V=9.5 (dotted line).

any supernova with respect to the $X-Y$ average color of local supernovae, as derived in (Nobili et al., 2003). First we applied this method to all local supernovae and used the results to establish the expected distribution in the $E(B-I)$ vs $E(B-V)$ plane, as showed in Figure 14.

As the high redshift SNe were not corrected for host galaxy extinction, we computed the local sample distribution for two cases: the left panels represent the distribution of color excess of 34 nearby SNe not corrected (top panel) and corrected (bottom panel) for host galaxy extinction. The size of the ellipses on each color axis is given by the estimated one-dimensional standard deviation of the distribution and the inclination is defined by the linear Pearson correlation coefficient computed on the same data sample. The solid contours represent 68.3%, 95.5% and 99.7% probability.

The right panels in Figure 14 show the combined values of color excess for the high redshift supernovae, where SN 1999Q is represented by a band (horizontal dashed-lines), as the $B-V$ color is missing. These are compared to the local supernova distribution (dotted lines), that represent the distribution expected in the absence of IG dust. Also plotted is the 68.3% level of the expected distribution in presence of "gray" dust with $R_V = 9.5$, represented by the ellipse (dashed line) displaced by (0.06,0.19) from the no-dust model. Only the case of $R_V = 9.5$ has been plotted for readability reasons, given the small difference between the two dust models. Note that this is the model closer to no-dust model. The ellipse corresponding to $R_V = 4.5$ would be displaced by (0.03,0.04), respectively in $E(B-V)$ and $E(B-I)$, from the latter.

We computed the χ^2 of the high redshift data for each model (with and without IG dust), for both the situation in the top and bottom panels of Figure 14. For each model, we sum the χ^2 contribution from all SNe. In particular, for SN 1999ff and SN 2000fr we take into account the correlation found between $E(B-V)$ and $E(B-I)$ in the nearby sample. The reduced χ^2 (for 5 degrees of freedom) are 1.38, 1.67 and 1.36 for the no-dust, IG dust with $R_V = 4.5$ and IG dust with $R_V = 9.5$ model respectively, for the host-galaxy extinction corrected case, and 1.69, 2.22 and 1.84 uncorrected. These results do not allow

	χ^2_{B-V}/dof	χ^2_{B-I}/dof
SN 2000fr		
no dust, $(\Omega_M, \Omega_\Lambda)$=(0.3,0.7)	1.61/4	2.04/3
dust R_v = 9.5, $(\Omega_M, \Omega_\Lambda)$=(1,0)	3.12/4	2.20/3
dust R_v = 4.5, $(\Omega_M, \Omega_\Lambda)$=(1,0)	4.02/4	2.41/3
SN 1999ff		
no dust , $(\Omega_M, \Omega_\Lambda)$=(0.3,0.7)	4.26/5	8.86/2
dust R_v = 9.5, $(\Omega_M, \Omega_\Lambda)$=(1,0)	3.37/5	4.69/2
dust R_v = 4.5, $(\Omega_M, \Omega_\Lambda)$=(1,0)	3.20/5	4.07/2
SN 1999Q		
no dust, $(\Omega_M, \Omega_\Lambda)$=(0.3,0.7)	—	5.82/4
dust R_v = 9.5, $(\Omega_M, \Omega_\Lambda)$=(1,0)	—	8.87/4
dust R_v = 4.5, $(\Omega_M, \Omega_\Lambda)$=(1,0)	—	9.65/4
All the SNe combined		
no dust , $(\Omega_M, \Omega_\Lambda)$=(0.3,0.7)	5.87/9	16.72/9
dust R_v = 9.5, $(\Omega_M, \Omega_\Lambda)$=(1,0)	6.48/9	15.75/9
dust R_v = 4.5, $(\Omega_M, \Omega_\Lambda)$=(1,0)	7.21/9	16.13/9

Table 12 χ^2 computed for the 3 different models and colors for each of the supernovae and for all of them combined.

us to reach any definitive conclusions. A Monte Carlo simulation was used to estimate the minimum sample size needed to test for presence of homogeneously distributed gray dust in the IGM. SNe colors were generated following the binormal distribution defined by the SN local sample. Under the assumption that the systematic effects are negligible and an average measurement uncertainty of 0.05 mag in both $E(B-V)$ and $E(B-I)$, we found that a sample of at least 20 SNe would be needed to be able to exclude the dust models at the 95% C.L.

6.1. Possible systematic effects.

As shown in the previous section, given the data sample available at high redshift it was not possible to draw any firm conclusions about presence of gray dust in the IG medium. Three data points are an inadequate sample to perform a robust statistical analysis. Moreover, the possibility for the result to be affected by systematic effects is not negligible. This becomes clear when looking at the behavior of single high redshift supernovae in Figure 13. In particular, the case of SN 1999ff seems worth examining. The first data point of $B-I$ color, lies about two standard deviations above all the models, while the second one fits all the models well. This difference, $\sim$ 0.5 mag, is not fully justified by the given uncertainties, and is larger than the intrinsic dispersion measured on nearby supernovae. Table 12 gives the χ^2 values computed for each of the SN to each of the model, and for all of the supernovae combined. In the case of SN 1999ff the χ^2 values for the $B-I$ to each of the model are too large. The same supernova in Figure 14, does not look as extreme, as it is the combination of the two data points shown in Figure 13. The anomaly of this SN does not necessarily indicate that unknown systematic effects are taking place, it may also be the result from possible underestimation of the measurement uncertainties. Increasing the sample and the time sampling for each object would allow us not only to improve the significance of our statistic, but it will also be a means to identify and quantify systematic effects involved.

	n	SN 1991bg	SN 1997cn
SN 2000fr	3	24.2	24.0
SN 1999ff	2	2.53	1.17
SN 1999Q	4	36.6	32.0

Table 13 $\Delta\chi^2$ for the fit of the high redshift SNe to the templates of the two sub-luminous SNe relative to the best fits (which are "normal" SN templates). n is the number of data points used in the one-parameter fit (see discussion in section 4.4).

7. Test for SN brightness evolution

Evolution of the properties of the supernova progenitors with redshift has been often proposed as an alternative explanation to the observed dimming of distant SNe. This is based on the fact that older galaxies show different composition distribution than younger ones, e.g. an increased average metallicity, therefore offering different environmental conditions to the exploding star. A simple way to test for evolution is to compare properties of nearby SNe with distant ones. This will not prove that there is no evolution, but it will exclude it on a supernova-by-supernova or property-by-property basis, finding always counterparts of distant events in the local sample.

In this work we compared colors of nearby and distant supernovae (primarily to test presence of "gray" dust). Although the size of the high redshift sample is very limited, our attempt does not give evidence for evolution of the average SN colors. Furthermore, the correlation found between the intensity of the secondary peak of I-band lightcurve and the supernova luminosity give an independent way of testing for evolution. The restframe I-band lightcurve for the high-redshift supernovae were all fitted by templates showing a prominent second peak, i.e. inconsistent with the intrinsically underluminous supernovae necessary to explain the apparent faintness of high redshift supernovae in a flat $\Lambda = 0$ universe. Note that, for at least one supernova, SN 2000fr, the secondary peak is evident on the data even prior to the lightcurve fit. Table 13 lists the $\Delta\chi^2$ for the fit of the high redshift SNe to the templates of the two sub-luminous SN 1991bg and SN 1997cn, relative to the best fit. The χ^2 values are significantly larger than the best fit value.

8. Summary and conclusions

In this work we have investigated the feasibility of using restframe I-band observations for cosmological purposes.

We have developed a five parameter lightcurve fitting procedure which was applied successfully to 42 nearby type Ia supernovae. The fitted lightcurve were used to build a set of templates which include a broad variety of shapes. We have found correlations between the fitted parameters, in particular between the time of the secondary peak and the B-band stretch, s_B, as well as the I-band stretch, s_I. Moreover, a width-luminosity relation was found for the I-band peak magnitude.

We built a restframe I-band Hubble diagram using 26 nearby supernovae at redshifts $0.01 \leq z \leq 0.1$, and measured an r.m.s. of 0.23 mag, smaller than the uncorrected dispersion corresponding to restframe B-band. The width-luminosity relation

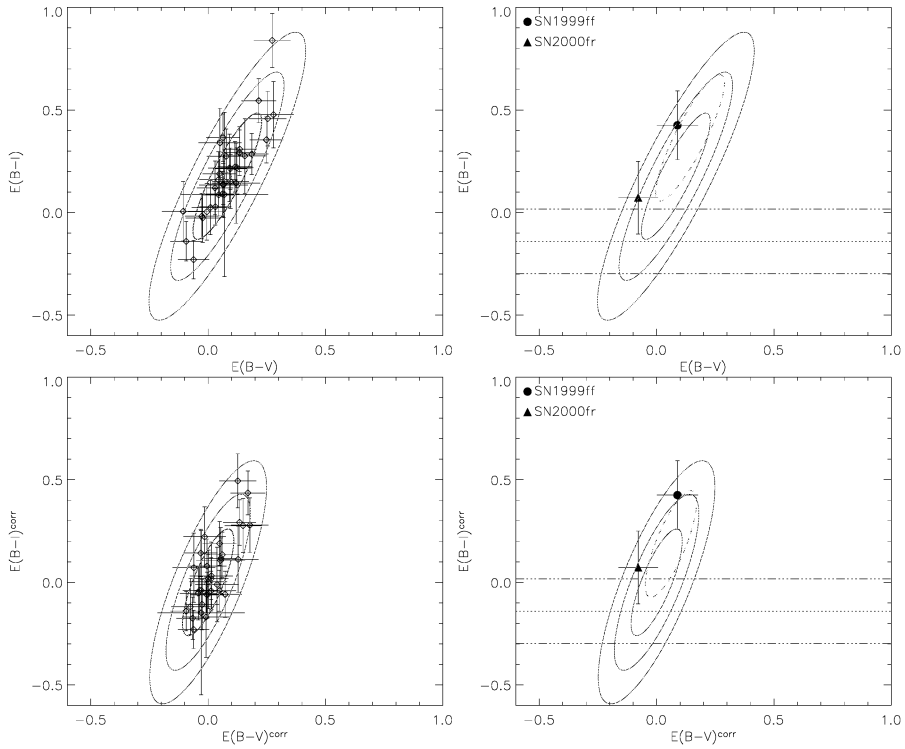

Fig. 14 Left panels: distribution of combined color measurements for the local sample of supernovae in the $E(B-I)$ vs $E(B-V)$ plane, not corrected (top panel) and corrected (bottom panel) for the host galaxy extinction. The solid contour is 68.3%, 95.5% and 99.7% of probability. Right panels: combined colors of the high redshift supernovae compared to the distribution in the absence of IG dust (solid ellipses), and the one expected in presence of gray dust in the IG medium with $R_V = 9.5$ (dashed ellipse). SN 1999Q is represented by an horizontal dashed-dotted line band, as the $B-V$ color is missing, SN 1999ff by the filled circle and SN 2000fr by the filled triangle. For simplicity only the 68.3% level has been plotted for the dust distribution.

was used to reduce the r.m.s. to 0.19 ± 0.02 mag, corresponding to an intrisic dispersion of 0.14 mag. Differences between the three data samples are also discussed.

J-band measurements of three high redshift supernovae were used to extend the Hubble diagram up to $z \sim 0.5$. Their restframe *I*-band lightcurve was fitted by the template set built on the local SNe sample, as the five parameter fit method could not be used for the poorly sampled high redshift lightcurve. The peak *I*-band magnitude of the high redshift SNe was compared to three different set of cosmological parameters. Although the "concordance model" of the universe, $(\Omega_M, \Omega_\Lambda)$=(0.3,0.7), is found in better agreement with the data than the other models, the large dispersion of the high redshift supernovae, together with the low statistics of the sample, do not allow to reach firm conclusions.

Alternative explanations of the observed dimming of supernova brightness, such as presence of gray dust in the IG medium or evolution effects in the supernova properties have also been addressed. Both the *I*-band Hubble diagram and multi color photometry have been used for testing gray dust. Although no firm limits on the presence of gray dust could be set, this study shows that with higher stastistics, the restframe *I*-band measurements could provide useful information on cosmological parameters, including tests for systematic effects. A Monte Carlo simulation indicates that a sample of at least 20 well observed SNe would be enough for testing the presence of a homogeneous dust distribution in the IGM, using only the color diagram technique. A similar technique, but using QSO colors was used by Mörtsell & Goobar (2003), to rule out gray dust being the sole explanation for the apparent faintness of SNe Ia at $z \sim 0.5$.

Possible systematic uncertainties affecting the restframe *I*-band Hubble diagram are discussed. Some sources are identified, for instance the different methods applied for fitting the low and the high redshift samples, selection effects for bright objects during the search campaign, uncertainties connected

with the *J*-band data calibration, as well as uncertainties in the *K*-correction calculations due to the presence of the Ca IR triplet feature in the near infrared region of the SN spectra. However, these systematic uncertainties differ from the ones that could affect the restframe *B*-band Hubble diagram. Thus,the use of *I*-band measurements of type Ia supernovae, can be complementary to the already well established tools.

Acknowledgements. S.N. is supported by a graduate student grant from the Swedish Research Council.

References

Aguirre, A. 1999, ApJ, 512, L19
Aguirre, A. 1999, ApJ, 525, 583
Balbi, A., Ade, P., Bock, J. et al., 2000, ApJ, 545, L1.
Borgani, S., Rosati, P., Tozzi, P. et al. 2001, ApJ, 561, 13
Cardelli, J. A, Clayton, G.C. & Mathis, J.S.1989, ApJ, 345, 245
Carpenter, J.M., 2001, AJ, 121, 2851C
Contardo, G., Leibundgut, B. & Vacca, W. D. 2000, A&A , 359, 876C
Cowan, G., 1998, Statistical data analysis, Oxford University Press
C. Csaki, N. Kaloper & J. Terning, hep-ph/0111311.
De Bernardis, P., Ade, P.A.R., Bock, J.J. et al., 2000, Nature, 404,955
C. Deffayet, D. Harari, J. P. Uzan & M. Zaldarriaga, hep-ph/0112118.
Drell, P., Loredo, T.& Wasserman, I., 2000, ApJ, 530, 593.
Efstathiou, G., Moody, S., Peacock, J.A. et al, 2002, MNRAS, 330, L29.
Filippenko, A.V., Richmond, M.W., Branch, D. et al., 1992, AJ,104,1543
Garavini, G. et al. 2004 (in prep)
Garnavich, P.M., Jha, S., Challis, P., 1998,ApJ, 509, 74
Goldhaber, G., Groom, D. E.,Kim, A. et al.,2001, ApJ, 558, 359G
Goobar, A., Bergström, L. & Mörtsell, E., 2002, A&A, 384, 1.
Goobar, A., Mörtsell, E., Amanullah, R., Goliath, M., Bergström, L. & T. Dahlen, 2002, A&A, 392, 757.
Hamuy, M., Maza, J., Wischnjewsky, M. et al. 1993, IAUC, 5723R
Hamuy, M., Phillips, M.M., Suntzeff, N.B. et al. 1996, AJ, 112, 2408
Hamuy, M., Phillips, M.M., Suntzeff, N.B. et al. 1996, AJ, 112, 2398H
Henry J. P. 2001, ApJ 534, 565
Howell, D.A, 2001, ApJ,554, 193
Jaffe, A.H., Ade, P.A., Balbi, A. et al., 2001, Phys. Rev. Lett. 86, 3475
Jha, S., 2002, PhD thesis, Harvard University.
Kim, A., Goobar, A. & Perlmutter, S., 1996, PASP, 108, 190
Knop, R. et al. 2003, submitted
Krisciunas, K., Phillips, M.M., Stubbs, C. et al., 2001, AJ, 122, 1616K
Krisciunas, K., Phillips, M. M. & Suntzeff, N. B., astro-ph/0312626
Leibundgut, B., Kirshner, R. P., Phillips, M.M. et al., 1993,AJ, 105, 301.
Li, W., Filippenko, A.V. & Treffers, R.R., 2001, ApJ, 546,734
Lidman, C. et al. 2004 (in prep)
Maza, J., Hamuy, M., Phillips, M., Suntzeff, N. & Aviles, R., 1994, ApJ,424,L107
Mörtsell, E., Bergström, L and Goobar, A., 2002, Phys. Rev. D66, 047702.
Mörtsell, E. & Goobar, A., 2003, JCAP, 09, 009M
Nobili, S., Goobar, A., Knop, R., & Nugent, P., 2003, A&A 404, 901-912
Nugent P., Kim A.& Perlmutter S., 2003, PASP 114, 803
Perlmutter, S., Gabi, S., Goldhaber, G., 1997,ApJ, 483, 565
Perlmutter, S., Aldering, G., Goldhaber, G. et al., 1999, ApJ, 517, 565
Persson, S.E., Murphy, D.C., Krzeminski, W., Roth, M. & Rieke, M.J., 1998 A.J. 116, 2475.
Phillips, M.M., Lira, P., Suntzeff, N.B., Schommer, R.A., Hamuy, M.& Maza, J., 1999, AJ, 118:1766-1776
Richmond, M.W., Treffers, R.R., Filippenko, A.V. et al. 1995, AJ 109,2121
Riess, A., et al. 1998, AJ, 116, 1009.
Riess, A.G., Filippenko, A.V., Challis, P. et al. 1999, ApJ. 117,707-724
Riess, A.G., Filippenko, A.V., Liu, M.C. et al., 2000, ApJ. 536,62-67
Rowan-Robinson, M.,2002,MNRAS, 332, 352.
Schlegel, D.J., Finkbeiner, D.P. & Davis, M. 1998, ApJ, 500, 525S
Sievers, J.L., Bond, J.R., Cartwright, J.K. et al., 2003, ApJ.,591, 599
Spergel, D.N., Verde, L., Peiris, H.V. et al., 2003, ApJS, 148, 175S
Tonry, J.L.,Schmidt B.P., Barris, B. et al 2003,astro-ph/0305008
Wang, L., Goldhaber, G., Aldering, G., Perlmutter, S.2003, ApJ, 590, 944
Wang, L., 2003, Submitted to ApJL
Wells, L.A., Phillips, M.M., Suntzeff, B. et al., 1994 AJ 108, 2233

Paper B

A&A 404, 901–912 (2003)
DOI: 10.1051/0004-6361:20030536

Astronomy & Astrophysics

The intrinsic colour dispersion in Type Ia supernovae

S. Nobili[1], A. Goobar[1], R. Knop[2], and P. Nugent[3]

[1] Department of Physics, Stockholm University, SCFAB, 106 91 Stockholm, Sweden
[2] Department of Physics & Astronomy, Vanderbilt University, USA
[3] Lawrence Berkeley National Laboratory, 1 Cyclotron Road, Berkeley, CA 94720, USA

Received 14 February 2003 / Accepted 6 April 2003

Abstract. The properties of low-redshift Type Ia supernovae are investigated using published multi-band optical broadband data from the Calan/Tololo and CfA surveys. The average time evolution of $B-V$, $V-R$, $R-I$, $B-I$ and $V-I$, the intrinsic dispersion and time correlations are studied. This information is required to deduce the extinction of such explosions from the measured colours. We find that extinction corrections on individual SNe based on their colours up to 40 days past the B-band lightcurve maximum are generaly limited to $\sigma_{A_V} \gtrsim 0.1$, due to intrinsic variations, as far as it can be conservatively deduced with the current sample of data. However, we find that the $V-R$ colour, especially at late times, is consistent with a negligible intrinsic spread, and may be the most accurate estimator for extinction.

Key words. supernovae: general – stars: statistics

1. Introduction

In the last few years Type Ia supernovae (SNe Ia) have proved to be excellent distance estimators and have been successfully used to investigate the fate of the universe (Perlmutter et al. 1999; Riess et al. 1998). Despite the broad use of these objects by cosmologists, the current knowledge of the nature of SNe Ia is rather limited. Thus, there is a strong demand for further understanding to assess important issues about these explosions. For cosmological implications, the main concerns are related to the possible evolution of the SN properties with redshift. Moreover, critical tests for extinction along the line of sight based on supernova colours require good knowledge of the intrinsic properties of these objects.

In this paper, a statistical study on 48 well observed nearby SNe Ia is carried out. In particular, the intrinsic dispersion in SN colours is investigated using published *BVRI* data. We also focus on the time correlation of intrinsic optical colours. This information is needed to address the possible host galaxy or intergalactic extinction by dust of supernovae used for cosmological tests (see e.g. Riess et al. 2000; Nobili et al. 2003), and also to probe for other exotic sources of dimming at high-z with differential extinction (Mörtsell et al. 2002).

2. The data set

Published *BVRI* lightcurves of well observed nearby SNe Ia were analysed. The considered sample consists of 48 SNe Ia from 2 different sets, the Calan/Tololo data published by Hamuy et al. (1996), and the set in Riess et al. (1999), usually referred to as the CfA data. The list of SNe is given in Table 1, along with the observed filter data available for each of them, their redshift and the B-band lightcurve "stretch", s, as defined in Perlmutter et al. (1997) and Goldhaber et al. (2001).

The selected samples include a broad variety of SNe, well distributed in stretch factor, s. This parameter, related to Δm_{15} (Phillips 1993), has been found to correlate with the supernova luminosity. Thus, a sample well distributed in stretch should imply a broad distribution in luminosity. Figure 1 shows the distribution of the B-band light curve stretch factor and SN redshifts ($0.003 \leq z \leq 0.12$), for both samples. The timescale stretch parameter was determined from the lightcurve fits as in Goldhaber et al. (2001) using their B-band lightcurve template with a parabolic behavior for the earliest epoch after explosion.

K-corrections were applied to account for the small cosmological redshift as described in e.g. Goobar et al. (2002), using the ($s = 1$) spectroscopic template of Nugent et al. (2002) as a starting point. The results of this analysis were used to improve the spectral template of SN Ia's (Sect. 6) and we iterated the analysis once re-calculating the K-corrections with the improved template. Note that even though the K-corrections for the used data set are small, typically of the order of a few hundreds of a magnitude, for some of the more distant objects in the sample considered, they reach up to ~0.5 mag.

The SNe light curves were corrected for both Milky Way and host galaxy extinction as in Phillips et al. (1999) using the method first proposed by Lira (1995) for estimating host galaxy extinction using late epoch light curves. There is empirical evidence that the $B-V$ colors of SNe Ia show extremely small scatter for the period between 30 and 90 days post B-band maximum, despite any difference in the light curve shapes at earlier

Send offprint requests to: S. Nobili, e-mail: serena@physto.se

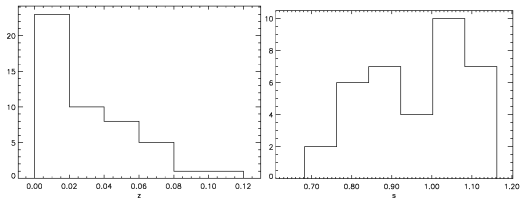

Fig. 1. Distribution of redshift, z, (binsize = 0.02), and stretch factor, s, (binsize = 0.08), for the analysed sample.

epochs. As the set of SNe used in this article is a subset of the one analysed in Phillips et al. (1999), the host galaxy extinctions listed in Table 2 of their paper were used. These were derived combining the late time $B-V$ colour with information on the $B-V$ and $V-I$ at maximum light.

The Cardelli et al. (1989) relation, modified by O'Donnell (1994), was used to compute the extinction in other colours given $E(B-V)$. Spectral templates of Type Ia SNe were used to compute the evolution of the extinction with the supernova epoch.

The extinction corrected lightcurves were further screened to exclude the most peculiar SNe, as the main emphasis of this work is to establish the properties of "normal" supernovae. Figure 2 shows the difference of the B-band lightcurve maximum, $B_{\max}$ and the V-band light curve maximum $V_{\max}$ plotted against the decline rate parameter, Δm_{15}, as reported in Phillips et al. (1999). A 3σ clipping rejection criteria was applied, iterating until no data points were further rejected. At least 5 SNe in the 2 data sets deviate significantly from the expected linear relation derived in Phillips et al. (1999) from an independent set of 20 non-reddened SNe (solid line in Fig. 2):

$$B_{\max} - V_{\max} = -0.07(\pm 0.012) + 0.114(\pm 0.037)(\Delta m_{15} - 1.1).$$

The outliers are SN 1993ae, SN 1995bd, SN 1996ai, and SN 1996bk for the CfA data, and SN 1992K for the Calan/Tololo set. Moreover SN 1995E and SN 1995ac have been excluded since they are similar to the peculiar SN 1991T (Branch et al. 1993)[1].

3. The average optical colours

Figures 3–8 show the time evolution of the extinction and K-corrected $B-V$, $V-R$, $R-I$, $B-I$ and $V-I$, colours. The plotted errors include the uncertainty on the host galaxy exinction correction. The time axis (t') has been corrected by the SN redshift and the B-band stretch factor s, to account for the dependence of colours on the stretch. This rescaling of the time axis was found very effective in reducing the measured intrinsic dispersion (Sect. 4)

$$t' = \frac{t - t_{B_{\max}}}{s \cdot (1+z)}. \quad (1)$$

For each colour lightcurve we have spline-interpolated the weighted mean values computed in four days wide, non-overlapping bins. The aim of this procedure was to find a curve that describes the *average* time evolution of the colours. This parameterization will be referred as a "*model*" in the

[1] Including these 2 SNe in the analysis does not change the results significantely.

Table 1. List of SNe used for the analysis.

SN	Band	z	s	Ref.
1993ac	*B*, *V*, *R*, *I*	0.049	0.865	(1)
1993ae[a]	*B*, *V*, *R*, *I*	0.019	0.846	(1)
1994ae	*B*, *V*, *R*, *I*	0.004	1.033	(1)
1994M	*B*, *V*, *R*, *I*	0.023	0.865	(1)
1994Q	*B*, *V*, *R*, *I*	0.029	1.116	(1)
1994S	*B*, *V*, *R*, *I*	0.015	1.061	(1)
1994T	*B*, *V*, *R*, *I*	0.035	0.890	(1)
1995ac[a]	*B*, *V*, *R*, *I*	0.050	1.123	(1)
1995ak	*B*, *V*, *R*, *I*	0.023	0.857	(1)
1995al	*B*, *V*, *R*, *I*	0.005	1.044	(1)
1995bd[a]	*B*, *V*, *R*, *I*	0.016	1.131	(1)
1995D	*B*, *V*, *R*, *I*	0.007	1.081	(1)
1995E[a]	*B*, *V*, *R*, *I*	0.012	1.024	(1)
1996ai[a]	*B*, *V*, *R*, *I*	0.003	1.110	(1)
1996bk[a]	*B*, *V*, *R*, *I*	0.007	0.761	(1)
1996bl	*B*, *V*, *R*, *I*	0.036	1.030	(1)
1996bo	*B*, *V*, *R*, *I*	0.017	0.902	(1)
1996bv	*B*, *V*, *R*, *I*	0.007	1.106	(1)
1996C	*B*, *V*, *R*, *I*	0.030	1.102	(1)
1996X	*B*, *V*, *R*, *I*	0.007	0.889	(1)
1990af	*B*, *V*	0.051	0.792	(2)
1990O	*B*, *V*, *R*, *I*	0.030	1.116	(2)
1990T	*B*, *V*, *R*, *I*	0.040	0.998	(2)
1990Y	*B*, *V*, *R*, *I*	0.039	1.007	(2)
1991ag	*B*, *V*, *R*, *I*	0.014	1.084	(2)
1991S	*B*, *V*, *R*, *I*	0.055	1.114	(2)
1991U	*B*, *V*, *R*, *I*	0.032	1.068	(2)
1992ae	*B*, *V*	0.075	0.970	(2)
1992ag	*B*, *V*, *I*	0.025	0.951	(2)
1992al	*B*, *V*, *R*, *I*	0.015	0.963	(2)
1992aq	*B*, *V*, *I*	0.102	0.868	(2)
1992au	*B*, *V*, *I*	0.061	0.787	(2)
1992bc	*B*, *V*, *R*, *I*	0.020	1.039	(2)
1992bg	*B*, *V*, *I*	0.035	0.983	(2)
1992bh	*B*, *V*, *I*	0.045	1.048	(2)
1992bk	*B*, *V*, *I*	0.058	0.825	(2)
1992bl	*B*, *V*, *I*	0.044	0.812	(2)
1992bo	*B*, *V*, *R*, *I*	0.019	0.767	(2)
1992bp	*B*, *V*, *I*	0.079	0.907	(2)
1992br	*B*, *V*	0.088	0.682	(2)
1992bs	*B*, *V*	0.064	1.030	(2)
1992J	*B*, *V*, *I*	0.045	0.798	(2)
1992K[a]	*B*, *V*, *I*	0.010	0.787	(2)
1992P	*B*, *V*, *I*	0.037	0.952	(2)
1993ag	*B*, *V*, *I*	0.049	0.917	(2)
1993B	*B*, *V*, *I*	0.070	1.023	(2)
1993H	*B*, *V*, *R*, *I*	0.024	0.774	(2)
1993O	*B*, *V*, *I*	0.051	0.950	(2)

(1), Riess et al. (1998); (2), Hamuy et al. (1996).
[a] Excluded from the analysis presented here.

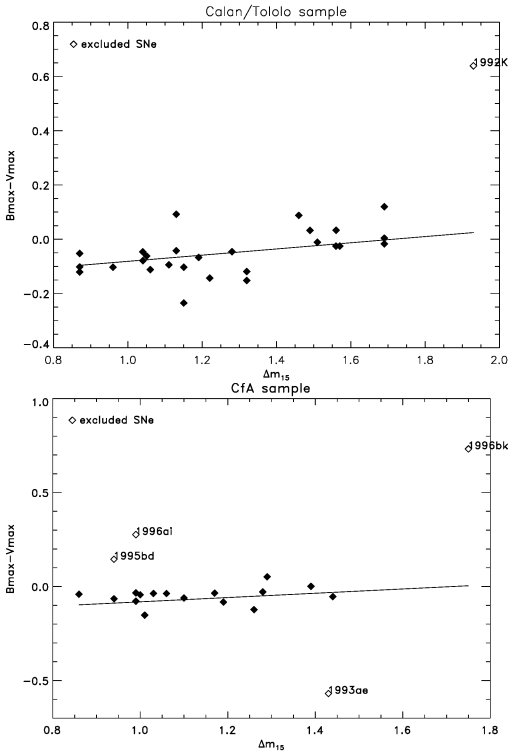

Fig. 2. B_{max}–V_{max} vs. Δm_{15} for the 2 sets of data, k-corrected, corrected for Galactic extinction and Host Galaxy extinction, compared with the result of Phillips et al. (1999).

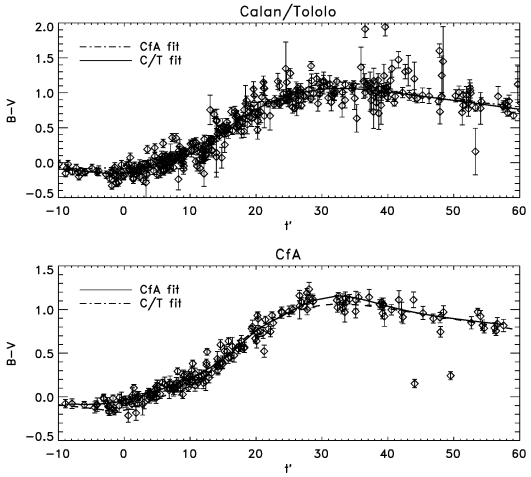

Fig. 3. $B - V$ for the two sets of data. The solid line represent alway the curve found for the current set, while the dashed line is the curve found for the same colour of the other set.

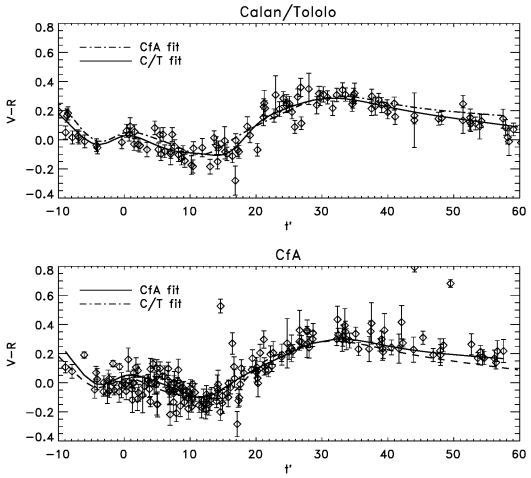

Fig. 4. $V - R$ for the two sets of data. The solid line represent alway the curve found for the current set, while the dashed line is the curve found for the same colour of the other set.

following discussion. Other methods were used to fit the data, as for example a least squares cubic spline fit. These result in curves that differ from the *model* typically by 0.01 mag. The *models* show some systematic discrepancies between the two data sets, especially in $R - I$ for which the C-T *model* is always redder than the CfA *model*. In Fig. 9 we investigate the differences of each of the *models* from the one built on both sets together. The differences are usually of the order of a few hundreds of a magnitude. The largest deviation was found for $R - I$ in the Calan/Tololo set, resulting in a difference of about 0.2 mag at maximum with respect to the *model* built up using data from both sets. Note, however, that the statistics in the Calan/Tololo set for $R - I$ colour, all along the evolution and in particular around the time of B_{max}, is extremely poor, as shown in Fig. 5. Due to the smaller quoted observational error bars, the CfA set dominates the weighted average used to build the *model* out of both data sets.

A source of uncertainty in this analysis is the ability of the observers to convert the instrumental magnitudes from the used filter+CCD system transmission into the standard *BVRI* system. The apparent systematic effects for $R - I$ in Fig. 9 may be indicative of this.

In order to assess systematic effects in builing the colour *models*, we checked whether the host galaxy extinction was over-corrected. Thus, we compared the *models* with the data of those SNe that, according to Phillips et al. (1999), suffered no extinction from the host galaxy. The comparison, shown in Fig. 7, exhibits no obvious deviations and we may conclude that the extinction corrected colours are consistent with the uncorrected sub-sample.

A possible remaining dependence of colours on the stretch factor s was investigated. For data points in a 5 days broad bin around time of B-maximum and around day 15, a linear

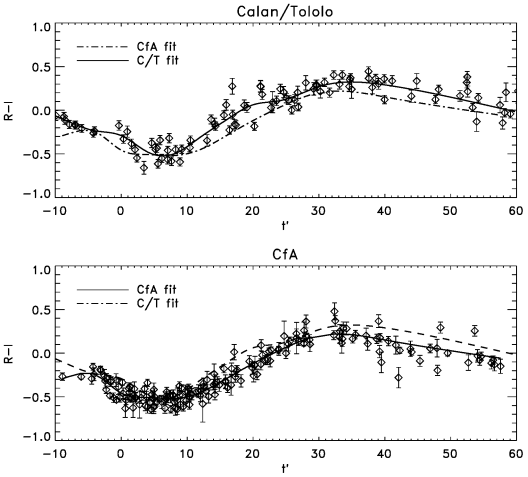

Fig. 5. $R - I$ for the two sets of data. The solid line represent alway the curve found for the current set, while the dashed line is the curve found for the same colour of the other set.

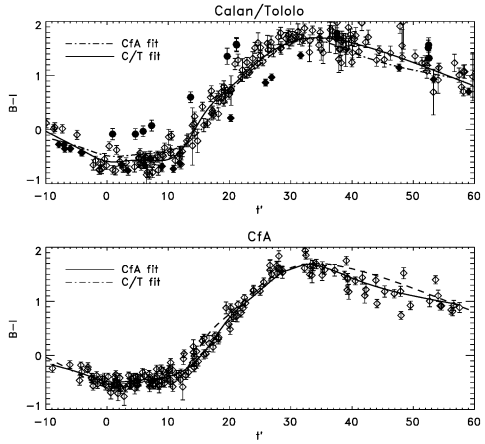

Fig. 6. $B - I$ for the two sets of data. The solid line represent alway the curve found for the current set, while the dashed line is the curve found for the same colour of the other set. The filled circles represent SN 1993H, while the filled diamonds are data of SN 1992bc. Refer to Sect. 7 for a discussion about these 2 SNe.

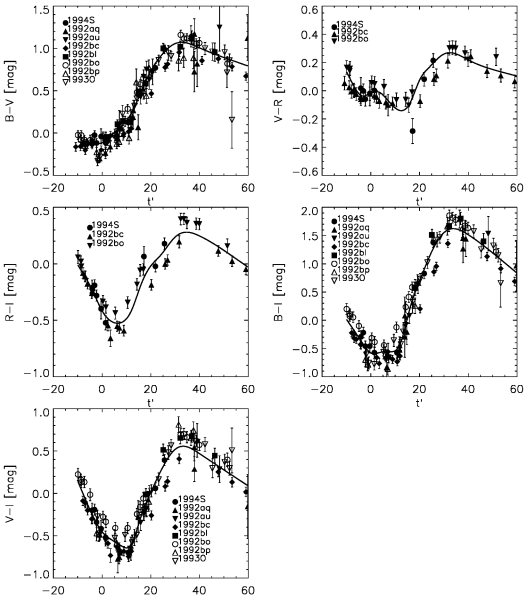

Fig. 7. Comparison of the models with data of unreddened SNe only.

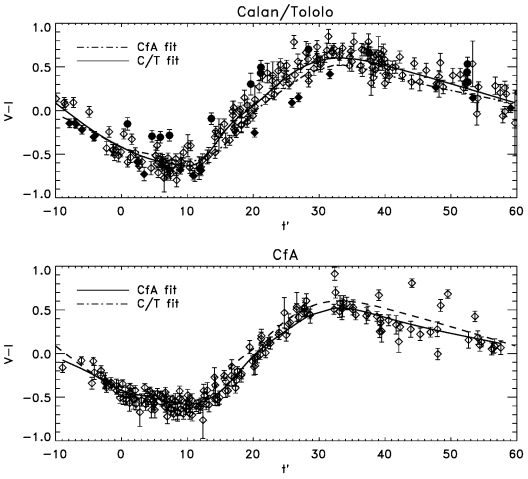

Fig. 8. $V - I$ for the two sets of data. The solid line represent alway the curve found for the current set, while the dashed line is the curve found for the same colour of the other set. The filled circles represent SN 1993H, while the filled diamonds are data of SN 1992bc. Refer to Sect. 7 for a discussion about these 2 SNe.

weighted fit was done on the residuals from the models not showing any further significant dependence on Δm_{15} or equivalently on the stretch parameter s. Note that this is not in contradiction with Fig. 2, as we are considering $(B-V)_{t_{B_{\max}}}$ instead of $B_{\max} - V_{\max}$. Moreover, our analysis includes data points in a broad bin around day zero, and not a fitted lightcurve maximum as in Fig. 2.

4. Intrinsic colour dispersion

The observed colour dispersion around the *models* is overall inconsistent with a statistical random distribution of the data with the reported measurement errors. The χ^2 value per degree of freedom computed for each model is typically between 3

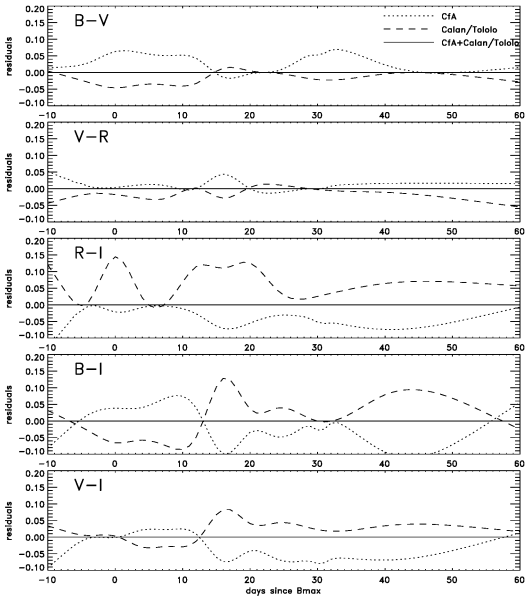

Fig. 9. Residuals of each of the models from the one built for all the data set.

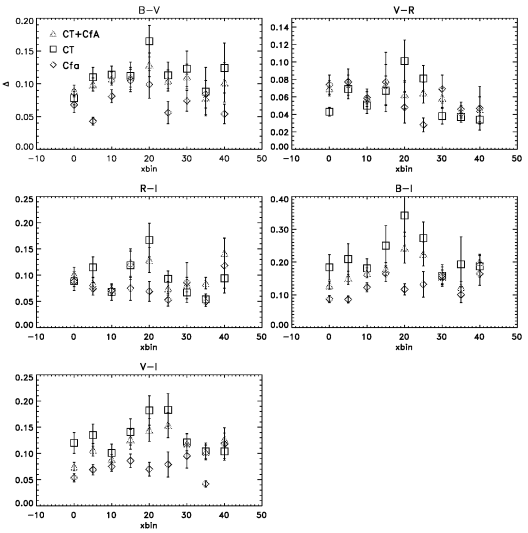

Fig. 10. Comparison of the results for the intrinsic dispersion in each colour given in Table 2 for both data sets (triangles) and the results obtained keeping the 2 sets of data separated (squares and diamonds for the C-T and CfA respectively).

and 6, giving indication of a very poor fit of the data. Thus, we conclude that the analysed data supports the existence of an *intrinsic colour dispersion* of Type Ia supernovae[2].

The intrinsic colour dispersion was computed on the residuals of each of the data sets from the corresponding *model*, built as explained above. Labeling XY_i any of the measured colours, $B-V$, $V-R$, $R-I$, $B-I$ and $V-I$, the residual with respect to the model expectation is referred as R_{XY_i}, i.e.,

$$R_{XY_i} = XY_i - XY_i^{\rm model}. \tag{2}$$

Next, the time axis was binned into 5 days wide bins to compensate for the modest statistics. The bins are centered at days $d = 5{\cdot}n$, with n ranging from 0 to 8. For each bin k, we compute the weighted average for the data XY, (see Appendix A)

$$XY^k = \frac{\sum_{i=1}^{N_k} w_i XY_i}{\sum_{i=1}^{N_k} w_i} \tag{3}$$

where N_k is the number of points in bin k and w_i is the inverse of the uncertainty on the ith measurement squared, $1/\sigma_i^2$, where σ_i include both measurement errors and uncertainty on the host galaxy extinction corrections. The weighted sample standard deviation was computed as the square root of the weighted second moment:

$$s_{XY}^k = \sqrt{m_{w_2}} = \sqrt{\frac{\sum_{i=1}^{N} w_i R_{XY_i}^2}{\sum_{i=1}^{N} w_i}}. \tag{4}$$

[2] This has been further investigated as described at the end of this section.

The uncertainty on the expression in Eq. (4) is given by the square root of the variance, $V[s_{XY}^k]$, computed as:

$$V[s_{XY}^k] = \frac{V[m_{w_2}]}{4m_{w_2}} \tag{5}$$

where $V[m_{w_2}]$ is the variance of the weighted second moment. We can consider the result of Eq. (4) as an estimate of the intrinsic dispersion in each bin, for each XY colour: $\Delta_{XY} = s_{XY}^k$. This has been applied at each one of the sets separately and at the whole set of data. The results of the method for the whole set of data are given in Table 2.

Figure 10 shows a comparison of the intrinsic dispersion computed for each of the sets separately and their combination. In most of the cases the differences exceed the statistical uncertainties, seemingly arising from systematic differences between the two data sets. The computed intrinsic dispersion for the CfA sample was found to be smaller than for the CT data set and the whole (combined) sample in most cases, again pointing at systematic differences in the reported magnitudes.

Note that the adopted method leads to an overestimation of the intrinsic colour dispersion due to the contribution from the measurement errors. However, the weighting procedure ensures that the most accurate measurements dominate the result. To asses the impact of the measurement accuracy, we run a Monte-Carlo simulation to generate a synthetic colour data set with a dispersion given by the measurement uncertainties alone, i.e. no *intrinsic* dispersion. Three hundred data sets, with the same distributions in epochs and formal error bars as the CfA and Calan/Tololo were simulated and the weighted standard deviation (and its error) were computed, according to Eqs. (4) and (5). Note that the simulation, for simplicity,

Table 2. Results of the analysis of all SNe. First column: central value in days for each time bin; N_k is the number of points for each bin; XY^k is the weighted mean value and its 1-sigma uncertainty; Δ_{XY} is the intrinsic dispersion computed according to Eqs. (4) and (5); $\Delta^{\rm corr}_{XY}$ is the corrected intrinsic dispersion, computed as in Eq. (6), and in the last column is the estimated lower limit at 99% C.L. (see text).

Day	N_k	BV^k	Δ_{BV}	$\Delta^{\rm corr}_{BV}$	L.L.
0	57	–0.11 ± 0.01	0.09 ± 0.01	0.07	0.05
5	70	0.02 ± 0.01	0.10 ± 0.01	0.08	0.05
10	75	0.16 ± 0.01	0.11 ± 0.01	0.09	0.06
15	59	0.47 ± 0.02	0.11 ± 0.01	0.09	0.06
20	47	0.75 ± 0.03	0.13 ± 0.02	0.11	0.08
25	39	0.95 ± 0.02	0.10 ± 0.02	0.08	0.06
30	34	1.08 ± 0.02	0.11 ± 0.02	0.09	0.07
35[a]	27	1.07 ± 0.02	0.08 ± 0.03	<0.05	
40	35	1.02 ± 0.02	0.10 ± 0.03	0.07	0.06
Day	N_k	VR^k	Δ_{VR}	$\Delta^{\rm corr}_{VR}$	L.L.
0	31	0.04 ± 0.02	0.07 ± 0.01	0.06	0.05
5	36	–0.01 ± 0.02	0.08 ± 0.01	0.06	0.05
10	38	–0.08 ± 0.01	0.06 ± 0.01	0.04	0.04
15	34	–0.07 ± 0.02	0.07 ± 0.02	0.06	0.05
20	24	0.09 ± 0.02	0.06 ± 0.02	0.05	0.04
25[a]	22	0.22 ± 0.02	0.06 ± 0.01	<0.04	
30[a]	18	0.31 ± 0.01	0.06 ± 0.01	<0.04	
35[a]	16	0.30 ± 0.01	0.04 ± 0.01	<0.03	
40[a]	19	0.25 ± 0.01	0.05 ± 0.01	<0.03	
Day	N_k	RI^k	Δ_{RI}	$\Delta^{\rm corr}_{RI}$	L.L.
0	30	–0.44 ± 0.02	0.10 ± 0.01	0.09	0.06
5	36	–0.50 ± 0.02	0.09 ± 0.01	0.07	0.05
10	32	–0.50 ± 0.02	0.07 ± 0.01	0.05	0.05
15	30	–0.25 ± 0.04	0.12 ± 0.03	0.11	0.08
20	20	–0.06 ± 0.04	0.13 ± 0.02	0.12	0.09
25	22	0.09 ± 0.02	0.08 ± 0.01	0.05	0.05
30	18	0.23 ± 0.03	0.08 ± 0.01	0.06	0.06
35[a]	16	0.27 ± 0.03	0.09 ± 0.01	<0.06	
40	17	0.22 ± 0.04	0.14 ± 0.03	0.13	0.10
Day	N_k	BI^k	Δ_{BI}	$\Delta^{\rm corr}_{BI}$	L.L.
0	39	–0.54 ± 0.02	0.13 ± 0.01	0.10	0.08
5	48	–0.52 ± 0.02	0.15 ± 0.02	0.13	0.09
10	48	–0.44 ± 0.03	0.17 ± 0.01	0.15	0.10
15	35	0.10 ± 0.05	0.18 ± 0.02	0.16	0.11
20	34	0.74 ± 0.06	0.24 ± 0.05	0.23	0.15
25	25	1.25 ± 0.05	0.22 ± 0.04	0.21	0.15
30	27	1.66 ± 0.03	0.16 ± 0.02	0.13	0.10
35[a]	23	1.65 ± 0.03	0.12 ± 0.02	<0.08	
40	33	1.51 ± 0.04	0.20 ± 0.02	0.17	0.13
Day	N_k	VI^k	Δ_{VI}	$\Delta^{\rm corr}_{VI}$	L.L.
0	37	–0.43 ± 0.02	0.08 ± 0.01	0.05	0.05
5	51	–0.54 ± 0.02	0.11 ± 0.01	0.09	0.06
10	48	–0.60 ± 0.01	0.09 ± 0.01	0.06	0.05
15	38	–0.34 ± 0.03	0.13 ± 0.02	0.11	0.08
20	36	0.01 ± 0.03	0.14 ± 0.02	0.13	0.09
25	28	0.33 ± 0.03	0.15 ± 0.02	0.14	0.10
30	28	0.57 ± 0.03	0.12 ± 0.02	0.10	0.08
35	25	0.58 ± 0.02	0.10 ± 0.01	0.08	0.07
40	33	0.48 ± 0.03	0.13 ± 0.01	0.11	0.08

[a] Compatible with null intrinsic dispersion at 99% C.L.; an upper limit is given instead of the corrected intrinsic dispersion.

generates Gaussian distributed and completely uncorrelated data. The averages, δ, were used to disentangle the contribution of the intrinsic dispersion from the measurement errors. First, an hypothesis test was run to verify whether the simulated data and the measured data had the same dispersion; e.g. implying null intrinsic dispersion:

$H_0 : \Delta = \delta$

$H_1 : \Delta \neq \delta.$

A level of significance $\alpha = 0.01$ was set for rejecting the null hypothesis (Cowan 1998). Only 10 cases were not rejected, indicated by a $^{(a)}$ in Table 2. For all the other cases, for which the H_0 hypothesis was rejected, the intrinsic dispersion was computed as:

$$\Delta^{\rm corr} = \sqrt{\Delta^2 - \delta^2} \tag{6}$$

and a lower limit on its value was set at a 99% confidence limit. The cases for which the null hypothesis was not rejected, were considered as compatible with *no intrisic dispersion*, and an upper limit on its value was set at a 99% confidence level. The corrected intrinsic dispersions are listed in the 5th column of Table 2, together with upper and lower limits. We notice that the narrowest colour dispersion happens for $V - R$, especially at late times. At 25 days after $B_{\rm max}$ and later, this colour is compatible with no intrinsic spread at all. Further, it should be noted that at day 35, all the colours but $V-I$ are consistent with vanishing intrinsic dispersion.

5. Correlation

The correlation between optical colours at different epochs was also estimated. The property that was tested is whether a supernova that is blue at a certain epoch for example, say at maximum, stays blue at all epochs. In Riess et al. (2000), the authors argue that data measurements more than 3 days apart may be considered as uncorrelated estimators of colour. Our analysis does not support that assumption[3]. We find significant correlations for data points up to a month apart, as shown below. The method followed is essentially the one used to compute the intrinsic dispersion. One can summarize the following steps:

- Bin the data in time;
- Select only the SNe present in all the time bins;
- For each bin compute the weighted average of the measurements belonging to the same SN;
- Compute the linear correlation coefficient between bins as in Eq. (A.8);
- Test the correlation coefficient significance (Appendix A.2).

We refer to Appendix A.2 for what follows. The correlation coefficient between different epochs h and k is:

$$r_{hk} = \frac{\sum_{i=1}^{n}\left(R^h_{XY_i} - \overline{R}^h_{XY}\right)\left(R^k_{XY_i} - \overline{R}^k_{XY}\right)}{\sqrt{\sum_{i=1}^{n}\left(R^h_{XY_i} - \overline{R}^h_{XY}\right)^2 \sum_{j=1}^{n}\left(R^k_{XY_j} - \overline{R}^k_{XY}\right)^2}} \tag{7}$$

[3] For high-z objects this is even more questionable when some of the main sources of uncertainty is the subtraction of a common image of the host galaxy and the K-corrections.

Table 3. Correlation coefficients between the different bins. The indicated *xbin* is the central value of each bin. The bin size is 7 days for all the bins. The errors indicate the 1 σ confidence level for the computed coefficients. See text for details.

$B-V$/xbin	0	7	15	22	30
0	1.00	$0.80^{+0.09}_{-0.14}$	$0.61^{+0.16}_{-0.24}$	$0.47^{+0.21}_{-0.28}$	$0.45^{+0.21}_{-0.28}$
7		1.00	$0.75^{+0.11}_{-0.17}$	$0.69^{+0.13}_{-0.20}$	$0.63^{+0.15}_{-0.23}$
15			1.00	$0.59^{+0.17}_{-0.24}$	$0.45^{+0.22}_{-0.28}$
22				1.00	$0.56^{+0.18}_{-0.25}$
30					1.00
$V-R$/xbin	0	7	15	22	30
0	1.00	$0.81^{+0.13}_{-0.31}$	$0.46^{+0.33}_{-0.54}$	$0.29^{+0.41}_{-0.56}$	$0.03^{+0.51}_{-0.53}$
7		1.00	$0.24^{+0.44}_{-0.56}$	$0.48^{+0.32}_{-0.53}$	$0.24^{+0.44}_{-0.56}$
15			1.00	$0.48^{+0.32}_{-0.53}$	$-0.15^{+0.55}_{-0.47}$
22				1.00	$-0.44^{+0.55}_{-0.34}$
30					1.00
$R-I$/xbin	0	7	15	22	30
0	1.00	$0.73^{+0.20}_{-0.51}$	$0.57^{+0.31}_{-0.63}$	$0.56^{+0.31}_{-0.63}$	$0.31^{+0.46}_{-0.68}$
7		1.00	$0.66^{+0.25}_{-0.57}$	$0.78^{+0.16}_{-0.45}$	$0.58^{+0.30}_{-0.63}$
15			1.00	$0.89^{+0.08}_{-0.28}$	$0.53^{+0.33}_{-0.65}$
22				1.00	$0.83^{+0.13}_{-0.38}$
30					1.00
$V-I$/xbin	0	7	15	22	30
0	1.00	$0.84^{+0.08}_{-0.17}$	$0.92^{+0.04}_{-0.09}$	$0.93^{+0.04}_{-0.08}$	$0.49^{+0.25}_{-0.36}$
7		1.00	$0.72^{+0.15}_{-0.26}$	$0.74^{+0.14}_{-0.25}$	$0.50^{+0.24}_{-0.36}$
15			1.00	$0.90^{+0.06}_{-0.12}$	$0.49^{+0.25}_{-0.36}$
22				1.00	$0.65^{+0.18}_{-0.30}$
30					1.00
$B-I$/xbin	0	7	15	22	30
0	1.00	$0.62^{+0.20}_{-0.35}$	$0.74^{+0.14}_{-0.27}$	$0.44^{+0.29}_{-0.42}$	$0.30^{+0.34}_{-0.44}$
7		1.00	$0.76^{+0.13}_{-0.26}$	$0.47^{+0.27}_{-0.41}$	$0.51^{+0.25}_{-0.39}$
15			1.00	$0.76^{+0.14}_{-0.26}$	$0.40^{+0.30}_{-0.42}$
22				1.00	$0.73^{+0.15}_{-0.28}$
30					1.00

where the summation is on the ith SN, which by construction is present in all the bins. The uncertainty on r_{hk} has been computed converting it into the normally distributed variable z, as described in Appendix A.2. The results, given in Table 3, show that the correlation is important and non-zero all along the time evolution. Figure 11 shows the weighted mean colours for the selected SNe in the bins centered at day 0, 15 and 30. Note that the supernovae selected are different in different colours, but, by construction, are the same in all the bins for each of the colour. It appears that supernovae that deviate from the average colour at a certain epoch are likely to keep their colour excess all along the 30 days evolution considered here.

6. Supernovae template

Nugent et al. (2002) analysed the relation between colours of SNe Ia and K-corrections. In particular they showed how K-corrections are mainly driven by the overall colour of the SN rather than by peculiarities of single features. Using spectra and colour light curves they give a recipe to build a *SN Ia template*, to be used for computing K-corrections of $s \sim 1.0$ SNe. As the sample used in our work is larger than the one considered in their paper, we have used our results to improve the spectral template. Note that this affects only the *BVRI* magnitudes, which are the only bands treated here. Referring to Nugent et al. (2002), we proceed as follows:

- correct the *BVRI* of their list of *UBVRIJHK* magnitudes using our $B-V$, $V-R$ and $R-I$ *models*;
- correct the corresponding spectral templates with this colours[4];
- iterate the whole analysis described in this paper, using the newly created templates to compute the K-corrections for both Calan/Tololo and CfA data set;
- correct again the templates using the most recent version of the *models*.

[4] The same code used by Nugent et al. (2002) was used for this.

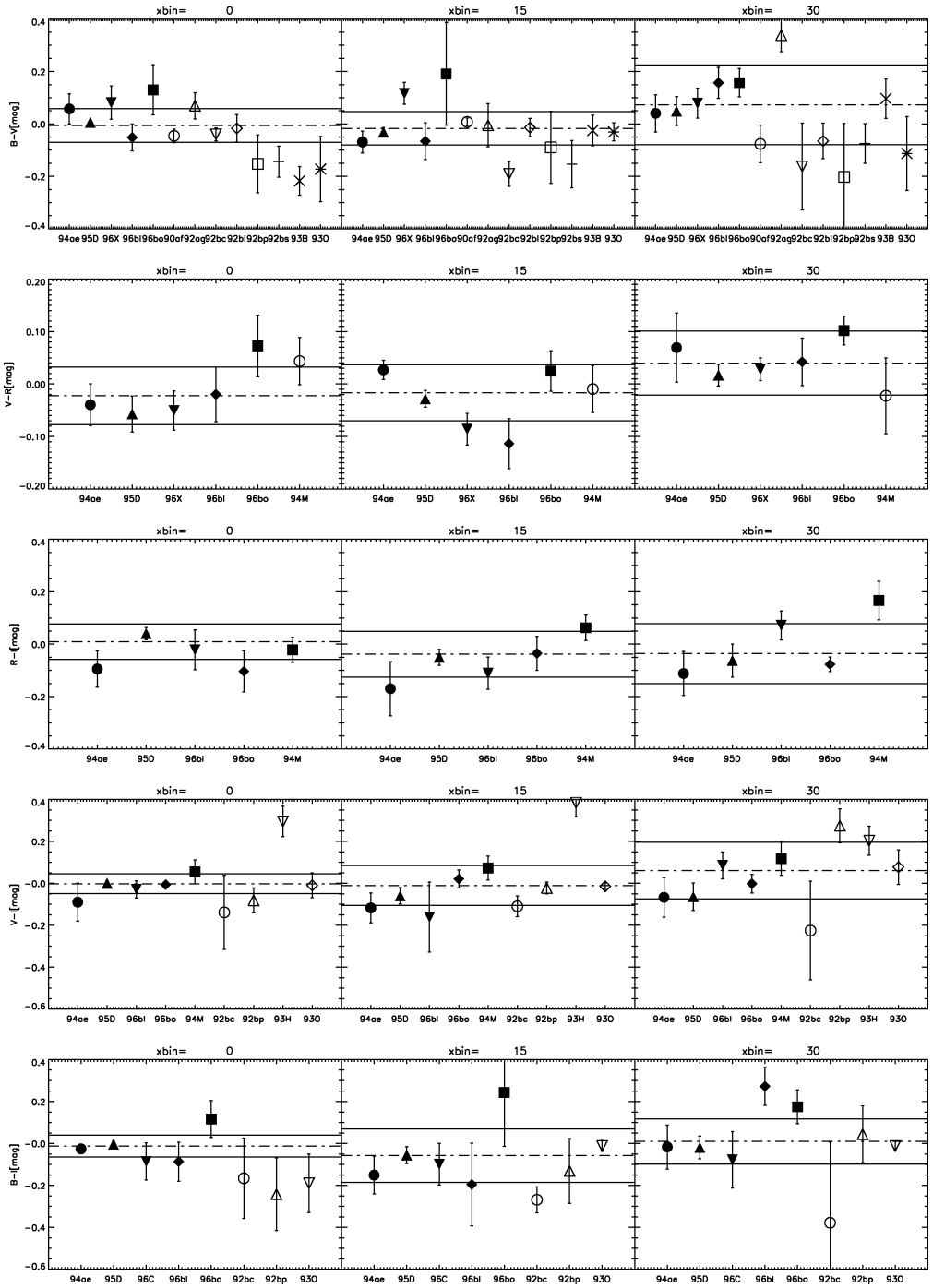

Fig. 11. From top to bottom and left to right. Residuals from the models for the SNe selected for each colour, in bin centered at day 0,15 and 30. The band defined by the solid lines correspond to the intrinsic dispersion found in at the same epoch.

Table 4. Results of the analysis done excluding SN 1992bc and SN 1993H (**) for $B-I$ and $V-I$. *xbin* is the central value in days for each bin; XY^k** is the weighted mean value and its uncertainty; Δ_{BI}** is computed according to Eqs. (4) and (5); $\Delta_{XY}^{\rm corr}$** is the corrected intrinsic disperion and L.L. is the lower limit at 99% C.L.; in the last column is the difference between the results given in Table 2 and this analysis; the errors are computed as sum in quadrature.

day	BI^k**	Δ_{BI}**	$\Delta_{BI}^{\rm corr}$**	L.L.	$\Delta_{BI}-\Delta_{BI}$**
0	–0.53 ± 0.02	0.13 ± 0.01	0.10	0.08	0.000 ± 0.017
5	–0.53 ± 0.02	0.13 ± 0.01	0.10	0.08	0.024 ± 0.025
10	–0.41 ± 0.02	0.15 ± 0.02	0.13	0.09	0.018 ± 0.022
15	0.10 ± 0.05	0.18 ± 0.02	0.16	0.11	0.003 ± 0.026
20	0.74 ± 0.05	0.15 ± 0.02	0.12	0.09	0.098 ± 0.052
25	1.31 ± 0.05	0.12 ± 0.02	0.09	0.08	0.101 ± 0.044
30	1.68 ± 0.03	0.12 ± 0.02	0.08	0.08	0.038 ± 0.028
35	1.65 ± 0.03	0.13 ± 0.02	<0.09		–0.006 ± 0.024
40	1.49 ± 0.04	0.20 ± 0.03	0.18	0.13	-0.004 ± 0.035
day	VI^k**	Δ_{VI}**	$\Delta_{VI}^{\rm corr}$**	L.L.	$\Delta_{VI}-\Delta_{VI}$**
0	–0.43 ± 0.02	0.07 ± 0.01	0.05	0.05	0.002 ± 0.011
5	–0.55 ± 0.01	0.09 ± 0.01	0.06	0.05	0.019 ± 0.014
10	–0.58 ± 0.01	0.09 ± 0.01	0.06	0.05	0.002 ± 0.013
15	–0.34 ± 0.03	0.11 ± 0.01	0.09	0.07	0.016 ± 0.022
20	0.01 ± 0.03	0.11 ± 0.02	0.09	0.07	0.036 ± 0.027
25	0.35 ± 0.03	0.09 ± 0.01	0.07	0.06	0.060 ± 0.028
30	0.57 ± 0.03	0.11 ± 0.02	0.09	0.07	0.007 ± 0.029
35	0.58 ± 0.02	0.10 ± 0.01	0.08	0.07	0.000 ± 0.019
40	0.47 ± 0.03	0.13 ± 0.01	0.11	0.08	0.000 ± 0.018

Even though the template itself is modified considerably from the original one, iterating once results in small corrections (~0.001–0.005 mag) in the intrinsic dispersion in all colours at any epoch, and a few percent in the colour *models*. As the correction obtained are small and well within the given uncertainties, we do not iterate further. The results of this analysis should *not* be considered definitive and may change as SNe Ia and their colour evolutions are studied in even more detail. However, it can be considered a good estimate of the average SN Ia template (in *BVRI*), as it is constructed from a quite broad sample of SNe. The final corrected template is available upon request.

7. Discussion

Throughout our analysis all data points were treated as independent measurements. This is particularly important for the cases with significant host galaxy light underneath the supernova where a single reference image was used, introducing a correlation between the data points not considered here.

A first estimate of the intrinsic dispersion was calculated for each data set separately and the two data sets together. A comparison of the results shows that the colours extracted from the CfA sample have smaller scatter indicating that the contribution from measurement errors is not negligible. Further, in the analysis the measurements are assumed to be Gaussian distributed and the weighted standard deviation has been taken as an estimate of the intrinsic dispersion. However, we noticed that 2 SNe, SN 1993H and SN 1992bc, seem to be rather deviant in $B-I$ and $V-I$ for the C-T set, as shown in Figs. 6 and 8. The effect of the "outliers" is particularly important around 20 days after B-maximum. For comparison, we recalculated the intrinsic spread in $B-I$ and $V-I$ excluding these 2 SNe. The results are shown on Table 4. The agreement between the intrinsic dispersion between the data sets improves when these 2 SNe are excluded. We emphasize that there are systematic differences between the Calan/Tololo and CfA data sets, and they might have been introduced while converting from the instrumental system used to the standard *BVRI* system.

An attempt of disentangling the intrinsic dispersion from the contribution of the uncertainties has been done resulting in upper limit values for the intrinsic dispersion in some cases. The most relevant is the case of $V-R$, that seems compatible with null intrinsic dispersion for most of the epochs at 99% C.L. Moreover this analysis brings out an important feature at day 35, when all the colours but $V-I$ are consistent with zero intrinsic dispersion. This indicates that further studies will be needed to investigate this intriguing finding. When computing the correlation coefficients we considered data up to 30 days after B-band maximum, even though later epoch data are available for several supernovae. However, the necessary condition of each SN being observed in all the time bins reduces the statistics if later epochs are introduced. This limitation is specific to the sample used and can be overcome with the use of a more extensively observed sample, such as what will be provide by SNfactory (Aldering et al. 2002).

The intrinsic dispersion sets constrains on the ability to determine the host galaxy extinction, A_V. This will depend on

the colour, as the intrinsic dispersion is different for different colours. As an example we used the Cardelli et al. (1989) relation at the effective wavelength for each bandpass to compute the expected uncertainty in the extinction, neglecting any dependence on the supernova phase.

$$\begin{aligned} \sigma_{A_V}^{B-V} &= 3.1 \cdot \Delta_{BV}^{\rm corr} \\ \sigma_{A_V}^{V-R} &= 6.2 \cdot \Delta_{VR}^{\rm corr} \\ \sigma_{A_V}^{R-I} &= 4.1 \cdot \Delta_{RI}^{\rm corr} \\ \sigma_{A_V}^{B-I} &= 1.4 \cdot \Delta_{BI}^{\rm corr} \\ \sigma_{A_V}^{V-I} &= 2.5 \cdot \Delta_{VI}^{\rm corr} \end{aligned} \quad (8)$$

where R_V was assumed equal to 3.1. Table 5 shows the results of the Eq. (8) for the epochs for which the intrinsic dispersion was calculated. The $\Delta_{XY}^{\rm corr}$ was used for this. The results indicate that, with the present knowledge, extinction by dust with $R_V = 3.1$ may only be determined to $\sigma_{A_V} \gtrsim 0.10$ with Type Ia restframe optical data within the first 40 days after B-band lightcurve maximum, for the colours and epochs with non-zero intrinsic dispersion. However observations in $V-R$ are preferable to other colours to set limit on the extinction of an observed supernova. To account for possible different extinction parameters R_V in the different supernova host galaxies (as noticed in e.g. Riess et al. 1996 and Krisciunas et al. 2000), we repeated the analysis considering a Gaussian uncertainty $\sigma_{R_V} = 1$ on R_V, propagating this scatter on the host galaxy extinction corrections. This changes the values of the intrinsic dispersion, but typically within the quoted errors in Table 2.

8. Conclusion

A statistical analysis of colours of SNe Ia using a sample of 48 nearby SNe was performed. Of this sample 7 SNe have been excluded based on their large extinction, or peculiar behavior of their colours at maximum. With the present knowledge and data quality we computed the average colour evolution for $B-V$, $V-R$, $R-I$, $B-I$ and $V-I$ with time and the derived intrinsic scatter. We find that the correlation of colours during the first 30 days after restframe B-band maximum is not negligible, i.e. arguing against the assumptions made in the analysis of SN 1999Q ($z = 0.46$; Riess et al. 2000) where five measurements of restframe $B-I$ along its lightcurve were treated as *independent* estimates of extinction. According to our findings, their limit on the presence of intergalactic grey dust must be revised. A reanalysis of the data from SN 1999Q is in preparation (Nobili et al. 2003). With the data at hand, host galaxy extinction corrections from restframe optical colours within the first 30 days after maximum light are generaly limited to $\sigma_{A_V} \gtrsim 0.1$ due to the intrinsic variation of Type Ia colours at those epochs, with the possible exception of extinction corrections derived from the rest-frame $V-R$ colour. The results of this analysis have been used to correct spectroscopic templates which are available upon request.

Acknowledgements. S. Nobili wishes to thank Christian Walck for his valuable help and constructive discussions on the statistical analysis presented in this paper and Don Groom, Chris Lidman and Vallery Stanishev for their careful reading and useful suggestions. SN is supported by a graduate student grant from the Swedish Research Council. AG is a Royal Swedish Academy Research Fellow supported by a grant from the Knut and Alice Wallenberg Foundation. PEN acknowledges support from a NASA LTSA grant and by the Director, Office of Science under U.S. Department of Energy Contract No. DE-AC03-76SF00098.

Table 5. σ_{A_V} represents the constrain on the extinction A_V that it is possible to compute for a given intrinsic dispersion. The $\Delta_{XY}^{\rm corr}$ and its L.L. given in Table 2 have been used for these estimates.

	xbin	σ_{A_V}	L.L.
$B-V$	0	0.23	0.16
$B-V$	5	0.25	0.17
$B-V$	10	0.28	0.18
$B-V$	15	0.28	0.20
$B-V$	20	0.34	0.24
$B-V$	25	0.25	0.20
$B-V$	30	0.27	0.22
$B-V$	35	<0.16	
$B-V$	40	0.21	0.20
$V-R$	0	0.36	0.28
$V-R$	5	0.38	0.29
$V-R$	10	0.27	0.22
$V-R$	15	0.36	0.29
$V-R$	20	0.29	0.26
$V-R$	25	<0.27	
$V-R$	30	<0.25	
$V-R$	35	<0.19	
$V-R$	40	<0.20	
$R-I$	0	0.37	0.27
$R-I$	5	0.28	0.22
$R-I$	10	0.22	0.19
$R-I$	15	0.46	0.32
$R-I$	20	0.48	0.36
$R-I$	25	0.22	0.21
$R-I$	30	0.25	0.23
$R-I$	35	<0.25	
$R-I$	40	0.54	0.41
$V-I$	0	0.12	0.12
$V-I$	5	0.22	0.16
$V-I$	10	0.16	0.13
$V-I$	15	0.27	0.20
$V-I$	20	0.32	0.22
$V-I$	25	0.35	0.25
$V-I$	30	0.25	0.19
$V-I$	35	0.19	0.17
$V-I$	40	0.26	0.20
$B-I$	0	0.14	0.11
$B-I$	5	0.18	0.13
$B-I$	10	0.20	0.14
$B-I$	15	0.22	0.16
$B-I$	20	0.32	0.21
$B-I$	25	0.29	0.21
$B-I$	30	0.18	0.14
$B-I$	35	<0.12	
$B-I$	40	0.24	0.18

Appendix A

A.1. Algebraic moments

In what follows we refer to Cowan (1998) and Kendall & Stuart (1958, see Vol. 1, Chap. 10), our aim here is to give uniformity to the notations used. Given n independent observations of a variable, $x_1, x_2, ..., x_n$, the rth moment or algebraic moment is given by:

$$m_r = \frac{1}{n}\sum_{i=1}^{n} x_i^r. \tag{A.1}$$

The expectation value, or mean value, and the variance of m_r are:

$$E[m_r] = \mu_r$$
$$V[m_r] = \frac{1}{n}\left(\mu_{2r} - \mu_r^2\right) \tag{A.2}$$

where μ_{2r} is the $2 \cdot r$th moment. Equations (A.2) are exact formulae as long as one knows μ_{2r} and μ_r. However this is not always the case, and one has to use their estimators m_{2r} and m_r from the sample itself. The variance of the standard deviation can be computed using standard error propagation:

$$V[\sigma] = V\left[\sqrt{m_2}\right] = \frac{V[m_2]}{4m_2} = \frac{m_4 - m_2^2}{4nm_2}. \tag{A.3}$$

In experimental situation each observation x_i is often attached to a certain weight w_i. Supposing that the weight themselves are known without errors, one can define the following formula for the rth weighted moments:

$$m_{w_r} = \frac{\sum_{i=1}^{n} w_i x_i^r}{\sum_{i=1}^{n} w_i}. \tag{A.4}$$

In order to evaluate the variance on the weighted standard deviation we simply extended Eq. (A.3) for the case of weighted moments, obtaining:

$$V[\sigma_w] = V[\sqrt{m_{w_2}}] = \frac{V[m_{w_2}]}{4m_{w_2}} = \frac{m_{w_4} - m_{w_2}^2}{4n_{\rm eff}m_{w_2}} \tag{A.5}$$

where the m_{w_4} and m_{w_2} are the 4th and 2nd weighted moments respectively and $n_{\rm eff} = (\sum_{i=1}^{n} w_i)^2 / \sum_{i=1}^{n} w_i^2$.

A simple Monte Carlo simulation has been run to verify the accuracy of the approximated formula (A.5).

A.2. Correlation coefficient

Given 2 random variables x and y the correlation coefficient is defined as

$$\rho_{xy} = \frac{V_{xy}}{\sigma_x \sigma_y}. \tag{A.6}$$

The unbiased estimator of the covariance V_{xy} is:

$$\widehat{V}_{xy} = \frac{1}{n-1}\sum_{i=1}^{n} (x_i - \overline{x})(y_i - \overline{y}) \tag{A.7}$$

so that the estimator of the correlation coefficient will be:

$$r_{xy} = \frac{\widehat{V}_{xy}}{s_x s_y} = \frac{\sum_{i=1}^{n} (x_i - \overline{x})(y_i - \overline{y})}{\sqrt{\sum_{i=1}^{n} (x_i - \overline{x})^2 \sum_{j=1}^{n} \left(y_j - \overline{y}\right)^2}}. \tag{A.8}$$

For Eq. (A.8) to be a good estimator of the correlation coefficient there are a few caveats to check. First condition is that the samples are randomly defined from the population, that is to make sure that the samples x and y are not selected in some ways that would operate as to increase or decrease the value of r. Even though one has random samples it is possible to compute the errors due to sampling. Commonly this is computed as $(1 - r^2)/\sqrt{n}$. Unfortunately this is just an approximation. Moreover r's for successive samples are not distributed normally unless n is large and the true value ρ is near zero. This yields to a distinction:

- if $n > 30$:
  in order to know whether the value calculated for r is significantly different from zero, one can compute its standard error as:

  $$\sigma_r = 1/\sqrt{n-1}. \tag{A.9}$$

  If r/σ is greater than 2.58, one can conclude that the universe value of r is likely to be greater than zero.
- if $n < 30$:
  the variable

  $$t = r\frac{\sqrt{n-2}}{\sqrt{1-r^2}} \tag{A.10}$$

  follows the t-distribution with $d.o.f. = n - 2$. This can be used only for testing the hypothesis of zero correlation.

R. A. Fisher developed a technique to overcome these difficulties. The variable r is transformed into another variable that is normally distributed. This is especially useful for high value of r, when none of the above test can be safely applied. The transformation to the variable z:

$$z = \frac{1}{2}\ln(1+r) - \frac{1}{2}\ln(1-r) \tag{A.11}$$

allows some important semplifications. The distribution of z's for successive samples does not depend on the universe value ρ and the distribution of z for successive samples is so near to normal that it can be treated as such without any loss of accuracy, see for example (Vol. 1, Chap. 16 and Vol. 2, Chap. 26) of Kendall & Stuart (1958). Moreover the standard error for z is independent on its σ:

$$\sigma_z = 1/\sqrt{n-3}. \tag{A.12}$$

The way to proceed is then very simple:

- Compute r according to (A.8);
- Transform r into z according to (A.11);
- Compute σ_z according to (A.12);
- In order to state a 1 sigma confidence limit for r, transform the 2 values $z \pm \sigma_z$ back to r, using the inverse of (A.11).

References

Aguirre, A. 1999, ApJ, 512, L19
Aguirre, A. 1999, ApJ, 525, 583
Aguirre, A., & Haiman, Z. 2000, ApJ, 532, 28
Aldering, G., et al. 2002, Supernova Factory Webpage, `http://snfactory.lbl.gov`
Branch, D., Fisher, A., & Nugent, P. 1993, AJ, 106, 2383
Cardelli, J. A., Clayton, G. C., & Mathis, J. S. 1989, ApJ, 345, 245
Cowan, G. 1998, Statistical data analysis (Oxford University Press)
Cramer, H. 1957, Mathematical methods of statistics (Princeton University Press, Seventh Printing)
Goldhaber, G., Groom, D. E., Kim, A., et al. 2001, ApJ, 558, 359
Goobar, A., Mörtsell, E., Amanullah, R., et al. 2002, A&A, 392, 757
Hamuy, M., Phillips, M. M., Suntzeff, N. B., et al. 1996, AJ, 112, 2408
Kendall, M. G., & Stuart, A. 1958, The advanced theory of statistics (London: Charles Griffin & Company Limited)
Krisciunas, K., Hastings, N. C., Loomis, K., et al. 2000, ApJ, 539, 658
Lira, P. 1995, Master Thesis, Univ. Chile
Mörtsell, E., Bergström, L., & Goobar, A. 2002, Phys. Rev. D, 66, 047702
Nobili, S., et al. 2003, in prep.
Nugent, P., Kim, A., & Perlmutter, S. 2002, PASP, 114, 803
O'Donnell, J. E. 1994, ApJ, 422, 158O
Perlmutter, S., Gabi, S., Goldhaber, G., et al. 1997, ApJ, 483, 565P
Perlmutter, S., Aldering, G., Goldhaber, G., et al. 1999, ApJ, 517, 565P
Phillips, M. M. 1993, ApJ, 413, L105
Phillips, M. M., Lira, P., Suntzeff, N. B., et al. 1999, ApJ, 118, 1766
Riess, A. G., Press, W. H., & Kirshner, R. P. 1996, ApJ, 473, 588R
Riess, A. G., Filippenko, A. V., Challis, P., et al. 1998, AJ, 116, 1009
Riess, A. G., Kirshner, R. P., Schmidt, B. P., et al. 1999, ApJ, 117, 707-724
Riess, A. G., Filippenko, A. V., Liu, M. C., et al. 2000, ApJ, 536, 62

Paper C

Astronomy & Astrophysics manuscript no. March 3, 2004
(DOI: will be inserted by hand later)

Search for spectral evolution in high-redshift Type Ia supernovae: evidence for SN 199 1T/SN 1999aa-like object at z=0.279

G. Garavini, G. Folatelli, A. Goobar, C. Lidman, S. Nobili, and the Supernova Cosmology Project Collaboration

Department of Physics, Stockholm University,
SCFAB, S–106 91 Stockholm, Sweden

Abstract. Spectroscopic data of 12 high-redshift supernovae ($0.279 < z < 0.912$) are analysed. A quantitative comparison between low and high-redshift SNe by means of spectral indicators is presented. Measurements of Ca II H&K expansion velocity and equivalent width-like measurements for the features we label "Fe II 4800", "Mg II 4300" and "Ca II H&K" are found statistically consistent with spectra of nearby supernovae. We find no indication that high redshift supernova spectra resemble those of sub-luminous, fast-decliner, supernovae found in the local sample. Furthermore, based on qualitative and quantitative classification SN 2002fd (z=0.279) showed spectral characteristics similar to a SN 1991T/SN 1999aa-like object.

1. Introduction

Precision estimations of cosmological parameters using high-redshift type Ia supernovae (SNe Ia) as distance indicators require good understanding of their brightness homogeneity and the reliability of the shape-brightness corrections derived from the local sample.

The spectral energy distribution is the most direct way to investigate the physics of supernova explosions and thus, to search for possible intrinsic differences between local and distant SNe used in cosmology. Possible signs of evolution in spectra of high-redshift SNe, such as those due to a drift toward low metallicity progenitors, have been modeled, e.g. by Hoeflich et al. (1998) and Lentz et al. (2000). These studies found that, because of the plausible lower progenitor metallicity, high-redshift supernovae are expected to show enhanced UV flux. Furthermore, the effect of lower metallicity in optical spectral features would be twofold: (a) the minima of the spectral lines tend to shift to longer wavelengths and (b) the depth of the absorption features decrease.

With the rapidly increasing number of local supernovae observed, a wide range of spectral diversities is being found (see e.g Branch (2003)). The physical origin of such diversities is still under investigation, thus, statistical studies are useful to probe possible inconsistencies between high and low redshift SN data sets. For example, comparisons of light curve parameters have been carried out, but as of yet, without conclusive results (Riess et al. 1999; Aldering et al. 2000). Possible systematic differences in the brightness of SNe Ia have been found in the local sample depending on host galaxy type: slow-decliner supernovae have been claimed to be more common among young progenitor systems and fast-decliners in old progenitors systems (Hamuy et al. 1995, 1996, 2000; Howell 2001). However, this trend could not be confirmed by Sullivan et al. (2003) in a study of 39 distant SNe in a redshift range of $0.3 < z < 0.8$, possibly due to the limited span of light curve widths in their SN sample.

Local supernovae are usually classified in three sub-groups according to their spectral appearance around B-band maximum light. Normal supernovae, represented by objects such SN 1981B (Branch et al. 1983), SN 1989B (Barbon et al. 1990), SN 1992A (Kirshner et al. 1993), and SN 1972E (Kirshner et al. 1973), show strong absorption features due to intermediate mass elements (IMEs, i.e. Si, S, Ca and Mg). Peculiar SN 1991bg-like supernovae (Filippenko et al. 1992a; Leibundgut et al. 1993; Turatto et al. 1996; Mazzali et al. 1997), are characterized by enhanced Si II lines and strong Ti II absorption features. Peculiar SN 1991T-like supernovae (Filippenko et al. 1992b; Phillips et al. 1992; Ruiz-Lapuente et al. 1992; Jeffery et al. 1992; Mazzali et al. 1995), have very weak IMEs – virtually absent in pre-maximum spectra – yet strong doubly ionized iron absorption features. Recently, supernovae with spectral characteristics in between those of normal and SN 1991T-like have been identified. These show weak Si II lines, yet a evident Ca II H&K absorption, and they are sometimes called SN 1999aa-like supernovae (Li et al. 2001b; Garavini 2004b). In general, objects resembling these two prototypes are, however, classified as SN 1991T/SN 1999aa-like supernovae.

So far, very few distant SN Ia spectra have been compared with local data sets, e.g. (Perlmutter et al. 1998; Coil et al. 2000; Barris et al. 2003; Riess et al. 2003; Blakeslee et al. 2003). Moreover, none of the spectroscopically confirmed high-redshift SNe has been reported as peculiar. The observed peculiarity rate mismatch between low and high-redshift data sets could be due to the limited statistical significance of the

Send offprint requests to: G. Garavini , gabri@physto.se

distant supernova sample, but should be taken under consideration as a possible sign of evolution (Li et al. 2001b,a).

During the 2000, 2001 and 2002 discovery campaigns, the Supernova Cosmology Project (SCP) carried out dedicated spectroscopy observations of 20 high-z SN Ia at the Very Large Telescope (Lidman 2004). In this work we analyze the 14 best signal-to-noise supernova spectra of these campaigns with the aim to pursue a quantitative test for supernova evolution.

We perform expansion velocity measurements as inferred from the blue-shift of Ca II H&K and "equivalent width-like" (EW) measurements of the absorption features we label "Fe II 4800", "Mg II 4300" and "Ca II H&K". In Folatelli (2004) EW measurements were shown to be useful spectral indicators to investigate supernova homogeneity. Furthermore, this newly introduced spectral indicators seem to correlate with the intrinsic brightness of local SN Ia. In this study we compare the EWs and the measured expansion velocities with those of a vast sample of published local supernova data. Additionally, a schematic approach for supernova type classification at $z \sim 0.5$ is presented. As the result of the analysis the spectral classification of the first peculiar SN 1991T/SN 1999aa-like supernova at redshift z=0.279 is also reported.

2. Data-set

The data set presented here consists of 12 high-redshift (z=0.279-0.912) supernovae for a total of 14 spectra observed by the SCP collaboration with the Very Large Telescope (VLT) during the supernova search campaigns carried out during 2000, 2001 and 2002. Further details about the VLT confirmation observations are reported in (Lidman 2004). Details of the supernova spectra are presented in table 1 where the (wavelength-averaged) signal to noise ratio per resolution element for each supernova spectrum is reported. The data is shown in Figs. 1 – 3 where light gray spectra are the original observed spectrum rebinned to 10 Å per pixel resolution and the black spectra have been smoothed using a inverse variance weighted Gaussian filter (Lombardi & Schneider 2002) with σ=20 Å.

All data were reduced using IRAF procedures. Special care was taken in the determination of the statistical error spectrum. This is calculated on regions that are near to the supernova spectrum on the sky subtracted two dimensional image and scaled to the area in the trace of the supernova.

High-redshift supernova spectra are likely to suffer from host galaxy contamination. The host galaxy is usually spatially unresolved making it difficult to estimate its contribution to the observed flux. The host galaxy contamination in our data was estimated using a statistical comparison with a large data set of nearby supernovae templates and galaxy models (Sainton 2004). The χ^2 minimization procedure is based on eq. (1) where S_i^{Obs}, S_i^{Gal} and S_i^{SN} are the observed flux, the galaxy model flux and the supernova template flux in the i-th bin, respectively:

$$\chi^2(z,q,N) = \sum_{i=0}^{N_{bin}-1} \sigma_i^{-2}\{S_i^{Obs}(\lambda_{Obs}) - \\ -N(qS_i^{Gal}(\lambda_{Rest}(1+z)) + (1-q)S_i^{SN}(\lambda_{Rest}(1+z))\}^2, \quad (1)$$

where the quantity $S^{Gal} + S^{SN}$ is normalized thus, q is the galaxy relative contribution to the observed spectrum. The fit parameter N is a global scale factor, σ_i the observed flux standard deviation in each bin and z the redshift. The estimated values for q from the fitting procedure are tabulated in column 10 of table 1. The epoch with respect to the $B-$band light curve maximum – reported in table 1 – was estimated using both preliminary light curve results and spectroscopic dating by means of statistical comparison with low-z SNe (Lidman 2004). The two methods usually agreed within two days. This value is assumed to be the uncertainty on the quoted epoch whenever an accurate light curve estimate of the maximum was not available. The redshift of the supernova, when quoted with 3 digits, was estimated from host galaxy lines in the spectrum. When this was not possible, the redshift was estimated from the supernova spectral features, and is then quoted with 2 digits.

3. High-redshift supernova identification

At redshifts above 0.5, the observation of the characteristic Si II feature at 6150 Å is beyond the wavelength instrumental range. Therefore, the classification of the supernova type has to rely on the spectral features on the blue side of the spectrum. Nugent et al. (2001); Hook (2004) showed that four different wavelength regions can be used to distinguish between photospheric SN Ia and core-collapse supernovae in this redshift range. Furthermore, the same regions can be used to identify possible spectral peculiarities among Ia's as those found in SN 1991T/SN 1999aa-like or SN 1986G/SN 1991bg-like supernova. In Table 2 the characteristics of these four wavelength regions for different types and sub-groups of supernovae are schematically reported. Each spectral feature is qualitatively described as *strong*, *weak* or *absent* based on the absorption strength and *broad* or *narrow* based on the wavelength span. In the absence of identification procedures based on quantitative measurements, this scheme helps in constraining the classification.

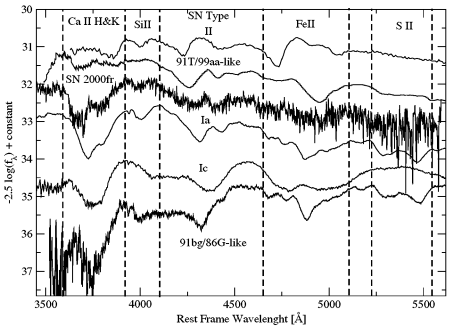

Fig. 4 SN 2000fr at day -6 compared with normal and peculiar Type Ia SNe, Type II and Type Ic SNe. The wavelength region highlighted in Table 2, are marked with dashed lines and labeled with region name. The SN type of the spectrum is also indicated.

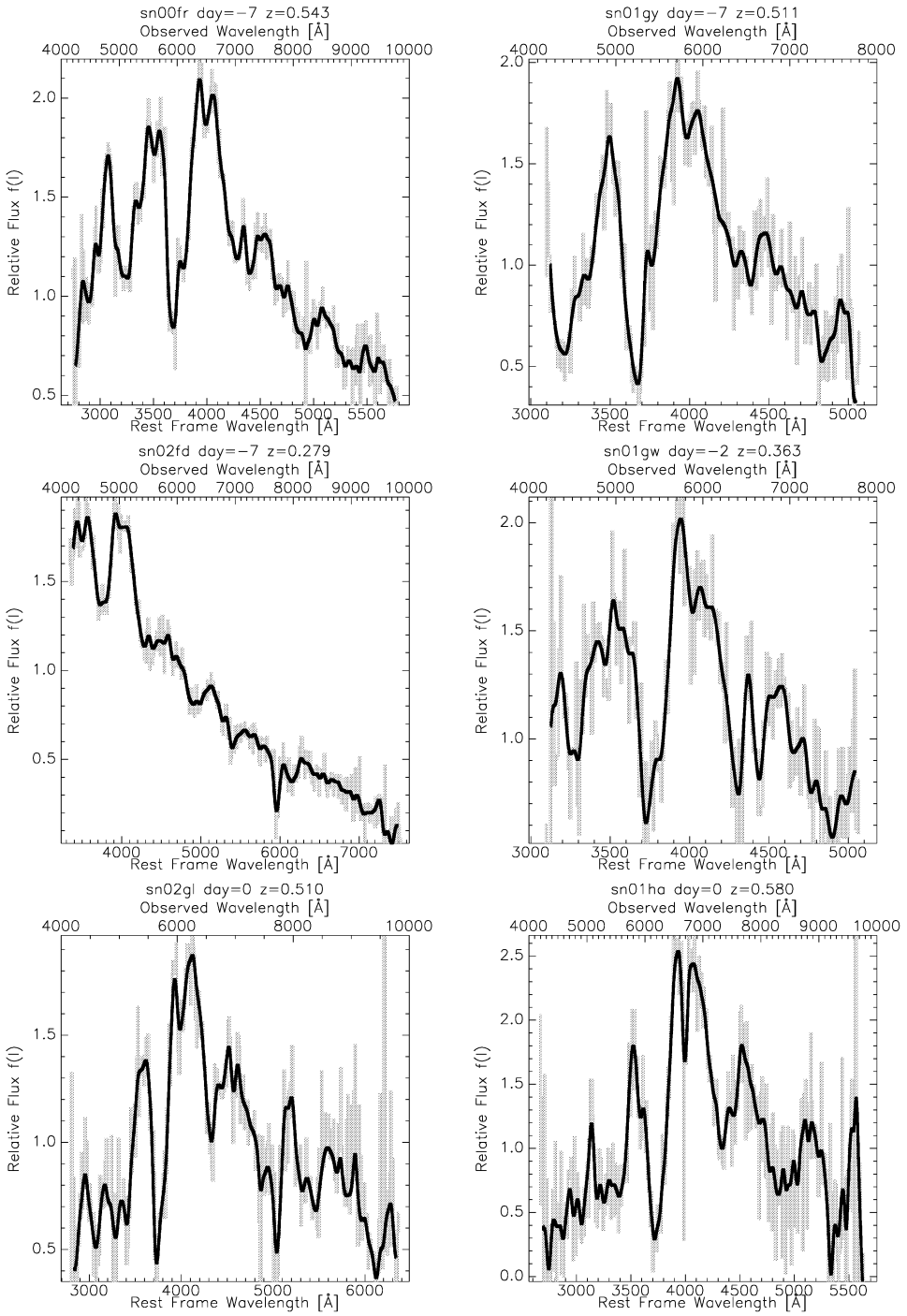

Fig. 1 Spectroscopy data set. In each plot the light gray spectrum is the origanal observed spectrum rebinned to 10 Å per pixel resulution. The black spectrum have been smoothed using a inverse variance weighted Gaussian filter with σ=20 Å. Specifications are reported in table 1

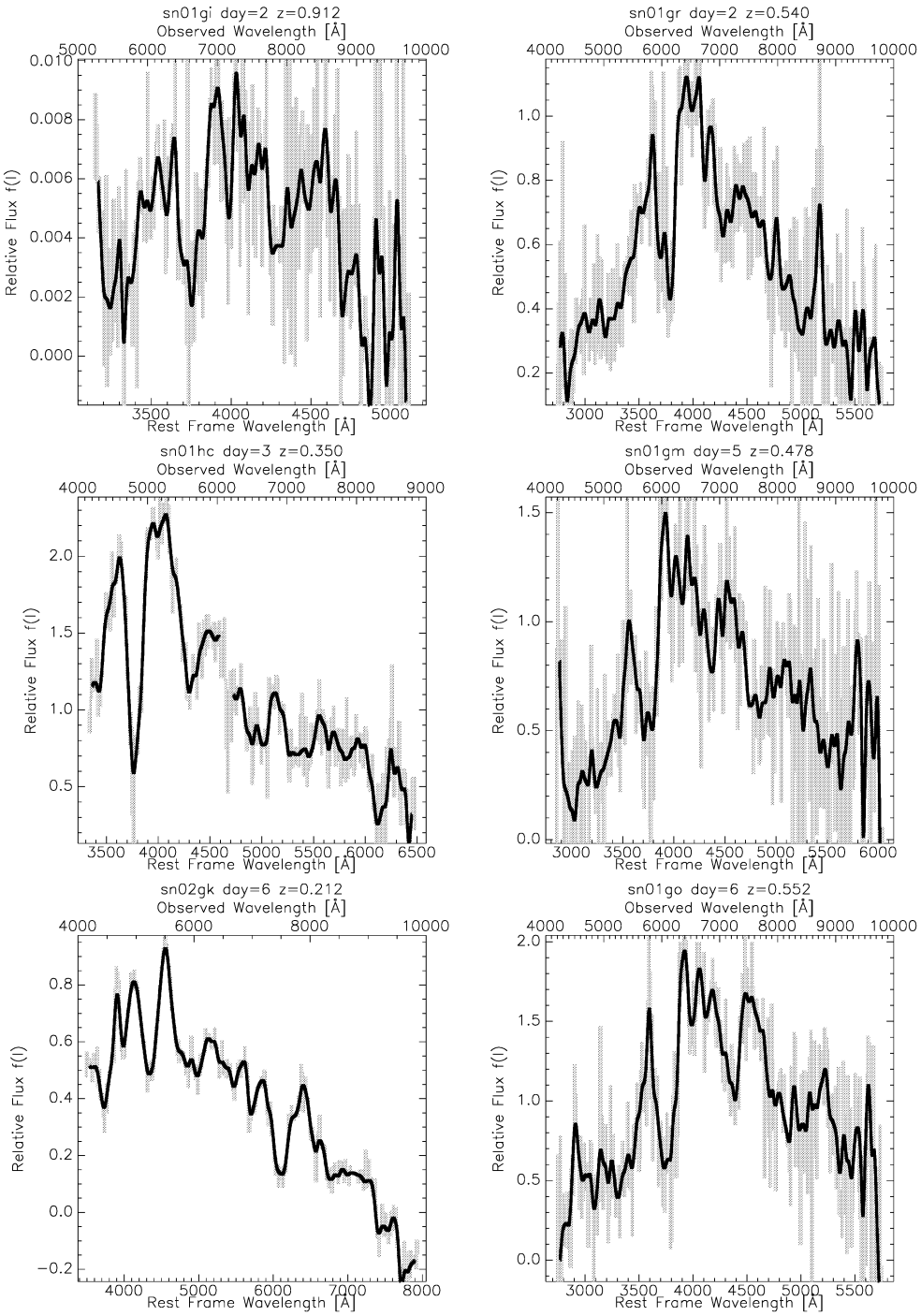

Fig. 2 Spectroscopy data set. In each plot the light gray spectrum is the origanal observed spectrum rebinned to 10 Å per pixel resolution. The black spectrum have been smoothed using a inverse variance weighted Gaussian filter with σ=20 Å. Specifications are reported in table 1

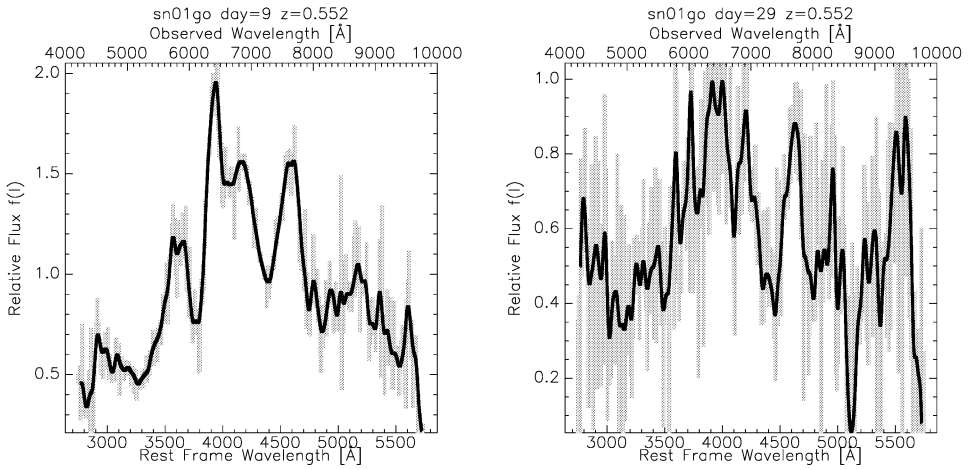

Fig. 3 Spectroscopy data set. In each plot the light gray spectrum is the origanal observed spectrum rebinned to 10 Å per pixel resolution. The black spectrum have been smoothed using a inverse variance weighted Gaussian filter with σ=20 Å. Specifications are reported in table 1

Table 1 Summary of spectroscopy data set. For each SN in our data set, redshift, reduced Julian date of observation, epoch since estimated B-band maximum light, telescope and instrument setting used for the observation, exposure time, signal to noise, total flux percentage of galaxy contamination and identification are given. See text for details

SN-name	Red-shift[a]	Date (MJD)	Days from[b] B-band Maximum	Instrument	setup	telescope	Exposure time (s)	S/N	Galaxy[c] %	ID
SN 2000fr	0.543	51676.2	-5.5(2)	FORS1	300V grism + GG435	VLT-UT1	7200	10	16	Ia
SN 2001go	0.552	52021.3	5.6(1)	FORS1	300V grism + GG435	VLT-UT1	2400	3	13	Ia
SN 2001go	0.552	52027.1	9.5(1)	FORS1	300V grism + GG435	VLT-UT1	7200	6	19	Ia
SN 2001go	0.552	52058.1	29.5(1)	FORS1	300V grism + GG435	VLT-UT1	9000	2	53	Ia
SN 2001gr	0.540	52021.0	2(2)	FORS1	300V grism + GG435	VLT-UT1	3600	3	57	Ia
SN 2001gw	0.363	52021.4	-1(2)	FORS1	300V grism + GG435	VLT-UT1	1200	3	19	Ia
SN 2001gy	0.511	52021.3	-7,5(1)	FORS1	300V grism + GG435	VLT-UT1	2400	4	20	Ia
SN 2001ha	0.58	52022.0	0(2)	FORS1	300V grism + GG435	VLT-UT1	3600	3	6	Ia
SN 2001hc	0.35	52022.1	0(2)	FORS1	300V grism + GG435	VLT-UT1	1800	7	14	Ia
SN 2001gm	0.478	52021.3	5(2)	FORS1	300V grism + GG435	VLT-UT1	2400	2	28	Ia
SN 2002gi	0.912	52407.2	2(2)	FORS1	300I grism + GG435	VLT-UT3	7200	2	37	Ia
SN 2002gk	0.212	52413.3	6(2)	FORS2	300I grism + GG435	VLT-UT4	900	10	66	Ia
SN 2002gl	0.510	52413.1	-5(2)	FORS2	300V grism + GG435	VLT-UT4	3000	5	23	Ia
SN 2002fd	0.279	52376.1	-7(2)	FORS2	300V grism + GG435	VLT-UT4	600	29	28	**Iapec**

[a]Determined from host galaxy lines if 3-digits

[b]Uncertainties quoted in parenthesis

[c]Estimated in percentage on the total observed flux by statistical methods – see text

Table 2 Summary spectroscopic fingerprints with relevance for different SN types at $z \geq 0.5$. Four wavelength regions are selected for performing the SN type identification. Each spectral feature, in these regions, is qualitatively described as *strong*, *weak* or *absent* based on the absorption strength and *broad* or *narrow* based on the wavelength span.

Region Id	λ-Region Rest Frame[Å]	Normal Type Ia	Type Ib/c	Type II	91T/99aa-like	91bg/86G-like	comments
'Ca II H&K'	3700-3900	strong/broad	evident/broad[d]	absent	weak or absent/broad[a,b]	strong/broad	[h]
'Si II'	3900-4100	evident/narrow[b]	absent	absent	weak[a,b]	absent	[e]
'Fe II'	4500-5100	strong/broad	strong/broad	absent	strong/narrow[a]	strong/broad	[f,g]
'S II W'	5000-5500	strong/narrow[a,b]	absent/narrow	absent	weak or absent[a]	strong/narrow[a,b]	

[a]Before max.

[b]Around max.

[d]Few peculiar exceptions.

[e]In 91bg/86G-like beginning of the distinctive strong Ti II absorption.

[f]In Normal Ia typical line profile time evolution.

[g]In 91T/99aa-like dominated by Fe III in pre-max.

[h]Splitted minimum in some Ia.

The application of this scheme is shown for two different epochs (one weak prior to maximum and one weak after maximum light in the supernova restframe) for SN 2000fr and SN 2001go. Fig. 4 shows the comparison of the spectrum of SN 2000fr at day -6 with the spectra of the normal and peculiar type Ia supernovae, as well as type II and type Ic supernovae. The wavelength ranges reported in Table 2, are marked in Fig. 4 with dashed vertical lines to select the spectral region in which perform the classification. In the 'Ca H&K' region a strong absorption is clearly visible in SN 2000fr as in type Ia and Ic supernovae, together with the split of the minimum of Ca H&K sometimes seen in SN Ia. A weak absorption is also visible in the 'Si II' region characteristic of type Ia SNe. The signal to noise ratio of our spectrum of SN 2000fr decreases in the 'Fe II' region where a broad absorption is present with no distinctive minima as in normal Ia's and Ic's. On the red end of the spectrum of SN 2000fr ('S II' region) the noise increases and the distinction of lines is uncertain. These characteristics are consistent with those generally found in normal type Ia supernovae.

The comparison for the highest S/N spectrum of SN 2001go is shown in Fig 5. At this epoch (8 days after B band maximum light), normal supernovae have a broad absorption feature between 3700 and 3900 Å ('CaH&K' region. This is seen in our spectrum of SN 2001go. In the 'Si II' region SN 2001go shows a weak absorption feature as normal Ia's and SN 1991T/SN 1999aa-like objects. The broad absorption feature in the 'Fe II' region of our spectrum resembles those of normal and peculiar type Ia's with a multiple minima. In the 'S II' region SN 2001go shows the typical 'W' shaped strong absorption features characteristics of normal or SN 1991bg/SN 1986G-like objects. The presence of Si II and S II features and the strength and width of Ca H&K in this object are typical of normal type Ia supernovae.

Based on this classification scheme and on the statistical comparison with a large data set of local supernovae, all but one of our high-z spectra were classified as "normal" type Ia

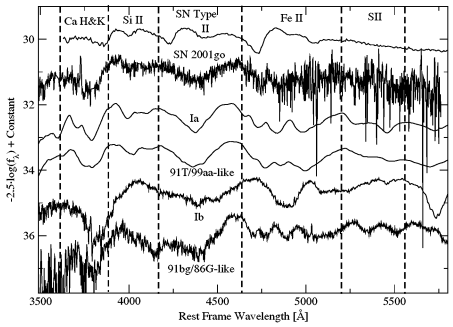

Fig. 5 SN 2001go at day +8 compared with normal and peculiar Type Ia SNe, Type II and Type Ic SNe. The wavelength region highlighted in Table 2 are marked with dashed lines and labeled with region name. The SN type of the spectrum is also indicated.

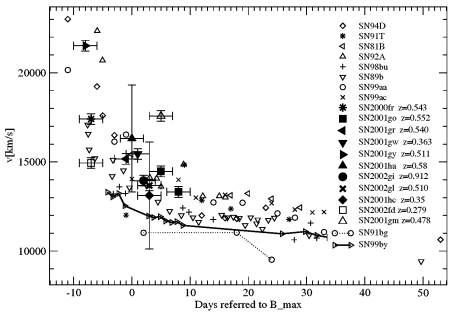

Fig. 6 Ca H&K expansion velocities of high-redshift supernovae presented in section 2 compared with local SNe. The solid and dotted lines indicate the values of extreme under-luminous SNe SN 1999by (Garnavich et al. 2001) and SN 1991bg (Leibundgut et al. 1993) respectively.

supernova. The only object (SN 2002fd) not classified as normal SN Ia will be discussed in section 5.1

4. Spectral Indicators

Next, we compare measurements of supernova spectral indicators of our high-redshift data set with those of a broad sample of local supernovae in order to probe for possible differences between the low and high-redshift populations.

4.1. Velocities

The faintness of distant supernovae discovered in the recent years has been attributed to large distances, as expected in the presence of a cosmological constant. In principle though, the faintness could be due to intrinsically dimmer SNe. Under-luminous SNe generally show lower and more rapidly decreasing expansion velocities compared to normal SNe, see for example Leibundgut et al. (1993); Wells et al. (1994); Patat et al. (1996); Garnavich et al. (2001); Li et al. (2003). The differences are more pronounced in the case of the Si IIλ6355 absorption line were differences of more than 2000 km s^{-1} are seen, Branch & van den Bergh (1993). The separation is less conspicuous for the Ca II H&K absorption – measurable in the redshift range of our data set – but the trend remains; see for example SN 1999by and SN 1991bg in Fig. 6 where the time evolution of the expansion velocity as inferred from the Doppler shift of the minimum of the Ca II H&K is shown.

Assuming that intrinsically low-luminosity high-z SNe were alike local fast decliners, the expansion velocities on the lower edge of the distribution shown in Fig. 6, would suggest a possible under-luminous SN. The measurements have been obtained performing an error weighted non-linear fit to a Gaussian model considering the whole line profile for performing the fit. The typical uncertainties on the redshift value (usually estimated by using the galaxy lines) is taken to be 300 km/s. In the cases of SN 2001ha and SN 2001hc we could not identify galaxy lines in the SN spectrum and thus, the redshift was estimated by comparing with other supernovae spectra. In these cases the uncertainty is taken to be 3000 km/s. This value dominates with respect to the measurement errors, which are added in quadrature to compute the total reported uncertainties. The velocities of Ca II H&K for normal supernovae show a pre-maximum light rapid drop from values around 22000 km/s to 14000 km/s. After maximum light the slope changes and the velocity decreases by about 4000 km/s in 50 days. The solid and dotted lines plotted in Fig. 6 show typical trends of extreme under-luminous supernovae (in this case SN 1999by (Garnavich et al. 2001) and SN 1991bg (Leibundgut et al. 1993) respectively).

All our high-redshift supernovae show velocities higher than what is indicated by the solid line, thus we note that the high-redshift SNe are consistent with spectroscopically normal SNe. Li et al. (2001b), estimated that 16% of all supernovae discovered in the local universe are under-luminous. However, for magnitude-limited high-redshift supernova searches – as those carried out by the SCP – the peculiarity rate for SN 1991bg-like SNe is expected to be less than 2% Li et al. (2001b). Thus, the lack of observed peculiar under-luminous high-redshift SNe is within expectations.

4.2. Equivalent Widths

Equivalent width (EW) time evolution measurements have been empirically shown to be spectral indicators of SN Ia intrinsic brightness (Folatelli 2004). Next, EW of high-redshift SNe are compared with those of local supernovae in search of possible evidence of evolution. The spectra of the high-redshift supernovae cover generally features 1 to 5 in the definition of Folatelli (2004). These are the features labeled "Ca II H&K", "Si II 4000", "Mg II 4300", "Fe II 4800", and "S II W" respectively. However, because of the moderate signal to noise ratio of our spectra, we focused only on three strong absorption features: "Mg II 4300", "Fe II 4800" and "Ca II H&K". Figures 7, 8 and 9 show the measurements on our high-redshift SNe com-

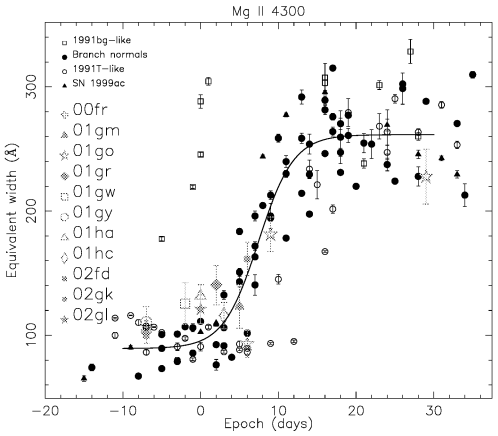

Fig. 7 'Mg II 4300' EW measurements of high-redshift supernovae presented in section 2 compared with local SNe. The solid line indicates the empirical model for normal supernovae as described in Folatelli (2004).

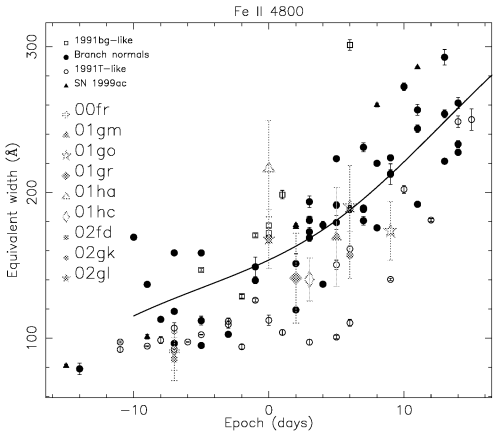

Fig. 8 'Fe II 4800' EW measurements of high-redshift supernovae presented in section 2 compared with local SNe. The solid line indicates the empirical model for normal supernovae as described in Folatelli (2004).

pared to those at low redshift. Note, that the higher redshift spectra have larger measurement errors in EW due to both the lower signal-to-noise and the possible residual host galaxy contamination left after the host subtraction. We assumed the latter to be about 10%, and estimated the corresponding uncertainty in the EW as in Folatelli (2004).

The EW time evolution of "Mg II 4300" shows a break at around one week after maximum for most of the SNe. This is related to blending with "Si II 4000" in coincidence with absorption deepening which makes the values of EW suddenly increase from ~100Å to ~250Å on time scales of less than a week. The actual phase at which this break takes place depends on the object characteristics: for under-luminous SNe Ia it seems to occur as early as 5 days before maximum light, while normal SNe Ia show this behavior around one week after maximum light, and SN 1991T/SN 1999aa-like objects show it later than day +10. Thus, the "Mg II 4300" results to be useful to discriminate among the different type Ia sub-classes. The solid line in Fig. 7 shows the step like function describing the average behaviour of Branch normal supernovae derived in (Folatelli 2004). The EW values for our high-redshift supernovae (all SNe in table 1 were measured but SN 2001gi) are consistent with corresponding local supernova values within their intrinsic spread. Moreover, SN 2001go, for which the measurements of three epochs are available, shows the typical break at around one week after maximum as most of the local SNe. Note, that some of the values prior to maximum appear to be slightly higher than those of local SNe, although the deviation is not statistically significant, as shown in the next section.

"Fe II 4800" EWs have a very smooth and homogeneous time evolution for all kind of type Ia SNe (see Fig. 8). EW values increase from around 100Å before maximum light to 350Å two weeks after. A mean evolutionary curve for the normal SNe can be represented by a cubic spline function (Folatelli 2004). The solid line in Fig. 8 shows this average curve. All SNe in table 1 but SN 2001gu, SN 2001gw, SN 2001gy and SN 2001gi were measured (for which the line was not easely identifiable) and found well within the intrinsic spread of local supernovae.

Fig. 9 shows the time evolution of "Ca II H&K" EW. The behavior is less homogeneous than for the other two features analyzed, especially before maximum light. The overall intrinsic spread of EW values is the largest among the features analyzed here. However, before maximum light, peculiar SN 1991T-like objects show systematically low values. The current set of high-redshift supernovae do not show significant deviations with respect to the local sample in the plot.

A statistical comparison betweenEW of high-z (all SNe in Table 1 were measured but SN 2001gi) and low-z supernova is carried out in section 5.

5. Evolution: High-z vs Low-z

In this section, a quantitative analysis of the high-redshift SNe is performed using the spectral indicators described in section 4.2. Folatelli (2004) identified empirical models to describe the time evolution of EW for 'Fe II 4800' and 'Mg II 4300' features in normal – low redshift – supernovae. These models can be used to test if high-redshift supernovae EW's follow the same evolution trends as local SNe. The results of a χ^2 test is shown in Table 3. The empirical models derived from local supernovae and high-redshift SNe data are plotted in Figs. 7 and 8. The intrinsic dispersion around the models for normal low-z supernovae – as quoted in Folatelli (2004) – was added in quadrature to the statistic and systematic (i.e. due to the host galaxy subtraction residuals) uncertainties to perform the test. The first two columns of Table 3 refer to the comparison with

Table 3 Result of the χ^2 test comparing EW measurements of high-redshift SNe with the models described is section 4 for 'Fe II 4800' and 'Mg II 4300' (column 2,3) and with values of under-luminous SNe (column 4,5)

Feature	χ^2/dof	P_{norm}	χ^2/dof	P_{faint}
Fe II	9.5/11	0.58	26.3/11	0.006
Mg II	18.1/13	0.15	386.5/13	0.00[1]

[1]Formally, this probability is $< 10^{-74}$. However, this assumes ideal conditions.

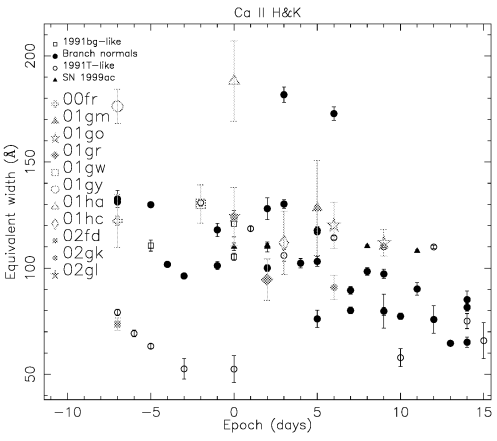

Fig. 9 'Ca II H&K' EW measurements of high-redshift supernovae presented in section 2 compared with local SNe.

the 'Fe II 4800' and 'Mg II 4300' EW models for normal supernovae. The last two columns refer instead to the comparison with under-luminous SNe (e.g. SN 1986G (Phillips et al. 1987) and SN 1991bg). The hypothesis that our high-redshift supernovae are well described by the same model as for local normal supernovae is statistically more significant that them being consistent with under-luminous SNe. Note however, that the statistical significance of our SNe being as local normal SNe is lower for 'Mg II 4300' than for 'Fe II 4800' because of the slightly higher than average EW values measured prior to maximum light.

Lentz et al. (2000) claim that the strength of supernova absorption lines should be affected by the drift toward lower metallicity progenitor expected at high-redshift. However, measuring the intrinsic spread of EWs of the absorption features of their models relative to those of the one solar metallicity synthetic spectrum, we found values lower than what is measured on the local supernovae. Thus, the range in which EW vary – studied in Folatelli (2004) – is dominated by other effects than their prediction from metallicity variations. The possible change of restframe U-B color in high-redshift SNe is probably a more sensitive parameter to investigate the effects of varying metallicity.

5.1. SN 2002fd: SN 1999aa-like Supernova

SN 2002fd is the only supernova in our data set that clearly deviates from the "normal" classification of Ia's (see table 2). According to our scheme SN 2002fd appears to be a SN 1991T/SN 1999aa-like supernova. The spectrum of SN 2002fd – the spectrum with highest signal to noise ration in our dataset – is shown in Fig. 10 compared with other well known peculiar and normal objects. The redshift of SN 2002fd

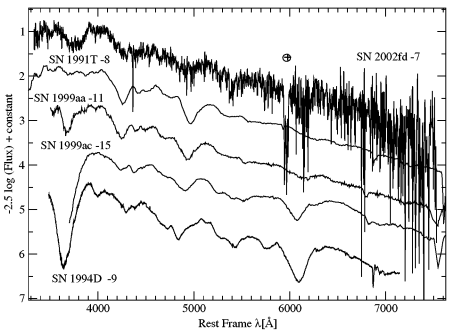

Fig. 10 SN 2002fd at day -7 compared with normal and peculiar SNe.

(z=0.279) is the lowest among the SNe in our sample. This supernova shows 'Ca II H&K' weaker than in normal but stronger than in SN 1991T. The 'Fe II' region appears similar to that of SN 1999ac (Garavini 2004a) and similarly does the 'S II W' region. Given the low redshift, Si II λ 6355 is also visible, – next to the marked telluric absorption – and appears stronger than in SN 1999aa but weaker than in SN 1999ac and normal SNe. Already from this qualitative analysis of the spectrum it is clear that SN 2002fd can be classified as a peculiar SN 1991T/SN 1999aa-like object with characteristics in between those of extreme cases (e.g. SN 1991T) and normal SNe (e.g. SN 1994D), close to SN 1999aa. The increasing rate of supernova discoveries in the local universe is showing that these two classes of objects are probably not separated but form a 'continuum'. The discovery of SNe with similar spectral characteristics at the redshift of SN 2002fd gives confidence that supernova populations at low and intermediate z do not differ.

By means of EW measurements we can make statistical tests of our qualitative classification of SN 2002fd. Prior to maximum light, EW measurements of CaH&K shown in Fig.

9, are useful to separate peculiar SN 1991T/SN 1999aa-like SN Ia from normals. If the identification of SN 2002fd as a peculiar object is correct, we expect the EW value to be lower than that average of normal SNe. The average EW prior to lightcurve maximum in normal SNe is <EW> = 114.06. The measured scatter around that mean is $\sigma_{<EW>}$= 14.16. For peculiar SN 1991T/SN 1999aa-like SNe we find <EW> = 68.69 and $\sigma_{<EW>}$ 6.08. The value measured for SN 2002fd (EW = 73.60 ± 2.90) is consistent (within one standard deviation) with what was found for peculiar objects.

SN 1991T/SN 1999aa-like supernovae appear to make up 20% of all supernovae observed at low-z (Li et al. 2001b). This high peculiarity rate, though, could be the result of our difficulty in classifying spectroscopically peculiar SN 1999aa-like (Branch 2001). Nevertheless, we should expect to find some of such SNe at high-redshift. Li et al. (2001b) used a Monte-Carlo simulation to estimate that in a magnitude-limited high redshift supernova searches, and considering an extra extinction of 0.4 mag, between 18.6% and 6% (for an age bias of +7 and −1 days respectively) SN 1991T/SN 1999aa-like SNe should be found. The expected number could be biased by the strengthening evidence that spectroscopically SN 1991T/SN 1999aa-like SNe do no always come with broad light curves and vice-versa, see for example SN 1999ee, SN 2002cx or SN 1999aw. SN 2002fd represents the first example of a SN 1991T/SN 1999aa-like supernova in the Hubble flow and thus, shows that these objects can indeed be found also at high-redshifts. Further studies are required to address the issue of whether the peculiarity rate of high-redshift SNe is consistent with what found in the local SNe or rather should be regarded as a sign of evolution.

6. Summary and Conclusions

Spectroscopic data of 12 high-redshift supernovae, in the redshift range z=0.279 to 0.912 are analized along with a qualitative classification scheme to be used for high-redshift supernovae. The first quantitative comparison between low and high-redshift SN Ia by means of spectral indicators is presented. The measurements of the expansion velocities as inferred from the minimum of Ca II H&K for the high-redshift supernovae are compared with those of local SNe with the aim to point out possible evolution effects. No signs of evolution with redshift were found in the spectral characteristics. Equivalent widths values and time evolution for the features we label "Fe II 4800", "Mg II 4300" and "Ca II H&K" are also found within the intrinsic distribution of nearby supernovae. Furthermore, by means of a χ^2 test, high-redshift SNe data are found statistically consistent with the empirical models describing the time evolution of "Fe II 4800", "Mg II 4300" EW's (Folatelli 2004) for local normal SNe.

Based on our classification scheme all our SNe, but one, were classified as normal type Ia. SN 2002fd (z=0.279) showed weaker Ca II H&K, Si II λ4000, S II 'W' and Si II λ6355 consistently with what observed in SN 1991T/SN1999aa-like objects in the local universe. This classification was confirmed by means of the EW measurements. Prior to maximum light, Ca II H&K equivalent widths show a clear distinction between the values typically found for normal and SN 1991T/SN1999aa-like SNe. The value measured for SN 2002fd (EW = 73.60 ± 1.89) results consistent with that of SN 1991T/SN 1999aa-like object (< EW > = 68.69, $\sigma_{<EW>}$ 6.08).

Supernova EWs intrinsic spread of optical absorption lines is found to be larger than what is predicted from metallicity variation alone. The ultra-violet flux is theoretically expected to be the more affected by possible progenitors population drift (Lentz et al. 2000), suggesting that accurate studies of rest frame $U-B$ color are useful to further investigate possible differences between the properties of low and high-z supernovae.

References

Aldering, G., Knop, R., & Nugent, P. 2000, AJ, 119, 2110

Barbon, R., Benetti, S., Rosino, L., Cappellaro, E., & Turatto, M. 1990, A&A, 237, 79

Barris, B. J., Tonry, J., Blondin, S., Challis, P., Chornock, R., Clocchiatti, A., Filippenko, A., Garnavich, P., Holland, S., Jha, S., Kirshner, R., Krisciunas, K., Leibundgut, B., Li, W., Matheson, T., Miknaitis, G., Riess, A., Schmidt, B., Smith, R. C., Sollerman, J., Spyromilio, J., Stubbs, C., Suntzeff, N., Aussel, H., Chambers, K. C., Connelley, M. S., Donovan, D., Henry, J. P., Kaiser, N., Liu, M. C., Martin, E. L., & Wainscoat, R. J. 2003, astro-ph/0310843

Blakeslee, J. P., Tsvetanov, Z. I., Riess, A. G., Ford, H. C., Illingworth, G. D., Magee, D., Tonry, J. L., Benítez, N., Clampin, M., Hartig, G. F., Meurer, G. R., Sirianni, M., Ardila, D. R., Bartko, F., Bouwens, R., Broadhurst, T., Cross, N., Feldman, P. D., Franx, M., Golimowski, D. A., Gronwall, C., Kimble, R., Krist, J., Martel, A. R., Menanteau, F., Miley, G., Postman, M., Rosati, P., Sparks, W., Strolger, L.-G., Tran, H. D., White, R. L., & Zheng, W. 2003, ApJ, 589, 693

Branch, D. 2001, PASP, 113, 169

—. 2003, astro-ph/0310685

Branch, D., Lacy, C. H., McCall, M. L., Sutherland, P. G., Uomoto, A., Wheeler, J. C., & Wills, B. J. 1983, ApJ, 270, 123

Branch, D., & van den Bergh, S. 1993, AJ, 105, 2231

Coil, A. L., Matheson, T., Filippenko, A. V., Leonard, D. C., Tonry, J., Riess, A. G., Challis, P., Clocchiatti, A., Garnavich, P. M., Hogan, C. J., Jha, S., Kirshner, R. P., Leibundgut, B., Phillips, M. M., Schmidt, B. P., Schommer, R. A., Smith, R. C., Soderberg, A. M., Spyromilio, J., Stubbs, C., Suntzeff, N. B., & Woudt, P. 2000, ApJ, 544, L111

Filippenko, A. V., Richmond, M. W., Branch, D., Gaskell, M., Herbst, W., Ford, C. H., Treffers, R. R., Matheson, T., Ho, L. C., Dey, A., Sargent, W. L. W., Small, T. A., & van Breugel, W. J. M. 1992a, AJ, 104, 1543

Filippenko, A. V., Richmond, M. W., Matheson, T., Shields, J. C., Burbidge, E. M., Cohen, R. D., Dickinson, M., Malkan, M. A., Nelson, B., Pietz, J., Schlegel, D., Schmeer, P., Spinrad, H., Steidel, C. C., Tran, H. D., & Wren, W. 1992b, ApJ, 384, L15

Folatelli, G. e. 2004, to be sub

Garavini, G. e. 2004a, to be sub

—. 2004b, AJ submitted

Garnavich, P. M., et al. 2001, astro-ph/0105490
Hamuy, M., Phillips, M. M., Maza, J., Suntzeff, N. B., Schommer, R. A., & Aviles, R. 1995, AJ, 109, 1
Hamuy, M., Phillips, M. M., Suntzeff, N. B., Schommer, R. A., Maza, J., & Aviles, R. 1996, AJ, 112, 2391
Hamuy, M., Trager, S. C., Pinto, P. A., Phillips, M. M., Schommer, R. A., Ivanov, V., & Suntzeff, N. B. 2000, AJ, 120, 1479
Hoeflich, P., Wheeler, J. C., & Thielemann, F. K. 1998, ApJ, 495, 617
Hook, I. M. 2004, to be submitted
Howell, D. A. 2001, ApJ, 554, L193
Jeffery, D. J., Leibundgut, B., Kirshner, R. P., Benetti, S., Branch, D., & Sonneborn, G. 1992, ApJ, 397, 304
Kirshner, R. P., Jeffery, D. J., Leibundgut, B., Challis, P. M., Sonneborn, G., Phillips, M. M., Suntzeff, N. B., Smith, R. C., Winkler, P. F., Winge, C., Hamuy, M., Hunter, D. A., Roth, K. C., Blades, J. C., Branch, D., Chevalier, R. A., Fransson, C., Panagia, N., Wagoner, R. V., Wheeler, J. C., & Harkness, R. P. 1993, ApJ, 415, 589
Kirshner, R. P., Oke, J. B., Penston, M. V., & Searle, L. 1973, ApJ, 185, 303
Leibundgut, B., Kirshner, R. P., Phillips, M. M., Wells, L. A., Suntzeff, N. B., Hamuy, M., Schommer, R. A., Walker, A. R., Gonzalez, L., Ugarte, P., Williams, R. E., Williger, G., Gomez, M., Marzke, R., Schmidt, B. P., Whitney, B., Coldwell, N., Peters, J., Chaffee, F. H., Foltz, C. B., Rehner, D., Siciliano, L., Barnes, T. G., Cheng, K.-P., Hintzen, P. M. N., Kim, Y.-C., Maza, J., Parker, J. W., Porter, A. C., Schmidtke, P. C., & Sonneborn, G. 1993, AJ, 105, 301
Lentz, E. J., Baron, E., Branch, D., Hauschildt, P. H., & Nugent, P. E. 2000, ApJ, 530, 966
Li, W., Filippenko, A. V., Chornock, R., Berger, E., Berlind, P., Calkins, M. L., Challis, P., Fassnacht, C., Jha, S., Kirshner, R. P., Matheson, T., Sargent, W. L. W., Simcoe, R. A., Smith, G. H., & Squires, G. 2003, PASP, 115, 453
Li, W., Filippenko, A. V., & Riess, A. G. 2001a, ApJ, 546, 719
Li, W., Filippenko, A. V., Treffers, R. R., Riess, A. G., Hu, J., & Qiu, Y. 2001b, ApJ, 546, 734
Lidman, C. e. 2004, in prep
Lombardi, M., & Schneider, P. 2002, A&A, 392, 1153
Mazzali, P. A., Chugai, N., Turatto, M., Lucy, L. B., Danziger, I. J., Cappellaro, E., della Valle, M., & Benetti, S. 1997, MNRAS, 284, 151
Mazzali, P. A., Danziger, I. J., & Turatto, M. 1995, A&A, 297, 509
Nugent, P., Aldering, G., Amanullah, R., Antilogus, P., Astier, P., Balland, C., Blanc, G., Burns, M. S., Conley, A., Deustua, S., Ellis, R., Fabbro, S., Folatelli, G., Fruchter, A., Garavini, G., Gibbons, R., Goldhaber, G., Goobar, A., Groom, D. E., Hardin, D., Hook, I. M., Howell, D. A., Irwin, M., Kasen, D., Kim, A., Knop, R. A., Levy, J.-M., Lidman, C., McMahon, R., Mouchet, M., Nobili, S., Pain, R., Panagia, N., Pécontal, E., Pennypacker, C. R., Perlmutter, S., Quimby, R., Raux, J., Regnault, N., Ruiz-Lapuente, P., Schaefer, B., Schahmaneche, K., Spadafora, A. L., Walton, N., Wang, L., Wood-Vasey, W. M., & Supernova Cosmology Project Collaboration. 2001, Bulletin of the American Astronomical Society, 33, 1427
Patat, F., Benetti, S., Cappellaro, E., Danziger, I. J., della Valle, M., Mazzali, P. A., & Turatto, M. 1996, MNRAS, 278, 111
Perlmutter, S., Aldering, G., della Valle, M., Deustua, S., Ellis, R. S., Fabbro, S., Fruchter, A., Goldhaber, G., Groom, D. E., Hook, I. M., Kim, A. G., Kim, M. Y., Knop, R. A., Lidman, C., McMahon, R. G., Nugent, P., Pain, R., Panagia, N., Pennypacker, C. R., Ruiz-Lapuente, P., Schaefer, B., & Walton, N. 1998, Nature, 391, 51
Phillips, M. M., Phillips, A. C., Heathcote, S. R., Blanco, V. M., Geisler, D., Hamilton, D., Suntzeff, N. B., Jablonski, F. J., Steiner, J. E., Cowley, A. P., Schmidtke, P., Wyckoff, S., Hutchings, J. B., Tonry, J., Strauss, M. A., Thorstensen, J. R., Honey, W., Maza, J., Ruiz, M. T., Landolt, A. U., Uomoto, A., Rich, R. M., Grindlay, J. E., Cohn, H., Smith, H. A., Lutz, J. H., Lavery, R. J., & Saha, A. 1987, PASP, 99, 592
Phillips, M. M., Wells, L. A., Suntzeff, N. B., Hamuy, M., Leibundgut, B., Kirshner, R. P., & Foltz, C. B. 1992, AJ, 103, 1632
Riess, A. G., Filippenko, A. V., Li, W., Treffers, R. R., Schmidt, B. P., Qiu, Y., Hu, J., Armstrong, M., Faranda, C., Thouvenot, E., & Buil, C. 1999, AJ, 118, 2675
Riess, A. G., Strolger, L., Tonry, J., Tsvetanov, Z., Casertano, S., Ferguson, H. C., Mobasher, B., Challis, P., Panagia, N., Filippenko, A. V., Li, W., Chornock, R., Kirshner, R. P., Leibundgut, B., Dickinson, M., Koekemoer, A., Grogin, N. A., & Giavalisco, M. 2003, astro-ph/0308185
Ruiz-Lapuente, P., Cappellaro, E., Turatto, M., Gouiffes, C., Danziger, I. J., della Valle, M., & Lucy, L. B. 1992, ApJ, 387, L33
Sainton, G. e. a. 2004, in prep
Sullivan, M., Ellis, R. S., Aldering, G., Amanullah, R., Astier, P., Blanc, G., Burns, M. S., Conley, A., Deustua, S. E., Doi, M., Fabbro, S., Folatelli, G., Fruchter, A. S., Garavini, G., Gibbons, R., Goldhaber, G., Goobar, A., Groom, D. E., Hardin, D., Hook, I., Howell, D. A., Irwin, M., Kim, A. G., Knop, R. A., Lidman, C., McMahon, R., Mendez, J., Nobili, S., Nugent, P. E., Pain, R., Panagia, N., Pennypacker, C. R., Perlmutter, S., Quimby, R., Raux, J., Regnault, N., Ruiz-Lapuente, P., Schaefer, B., Schahmaneche, K., Spadafora, A. L., Walton, N. A., Wang, L., Wood-Vasey, W. M., & Yasuda, N. 2003, MNRAS, 340, 1057
Turatto, M., Benetti, S., Cappellaro, E., Danziger, I. J., della Valle, M., Gouiffes, C., Mazzali, P. A., & Patat, F. 1996, MNRAS, 283, 1
Wells, L. A., Phillips, M. M., Suntzeff, B., Heathcote, S. R., Hamuy, M., Navarrete, M., Fernandez, M., Weller, W. G., Schommer, R. A., Kirshner, R. P., Leibundgut, B., Willner, S. P., Peletier, S. P., Schlegel, E. M., Wheeler, J. C., Harkness, R. P., Bell, D. J., Matthews, J. M., Filippenko, A. V., Shields, J. C., Richmond, M. W., Jewitt, D., Luu, J., Tran, H. D., Appleton, P. N., Robson, E. I., Tyson, J. A., Guhathakurta, P., Eder, J. A., Bond, H. E., Potter, M., Veilleux, S., Porter, A. C., Humphreys, R. M., Janes, K. A., Williams, T. B., Costa, E., Ruiz, M. T., Lee, J. T., Lutz, J. H., Rich, R. M., Winkler, P. F., & Tyson, N. D. 1994, AJ, 108, 2233

Paper D

The Nearby Supernova Cosmology Project Spectroscopic Follow-up: Uncertainty Estimation for Quantitative Studies

G. Folatelli, G. Garavini, S. Nobili,...

Department of Physics, Stockholm University,
SCFAB, S–106 91 Stockholm, Sweden

ABSTRACT

We present a method to prepare supernova spectra for further quantitative analysis. The method was developed to treat the extensive spectroscopic data of low-redshift type Ia supernovae (SNe Ia) obtained during the Spring 1999 Nearby Supernova Campaign which was coordinated by the *Supernova Cosmology Project* (SCP). Over one hundred low-resolution, long-slit spectra from 18 SNe Ia discovered in that campaign were treated. The resulting calibrated spectra include estimated statistical uncertainties in the flux as a function of wavelength. In addition, systematic effects are addressed and an estimate of their residual significance is given. Finally, we correct the effect of host-galaxy contamination using a fitting procedure to subtract its contribution from the one-dimensional spectra. Though we focus on the SNe from the SCP campaign, this method can be extended to optical spectroscopy in general.

1. Introduction

Type Ia supernovae (SNe Ia) have been proven to be remarkably precise standardizable candles. The high intrinsic brightness and uniformity in absolute B magnitude that these objects show have turned them into one of the most powerful means of measuring relative distances on cosmological scales. In the past few years, this has led to some outstanding results in cosmology which favor the case of an accelerating universe (Riess et al. 1998; Perlmutter et al. 1999; Tonry et al. 2003; Knop et al. 2003). Yet, the intrinsic dispersion in luminosity and the peculiarity of some of the observed SNe Ia requires a better understanding of their properties and asserting their homogeneity as standard candles. Moreover, any possible source of systematic effects that might mimic the acceleration in the Hubble diagram should be thoroughly studied. In that sense, spectroscopy data plays a crucial role as a complement of photometry in characterizing SNe Ia.

With the purpose of tackling the problem of systematic effects in the use of SNe Ia to determine the value of the cosmological parameters, the Supernova Cosmology Project (SCP) coordinated the Spring 1999 Nearby Supernova Campaign (in the following, the "Spring '99" campaign). During this campaign, 19 nearby SNe Ia ($z < 0.2$) were discovered and followed-up and a similar number of SNe of all types was also discovered but not followed-up (Aldering 2000; Nugent et al. 2000). The follow-up observations consisted of ground based optical multi-filter photometry and low to medium resolution spectroscopy. The spectroscopic data were obtained using a total of 9 telescopes on more than 30 observing nights during three

months. Based on a vast set of spectra from that campaign, this paper describes the procedure by which the SN spectra are made suitable for future quantitative analysis. This involves the development of a data treatment method which produces calibrated spectra with estimated statistical and systematic uncertainties. The spectroscopic data as well as the photometry will be published in forthcoming papers.

While qualitative studies help in classifying SNe Ia as such and in performing comparisons of spectral feature shapes, robust conclusions should be derived from quantitative analyses, through parametrization of spectral characteristics and accurate modeling. This requires a careful treatment of the observations, the estimation of uncertainties and the control of possible systematic effects. Some previous work has proven that spectral parameters can yield detailed information about the properties of SNe Ia as standard candles, in an independent way from lightcurve properties. Nugent et al. (1995) introduced the so called silicon and calcium intensity ratios and their correlation with peak luminosity. Using synthetic spectra, the authors were able to parametrize this empirical correlations through the effective temperature of the SNe. Also, the velocity of Si II λ6355 measured 10 days after maximum light has been used to study the degree of spectral inhomogeneity among SNe Ia (Branch & van den Bergh 1993) and more recently assess the issue of possible coexisting explosion mechanisms (Hatano et al. 2000). Our aim is to treat the extensive set of spectra coming from the Spring '99 campaign in order to carry out similar quantitative analyses and study the homogeneity and possible refinement of the standard candle calibration.

The next section briefly presents the data and describes the reduction method. Section 3 deals with the issues of uncertainty estimation and control of systematic effects. In section 4, the problem of host-galaxy contamination in SN spectra is addressed. Section 5 summarizes the method and discusses its reach for future work.

2. Data and Reduction Method

The spectroscopic data collected in the Spring '99 campaign consists of low-dispersion, long-slit spectra covering a broad wavelength range (typically between 3500 and 9500 Å). These spectra are separated in two sets. First, the *follow-up* set, which consists of over 100 optical spectra from 9 different ground-based telescopes: APO 3.5m, CTIO 4m, ESO 3.6m, INT, KPNO 4m, Lick 1m, Lick 3m, MDM 2.4m, and NOT. This set is to be used in monitoring the evolution of SNe Ia in their early stages (see, for example, Garavini et al. (2004a,b); Folatelli et al. (2004)). The time coverage for this set goes from 15 days before maximum light to 60 days after. Second, a *reference* set consisting of at least one spectrum per followed-up SN taken around one year after maximum light or later. By that time, the SN had faded enough for the spectra to show only the host galaxy. This second set of spectra was used to subtract any remaining host-galaxy light from the follow-up spectra, as described in section 4.

The following description of the reduction method and the analysis carried out in section 3 focuse on the bulk of the follow-up observations. These observations are presented in Table 1. They include 7 of the 9 telescopes used, which covers the data from 18 out of the 19 SNe Ia, with the only exception of three spectra observed at one of the missing telescopes (INT). The data from the other telescope which was left aside

(Lick 1m) involves exclusively the very nearby SN 1999by which is therefore not included in this work. The first 5 columns of Table 1 list telescope and instrument name, observing date, dispersor or channel name, approximate total wavelength coverage, and average dispersion. The values on the last two columns are the estimate of the systematic uncertainties and the number of standard-star spectra obtained on each night, as explained in section 3.2.1.

Every spectrum was reduced by means of standard IRAF[1] routines. Two-dimensional images were bias-subtracted and flat-fielded using appropriate calibration images. The result of flat-fielding was checked for non-uniform illumination effects on the slit by use of twilight exposures. Sky background subtraction was performed on the resulting images. A cubic apline function was fitted to the sky signal along the whole spatial axis (its length depending on the projection of the slit on the detector) and subtracted from the signal of the object. This background subtraction procedure, when compared to another where a low order polynomial was fitted in the vicinity of the object, proved to be more straight-forward and equally accurate. When the SN was well separated from the core of its host, the background fit included the profile of the host. In other cases, a narrow aperture was taken in order to minimize the contribution from the host in the total flux. Any residual contamination from the host was removed at a final stage with use of the reference spectra. After background subtraction, one-dimensional object spectra were obtained by variance weighted (*optimal*) aperture extraction (Horne 1986). At the same location of the SNe, sky background spectra were extracted from "sky only" images obtained as the difference between the original and the background-subtracted two-dimensional spectra.

Comparison arc lamp spectra were used to perform wavelength calibration for each instrumental setting. The conversion to wavelength was done preserving the original pixel sampling in order not to introduce any further correlation between pixel values. The result was corroborated with the position of emission lines on the sky background spectra and using the wavelength values tabulated by Osterbrock et al. (1992). Figure 1 shows some of the sky lines identified on a 1500 second exposure at the KPNO 4m telescope. This case represents the typical shape of the sky spectrum on a relatively dark night although the realtive strength of different sky lines is site-dependent since some lines, especially on the blue, are of man-made origin. In a few cases the arc-lamp calibration was not accurate enough and a correction based on the sky lines was needed. These corrections were always lower than 15 Å. In general, a final accuracy below ~2 Å was achieved for the whole set of spectra, which is satisfactory given the dispersion values listed in column 5 of Table 1. This accuracy is also good in the case of SN spectra, whose lines are broadened by expansion velocities of ~10000 km/s.

Spectrophotometric standard stars observed on each night were used to calibrate the spectra to absolute flux. The spectra of these stars were reduced in the same manner as those of the science objects. The observed fluxes were compared with the tabulated ones in order to fit the *sensitivity function* for each night and instrumental setting. These functions were applied to the science spectra of the corresponding nights. A correction for atmospheric extinction was also performed, depending on the object's zenith distance and

[1]IRAF is distributed by the National Optical Astronomy Observatories, which are operated by the Association of Universities for Research in Astronomy, Inc., under cooperative agreement with the National Science Foundation.

using tabulated mean extinction coefficients for each observatory site.

Different individual spectra of the same object taken during the same night were combined as described in section 3.1. Finally, a correction for Galactic extinction was applied using an average R_V-dependent extinction law (Cardelli et al. 1989), assuming $R_V = 3.1$ and taking the value of A_V for each SN from Schlegel et al. (1998). No correction for extinction in the host galaxy was applied.

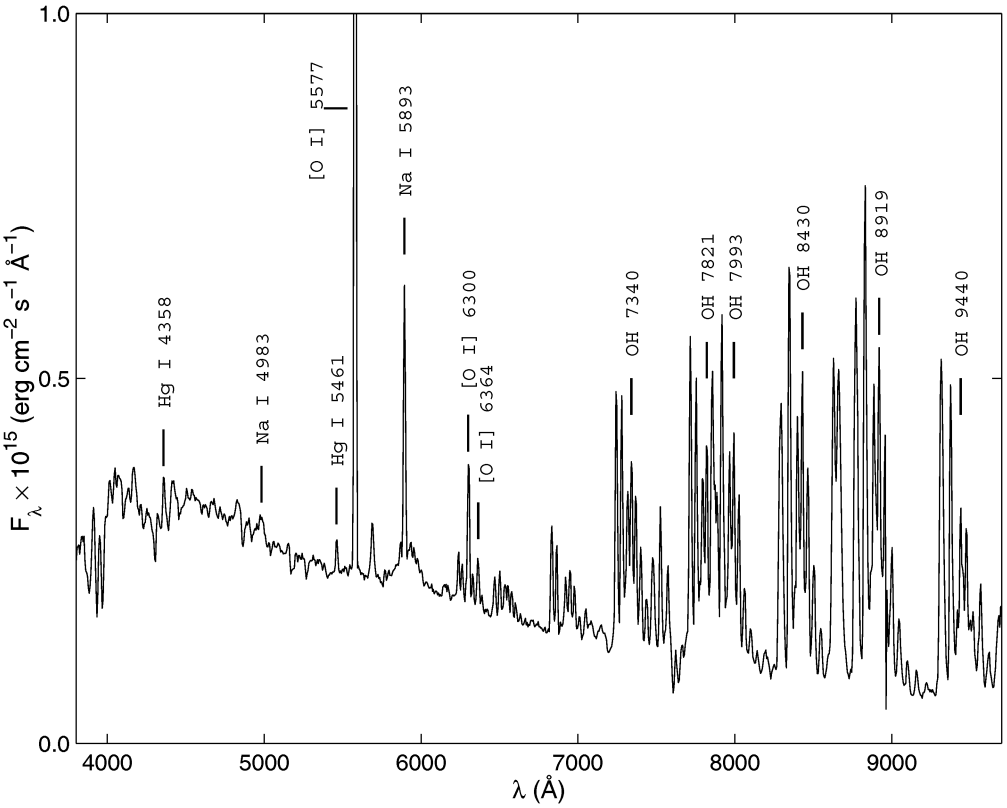

Fig. 1.— Night sky spectrum observed with the Mayall 4-m telescope at KPNO. Exposure time: 1500s. The tabulated line positions are shown. Measured positions agree well within the resolution achieved by the spectrograph.

3. Uncertainty Estimation

A quantitative spectral analysis requires the availability of associated uncertainties. In the following, we will discuss how the uncertainties in the measured flux were estimated. Statistical and systematic effects are addressed separately. Table 2 provides a summary of these analyses for all the SN Ia spectra corresponding to the observations listed in Table 1. Columns 1 to 8 of Table 2 show SN name, redshift, telescope, observation date, epoch in days since maximum light, exposure time in seconds, approximate wavelength range of the final spectrum in the SN rest frame, and the average wavelength bin size in the SN rest frame. The quantities listed in columns 9 and 10 of Table 2 are the estimated systematic uncertainties (section 3.2.1), the average signal-to-noise ratios per 10 Å (section 3.1), respectively. Columns 11 and 12 summarize the results of cross-instrument comparisons (section 3.2.2).

3.1. Statistical Uncertainties

Statistical error estimation is based on the use of *optimal* extractions, as described by Horne (1986) and implemented in IRAF. When extracting the one-dimensional spectra the signal of the object is summed inside an aperture along the spatial direction on the two-dimensional images. In the case of optimal extractions, this is done using a variance-weight based algorithm which takes into account both photon and instrumental noise. Since the photon noise is estimated from the total flux measured, it is necessary to consider the contribution from the sky background, which in our case was stored in the "sky-only" spectra. In addition to providing with an estimate of the statistical uncertainties, variance-weighted extractions improve bad-column and cosmic ray cleaning. This procedure produces a *sigma spectrum* (the 1-σ statistical uncertainty along the dispersion direction) as the square root of the estimated variance. The sigma spectrum is calibrated in the same fashion as the *signal* spectrum to be finally taken as a measure of the statistical uncertainties on the flux. A typical example of a sigma spectrum can be seen in Figure 2.

The computation of the sigma spectrum does not take into account the possible correlation among pixel values. Depending on the projection of the slit on the detector, a certain amount of correlation is expected among neighboring pixels. The uncertainties would then be represented in the general case by a band-shaped covariance matrix. In this work, we neglect the off-diagonal terms and consider the uncertainties to be represented by the sigma spectrum.

An additional cause of pixel correlation arises during spectral combination. In many cases, the observation of a supernova was split up into a number of individual exposures which were finally combined. Each individual spectrum was reduced as described above and thus included associated statistical uncertainties. Since the dispersion solution was computed for each exposure separately, the wavelength sampling was slightly different among the spectra (differences being normally within a few parts in a thousand). To account for this, the spectra to be combined were first resampled to a common wavelength grid by linear interpolation. In general, this process introduces an additional amount of correlation among neighboring pixels, which can also be represented with a band-shaped covariance matrix. For a fixed order of interpolation (linear, in our case), the amount of correlation depends on the wavelength bin size the spectra were

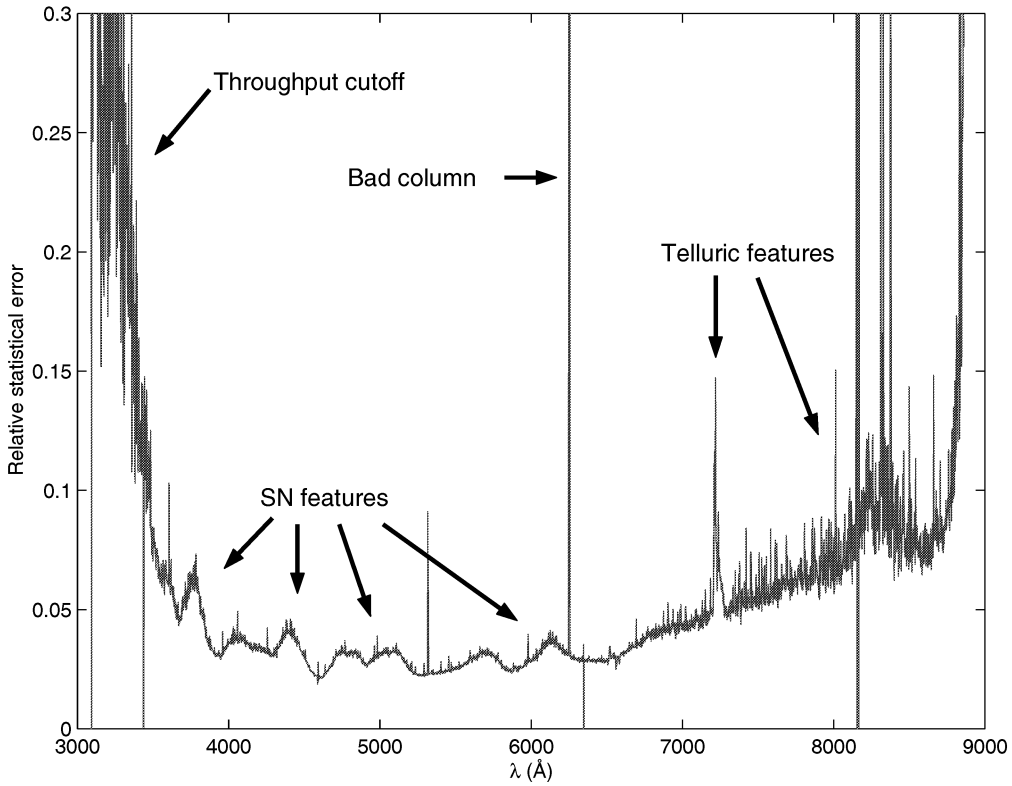

Fig. 2.— Ratio of the estimated *sigma* spectrum to the measured flux for a SN exposure from the CTIO-4m telescope. Typical features are marked.

originally sampled on (i.e., on the dispersion and the pixel size) and on the difference between the original wavelength grid and the one it was interpolated to. In particular, for larger wavelength bin sizes, the correlation becomes less important —and the interpolation less accurate. In our case, the correlation is neglected and the uncertainties are propagated from the individual sigma spectra.

Once the individual spectra were interpolated, the combination was performed using the method of least-squares (LS) described in Appendix A for the general case of non-diagonal covariance matrices. We applied the method in the case of uncorrelated uncertainties, i.e. considering only the sigma spectra squared in the diagonals. The combined spectrum were therefore obtained with associated sigma spectra.

The results were used to compute ratios of signal to sigma spectra in bins of 10 Å averaged over the entire wavelength range. This signal-to-noise ratios, $\langle S/N \rangle$, are listed in column 10 of Table 2. Values given between brackets correspond to spectra with uncorrected host-galaxy contamination. The computed signal-to-noise ratios range from ∼1 to several hundred, with the lowest values belonging to the most distant SNe. Figure 3 shows the distribution of signal-to-noise ratios with a median of $\overline{\langle S/N \rangle} = 38$ found for the sample of non-contaminated SN Ia spectra in Table 2.

3.2. Systematic Uncertainties

3.2.1. The Standard-Star Method

High signal-to-noise ratio spectra of spectrophotometric standard stars were used to build a sensitivity function for each instrumental setting on each observing night. The fit of the sensitivity function was performed by comparing the observed flux on the calibration spectra with published tabulated flux values. The accuracy of the fit depended on the wavelength sampling both in the published tables and our data, being these normally good enough to follow the continuum but not the narrow spectral lines. The points overlapping these lines and the strongest telluric features were rejected when performing the fits. Any wavelength-independent deviation (due to the presence of clouds, light loss outside the slit or extraction aperture, etc.) was allowed for in building the sensitivity function by scaling every spectrum to the same level. In general, wavelength-dependent deviations among the different standard stars indicate the presence of remaining systematic errors in the observation and/or reduction. In order to quantify these errors in a conservative way a three-step method was developed:

1. The sensitivity function was used to calibrate each standard star spectrum of the corresponding night. The result was interpolated to the wavelength sampling of the table and then scaled by the median of the flux to allow for any gray absorption. A root mean square (rms) was computed for each standard-star spectrum, as

$$\sigma = \sqrt{\sum_{i=1}^{N} \left(\frac{A S_i^{Obs} - S_i^{Tab}}{S_i^{Tab}} \right)^2}, \quad (1)$$

where S_i^{Obs} is the interpolated observed flux and S_i^{Tab} is the tabulated flux in wavelength bins i =

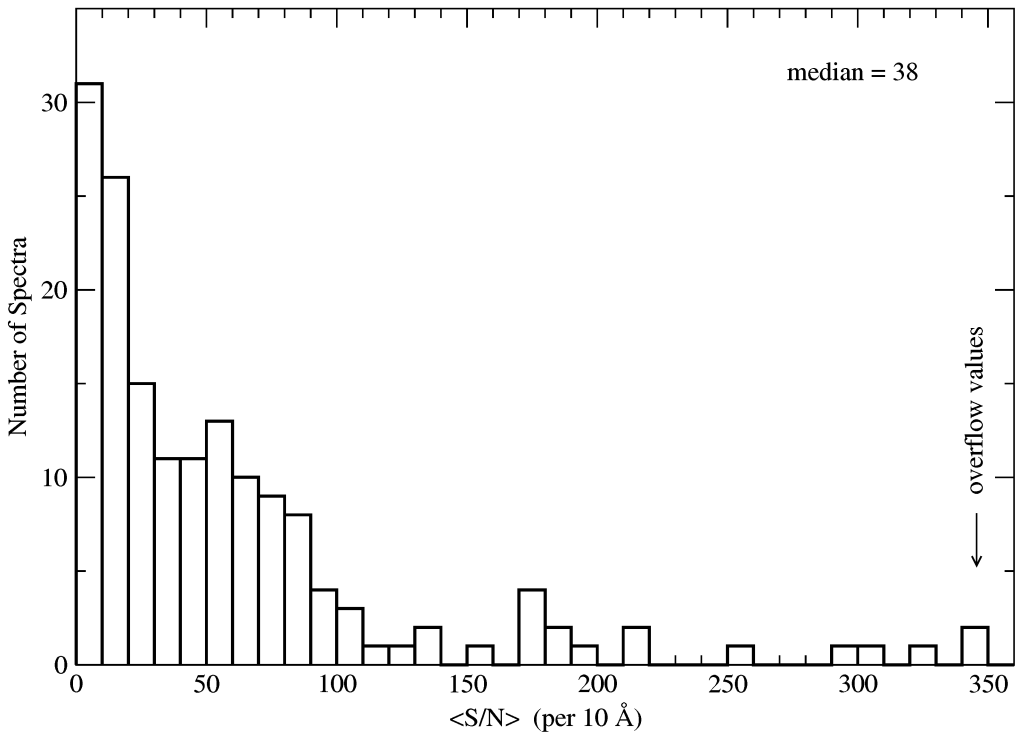

Fig. 3.— Distribution of average signal-to-noise ratios per 10 Å for the Spring '99 SN Ia spectra. The median of the distribution is 38.

$1, \ldots, N$, and $A \equiv \langle S^{Tab}/S^{Obs} \rangle$ is the median-based scaling factor. The calculation of σ was done using a 3σ-clipping iterative procedure.

2. The spectrum with the highest standard deviation was selected and excluded from the subsequent fit of a new sensitivity function. This new sensitivity function is therefore independent of the selected spectrum.

3. The excluded standard-star spectrum was calibrated using the new sensitivity function and a new rms, σ_{syst}, was computed using Eqn. 1. This value was taken as the *systematic uncertainty* measure for all science spectra of the night which were obtained with the same instrumental settings. Thus, the method is conservative in the sense that the most deviant spectrum is used to compute σ_{syst}.

This procedure was performed separately for each instrumental setting used on each night. Figure 4 shows the example for a night at the ESO-3.6m telescope (grism #11). The inset graph shows a histogram of the residuals and the value $\sigma_{syst} = 0.031$ found in that case. The values of σ_{syst} for all nights and instrumental settings and the amount of standard-star spectra observed in the follow-up part of the Spring '99 campaign are given in column 6 and 7 of Table 1, respectively. Column 9 in Table 2 lists the same values of σ_{syst} for each SN spectrum as a comparison to the other uncertainty estimations. In a few cases, only one standard star spectrum was available and therefore the iterative procedure described was not applicable. We provide uncertainty estimates for some of those cases by using the sensitivity function corresponding to another observing night from the same telescope, when the observations were done in a similar way and the interval between the nights was not greater than a few days. Only the night of February 23rd at the Lick-3m telescope lacks an estimate of σ_{syst} because the other nights were too distant in time (April) and the instrumental settings were different. Figure 5 shows the distribution of σ_{syst}, with a median value $\overline{\sigma_{syst}} = 0.042$.

The reported σ_{syst}, although it was computed pixel by pixel, is treated as a measure of the *overall* systematic uncertainties. Therefore, when analysing a *portion* of the spectrum, these uncertainties should be scaled by the fraction of the total wavelength coverage under consideration. One would feel tempted to interpret the deviations seen in Fig. 4 as, for example, the effect of uncorrected atmospheric extinction and to correct every spectrum by the systematic trends present in the standard star spectrum. However, this trends varied from star to star and we were unable to find a general correction to be applied to all of the science spectra of a certain night. In section 3.2.3 we explain how the systematic effects are monitored by comparing the spectrophotometry with direct imaging measurements.

3.2.2. Cross-Instrument Checks

An alternative way to examine the accuracy of the spectra was possible when different telescopes or instrumental settings provided independent measurements of the same object. Since the Spring '99 campaign was so thorough, this situation was often encountered.

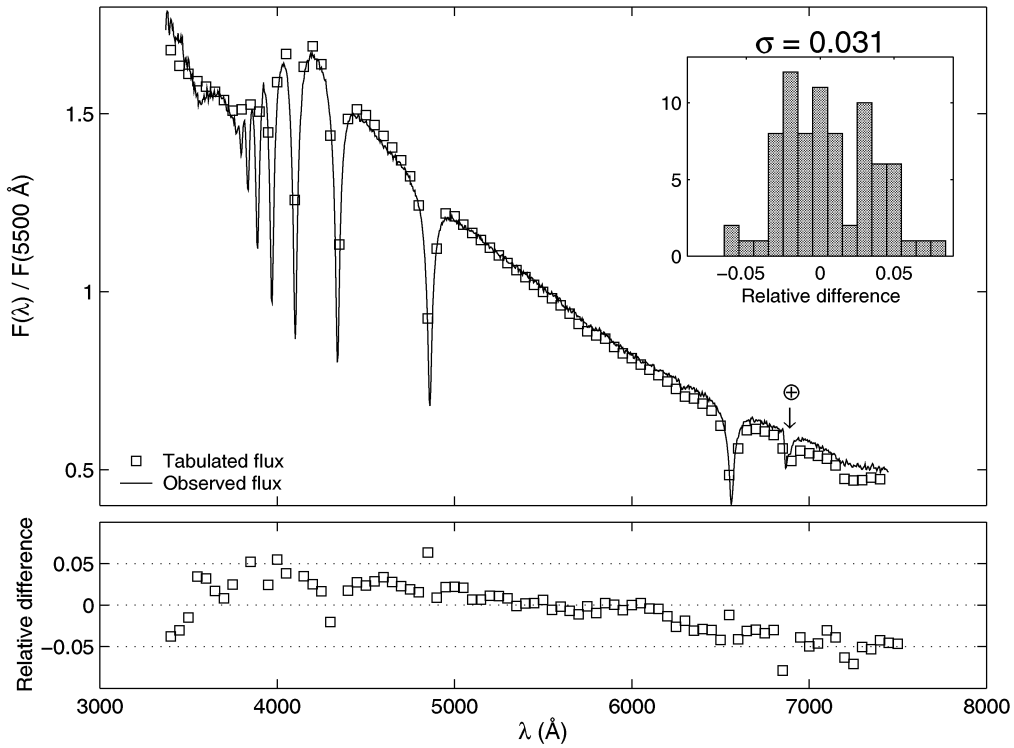

Fig. 4.— *Upper panel*: Comparison of a spectrum of the standard star LTT-3218 observed with the ESO-3.6m telescope (solid line), and its tabulated flux (boxes). The arrow marks a telluric absorption band. *Lower panel*: Residuals relative to the tabulated values. The inset histogram shows the distribution of residuals and the resulting σ (rms).

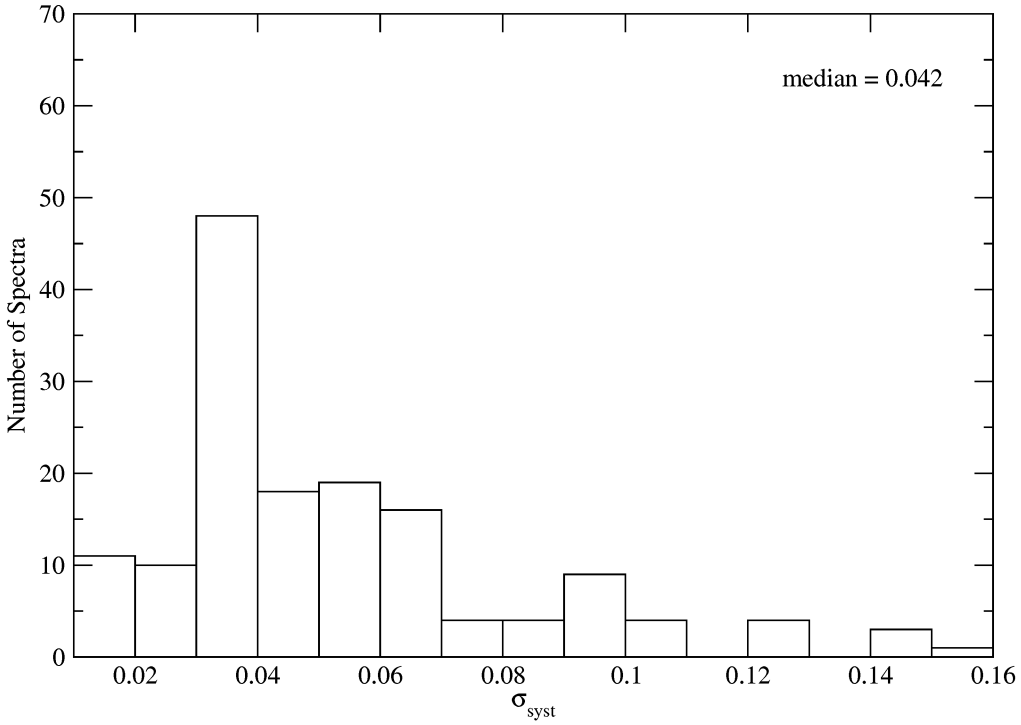

Fig. 5.— Distribution of systematic uncertainties for all the observing nights belonging to the follow-up spectroscopy of the Spring '99 campaign.

Whenever a SN was observed at the same telescope in the same night using two different instrumental settings (different grisms, gratings or channels), the consistency of the results in the overlapping wavelength range was tested. An rms was calculated from the relative differences between the two measurements, as

$$\sigma_{grism} = \sqrt{\sum_{i=1}^{N} \left(\frac{2(AS_i^B - S_i^R)}{AS_i^B + S_i^R} \right)^2}, \quad (2)$$

where S_i^B and S_i^R are the fluxes observed using each instrumental setting, in each bin $i = 1, \ldots, N$ of the overlapping range, and $A \equiv \langle S^R / S^B \rangle$ is a scaling factor based on the median of the fluxes in the same range. This calculation was done using a 3σ-clipping iterative algorithm. The values of σ_{grism} are listed in column 11 of Table 2. Column 12 in the same table shows the overlapping wavelength regions, given in the SN rest frame. The ranges of overlap vary from several hundred to several thousand Å for the different teslescopes. In general, the values of σ_{grism} are comparable with those of σ_{syst} from section 3.2.1. An advantage of this procedure is that it directly involves the object instead of the standard stars. However, its applicability is limited to the overlapping wavelength range and to the cases when the two measurements are available. Figure 6 shows the example of high signal-to-noise ratio spectra of SN 1999ac obtained at the ESO 3.6m telescope using grisms #11 and #12. The two spectra agree at the percent level ($\sigma_{grism} = 0.01$).

These comparisons also served in finding systematic mismatches produced by some instrumental settings. The comparison of grisms #4 and #5 from the NOT yielded significant deviations redward of 6000 Å. We used data from other telescopes to demonstrate that the problem resided in grism #4 only. It was later found that the deviations were due to a second order contamination effect. The data from grism #4 was therefore cut at 6000 Å (in observed frame) and the values of σ_{grism} for the NOT listed in Table 2 correspond to the remaining overlapping region.

Less common was the case where spectra of the same object were taken almost simultaneously with two different telescopes. Their comparison adds an independent check for systematic effects. A case like this is shown in Figure 7 where two spectra of SN 1999ac taken almost simultaneously at the CTIO-4m telescope and the NOT agree within a few percent in the range 4000 Å$< \lambda <$ 8000 Å. Somewhat greater deviations, up to 10%, are found on both ends of the spectra.

3.2.3. Residual Correction from Spectrophotometry

The presence of residual systematic effects on the spectral distribution of the calibrated spectra may have several causes. One important source of inaccuracies when observing through long slits is the effect of *differential atmospheric refraction* (DAR). This effect is originated by the apparent vertical displacement of objects produced as light traverses the Earth's atmosphere. The magnitude of the displacement increases at lower altitudes and is wavelength-dependent —it is greater at shorter wavelengths. This may result in light losses that vary with wavelength if the object is moved perpendicular to the axis of the slit. For a detailed analysis on the possible impact of DAR on long-slit spectrophotometry, see Filippenko (1982). A common procedure that minimizes this effect during the observations is to position the slit along the parallactic

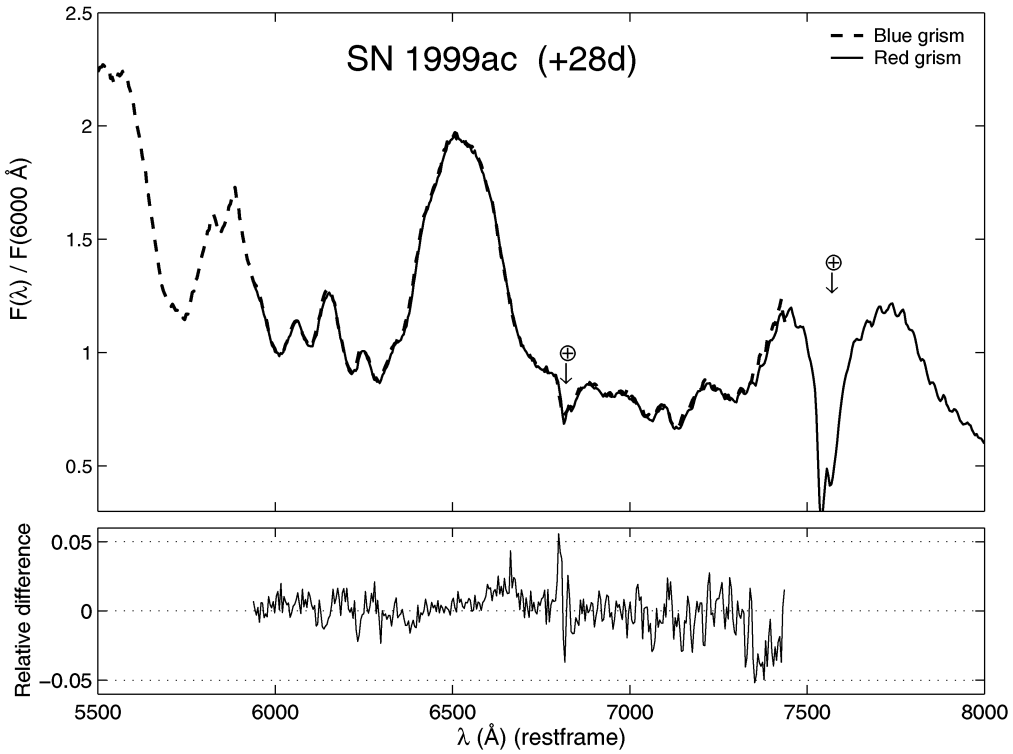

Fig. 6.— *Upper panel*: Two spectra of SN 1999ac taken through different grisms at the ESO-3.6m telescope on the same night. Two telluric absorption features are signaled with arrows. *Lower panel*: Relative difference in the overlapping region. In this example, there is agreement to within a few per cent.

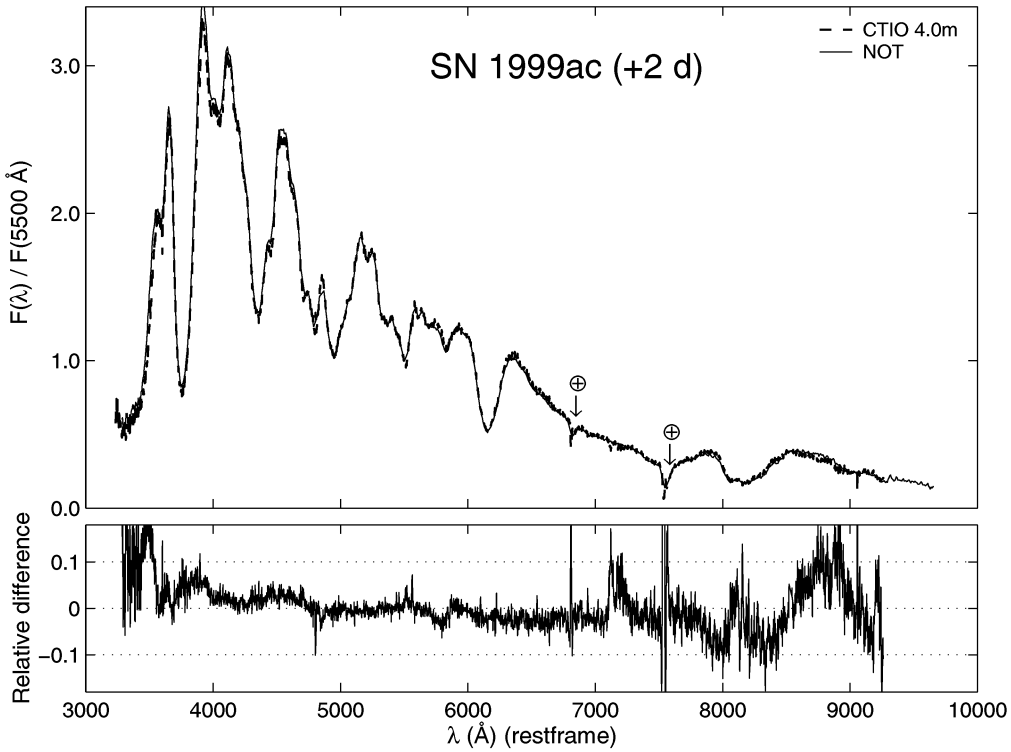

Fig. 7.— *Upper panel*: Two spectra of SN 1999ac taken at the CTIO-4m telescope and the NOT with a few hours of interval. The spectrum from the NOT is the combination of two spectra taken with different grisms. Telluric absorption features are marked with arrows. *Lower panel*: Relative difference between the two spectra above. In this case, the agreement is within a few percent over the whole wavelength range.

direction (i.e. toward the zenith) so that the object is displaced inside the slit for all wavelengths. In the case of the Spring '99 campaign, this prescription was not always fulfilled. Instead, in order to ensure locating the ever fading SNe inside the slit, the latter was often aligned through the center of the host galaxy or some reference field star. In those cases, care was taken to observe at low zenith distances or using wider slits. However, a fraction of the Spring '99 spectra may be subject to the effect of DAR. Any attempt to simulate this effect and correct for it in practice would require a model of the atmosphere at the observing site, and the knowledge of an amount of parameters such as airmass, accuracy of the slit-positioning and tracking precision, location of the object in the slit, image quality, etc. Such a detailed analysis is beyond our possibilties and would only be justified for high precision spectrophotometry observations.

Nevertheless, regardless of its origin, any residual inacuracy on the spectra can be detected and corrected using photometric measurements. Synthetic magnitudes computed by integrating the spectral flux through different bandpasses can be compared with the usually more accurate results of direct photometry. The Spring '99 campaign involved multi-filter photometry observations covering roughly the same time range as the spectra. The resulting preliminary light-curves were used to correct the spectra when needed, through the procedure described next.

The spectral flux was integrated through every bandpass used in the direct imaging observations that was covered by the spectrum. The ratio of spectrophotometric to photometric fluxes yielded the ordinates of a series of points to which the effective wavelength of each filter was assigned as abscissa. These points were used to interpolate a smooth correction function (a polynomial of order equal to the amount of points available) which was extrapolated to cover the wavelength range of the spectrum. The correction was refined by performing a non-linear least-squares fit that varied the ordinates of the points, treated as independent from each other even though some correlation is expected from the overlap of the different bandpasses. The type of correction achieved in this way has a smooth wavelength dependence. Thus, the overall continuum level is modified while line profiles or other high-frequency features remain unaffected.

4. Host-galaxy Contamination

When analysing spectra of distant SNe it is important to control the possible contamination due to host galaxy light. If the SN and its host are not well resolved, the subtraction of the background flux becomes non-trivial. The situation worsens as the SN fades away with time. In order to cope with this problem the Spring '99 campaign included a set of *reference* spectra. These spectra were taken on the same location of the SNe, more than one year after they went off. Therefore, the reference spectra provide clean measurements of the host-galaxy background to be subtracted, when needed, from the *follow-up* spectra.

Host-galaxy contamination is usually noticed by an overall change in the spectral continuum (and in the color indices), and by the presence of narrow absorption and emission lines originated in the galaxy. When well resolved, these lines serve in detemining the amount of galaxy flux present in the SN spectrum by comparing their intensities in the follow-up and reference spectra. The Spring '99 spectra were generally taken at too low resolutions to achieve such a direct measure. Therefore, an indirect method had to be used

to find the correct estimate of the host galaxy level to be subtracted from the follow-up SN spectra. This was done by *chi-square* minimization of the difference between the subtraction and a template, non-contaminated SN spectrum at a similar evolutionary phase. The ratio of galaxy line intensities, when available, was used as an approximate initial value for the fitting procedure. The knowledge of statistical uncertainties both in the follow-up and reference spectra ensured the robustness of the minimization procedure. Final error-bars in the subtracted spectrum were computed by propagation of the uncertaities in the measurements and in the fitted parameters.

In general, the subtraction procedure was accurate to a ∼5% of the contamination level. Therefore, the subtractions were performed only in the cases when the contamination was larger than that. Table 3 summarizes the resulting contamination levels in the U, B, V, R, and I bands for the cases where the subtraction was applied. Figure 8 shows an example of a contaminated spectrum of SN 1999au and the result of the subtraction. In this case, emission line intensities of Hα and N II λ6584 from the host galaxy were used to verify that very little scaling was needed for the reference spectrum (the scale factor was found to be 0.92). In this case, the contamination level found accounted for 79% of the total flux in the B band. The lower panel shows the subtracted spectrum and its fit to a non-contaminated spectrum of SN 1999be at a similar epoch. Clearly, any quantitative analysis of SN spectral characteristics is only possible after subtraction.

5. Discussion

Based on a large set of SN Ia spectroscopic data from the SCP Spring '99 campaign, we have developed a method to estimate uncertainties involved in SN Ia spectra. The final aim of this work is to produce suitable data for performing quantitative studies of the properties of these objects as distance indicators. These studies involve spectral feature measurements and modeling, and therefore benefit from the knowledge of uncertainties in the data.

The final calibrated spectra are produced with associated statistical uncertainties in the form of pixel-to-pixel correlation matrices. The signal-to-noise ratios found for the sample of over 100 spectra studied ranges between ∼1 and several hundred. Additionally, systematic uncertainties that cannot be corrected for are estimated by several independent means. The values found, ranging from 2% to 14% of the measured flux, apply to the whole wavelength coverage of the spectra. When analysing a certain region of the spectrum, these uncertainties can be scaled as the fraction of the total wavelength range that is under consideration.

The method for estimating systematic effects described in this paper was developed after the Spring '99 campaign was completed and is thus limited by the availability of calibration data. The spectra were obtained using an amount of telescopes during many observing nights rendering some heterogeneity in the observational techniques. This does not prevent the method from being of general use and, furthermore, from being considered when planning new campaigns.

The subtraction of host-galaxy light from the follow-up spectra by fitting to non-contaminated SN spectra can be regarded as a first quantitative study where the knowledge of uncertainties in both SN and

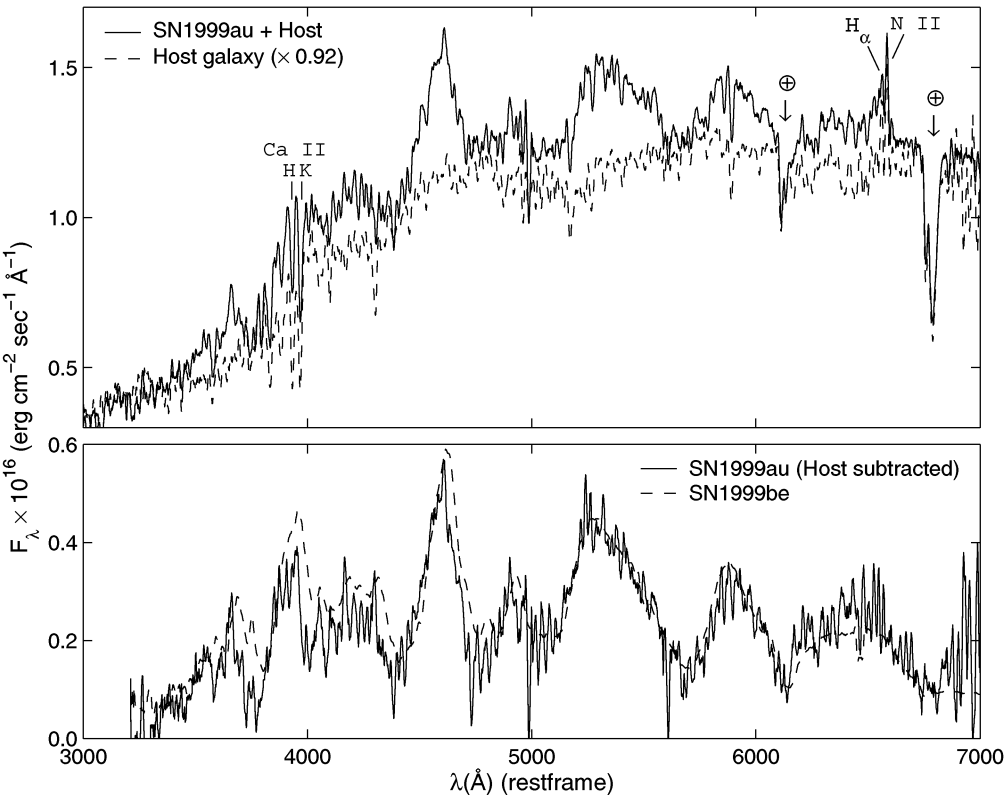

Fig. 8.— Example of host-galaxy subtraction by fitting to a non-contaminated SN spectrum. *Upper panel*: The observed spectrum of SN 1999au at 17 days after maximum light (*solid line*), and the corresponding reference spectrum where only the host is seen (*dashed line*), scaled by the fitted factor of 0.92. Some host-galaxy lines are marked as well as the most prominent telluric absorptions. *Lower panel*: The result of the subtraction (*solid line*), compared with the template, non-contaminated spectrum of SN 1999be at 19 days after maximum (*dashed line*). All the data was taken at the CTIO-4m telescope.

galaxy spectra lead to reliable results. The cases for which the subtraction method was applied are presented. The results yield a wide range of contamination levels, from a few percent to cases where the flux was largely dominated by the host galaxy. This kind of subtraction is essential for subsequent analysis such as spectral feature measurements or modeling.

The vast amount of low-redshift SNe Ia spectra from the Spring '99 campaign produced in this manner has been used in a number of studies. The analysis of spectral evolution, including measurements of expansion velocities, and detailed comparisons with synthetic spectra for the two most extensively followed up SNe in the sample (SN 1999aa and SN 1999ac) are found in Garavini et al. (2004a) and Garavini et al. (2004b), respectively. The application of a newly defined set of measurements, similar to equivalent widths, performed on the whole spectra sample and their possible correlation with luminosity is given in Folatelli et al. (2004).

A. Spectra combination using least-squares

This is an application of the least-squares method (LS) to the combination of several spectra of the same object. LS can be used to combine independent measurements of the same quantity, e.g. see Cowan (1998). In a general case, a linear model is given,

$$\vec{P} = A\vec{\theta}, \tag{A1}$$

where m unknown parameters $\vec{\theta} = (\theta_1, \theta_2, \cdots, \theta_m)$ are related to n expected values of a measurable quantity $\vec{P} = (P_1, P_2, \cdots, P_n)$ through an $n \times m$ matrix of coefficients A. If the results of measuring $\vec{P}$ are $\vec{Y}$, considered as random variables with covariance matrix V $(n \times n)$, and the entries of A are supposed to be known with no errors, then an estimate for the parameters can be calculated as,

$$\hat{\vec{\theta}} = (A^T V^{-1} A)^{-1} A^T V^{-1} \vec{Y}, \tag{A2}$$

and the errors on the parameters given by an $(m \times m)$ covariance matrix,

$$U = (A^T V^{-1} A)^{-1}. \tag{A3}$$

In the case of spectral combination, there is N measurements of the same object, i.e. the individual, interpolated spectra $S^{(i)}$, $1 \leq i \leq N$, each containing M wavelength bins. The parameters to be estimated are the values of the combined flux for each of the M bins. Therefore, if the measurement vector $\vec{Y}$ is the alignment of all the $S^{(i)}$ in a vector of dimensions $(NM \times 1)$ and if these are considered to be independent, then the covariance matrix V will be block-shaped, each block being the covariance of the individual measurements, $V^{(i)}$:

$$V = \begin{pmatrix} V^{(1)} & 0 & \cdots & 0 \\ 0 & V^{(2)} & \cdots & 0 \\ \vdots & \vdots & \ddots & \vdots \\ 0 & 0 & \cdots & V^{(N)} \end{pmatrix}, \tag{A4}$$

and the model matrix A will have the form,

$$A = \begin{pmatrix} I \\ -- \\ I \\ -- \\ \vdots \\ -- \\ I \end{pmatrix}, \tag{A5}$$

where I is the $(M \times M)$ identity matrix. The solution to the system (from Eq. A2) results in the combined spectrum $\hat{\vec{\theta}}$

$$\hat{\vec{\theta}} = \left(\sum_{i=1}^{N} \left[V^{(i)} \right]^{-1} \right)^{-1} \left(\sum_{i=1}^{N} \left(\left[V^{(i)} \right]^{-1} S^{(i)} \right) \right). \tag{A6}$$

And the final covariance matrix of the combined spectrum is (from Eq. A3):

$$U = \left(\sum_{i=0}^{N} \left[V^{(i)} \right]^{-1} \right)^{-1}. \tag{A7}$$

Table 1: Follow-up spectroscopic observations of the Spring '99 campaign.

Telescope + Instrument	Observation Date	Dispersor/ Channel	λ range[a] (Å)	$\langle\Delta\lambda\rangle$[b] (Å/pix)	σ_{syst}	No. of Stds.[c]
APO 3.5m	1999-02-17	blue	3650 - 6000	6.25	0.035	5
+ DIS	1999-02-17	red	4900 - 10400	7.0	0.045	5
	1999-02-26	blue	3650 - 6000	6.25	0.033	2
	1999-02-26	red	4900 - 10400	7.0	0.067	2
	1999-03-10	blue	3650 - 6000	6.25	0.143	2
	1999-03-10	red	4900 - 10400	7.0	0.039	2
	1999-04-06	blue	3650 - 6000	6.25	0.053	4
	1999-04-06	red	4900 - 10400	7.0	0.066	4
	1999-04-17	blue	3650 - 6000	6.25	0.043	5
	1999-04-17	red	4900 - 10400	7.0	0.053	5
CTIO 4m	1999-03-15	KPGL #2	3200 - 9300	1.99	0.032	9
+ RCSP	1999-03-17	KPGL #2	3200 - 9300	1.99	0.034	9
	1999-03-21	KPGL #2	3200 - 9300	1.99	0.057	13
	1999-03-24	KPGL #2	3280 - 9350	1.98	0.064	6
	1999-03-24	KPGL #2[d]	4880 - 9350	2.0	0.020	6
	1999-03-29	KPGL #2	3260 - 9350	1.98	0.041	8
	1999-03-29	KPGL #2[d]	4840 - 9350	2.0	0.032	6
ESO 3.6m	1999-03-13	#11	3350 - 7550	4.09	0.033	6
+ EFOSC 1.16	1999-04-10	#11	3400 - 7600	4.1	0.031	5
	1999-04-10	#12	6000 - 10300	4.2	0.023	5
	1999-04-15	#11	3420 - 7430	4.09	0.032	6
	1999-04-15	#12	6060 - 10220	4.24	0.037	6
	1999-04-18	#11	3400 - 7600	4.1	0.031	2
	1999-04-21	#11	3400 - 7600	4.1	0.040	8
	1999-04-21	#12	6000 - 10300	4.2	0.026	7
KPNO 4m + R-C	1999-04-06	BL 250	3050 - 10500	5.5	0.092	7
Lick 3m	1999-02-23	blue	3300 - 5500	1.8	···	1
+ KAST	1999-02-23	red	5050 - 10600	4.6	···	1
	1999-04-13	blue	3100 - 5500	1.85	0.107	7
	1999-04-13	red	3800 - 11000	4.6	0.089	7
	1999-04-24	blue	3300 - 5450	1.8	0.028	5
	1999-04-24	red	5280 - 8050	2.3	0.048	5
MDM 2.4m	1999-03-01	300 l/mm	3950 - 8950	5.4	0.043	2
+ Mark III	1999-03-02	300 l/mm	3950 - 8950	5.4	0.078	4
	1999-03-04	300 l/mm	3950 - 8950	5.4	0.08[e]	1
NOT	1999-02-13	#4	3050 - 9100	6.0	0.077	4
+ ALFOSC	1999-02-13	#5	3900 - 10150	6.2	0.024	2
	1999-02-14	#4	3000 - 9000	5.95	0.098	3
	1999-02-21	#4	3030 - 8980	5.9	0.13	4
	1999-02-21	#5	3950 - 10150	6.2	0.058[f]	1
	1999-03-15	#4	3000 - 9000	5.93	0.035	4
	1999-03-15	#5	3900 - 10150	6.15	0.015	3
	1999-03-23	#4	3000 - 9000	5.93	0.016[g]	1
	1999-03-23	#4	3000 - 9000	6.18	0.020[g]	1

[a] Approximate wavelength coverage in the observed frame.

[b] Average wavelength bin size in the observed frame. Typical resolution was ~2 to 3 pixels.

[c] Number of standard-star spectra observed.

[d] Using the order-cutting filter GG495.

[e] Value found using the sensitivity function from 1999-03-02.

[f] Value found using the sensitivity function from 1999-02-13.

[g] Value found using the sensitivity function from 1999-03-15.

Table 2:: Statistical and systematic uncertainties of the follow-up Spring '99 spectra.

SN Name (1)	z (2)	Telescope (3)	Obs. date (4)	Epoch (d) (5)	Exposure (s) (6)	λ range[a] (Å) (7)	$\langle\Delta\lambda\rangle$[a] (Å) (8)	σ_{syst} (9)	$\langle S/N\rangle$[b] (10)	σ_{grism} (11)	λ range[a] (Å) (12)
1999aa	0.0144	NOT	1999-02-13	-11	116+180	3500 - 9000	6.1	0.077	57	0.028	5160 - 5910
		NOT	1999-02-13	-11	2×180	5200 - 9300	6.1	0.024	57		
		APO 3.5m	1999-02-17	-7	600	3700 - 5900	6.2	0.035	109	0.069	5276 - 5887
		APO 3.5m	1999-02-17	-7	600	5200 - 10300	6.9	0.045	75		
		NOT	1999-02-21	-3	300+600	3350 - 8900	6.0	0.13	51	0.034	5164 - 5910
		NOT	1999-02-21	-3	600	5200 - 9700	6.2	0.058	41		
		Lick 3m	1999-02-23	-1	3×300	3300 - 5400	1.8	···	67	0.064	5171 - 5428
		Lick 3m	1999-02-23	-1	3×300	5000 - 10300	4.6	···	66		
		MDM 2.4m	1999-03-01	5	2×300	3900 - 8800	5.3	0.043	61		
		MDM 2.4m	1999-03-02	6	3×300	3900 - 8800	5.3	0.078	85		
		APO 3.5m	1999-03-10	14	1200	3600 - 5900	6.2	0.143	138	0.080	5036 - 5892
		APO 3.5m	1999-03-10	14	1200	4900 - 10300	6.9	0.039	75		
		NOT	1999-03-15	19	2×600	3350 - 8900	6.0	0.035	115	0.022	5038 - 5913
		NOT	1999-03-15	19	300	4900 - 10000	6.1	0.015	50		
		CTIO 4m	1999-03-21	25	500	3200 - 9200	2.0	0.057	88		
		CTIO 4m	1999-03-24	28	500	3200 - 9200	2.0	0.064	61	0.080	4880 - 9219
		CTIO 4m	1999-03-24	28	500	4800 - 9200	2.0	0.020	71		
		CTIO 4m	1999-03-29	33	500	3200 - 9200	2.0	0.041	64	0.058	4882 - 9198
		CTIO 4m	1999-03-29	33	500	4800 - 9200	2.0	0.032	74		
		APO 3.5m	1999-04-06	40	1800	3600 - 5900	6.2	0.053	47	0.070	5130 - 5881
		APO 3.5m	1999-04-06	40	1800	4900 - 10300	6.9	0.066	44		
		Lick 3m	1999-04-13	47	1200	3300 - 5500	1.8	0.107	31		
		Lick 3m	1999-04-13	47	1200	5000 - 10400	4.5	0.089	23		
		APO 3.5m	1999-04-17	51	2×1800	3600 - 5900	6.2	0.043	86	0.164	4999 - 5458
		APO 3.5m	1999-04-17	51	2×1800	4900 - 10300	6.9	0.053	67		
		Lick 3m	1999-04-24	58	1200	3250 - 5400	1.8	0.028	14	0.132	5211 - 5389
		Lick 3m	1999-04-24	58	1200	5200 - 8000	2.3	0.048	25		
1999ac	0.0095	APO 3.5m	1999-02-26	-15	3×1200	3600 - 5900	6.2	0.033	177	0.104	5227 - 5872
		APO 3.5m	1999-02-26	-15	3×1200	4900 - 10400	6.9	0.067	109		
		MDM 2.4m	1999-03-02	-11	300	3900 - 8850	5.3	0.078	38		
		MDM 2.4m	1999-03-04	-9	900	3800 - 8850	5.4	0.08	86		
		ESO 3.6m	1999-03-13	0	2×900	3300 - 7500	4.1	0.033	511		

Table 2:: (continued)

SN Name (1)	z (2)	Telescope (3)	Obs. date (4)	Epoch (d) (5)	Exposure (s) (6)	λ range[a] (Å) (7)	$\langle\Delta\lambda\rangle$[a] (Å) (8)	σ_{syst} (9)	$\langle S/N\rangle$[b] (10)	σ_{grism} (11)	λ range[a] (Å) (12)
		CTIO 4m	1999-03-15	2	300	3200 - 9300	2.0	0.032	171		
		NOT	1999-03-15	2	3×600	3300 - 8900	6.0	0.035	301	0.018	5062 - 5935
		NOT	1999-03-15	2	600	5150 - 9650	6.2	0.015	152		
		CTIO 4m	1999-03-21	8	2×300	3200 - 9250	2.0	0.057	213		
		CTIO 4m	1999-03-24	11	2×300	3250 - 9300	2.0	0.064	187	0.015	4901 - 9258
		CTIO 4m	1999-03-24	11	2×300	4800 - 9300	2.0	0.020	177		
		CTIO 4m	1999-03-29	16	400	3200 - 9250	2.0	0.041	126	0.059	4902 - 9242
		CTIO 4m	1999-03-29	16	2×400	4800 - 9250	2.0	0.032	181		
		KPNO 4m	1999-04-06	24	1200	3000 - 10400	5.4	0.092	81		
		ESO 3.6m	1999-04-10	28	2×900	3350 - 7450	4.0	0.031	322	0.010	5931 - 7419
		ESO 3.6m	1999-04-10	28	2×900	5950 - 10250	4.2	0.023	342		
		Lick 3m	1999-04-13	31	1500	3300 - 5500	1.8	0.107	69	0.101	5023 - 5487
		Lick 3m	1999-04-13	31	1500	5000 - 10500	4.6	0.089	84		
		ESO 3.6m	1999-04-15	33	2×600	3400 - 7350	4.1	0.032	255	0.014	6009 - 7360
		ESO 3.6m	1999-04-15	33	2×600	6000 - 10100	4.2	0.037	291		
		ESO 3.6m	1999-04-21	39	2×900	3350 - 7450	4.0	0.040	215	0.011	5944 - 7432
		ESO 3.6m	1999-04-21	39	2×600	5950 - 10200	4.2	0.026	194		
		Lick 3m	1999-04-24	42	2×900	3250 - 5400	1.8	0.028	77	0.085	5236 - 5415
		Lick 3m	1999-04-24	42	2×900	5250 - 8000	2.3	0.048	131		
1999af	0.097	APO 3.5m	1999-02-17	-5	2×1800	3400 - 9500	5.7	0.035	2		
		APO 3.5m	1999-02-17	-5	2×1800	3400 - 9500	6.4	0.045	5		
		Lick 3m	1999-02-23	1	2×1800	3050 - 5000	1.7	···	2		
		Lick 3m	1999-02-23	1	2×1800	4600 - 9700	4.4	···	1		
		ESO 3.6m	1999-03-13	17	2×900	3050 - 6900	3.7	0.033	0.6		
		CTIO 4m	1999-03-15	19	2×1800	3000 - 8500	1.8	0.032	(20)		
		NOT	1999-03-15	19	2×1800	3250 - 8200	5.6	0.035	(12)		
		NOT	1999-03-15	19	1800	4650 - 9250	5.7	0.015	(7)		
		CTIO 4m	1999-03-24	27	2×1800	3000 - 8500	1.8	0.064	(21)		
1999ao	0.054	CTIO 4m	1999-03-15	5	1500	3100 - 8850	1.9	0.032	25		
		CTIO 4m	1999-03-17	7	900	2950 - 8750	1.9	0.034	15		
		CTIO 4m	1999-03-21	10	1500	3100 - 8850	1.9	0.057	19		
		CTIO 4m	1999-03-24	13	1200	3100 - 8900	1.9	0.064	9		
		CTIO 4m	1999-03-29	18	693+1108	3100 - 8850	1.9	0.041	40		

Table 2:: (continued)

SN Name (1)	z (2)	Telescope (3)	Obs. date (4)	Epoch (d) (5)	Exposure (s) (6)	λ range[a] (Å) (7)	$\langle\Delta\lambda\rangle$[a] (Å) (8)	σ_{syst} (9)	$\langle S/N\rangle$[b] (10)	σ_{grism} (11)	λ range[a] (Å) (12)
		ESO 3.6m	1999-04-10	29	2×900	3200 - 7150	3.9	0.031	42	0.056	5681 - 7106
		ESO 3.6m	1999-04-10	29	2×900	5700 - 9800	4.0	0.023	48		
		ESO 3.6m	1999-04-15	34	3×900	3250 - 7050	3.9	0.032	11		
		ESO 3.6m	1999-04-21	40	3×1200	3200 - 7100	3.9	0.040	10		
1999ar	0.15	CTIO 4m	1999-03-15	6	2×1800	2850 - 7850	1.7	0.032	3		
1999at	0.027	APO 3.5m	1999-03-10	···	3600	3600 - 5800	6.1	0.143	(45)		
		APO 3.5m	1999-03-10	···	3600	4800 - 10200	6.8	0.039	(51)		
1999au	0.124	NOT	1999-03-15	12	3×1800	3000 - 8000	5.4	0.035	1	0.030	4541 - 5336
		NOT	1999-03-15	12	1800	4600 - 9000	5.4	0.015	4		
		CTIO 4m	1999-03-21	17	1800	2900 - 8300	1.8	0.057	11		
		CTIO 4m	1999-03-24	20	2×1200	2900 - 8350	1.8	0.064	10		
		CTIO 4m	1999-03-29	24	2×1500	2900 - 8300	1.8	0.041	9		
		KPNO 4m	1999-04-06	31	2×1500	2700 - 9350	4.9	0.092	6		
		ESO 3.6m	1999-04-15	39	4×1200	3050 - 6600	3.6	0.032	(99)		
1999av	0.05	APO 3.5m	1999-03-10	2	3×1800	3500 - 5700	6.3	0.143	39	0.027	5400 - 5692
		APO 3.5m	1999-03-10	2	3×1800	4700 - 9600	6.7	0.039	5		
		ESO 3.6m	1999-03-13	5	2×900	3200 - 7200	3.9	0.033	21		
		CTIO 4m	1999-03-17	9	2×900	3000 - 8800	1.9	0.034	20		
		CTIO 4m	1999-03-21	12	2×1500	3100 - 8900	1.9	0.057	17		
		CTIO 4m	1999-03-24	15	1200+831+1800	3150 - 8900	1.9	0.064	24		
		ESO 3.6m	1999-04-10	31	3×1200	3200 - 7150	3.9	0.031	11		
		ESO 3.6m	1999-04-21	41	2×1800	3200 - 7150	3.9	0.040	(175)		
1999aw	0.038	NOT	1999-03-15	3	3×900	3150 - 8650	5.8	0.035	86	0.024	4918 - 5778
		NOT	1999-03-15	3	2×900	4900 - 9750	6.0	0.015	54		
		CTIO 4m	1999-03-17	5	450+342+120	3000 - 8850	1.9	0.034	75		
		CTIO 4m	1999-03-21	9	1500	3150 - 9000	1.9	0.057	109		
		CTIO 4m	1999-03-24	12	1200	3150 - 9000	1.9	0.064	88		
		CTIO 4m	1999-03-29	16	2×1200	3150 - 9000	1.9	0.041	98		
		KPNO 4m	1999-04-06	24	1800	2950 - 10100	5.3	0.092	26		
		Lick 3m	1999-04-13	31	2×1500	3200 - 5250	1.8	0.107	24	0.175	4888 - 5299
		Lick 3m	1999-04-13	31	2×1500	4900 - 10150	4.4	0.089	14		
		ESO 3.6m	1999-04-21	38	2×900	3250 - 7200	3.9	0.040	65	0.030	5777 - 7228
		ESO 3.6m	1999-04-21	38	2×600	5750 - 9900	4.1	0.026	51		

Table 2:: (continued)

SN Name	z	Telescope	Obs. date	Epoch (d)	Exposure (s)	λ range[a] (Å)	$\langle\Delta\lambda\rangle$[a] (Å)	σ_{syst}	$\langle S/N\rangle$[b]	σ_{grism}	λ range[a] (Å)
(1)	(2)	(3)	(4)	(5)	(6)	(7)	(8)	(9)	(10)	(11)	(12)
1999be	0.019	CTIO 4m	1999-03-24	14	300	3200 - 9200	1.9	0.064	60		
		CTIO 4m	1999-03-29	19	500	3200 - 9150	1.9	0.041	72	0.064	4861 - 9155
		CTIO 4m	1999-03-29	19	500	4750 - 9150	2.0	0.032	66		
		APO 3.5m	1999-04-06	26	1800	3600 - 5850	6.1	0.053	72	0.089	5101 - 5855
		APO 3.5m	1999-04-06	26	1800	4850 - 10300	6.8	0.066	59		
		Lick 3m	1999-04-13	33	1200	3300 - 5450	1.8	0.107	35	0.133	4976 - 5435
		Lick 3m	1999-04-13	33	1200	5000 - 10400	4.5	0.089	34		
		APO 3.5m	1999-04-17	37	1800	3600 - 5850	6.1	0.043	50	0.074	5006 - 5851
		APO 3.5m	1999-04-17	37	1800	4850 - 10250	6.8	0.053	51		
		Lick 3m	1999-04-24	44	2×1200	3250 - 5350	1.8	0.028	12	0.117	5189 - 5364
		Lick 3m	1999-04-24	44	2×1200	5200 - 7900	2.3	0.048	24		
1999bf	0.2	CTIO 4m	1999-03-21	···	1800	2650 - 7550	1.6	0.057	11		
1999bh	0.0172	KPNO 4m	1999-04-06	···	1200	3000 - 10300	5.4	0.092	(32)		
		APO 3.5m	1999-04-17	···	1800	3600 - 5850	6.1	0.043	(30)	0.112	5015 - 5862
		APO 3.5m	1999-04-17	···	1800	4850 - 10300	6.8	0.053	(38)		
		Lick 3m	1999-04-24	···	1200	3250 - 5350	1.8	0.028	(17)		
		Lick 3m	1999-04-24	···	1200	5200 - 7950	2.3	0.048	(46)		
1999bi	0.123	CTIO 4m	1999-03-15	6	1800+800	2900 - 8300	1.8	0.032	20		
		CTIO 4m	1999-03-21	12	2×1500	2900 - 8300	1.8	0.057	14		
		NOT	1999-03-23	13	418	4600 - 8500	5.5	0.020	7		
		ESO 3.6m	1999-04-10	29	3×1200	3000 - 6650	3.7	0.031	6		
		ESO 3.6m	1999-04-18	36	2×1800	3000 - 6650	3.7	0.031	5		
1999bk	0.096	CTIO 4m	1999-03-17	4	2×600	2850 - 8400	1.8	0.034	19		
		CTIO 4m	1999-03-21	7	2×1200	2950 - 8500	1.8	0.057	37		
		NOT	1999-03-23	9	2×1500	4600 - 8500	5.7	0.020	24		
		CTIO 4m	1999-03-24	10	1800	6750 - 8550	1.8	0.064	14		
		KPNO 4m	1999-04-06	22	1800	2800 - 9600	5.0	0.092	(55)		
		ESO 3.6m	1999-04-15	30	1800+1600+1800	3100 - 6800	3.7	0.032	32		
1999bm	0.143	CTIO 4m	1999-03-21	3	1800	2850 - 8150	1.7	0.057	15		
		CTIO 4m	1999-03-24	6	2×1500	2850 - 8200	1.7	0.064	15		
		ESO 3.6m	1999-04-10	21	4×1200	2950 - 6600	3.6	0.031	8		
		ESO 3.6m	1999-04-18	28	1800	2950 - 6550	3.6	0.031	5		
1999bn	0.129	NOT	1999-03-23	2	2×1350	3300 - 8000	5.4	0.016	16		

Table 2:: (continued)

SN Name (1)	z (2)	Telescope (3)	Obs. date (4)	Epoch (d) (5)	Exposure (s) (6)	λ range[a] (Å) (7)	$\langle\Delta\lambda\rangle$[a] (Å) (8)	σ_{syst} (9)	$\langle S/N\rangle$[b] (10)	σ_{grism} (11)	λ range[a] (Å) (12)
		KPNO 4m	1999-04-06	14	2×1800	3000 - 9300	4.8	0.092	5		
		ESO 3.6m	1999-04-15	22	2×1800	3050 - 6600	3.6	0.032	20		
		ESO 3.6m	1999-04-21	27	2×1800	3000 - 6650	3.6	0.040	18		
1999bp	0.077	CTIO 4m	1999-03-21	-2	900	3000 - 8650	1.8	0.057	35		
		NOT	1999-03-23	0	1500	4800 - 8800	5.8	0.020	21		
		CTIO 4m	1999-03-24	1	1500	3050 - 8700	1.8	0.064	50		
		CTIO 4m	1999-03-29	6	2×1500	3050 - 8700	1.8	0.041	63		
		KPNO 4m	1999-04-06	13	1500	2850 - 9750	5.1	0.092	(53)		
		ESO 3.6m	1999-04-10	17	2×900	3150 - 6950	3.8	0.031	54		
		APO 3.5m	1999-04-17	23	2×2100	3400 - 5550	5.8	0.043	26	0.146	4730 - 5536
		APO 3.5m	1999-04-17	23	2×2100	4600 - 9700	6.5	0.053	19		
		Lick 3m	1999-04-24	30	2×1800	3050 - 5100	1.7	0.028	4		
		Lick 3m	1999-04-24	30	2×1800	4900 - 7500	2.2	0.048	9		
1999bq	0.149	NOT	1999-03-23	3	1350	2900 - 7850	5.3	0.016	5		
		CTIO 4m	1999-03-24	3	1800	2900 - 8150	1.8	0.064	9		
		ESO 3.6m	1999-04-10	18	4×1200	2950 - 6550	3.5	0.031	9		
		ESO 3.6m	1999-04-15	23	2×1800	3000 - 6450	3.6	0.032	6		
		ESO 3.6m	1999-04-21	28	2×1800	2950 - 6550	3.6	0.040	4		

[a] Wavelength values in the SN rest frame.

[b] Average signal-to-noise ratio per 10 Å. Values between brackets correspond to spectra with uncorrected host-galaxy contamination.

Table 3: Host-galaxy contamination levels.

SN	Host	Epoch	Contamination level (%)[b]				
Name	Type[a]	(d)	f_U	f_B	f_V	f_R	f_I
1999ao	Sa	5		12	17	27	
		7	39	25	26	37	
		10		19	22	32	
		13		35	37	47	
		18		9	7	9[c]	
		29		40	33	36	39
		34		45	42		
		40		45	40		
1999au	Sb	12		52	59	67	
		17	79	79	80	88	
		20	77	73	71	78	
		24	87	75	70	74	
1999av	E/S0	2		60	81	83	87
		5		33	50		
		31		46	47		
1999bi	Sb	6	22	24	33	44	
		12	35	34	42	50	
		29	94	85			
		36	97	93			

[a] Classification based on the host-galaxy *reference* spectra and the catalog given in Kennicutt (1992).

[b] Percentage of host-galaxy flux in the total U, B, V, R, and I fluxes.

[c] The higher quality and signal of this spectrum allowed a cleaner extraction of the SN separated from its host.

REFERENCES

Aldering, G. 2000, *Cosmic Explosions: Tenth Astrophysics Conference. AIP Conference Proceedings, Vol. 522*, Edited by Stephen S. Holt and William W. Zhang, p 75

Barrell, H. 1951, J.Opt.Soc.Am., 41, 295

Branch, D., & van den Bergh, S. 1993, AJ, 105, 2231

Cardelli, J. A., Clayton, G. C., & Mathis, J. S. 1989, ApJ, 345, 245

Coleman, C. D., & Bozman, W. R., and Meggers, W. F. 1960, Tables of Wavenumbers, N.B.S. Monograph 3, Washington, p. IV

Cowan, G. 1998, Statistical data analysis, Oxford University Press, p. 106

Edlen, B. 1953, J. Opt.Soc.Am., 43, 339

Filippenko, A. V. 1982, PASP, 94, 715-721 and references therein

Folatelli, G. et al. 2004, ...

Garavini, G. et al 2004, ...

Garavini, G. et al 2004, ...

Hatano, K. et al. 2000, ApJ, 543, L49

Horne, K. 1986, PASP, 98, 609

Kennicutt, R. C. 1992, ApJS, 79, 255

Knop, R. A. et al. 2003, ApJ, 598, 102

Nugent, P. et al. 1995, ApJ, 455, L147

Nugent, P., Aldering, G. & The Nearby Campaign 2000, *Supernovae and gamma-ray bursts: The Greatest Explosions Since the Big Bang*, Mario Livio, Nino Panagia, Kailash Sahu, editors, p. 47

Osterbrock, D. E., & Martel, A. 1992, PASP, 104, 76

Perlmutter, S. et al. 1999, ApJ, 517, 565

Riess, A. G. et al. 1998, AJ, 116, 1009

Schlegel, D. J., Finkbeiner, D. P., & Davis, M. 1998, ApJ, 500, 525

Tonry, J. L. et al. 2003, ApJ, 594, 1
